La Dynamique Moléculaire Classique au service de la spectroscopie des plasmas non-idéaux

Sandrine Ferri

UNIVERSITÉ d'AIX-MARSEILLE

Document de Synthèse

présenté par

Sandrine FERRI

en vue de l'obtention de

l'Habilitation à Diriger des Recherches

La Dynamique Moléculaire Classique au service de la spectroscopie des plasmas non-idéaux

soutenue le 30 juin 2015

Jury :

Rapporteurs :	Jean Clérouin	-	CEA DAM
	Richard W Lee	-	University of Berkeley
	Gilles Maynard	-	LPGP / Université Paris Sud - CNRS
Examinateurs :	Fabien Dorchies	-	CELIA / Université de Bordeaux - CNRS
	Annie Klisnick	-	ISMO / Université Paris Sud - CNRS
	Guy Le Lay	-	PIIM / Aix-Marseille Université
	Laurence Mouret	-	PIIM / Aix-Marseille Université
Invitée :	Annette Calisti	-	PIIM / Aix-Marseille Université - CNRS

Il est grand temps de rallumer les étoiles.
G. Apollinaire (1916).

Table des matières

Chapitre 1

Introduction

La spectroscopie des plasmas est une des disciplines de la physique des plasmas qui s'intéresse au rayonnement émis par ce dernier. Les caractéristiques du spectre des raies émises peuvent être interprétées en terme de propriétés du plasma. En effet, la position des raies, leur intensité (ainsi que l'émission du continuum), leur élargissement et leur déplacement sont intimement liés à la composition, la température, la densité, l'état d'ionisation du plasma. Ces caractéristiques mesurées expérimentalement et comparées aux modèles théoriques permettent indirectement une mesure des paramètres du plasma. Ce type de *diagnostic* est largement utilisé en astrophysique mais aussi dans les plasmas de laboratoire comme sonde non intrusive, comme par exemple dans les plasmas de fusion par confinement magnétique, dans les plasmas de fusion par confinement inertiel, dans les plasmas de décharges ou dans ceux créés par l'interaction laser sur une cible solide. Évidemment cette technique est très dépendante des modèles utilisés.

La modélisation des propriétés radiatives des plasmas s'appuie sur un amalgame complexe de connaissances pour lesquelles la physique atomique, la physique statistique, l'hydrodynamique, la physique des plasmas et le transfert radiatif ont tous un rôle à jouer. Un plasma est un milieu globalement neutre, partiellement ou totalement ionisé constitué d'atomes neutres, d'ions (pouvant présenter différents états de charges) et d'électrons. Du fait des interactions électromagnétiques entre les particules chargées (attractives ou répulsives suivant la charge en jeu), chaque particule peut interagir simultanément avec un très grand nombre de particules. Les ions et les électrons du plasma présentent donc un comportement collectif et leur lien au plasma environnant sera d'autant plus important que la densité augmentera et/ou la température diminuera. Ainsi, dans un plasma de densité donnée, le potentiel électrique produit dans et autour d'un ion peut être influencé non seulement par ses propres électrons liés mais aussi par les électrons libres, par les ions au voisinage et (très faiblement) par les atomes neutres. Ces perturbateurs produisent sur l'ion deux types d'effets : leur effet moyenné dans le temps est d'altérer la distribution des niveaux d'énergie de l'ion en question et leur effet dépendant du temps est d'élargir ces niveaux par un déplacement adiabatique et de produire des transitions entre eux :

— Le premier effet diminue le potentiel d'ionisation : les interactions avec les ions et les électrons environnants modifient les niveaux d'énergie des états liés dont certains disparaissent dans le continuum. Plus important aux hautes densités, il est généralement connu sous le nom de *d'ionisation par*

effet de pression, [1]. C'est le processus dominant qui détermine les abondances ioniques et les populations des niveaux d'énergie dans les études de la matière à haute densité. La prise en compte de l'*abaissement du potentiel d'ionisation* (IPD) est inévitable dans plusieurs domaines. Pour produire les équations d'états, il faut fournir les abondances ioniques avant de calculer la pression électronique. Le calcul des coefficients de transport tels que la conductivité, les sections efficaces, etc, nécessite la connaissance de la densité électronique et donc de l'état d'ionisation du plasma. Finalement, les opacités sont gouvernées par les abondances ioniques et les populations des niveaux, [2].

— Le second effet relève de *l'élargissement par effet de pression* : les particules chargées du plasma créent des microchamps électriques fluctuants, qui, par effet Stark, modifient la structure atomique des émetteurs et par conséquent la forme des profils des raies émises. La prise en compte de ces champs électriques ioniques et électroniques dans le formalisme des profils de raies est un problème compliqué de part la nature aléatoire et fluctuante de la perturbation mais elle est essentielle tant sur le plan fondamental (pour une meilleure compréhension des processus sous-jacents) que sur le plan expérimental (pour un meilleure analyse des spectres). L'élargissement Stark des raies dans les plasmas a été le sujet de nombreuses études, [3], depuis la publication en 1958 des travaux de Baranger, [4] et de Griem, Kolb et Shen, [5]. Les points de vues généralement adoptés sont : i) l'émetteur est couplé individuellement avec chaque perturbateur du bain thermique. L'interaction est alors représentée par des chocs binaires. C'est l'*approximation d'impact* (généralement utilisée pour décrire les interaction électrons-émetteur), ii) l'émetteur échange de l'énergie avec l'ensemble du bain thermique. On adopte ici une vision statistique de l'environnement dans laquelle les microchamps fluctuant lentement sont représentés par leur distribution statique. C'est l'*approximation quasi-statique* (généralement utilisée pour décrire les interactions ions-émetteurs). Cette approximation n'est valable que si tous les mécanismes d'élargissement des raies provoquent une perte de mémoire avant que les ions n'aient eu le temps de bouger de manière significative. Dans le cas contraire, il faut tenir compte de la *dynamique des ions*.

Les particules neutres ou chargées émettent donc un rayonnement dont les spectres portent la « marque » du plasma environnant (présence de champs électriques locaux fluctuants, opacités, processus collisionnels, etc.). L'étude des propriétés d'un tel milieu passe par l'analyse des propriétés à l'équilibre et hors équilibre d'un système statistique contenant de nombreuses particules chargées électriquement qui interagissent entre elles. Le système étant caractérisé par un très grand nombre de degrés de liberté, le traitement théorique de ce problème relève des problèmes à *N-corps* et passe obligatoirement par la statistique. L'étude

complète de tous les phénomènes apparaissant dans le processus d'émission de rayonnement d'un plasma est à ce jour impossible que ce soit analytiquement ou numériquement.

Néanmoins, les *simulations numériques* jouent un rôle important dans la mesure où elles fournissent des résultats exacts à des problèmes de mécanique statistique qui n'auraient pu être résolus que de manière approchée, voire non résolus du tout. Cependant, leur *réalisme* est intimement lié au modèle choisi pour décrire le phénomène physique. Tous les modèles de plasma développés sont des simplifications initiales du problème, judicieusement établies afin de préserver le phénomène physique que l'on souhaite étudier, [6] :

> *« ... it seems appropriate to ... study the properties of some simple models which share at least some of the essential features of real physical systems. »*

Les modèles de simulation numérique mettant en jeu des particules classiques qui interagissent entre elles appartiennent à la catégorie des *modèles particulaires* et la méthode que nous avons adoptée est la *Dynamique Moléculaire Classique (DM)*, [7]. À chaque particule (ion et électron du plasma), on attribue un ensemble de caractéristiques physiques telles la masse, la charge, la position, la quantité de mouvement, etc. L'état du système est défini par la connaissance de ces caractéristiques pour un ensemble fini de particules et l'évolution du système est déterminée par les lois de forces entre ces particules. Le système dans la boite de simulation est neutre et les conditions aux limites périodiques sont utilisées pour modéliser un système infini. Ainsi, avec la DM, toutes les interactions entre les charges sont prises en compte, les aspects collectifs apparaissent naturellement et les mécanismes dépendants du temps peuvent être étudiés. Elle permet, par exemple, de mesurer les microchamps électriques sur chaque particule à chaque instant. Ces derniers peuvent être utilisés pour le calcul exact de l'opérateur d'évolution moyen du système émetteur, par intégration de l'équation de Schrödinger sur un grand nombre de configurations. Cette méthode est jusqu'à présent la méthode qui possède la meilleure base théorique pour traiter l'effet des fluctuations des microchamps électriques sur les profils de raies et des effets de couplages entre les particules chargées. Elle possède cependant des limitations. Par exemple, pour le calcul des profils de raies, elle s'avère lente et inadaptée aux systèmes émetteurs de structure atomique complexe. Nous ne l'utilisons donc pas à des fins de diagnostics mais en accompagnement au développement de modèles théoriques plus rapides et plus efficaces.

Ainsi, le fil conducteur de ce travail de synthèse est l'utilisation de la dynamique moléculaire classique comme outil de validation des modèles développés pour la spectroscopie des plasmas. Après avoir présenté la méthode de dynamique mo-

léculaire classique et les possibilités que cette méthode offre dans le domaine de la mécanique statistique, nous décrirons plus précisément son apport dans l'étude des *plasmas non-idéaux*. Nous verrons notamment qu'elle permet de discuter de certaines propriétés de la *matière tiède et dense* dont l'étude s'avère être un véritable challenge tant sur le plan expérimental que théorique. Quelques résultats sur des mesures d'abaissement du potentiel d'ionisation et des calculs de facteurs de structure dynamique seront présentés. Nous développerons ensuite l'aspect profils de raies dans les plasmas en montrant combien la dynamique moléculaire est omniprésente dans la validation des modèles tel que le *Modèle de Fluctuation de Fréquence* (FFM) développé pour tenir compte de la dynamique des ions, [8, 9]. Son côté robuste et versatile a permis aussi d'étudier l'effet des perturbations extérieures comme des champs électriques oscillants ou des champs magnétiques et de valider l'extension du FFM au calcul des profils de raies élargies par effet Stark et Zeeman. Finalement nous verrons une application de la DM pour l'étude des effets de corrélation sur les profils Doppler des raies utilisées pour le développement des lasers X.

Bibliographie

[1] R.M. More, *Pressure Ionization, Resonances, and the Continuity of Bound and Free States*, Adv. At. Mol. Phys. **21**, 305-356 (1985).

[2] G. Chiu and A. Ng, *Pressure ionization in dense plasmas*, Phys. Rev. E **59**, 1024-1032 (1998).

[3] H.R. Griem, *Spectral line broadening by plasmas* Academic Press, New York (1974).

[4] M. Baranger, *Problem of Overlapping Lines in the Theory of Pressure Broadening*, Phys. Rev. **111**, 494-504 (1958).

[5] H.R. Griem, A.C. Kolb, K.Y. Shen, *Stark broadening of hydrogen lines in plasma*, Phys. Rev. **116**, 4-16 (1959).

[6] S.G. Brush, H.L Sahlin, E. Teller, *Monte Carlo study of a one-component plasma*, J. Chem. Phys. **45**, 2102-2118 (1966).

[7] B.J. Alder and T.E. Wainwright, *Phase Transition for a Hard Sphere System*, J. Chem Phys. **27**, 1208-1209 (1957) ; *Studies in Molecular Dynamics. I. General Method*, J. Chem Phys. **31**, 459-466 (1959).

[8] B. Talin et al., *Frequency-fluctuation model for line-shape calculations in plasma spectroscopy*, Phys. Rev. A **51**, 1918-1928 (1995).

[9] A. Calisti et al., *Dynamic Stark broadening as the Dicke narrowing effect*, Phys. Rev. E **81**, 016406 (2010).

Chapitre 2

État de l'art de la dynamique moléculaire classique

La simulation numérique est devenue un outil incontournable de nos jours pour la modélisation des systèmes naturels en sciences et en ingénierie, mais également des systèmes humains en économie et en sciences sociales. Le terme *simulation numérique* désigne l'exécution d'un programme informatique en vue de simuler un phénomène physique (ou humain) réel et complexe. Elle se base sur la modélisation mathématique du phénomène d'intérêt et la résolution des équations utilise souvent la technique des éléments finis conduisant à des solutions numériques.

La démarche de modélisation numérique suit généralement trois grande étapes. La première consiste à définir de façon précise le modèle physique correspondant au phénomène à étudier, avec les équations correspondantes. Ceci nécessite une très bonne connaissance des conditions dans lesquelles ces équations sont valides : échelle de temps et d'espace, nature des interactions mises en jeu, etc. La deuxième étape consiste à définir l'algorithme qui permet de traduire de manière la plus simple et la plus efficace les équations résultants du modèle choisi. Cette étape doit être menée en adéquation avec les machines utilisées, le choix du langage de programmation et la relation avec les bibliothèques existantes. Enfin, la troisième étape consiste à exécuter le modèle dans un environnement informatique afin de produire les résultats informatiques. Au temps $t = 0$, l'état initial du système est spécifié dans une région finie de l'espace (*la boîte de simulation*) dont les surfaces sont soumises à certaines conditions aux limites. L'évolution du système est suivie temporellement. À chaque instant $t' = t + \Delta t$, avec Δt le pas de temps élémentaire, l'état du système est calculé, ce qui produit une quantité d'information énorme. Tout l'art réside dans l'interprétation de ces résultats et dans la vérification de la validité des modèles utilisés par confrontation aux résultats expérimentaux ou à d'autres modèles. C'est en ce sens qu'on qualifie la simulation numérique d'*expérience numérique*.

Les phénomènes qui nous intéressent ici, concernent la physique des plasmas et plus particulièrement les propriétés statistiques statiques et dynamiques à l'équilibre ou non des plasmas. Il existe plusieurs modèles pour décrire l'état plasma : particulaires, cinétiques, fluides, hybrides, etc... Suivant le modèle utilisé, on obtient des codes de simulations numériques très différents qui permettent de résoudre des problèmes très différents. Le choix du modèle (et du code) dépend donc des pro-

priétés physiques que l'on souhaite extraire. Par exemple, dans les codes MHD [1], le plasma est considéré comme un fluide, avec un comportement proche de l'équilibre thermodynamique à grande échelle. Ces codes décrivent les propriétés des moyennes statistiques des particules du plasma, telles que les densités, les vitesses, et les énergies moyennes, plutôt que leurs propriétés individuelles. Les codes cinétiques par contre considèrent le plasma comme une collection de particules interagissant entre elles via le champ électromagnétique qu'elles produisent. Dans ces codes, soit les équations cinétiques de type Vlasov ou Fokker-Planck sont résolues numériquement, soit un modèle particulaire du type PIC (*Particle in Cells*) est utilisé. Dans ce dernier type de simulation, les ions et les électrons du plasma sont suivis comme des particules individuelles ou sont regroupés en super-particules sur une grille de champ de forces. Elles sont utilisées principalement pour l'analyse des processus à petites échelles essentielle dans les régions d'interface plasma-surface où ont lieu des transferts d'énergie entre les ondes électromagnétiques et les particules chargées. Lorsque l'on s'intéresse aux interactions entre les particules chargées du plasma et aux champs électriques qu'elles produisent, les deux méthodes de simulation les plus adaptées sont la méthode de Monte Carlo (MC), [1], et *la Dynamique Moléculaire* (DM), [2]. Elles ont été mises au point dans le but de résoudre numériquement les problèmes à N corps de la mécanique classique (et plus particulièrement des systèmes moléculaires). Initialement, elles ont été développées pour l'étude des fluides neutres et denses dans lesquels les interactions à courte portée entre sites peuvent être décrits par un potentiel de Lennard-Jones, [2, 3, 4, 5, 6]. Depuis, elles ont montré qu'elles pouvaient être très puissantes pour l'étude des systèmes avec des potentiels d'interaction à longue portée ou pour l'étude des plasmas où les interactions entre les particules chargées sont représentées par un potentiel de Coulomb écranté. Par contre, la méthode MC permet seulement d'obtenir les propriétés statiques du système alors que la DM, qui résout les équation du mouvement pour chaque particule et donne accès aux trajectoires dans l'espace des phases est plus spécifiquement adaptée au calcul des propriétés dynamiques.

Dans la suite de ce chapitre, la méthode de dynamique moléculaire est rappelée dans ses grandes lignes puis nous verrons son adaptation à la simulation des plasmas qui réside essentiellement dans le choix des potentiels d'interaction. Finalement, nous rappellerons les outils de mesures statistiques d'intérêt pour l'étude des propriétés radiatives et des effets de corrélations entre les charges qui seront utilisés dans les chapitres suivants.

2.1 La DM : qu'est-ce que c'est ?

La *dynamique moléculaire* est une technique de simulation numérique où l'évolution temporelle d'un ensemble de particules en interaction est suivie en intégrant

1. magnétohydrodynamique

leurs équations du mouvement. Elle utilise les lois de la mécanique classique, notamment les équations de Newton, qui pour chaque particule i de masse m_i s'écrivent :

$$\begin{cases} m_i \frac{d^2\vec{r}_i(t)}{dt^2} = \vec{F}_i(t), \\ \vec{F}_i(t) = -\frac{\partial V(\vec{r}^N)}{\partial \vec{r}_i} \quad \text{avec } \frac{\partial}{\partial \vec{r}} : \text{opérateur gradient.} \end{cases} \tag{2.1}$$

Ici, on considère des particules à symétrie sphérique. $V(\vec{r}^N)$ est le potentiel d'interaction du système à N particules où l'ensemble des positions $\vec{r}^N = \{\vec{r}_1, \vec{r}_2, ..., \vec{r}_N\}$ définit une *configuration* du système. $\vec{F}_i(t)$ est la force exercée sur la particule i par les $(N-1)$ autres particules. Cette forme implique une loi de conservation de l'énergie totale $E = K + V$, où K est l'énergie cinétique moyenne des particules.

Dans la plupart des simulations (et ce sera notre cas), le potentiel est choisi comme étant la somme d'interactions par paires de particules :

$$V(\vec{r}^N) = \sum_i \sum_{j>i} V_{ij}(\vec{r}_{ij}) \quad \text{avec } \vec{r}_{ij} = |\vec{r}_i - \vec{r}_j|. \tag{2.2}$$

On a donc un système de $3N$ équations différentielles couplées que l'on se propose de résoudre numériquement en discrétisant celles-ci sur un pas de temps δt. Il doit être suffisamment petit pour que les forces puissent être considérées constantes dans cet intervalle de temps. À chaque itération, les forces agissant sur les particules sont calculées et les nouvelles positions et les nouvelles vitesses en sont déduites. En répétant ces opérations plusieurs milliers de fois, on obtient les trajectoires individuelles dans l'espace des phases.

Les trajectoires ainsi déterminées sont utilisées pour évaluer les propriétés statiques et dynamiques par des moyennes temporelles, qui coïncident avec les moyennes statistiques pour des systèmes ergodiques :

$$\lim_{t\to\infty} \overline{A}_t = \langle A \rangle, \tag{2.3}$$

où A désigne une propriété quelconque, observable, $\overline{A}_t$ sa moyenne temporelle, et $\langle A \rangle$, sa moyenne d'ensemble statistique.

La mesure d'une quantité physique par la simulation est donc obtenue par la moyenne arithmétique des valeurs instantanées de cette quantité mesurée au cours de l'exécution de la simulation. Elle permet donc d'obtenir différentes propriétés macroscopiques du système étudié à partir du comportement collectif des particules individuelles. Cependant, on ne peut pas faire une simulation sur un temps infini et sur un système infini. En effet, la DM est limitée par la vitesse et les capacités de calculs des ordinateurs. Typiquement, les simulations de DM sont appliquées à des systèmes contenant des centaines voire des milliers de particules interagissant par l'intermédiaire de forces à relativement courte portée [2]. Les échelles de temps

2. c'est-à-dire que les forces inter-particules doivent être faibles quand les particules sont séparées par une distance égale à la moitié de la plus petite dimension du système.

vont de quelques picosecondes aux centaines de nanosecondes. Une simulation est *bonne* du point de vue de sa durée, si cette dernière est bien plus grande que le temps de relaxation caractéristique de la quantité considérée afin de générer un très grand nombre de fois ce temps. La taille limitée du système peut aussi constituer un problème. Dans ce cas, il faut comparer la taille de la boîte de simulation aux longueurs de corrélation des fonctions de corrélations d'intérêt. Par exemple, dans les plasmas où la cinétique est importante, il faudra une taille de la boîte de simulation très grande comparée à la longueur d'écran naturelle du potentiel d'interaction.

L'ingrédient essentiel qui contient la physique dans la DM est les forces qui agissent sur chaque particule. Une simulation est réaliste, c'est-à-dire imite le comportement d'un système réel, seulement si les forces inter-particules sont similaires à celles que les particules réelles du système subiraient dans les conditions dans lesquelles est exécutée la simulation. La méthode utilisée pour calculer les forces d'interactions (ou le potentiel dont elles dérivent) caractérise donc une simulation, [7]. Par exemple, on parle de *dynamique moléculaire ab initio* (ou quantique), si le potentiel est calculé à partir des premiers principes de la mécanique quantique. Si par contre, les forces dérivent d'un potentiel qui présuppose un type d'interaction, un état de charge Z, etc., on parlera de *dynamique moléculaire classique*. C'est cette dernière technique que nous développons pour simuler différents types de plasmas et le problème du choix du potentiel sera discuté dans la section 2.3.1.

2.2 Sa mise en œuvre

On travaille généralement sur un petit nombre de particules ($N \sim 10^2 - 10^3$) localisée dans une boîte cubique choisie pour sa simplicité géométrique. Cependant, une grande portion de ces particules (de l'ordre de $N^{2/3}$) se trouvent près de la surface de la boîte. Elles ne sont pas dans les mêmes conditions que les particules au centre de la boîte. Pour s'affranchir de cette difficulté, on utilise des conditions aux limites périodiques, [7] :

— la boîte cubique est répliquée dans l'espace pour former un système infini,
— les particules d'intérêt sont dans la boîte centrale, quand une particule en sort avec une vitesse donnée, son image y entre par le côté opposé avec la même vitesse.

La densité dans la boîte et donc dans le système en entier est ainsi conservée. L'avantage de cette représentation est qu'il n'est pas nécessaire de conserver les coordonnées de toutes les images de la simulation mais seulement celles de la boîte centrale.

Pour calculer les forces qui agissent sur une particule P donnée, on utilise la convention de l'image minimale qui est une conséquence directe des conditions aux limites périodiques, [1]. La particule P est considérée au centre d'une région identique à la boîte de simulation. P interagit avec toutes les particules qui se trouvent dans cette région, c'est-à-dire les $N-1$ plus proche particules (appartenant à la boîte de simulation ou ses images). Le calcul des forces ne met en jeu que $\frac{1}{2}N(N-1)$ termes au lieu d'une infinité si on tient compte de toutes les interactions avec les images tombant dans les boîtes environnantes. Cette technique tire avantage du fait que dans la plupart des cas les potentiels d'interaction utilisés sont à courte portée. En ce qui nous concerne, pour la simulation des plasmas, on utilise généralement des potentiels de Coulomb écrantés. Mais ceci implique que la longueur d'écran doit être plus petite que la demi-longueur de la boîte. C'est ce critère qui fixe le nombre de particules minimum dans la boîte de simulation dont la dimension est définie par :

$$c = (N/n)^{1/3}, \tag{2.4}$$

où n est la densité de particules (ions ou électrons) exprimée en cm^{-3}. On verra dans les Chapitre 3 et 4, qu'un critère supplémentaire lié à la longueur d'onde du rayonnement contraint le nombre de particules dans la boîte de simulation.

Remarques : Dans le cas où la portée des potentiels est courte, la boîte peut être dotée de parois réfléchissantes à la place des conditions aux limites périodiques, [8]. Dans le cas où les interactions sont à plus longue portée, une méthode pour éviter une coupure explicite à la taille de la boîte, repose sur la technique de somme d'Ewald, [9].

Pour intégrer numériquement les équations du mouvement, il est nécessaire de les discrétiser en temps. Plusieurs méthodes existent mais il est important d'en choisir une qui conserve l'énergie du système au cours du temps. Nous utilisons l'algorithme de Verlet Vitesse, [4, 10], réputé pour sa stabilité (conservation de l'énergie et de la température), sa facilité de programmation et sa rapidité.

L'énergie cinétique, $K = \frac{1}{2}\sum_i m_i[\vec{v}_i(t)]^2$ (avec $\vec{v}_i(t)$ la vitesse de la particule i), est connue à chaque pas de temps et l'énergie potentielle est évaluée dans la routine du calcul des forces. On peut donc contrôler l'énergie totale régulièrement afin de s'assurer de la stabilité de la méthode d'intégration.

2.3 La simulation des plasmas

Pour les plasmas, c'est-à-dire un milieu neutre constitué d'atomes et de particules chargées (ions et électrons) présentant un comportement collectif, le problème initial est de déterminer l'interaction effective entre les différentes particules. Ce problème sera résolu différemment selon la nature du plasma étudié. Pour cela on définit un paramètre de couplage sans dimension qui caractérise la force d'interaction entre les

particules du système. Il est égal au rapport entre l'énergie potentielle inter-particule moyenne et l'énergie cinétique moyenne. Par exemple, pour un système contenant une densité n de particules de charge Z et de température T, on a :

$$\Gamma = \frac{(Ze)^2}{r_0 k_B T}, \text{ avec } r_0 = (\frac{3Z}{4\pi n})^{1/3}, \tag{2.5}$$

où r_0 est la distance inter-particule ; il correspond au rayon de la sphère de volume caractéristique $1/n$.

Pour $\Gamma \ll 1$, le plasma est faiblement couplé ; il est dit idéal ou cinétique. C'est le cas par exemple, des plasmas de basse densité ou de haute température dans lesquels les particules se déplacent sur des trajectoires balistiques entre deux « collisions » et les interactions à plusieurs particules sont rares. Pour $\Gamma \approx 1$ le plasma est couplé ; l'énergie moyenne d'interaction coulombienne devient comparable à l'énergie cinétique moyenne. L'effet des interactions à plusieurs corps devient important et le plasma est dit non-idéal. Il est fortement couplé pour $\Gamma \gg 1$, ce qui correspond à des plasmas de faibles températures et hautes densités. L'étude de ce type de plasma devient problématique avec notre technique classique car les effets quantiques sur les électrons deviennent importants. Nous verrons ces effets plus en détail dans le prochain chapitre.

2.3.1 Choix des potentiels

Le choix du potentiel d'interaction entre les particules va donc dépendre de Γ. Dans la plupart des cas, on calcule un potentiel effectif en tenant compte explicitement de la distribution statique des autres charges autour de la particule chargée d'intérêt. Le champ de forces autour de la particule chargée est écranté par le nuage des autres particules ; la portée des forces est déterminée par une longueur caractéristique qui dépend de la densité et de la température.

Le modèle de référence est le modèle *One Component Plasma (OCP)* qui consiste en un système de charges électriques ponctuelles, identiques, interagissant exclusivement entre elles à travers un potentiel Coulombien. On considère alors un fond uniforme de charges opposées pour assurer la neutralité du système. Généralement, la polarisation du milieu par les ions est prise en compte à travers un potentiel de type Yukawa (appelé dans la suite OCP Yukawa). Dans ce modèle, la longueur d'écran est définie par la longueur de Debye :

$$\lambda_D = \sqrt{\frac{k_B T_e}{4\pi n_e e^2}}, \tag{2.6}$$

où k_B est la constante de Bolztmann, T_e et n_e les température et densité électroniques.

Le potentiel d'interaction entre deux particules i et j de charge Z, ($Z = -1$ pour un OCP Yukawa électronique), séparées d'une distance r_{ij} est de la forme :

$$V_{ij}(r_{ij}) = Z^2 e^2 e^{-r_{ij}/\lambda_D}/r_{ij}. \tag{2.7}$$

Il faut garder à l'esprit que le potentiel de Debye est un modèle statistique et qu'il résulte du comportement collectif des particules environnantes. Ce modèle fluide continu reste valable tant que le nombre de particules dans la sphère de Debye (de rayon λ_D) reste suffisamment grand (ce qui est le cas dans les plasmas idéaux) :

$$n_D = \frac{4\pi}{3} n\lambda_D^3 \gg 1, \tag{2.8}$$

où n est la densité de particules par unité de volume.

Dans le cas de la modélisation d'une impureté ionique de charge Z_i dans un plasma d'ions de charge Z_j ou d'un plasma contenant deux types d'ions, le modèle fluide précédent reste valable et le potentiel d'interaction s'écrit simplement :

$$V_{ij}(r_{ij}) = Z_i Z_j e^2 e^{-r_{ij}/\lambda_D}/r_{ij}. \tag{2.9}$$

Les simulations reposant sur ces modèles ont fait leurs preuves depuis des décennies. Par exemple, elles ont été utilisées pour l'étude de la dynamique des microchamps électriques autour de points neutres, [11], et chargés, [12] ou encore pour générer des fonctions de distribution de microchamps dans l'étude des propriétés radiatives dans les plasmas denses, [13].

Depuis quelques années, la DM est utilisée pour simuler des plasmas à deux composantes, l'une ionique et l'autre électronique, afin d'étudier les corrélations entre les charges et les mécanismes d'écrantage ions-électrons, [14, 8, 15, 16, 17]. Dans ces simulations TCP (*Two Component Plasma*), les ions et les électrons sont simulés simultanément. Dans ce système de charges opposées, il est clair que le problème est de manière inhérente de nature quantique. Une approche est de postuler la validité de la mécanique classique en prenant en compte les effets quantiques de façon approximative par des modifications du potentiel d'interaction ion-électron. Ainsi pour éviter la divergence à l'origine, le potentiel donné par l'équation (2.9) est remplacé par un potentiel régularisé qui est fini pour des distances inférieures à δ, la distance de régularisation :

$$V_{ie}(r) = -Ze^2(1 - e^{-r/\delta})e^{-r/\lambda}/r, \tag{2.10}$$

avec Z la charge de l'ion, λ la longueur d'écran telle que $\lambda \simeq c/2$ où c est la taille de la boîte de simulation.

Généralement, pour tenir compte des effets de diffraction à courte distance, la distance de régularisation est définie par la longueur d'onde thermique de de Broglie, [18, 19] :

$$\delta = \lambda_{th} = \frac{h}{\sqrt{2\pi m_e k_B T_e}}, \tag{2.11}$$

où h est la constante de Planck et m_e la masse de l'électron. Tant que la densité est suffisamment faible et que la distribution de Fermi peut-être remplacée par la distribution de Maxwell, les effets de symétrie tels que le principe d'exclusion de Pauli peuvent être négligés. Cependant, il existe des formes de potentiels semi-classiques plus sophistiqués qui permettent de tenir compte de ces effets de symétrie, [20, 21]. Dans ce travail, nous avons choisi une distance de régularisation non pas dépendante de la température, mais qui dépend de l'état de charge de l'ion de manière à ce que le potentiel donné par l'équation (2.10) soit en accord avec l'énergie d'ionisation des différents états de charge ionique, [22] :

$$\delta = \frac{Ze^2}{E_Z} \tag{2.12}$$

avec E_Z l'énergie d'ionisation d'un ion de charge $Z-1$, [23].

Les interactions ion-ion et électron-électron sont considérées quant à elles coulombiennes :

$$V_{ii,ee}(r) = Z_{i,e}^2 e^2 e^{-r/\lambda}/r. \tag{2.13}$$

Il est à noter que ces formes de potentiels sont toutes qualitativement équivalentes (ils présupposent un type d'interaction, un état de charge, etc.) et que l'objet ici n'est pas de discuter de la pertinence du choix du potentiel mais, après s'être fixé un modèle, d'étudier l'effet des corrélations entre les charges sur les propriétés statistiques et radiatives des plasmas.

La simulation DM-TCP permet donc de tenir compte sans restriction des effets de corrélations entre les particules. Elle a permis entre autres l'étude de l'écrantage des forces entre deux ions dans un gaz d'électrons chaud et dense, [24] et l'étude de la dynamique des électrons autour des ions dans les plasmas chauds et denses, [25, 16]. Sa contribution à la spectroscopie des plasmas chauds et denses sera évoquée dans le Chapitre 4, mais l'on peut déjà citer le travail réalisé sur les émetteurs ioniques, [17] et sur l'hydrogène, [26]. Avec l'amélioration des performances des outils informatiques, elle commence à être utilisée dans l'étude des plasmas non-idéaux comme outil de comparaison pour les modèles. On verra dans le Chapitre 3 comment notre simulation TCP est utilisée pour le calcul des facteurs de structure dynamique incluant la dynamique des électrons et les effets des corrélations entre les ions et les électrons. Dans le Chapitre 4, elle est utilisée pour discuter des effets de corrélations sur les profils de raies.

Cependant, sa mise en œuvre comporte des difficultés spécifiques. En effet, la présence simultanée des ions et des électrons implique de suivre, d'une part, les trajectoires sur des pas de temps très courts ($\simeq 0.1\ as$) pour pouvoir décrire correctement le déplacement des électrons autour des ions, et d'autre part, de suivre ces trajectoires suffisamment longtemps pour que les ions (au moins 2000 fois plus lourds que les électrons) parcourent plusieurs fois la boîte de simulation. Il faut

aussi laisser évoluer le système suffisamment longtemps pour dépasser les temps de relaxation des grandeurs d'intérêts et obtenir une bonne statistique. Plusieurs millions de pas de temps sont donc nécessaires dans les simulations DM-TCP.

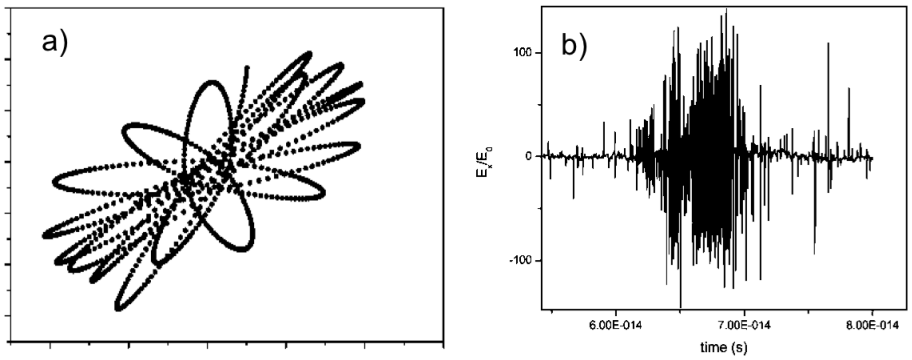

FIGURE 2.1 – (a) Projection dans le plan de la trajectoire d'un électron piégé au cours d'une simulation DM-TCP. (b) Évolution temporelle d'une composante du microchamp électrique.

De plus, le potentiel attractif entre les ions et les électrons est à l'origine d'une augmentation de densité autour des ions avec un changement de la cinétique des électrons. Des électrons d'énergie négative se retrouvent piégés autour d'un ion, comme le montre la figure 2.1 (a). Pendant la capture, cet électron va générer de forts microchamps électriques oscillants (cf. figure 2.1 (b)). Ce mécanisme de « piégeage » est réversible dans le temps grâce aux interactions avec toutes les autres particules du plasma. Par extension, ce processus temporaire peut-être interprété comme un mécanisme d'ionisation-recombinaison à trois corps, [22]. Nous allons voir dans le Chapitre suivant comment ce processus a été implémenté dans la simulation DM-TCP.

2.3.2 Exécution

Pour démarrer une simulation MD, il faut définir la boîte et l'ensemble des positions et des vitesses initiales des particules. Il y a deux façons de faire : soit partir de zéro, soit à partir des données d'une simulation précédente.

Lorsque l'on part de zéro, il faut créer un ensemble de positions et de vitesses. Dans nos simulations, les positions initiales des particules sont aléatoirement choisies et les vitesses initiales sont distribuées suivant la distribution de Maxwell à une température T donnée[3].

3. Il est aussi possible de démarrer les simulations avec des particules de températures différentes.

L'autre alternative est de reprendre pour positions et vitesses initiales les positions et les vitesses d'un *run* précédent. Cette technique est généralement utilisée lorsque la simulation de certaines propriétés demande un très grand nombre de pas de temps et que des mesures macroscopiques doivent être faites à différents temps. Nous utilisons cette technique par exemple dans le cas des simulations des plasmas TCP qui demandent des millions de pas de temps et qui nécessitent une bonne préparation du système dans un état d'équilibre donné.

Pour amener le système à l'équilibre thermodynamique dans les conditions de température et de couplage voulues, on laisse évoluer les particules pendant un temps transitoire suffisant au cours duquel on contrôle l'énergie potentielle et la température. On applique un thermostat (par ajustement des vitesses) de manière à rectifier la température si la déviation est trop importante.

Il s'en suit alors la phase des mesures liées aux trajectoires des particules. Afin de limiter les artéfacts numériques, on recommence régulièrement le calcul des trajectoires avec d'autres conditions initiales.

2.3.3 Mesures statistiques d'intérêt

Les propriétés physiques sont en général une fonction des coordonnées et des vitesses des particules. Une fois les trajectoires dans l'espace des phases connues, plusieurs mesures physiques sont donc réalisables. Outre les moyennes thermodynamiques usuelles comme la température, l'énergie cinétique et l'énergie potentielle par exemple, nous nous intéressons à certaines fonctions de distribution et de corrélation.

Parmi les *fonctions de distribution*, nous pouvons évoquer les distribution des vitesses qui, à l'équilibre, obéissent à une loi de Maxwell. La comparaison de la distribution des vitesses obtenue par simulation à cette loi permet, par exemple, de tester l'équilibre thermodynamique du système simulé. Comme on le verra dans la suite, la distribution d'énergie totale des électrons met en évidence les électrons piégés autour des ions dans les plasmas couplés. Elle donne accès à la mesure de la charge moyenne du plasma.

Une autre distribution d'importance dans l'étude des plasmas est la fonction distribution de paires, $g(r)$. Cette fonction donne la probabilité de trouver deux particules séparées d'une distance r, relativement à la probabilité attendue avec une loi uniforme à la même densité ρ

$$\rho\ g(r) = \frac{1}{N}\Big\langle \sum_{i}^{N}\sum_{j\neq i}^{N} \delta(r - r_{ij})\Big\rangle. \tag{2.14}$$

Cette fonction, qui représente les corrélations spatiales, permet de caractériser la structure du milieu étudié. Dans les plasmas, elle apporte une information sur la

structure statique moyenne des particules et plus particulièrement sur les effets d'écrans entre particules.

Une autre mesure qui nous intéresse spécifiquement dans ce travail, est celle du champ électrique créé par les particules chargées sur une particule d'intérêt (émetteur). Connaissant la position des particules à chaque instant, le champ électrique mesuré sur la particule P est

$$\vec{E}_P(t) = \sum_i^N \frac{\vec{F}_i}{Z_p e}, \tag{2.15}$$

avec Z_p la charge de la particule P.

Une manière de caractériser ces microchamps est d'étudier la fonction de distribution statique du champ électrique définie comme la probabilité de trouver un champ $\vec{E}$ égal à $\vec{E}_P$ sur la particule P. Pour un plasma isotrope cette distribution s'écrit :

$$W(E) = 4\pi E^2 Q(\vec{E}) \text{ où } \; Q(\vec{E}) = \Big\langle \delta(\vec{E} - \vec{E}_P) \Big\rangle. \tag{2.16}$$

Généralement, cette fonction de distribution est présentée sous sa forme normalisée $W(E/E_0)$ où $E_0 = e/r_0^2$ est le champ moyen. Comparées aux modèles existants, [27, 28, 29, 30, 31], les distributions simulées permettent de discuter des effets de corrélations sur les microchamps [4]. Concernant les propriétés dynamiques du plasma, la DM donne accès aux fonctions de corrélations temporelles. Elles mesurent les corrélations entre deux quantités A et B à des temps différents t_0 et $t_0 + t$. Ces fonctions sont dépendantes du temps et s'écrivent sous la forme :

$$C_{AB}(t) = \lim_{\tau\to\infty} \frac{1}{\tau} \int_0^\tau A(t_0)B(t_0+t)dt_0 = \Big\langle A(t_0)B(t_0+t) \Big\rangle. \tag{2.17}$$

Si $A \equiv B$, $C_{AA}(t)$ est appelée fonction d'autocorrélation et mesure comment la grandeur A perd la mémoire de sa phase initiale. Ces fonctions sont d'un grand intérêt car elles donnent une image de la dynamique dans le milieu plasma. Par exemple, leur intégrale sur le temps peut être directement reliée aux coefficients de transports macroscopiques (coefficients de diffusion, pouvoir d'arrêt, etc), leur transformée de Fourier peut être reliée aux spectres expérimentaux (cf. Chapitre 4). Dans le cadre du calcul des profils de raies dans les plasmas, nous nous intéressons plus particulièrement à la fonction d'autocorrélation du microchamp électrique :

$$C_{EE}(t) = \lim_{\tau\to\infty} \frac{1}{\tau} \int_0^\tau \vec{E}(t+t') \cdot \vec{E}(t)dt' = \Big\langle \vec{E}(t) \cdot \vec{E}(0) \Big\rangle. \tag{2.18}$$

Par exemple son intégrale est reliée à la largeur homogène des profils de raies dans la limite des fluctuations rapides et la comparaison de cette fonction entre les modèles

4. Ce sujet a fait l'objet du stage de M2 RES de Thomas Plaindoux, *Effets des corrélations de charges sur les microchamps électriques dans les plasmas chauds et denses*, (2014)

OCP et TCP permettent de discuter les effets des couplages entre les particules. Il a été montré entre autre que des effets de couplages apparaissent lorsque la charge de l'émetteur augmente même à haute température avec pour conséquence le rétrécissement du profil de raies final, [32].

Bibliographie

[1] N. Metropolis, A.W. Rosenbluth, M.N. Rosenbluth, et al., *Equation of state calculations by fast computing machines*, J. Chem. Phys. **21**, 1087-1092 (1953).

[2] B.J. Alder and T.E. Wainwright, *Phase Transition for a Hard Sphere System*, J. Chem Phys. **27**, 1208-1209 (1957) ; *Studies in Molecular Dynamics. I. General Method*, J. Chem Phys. **31**, 459-466 (1959).

[3] A. Rahman, *Correlations in the Motion of Atoms in Liquid Argon*, Phys. Rev. **136A**, 405 (1964).

[4] L. Verlet, *Computer "Experiments" on Classical Fluids. I. Thermodynamical Properties of Lennard-Jones Molecules*, Phys. Rev. **159**, 98 (1967).

[5] J.-P. Hansen and L. Verlet, *Phase Transitions of the Lennard-Jones System*, Phys. Rev. **184**, 151 (1969).

[6] D. Levesque, J. J. Weis, J. P. Hansen, *Simulation of Classical Fluids*, Monte Carlo Methods in Statistical Physics, Topics in Current Physics Volume **7**, 47 (1986).

[7] D.C. Rapaport, *The Art of Molecular Dynamics Simulation*, 2nd ed. Cambridge University Press (2004). *ISBN 0521825687*

[8] D.V. Fisher, Y. Maron, *Statistics of inter-particle distances and angles in plasmas*, Eur. Phys. J. D **14**, 349-359 (2001).

[9] J.M. Ziman, *Principles of the Theory of Solids*, Cambridge University Press, Cambridge, 2nd edition, (1972).

[10] W.C. Swope, et al., *A computer simulation method for the calculation of equilibrium constants for the formation of physical clusters of molecules : application to small water clusters*, J. Chem. Phys. **76**, 637 (1982).

[11] M. Berkovsky et al., *Nonlinear response of electric fields at a neutral point*, Phys. Rev. E **51**, 4917 (1995).

[12] M. Berkovsky et al., *Electric field dynamics at a charged point*, Phys. Rev. E **54**, 4087 (1996).

[13] P. Gauthier et al., *Modeling the radiative properties of dense plasmas*, Phys. Rev. E **58**, 942 (1998).

[14] J.P. Hansen and I.R. McDonald, *Microscopic simulation od a strongly coupled hydrogen plasma*, Phys. Rev. A **23**, 2041 (1981).

[15] T. Pschiwul and G. Zwicknagel, *MD-Simulations of the Dynamic Properties of a Nonideal Two-Component Plasma*, Contrib. Plasma Phys. **41**, 271-274 (2001).

[16] B. Talin, A. Calisti and J. Dufty, *Classical description of electron structure near a positive ion*, Phys. Rev. E **65**, 056406 (2002).

[17] B. Talin et al., *Molecular dynamics simulation for modelling plasma spectroscopy*, J. Phys. A : Math. Gen. **36**, 6049 (2003).

[18] G. Kelbg, *Theorie des Quanten-Plasmas*, Ann. Phys. **12**, 219-224 (1963).

[19] C. Deutsch, *Nodal expansion in a real matter plasma*, Phys. Lett. **60A**, 317-318 (1977).

[20] F.J. Rogers, *Formation of composites in equilibrium plasmas*, Phys. Rev. A **19**, 375-388 (1979).

[21] H. Minoo, M.M. Gombert and C. Deutsch, *Temperature-dependent Coulomb interactions in hydrogenic systems*, Phys. Rev. A **23**, 924-943 (1981).

[22] A. Calisti, T. del Río Gaztelurrutia and B. Talin, *Classical molecular dynamics model for coupled two component plasmas*, High Energy Density Physics **3**, 52 (2007).

[23] R.D. Cowan, *The Theory of Atomic Structure and Spectra*, University of California Press, Berkeley and Los Angeles, California, p. 12, (1981)

[24] B. Talin, A. Calisti, J. Dufty, *Screened forces between two positive ions in an electron bath*, Contrib. Plasma Phys. **41**, 323 (2001).

[25] B. Talin, A. Calisti, E. Dufour and J. Dufty, *Classical dynamics of electrons surrounding ions in hot and dense plasmas - related topics*, J. Quant. Spectrosc. Radiat. Transfer. **71**, 729 (2001).

[26] E. Stambulchik et al., *Correlation effects and their influence on line broadening in plasmas : Application to H_α*, High Energy Density Physics **3**, 272 (2007).

[27] J. Holstmark, *Über die Verbreiterung von Spektrallinien*, Annalen der Physik **363**, 577-630 (1919).

[28] M. Baranger and B. Mozer, *Electric Field Distributions in an Ionized Gas*, Phys. Rev. **115**, 521-525 (1959) ; B. Mozer and M. Baranger, *Electric Field Distributions in an Ionized Gas. II* Phys. Rev. **118**, 626-631 (1960).

[29] C.F. Hooper, Jr., *Electric Microfield Distributions in Plasmas*, Phys. Rev. **149**, 77-90 (1966) ; *Low-Frequency Component Electric Microfield Distributions in Plasmas*, Phys. Rev. **165**, 215-222 (1968).

[30] C.A. Iglesias, J.L. Lebowitz, D. McGowan, *Electric microfield distributions in strongly coupled plasmas*, Phys. Rev. A **28**, 1667-1672 (1983).

[31] C.A. Iglesias et al., *Low-frequency electric microfield distributions in plasmas*, Phys. Rev. A **31**, 1698-1702 (1985).

[32] E. Dufour et al., *Charge-charge coupling effects on dipole emitter relaxation within a classical electron-ion plasma description*, Phys. Rev. E **71**, 066409 (2005).

Chapitre 3

Application à l'étude des plasmas non-idéaux

La physique de la matière à haute densité d'énergie (*HEDP*) est un domaine émergeant d'un grand intérêt pour la physique moderne, [1]. Elle bénéficie de programme ambitieux et d'une grande diversité de dispositifs expérimentaux. Elle se développe en particulier autour des grands lasers de puissance (NIF, LMJ, OMEGA, ...), des sources intenses de rayonnement X monochromatique (LCLS, FLASH/XFEL, SACLA ...), des Z-pinch et des prototypes de tokamak (ITER, ...). Ces expériences regroupent un large champ disciplinaire incluant entre autres la physique des plasmas, la physique des lasers et des faisceaux de particules, la physique de la matière condensée, la physique nucléaire, atomique et moléculaire, la physique des interactions rayonnement intense / matière, l'astrophysique. Le challenge intellectuel de cette physique réside dans la complexité et la non-linéarité des processus d'interaction qui caractérisent tous ces champs disciplinaires.

Parmi les différents états extrêmes de la matière à haute densité d'énergie se trouvent des plasmas dont les conditions thermodynamiques (i.e. densité et température) sont telles que le cadre conventionnel de la physique des plasmas ne s'applique plus. On les appelle les *plasmas non-idéaux*. On les retrouve aussi à l'état naturel dans le cœur des planètes géantes, du Soleil, des naines blanches, etc, [2]. Lorsque le paramètre de couplage Γ augmente, le plasma change d'un régime collisionnel, proche de l'état gazeux (idéal) à un régime plus corrélé, dense, proche de l'état liquide (non-idéal). Par convention, un plasma est dit non-idéal lorsque $\Gamma \geqslant 1$. Les propriétés physiques des plasmas non-idéaux sont donc caractérisées par les fortes corrélations. Les équations d'état (EOS) et le degré d'ionisation, les propriétés de transports telles que la conductivité électrique, les propriétés structurelles et dynamiques telles que la fonction de corrélation de paire et le facteur de structure dynamique seront affectés par ces effets à N-corps. Aussi, on distingue généralement la *matière tiède et dense* (Warm and Dense Matter, WDM) de la *matière chaude et dense* (Hot and Dense Matter, HDM) par la présence d'électrons partiellement dégénérés dans la WDM. Avec des densités de l'ordre de la densité du solide et des températures variant de $0,1$ à quelques centaines d'eV pour les plasmas les plus chauds, ce régime présente une grande complexité. Il est trop dense pour être décrit comme un plasma quasi-idéal, pour lequel les modèles cinétiques et fluides sont adaptés. Il est trop chaud pour être décrit par les modèles de la matière condensée, [3, 4]. La modélisation de tels plasmas représente donc un

véritable challenge.

Actuellement, la majorité des méthodes utilisées sont basées soit sur une description statistique du plasma (méthode d'atome moyen), soit sur une description de la dynamique des ions à partir des premiers principes (méthodes *ab initio*). Les modèles d'atomes moyens permettent de représenter le système à N-corps comme un jeu de systèmes à 1-corps dans lesquels les configurations électroniques sont construites. Ils trouvent leur origine dans la physique de la matière condensée et la première adaptation de ce modèle à la physique des plasmas, tenant compte des effets de température finie, fut proposée par Feynman, Metropolis et Teller en 1949, [5]. Dans les méthodes *ab initio* telles que la dynamique moléculaire quantique (QMD) appliquée aux plasmas tièdes et denses, les ions sont traités classiquement et la DFT, à température finie et sans orbitale, est utilisée pour les électrons afin de prendre en compte au mieux les effets des corrélations et les effets quantiques, (voir [6] et les références citées). Cependant, pour la plupart des conditions rencontrées dans la WDM, ces méthodes sont poussées à leur limite intrinsèque et les expériences sont le seul moyen de vérifier leur validité. Mais, créer ces plasmas non-idéaux en laboratoire pour pouvoir les étudier est aussi un véritable challenge.

Depuis quelques années, il est devenu possible de créer la WDM en utilisant des lasers de puissance. Une méthode commune pour obtenir de telles conditions est le chauffage isochore d'une cible solide grâce au développement de lasers femtosecondes délivrant un pulse intense ($> 10^{14}\ W/cm^2$). Sous une irradiation ultra-brève et intense, la cible solide chauffe rapidement ($\sim 150 fs$) en maintenant son volume initial. Sous cette forte excitation, la température électronique s'élève à quelques dizaines de milliers de degrés Kelvin ($1\ eV$) pendant que le support reste froid, ce qui implique des conditions hors équilibre. Avant que l'équilibre ne se rétablisse en quelques dizaines de picosecondes, l'échantillon garde sa densité initiale par effet d'inertie. La matière est tiède comparée aux plasmas chauds mais toujours aussi dense qu'un solide, c'est la matière tiède et dense. Puis, sur une échelle de temps plus longue ($> 100\ ps$), la matière se détend sous forme de plasma. Sonder la matière tiède et dense n'est pas une tache facile de par son aspect hautement transitoire.

À cause des densités proches de celle du solide, la plupart des méthodes de diagnostic employées pour caractériser les plasmas « plus idéaux » ne sont plus utilisables ou requièrent des sondes d'énergie plus élevées. Par exemple, l'utilisation des profils de raies à des fins de diagnostic, comme cela est développée dans le Chapitre 4, devient très compliquée à cause de la forte opacité de ces plasmas et de la physique atomique exotique. Nous l'avons toutefois utilisée dans des expériences réalisées à l'aide de lasers à électrons libres (FEL) pour l'étude de la transition solide/matière tiède et dense/plasmas fortement couplés avec l'analyse des profils de raies émises par des états excités d'ions creux, [7, 8]. Pour sonder l'ordre structural des ions et plus généralement la frontière entre les états électroniques

liés et libres de la WDM, la spectroscopie d'absorption X ultra-rapide près des seuils (XANES) est utilisée, [9, 10, 11]. La dynamique des électrons libres peut-être mesurée par une technique d'interférométrie dans le domaine de Fourier, [12]. Une autre technique qui s'est développée pour mesurer les paramètres plasmas tels que la température électronique, la densité et l'état d'ionisation est la diffusion Thomson du rayonnement X (DTX),[13]. Comme nous le verrons dans la suite, ce diagnostic repose sur le fait que les radiations X de haute énergie peuvent pénétrer le matériau et sont diffusées par les électrons du plasma.

Que pouvons-nous apporter à cette étude ?

À l'heure actuelle, il n'existe pas de modèles appropriés pour décrire ces plasmas non-idéaux. Les outils théoriques sont empruntés soit à la physique de la matière condensée soit à la physique des plasmas. Notre technique de dynamique moléculaire classique à composantes multiples a été développée initialement pour l'étude des plasmas faiblement et moyennement couplés. Par le choix des potentiels binaires utilisés, la DM-TCP ne permet pas de décrire les électrons dégénérés. Mais son application à l'étude de matière tiède et dense, et, chaude et dense présente plusieurs avantages. Elle permet une bonne description de la transition entre les plasmas cinétiques classiques et les plasmas couplés car toutes les interactions sont prises en compte. Elle donne accès à la dynamique des électrons et ne découple pas le mouvement des électrons à celui des ions (approximation de Born-Oppenheimer) contrairement aux méthodes d'atome moyen et de QMD. Et, comme on va le voir dans la suite, avec l'implémentation du processus d'ionisation/recombinaison, elle permet de suivre l'évolution d'un plasma impliquant plusieurs états de charge. L'idée ici est donc de montrer qu'elle contient suffisamment de physique pour décrire correctement cet état de la matière, en complément des modèles empruntés à la physique du solide. Dans la suite du Chapitre, nous montrons son application aux calculs des facteurs de structure dynamique, élément essentiel pour le diagnostic par diffusion Thomson X ainsi que la possibilité d'accéder à la mesure de l'abaissement du potentiel d'ionisation.

3.1 Le problème de la modélisation de ces plasmas

À basse densité et relativement haute température, un plasma partiellement ionisé peut être vu comme un mélange idéal de gaz d'électrons, d'ions et d'atomes. Ces particules se déplacent avec une vitesse donnée le long de trajectoires généralement rectilignes et n'interagissent entre elles que très rarement. Lorsque la densité augmente ou la température diminue, la distance entre les particules diminue et celles-ci commencent à interagir entre elles plus fréquemment. L'énergie potentielle moyenne devient prépondérante. Comme on l'a défini dans le Chapitre 2, le paramètre de couplage devient de l'ordre de l'unité voir plus grand. Le plasma

devient non-idéal et la théorie cinétique des gaz n'est plus applicable. Les études théoriques deviennent alors compliquées car elles relèvent d'un *problème à N-corps*.

Lorsque la densité augmente et la température diminue la distance entre les particules diminue. Les fonctions d'onde se recouvrant on ne peut plus négliger les effets quantiques. Ces effets vont se manifester d'abord sur les électrons. Les *ions sont fortement couplés* mais peuvent être encore décrits classiquement alors que les *électrons sont partiellement dégénérés*. Dans ce cas, ils doivent être décrits par une distribution de Fermi.

On définit un paramètre de dégénérescence électronique par le rapport entre la température électronique T_e et la température de Fermi $T_F = \hbar^2(3\pi^2 n_e)^{2/3}/2m_e k_B$:

$$\theta_e = \frac{T_e}{T_F} = \frac{2m_e k_B T_e}{\hbar^2}(3\pi^3 n_e)^{-2/3}. \tag{3.1}$$

— Lorsque $\theta_e > 5$, les effets quantiques sont négligeables. La modélisation du plasma reste un problème à N-corps du fait des forts couplages mais les particules peuvent être considérées classiquement,
— Lorsque $\theta_e < 5$, les effets quantiques deviennent importants.

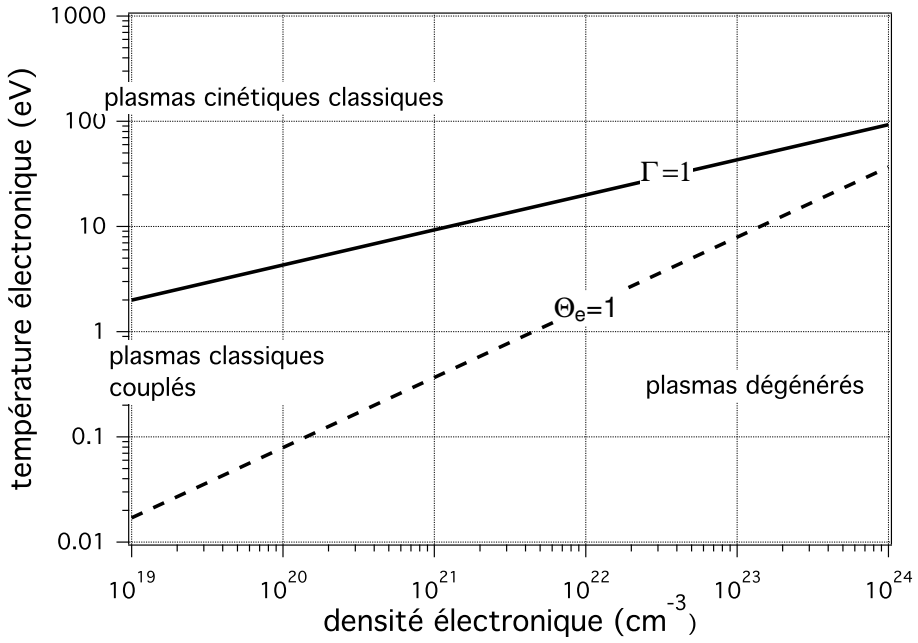

FIGURE 3.1 – Diagramme de classification des plasmas.

La figure 3.1 représente les différents régimes des plasmas faisant l'objet de notre étude. On y distingue plusieurs zones séparées par les droites représentant

les limites plasmas idéaux/non-idéaux ($\Gamma = 1$) et électrons classiques/dégénérés ($\theta_e = 1$). La WDM est localisée à des densités et températures telles que Γ et θ_e sont proches de l'unité, ce qui correspond à des densités proches du solide ($n_e \sim 10^{23} - 10^{26}\ cm^{-3}$) et des températures variant de 0.1 à quelques dizaines d'eV.

Ainsi, contrairement aux autres états du plasma, la WDM contient deux espèces distinctes : des ions fortement couplés mais classiques et des électrons modérément couplés mais partiellement dégénérés. Alors que les effets de dégénérescence dans les systèmes faiblement couplés peuvent être relativement bien traités par des pseudo-potentiels binaires, [14, 15], à haute densité et faible température, les effets de corrélations entre les charges sont tels que les propriétés quantiques sont mal reproduites par ces potentiels. Une solution serait de tenir compte des effets de densité de manière explicite dans le potentiel binaire (voir la discussion dans [16] et les références citées) ou bien d'utiliser d'autres formes de potentiels effectifs dans lesquels un terme d'interaction dépendant des moments serait ajouté, [17].

Dans les plasmas classiques, la structure de l'ion ou de l'atome est indépendante de l'environnement. Le modèle de l'atome isolé est adopté et les effets du plasma sont traités comme une perturbation (cf. Chapitre 4). Sa description en terme de niveaux d'énergie discrets relève de la physique atomique. Dans la matière condensée, les ions ou les atomes sont organisés en réseau, les électrons sont dégénérés et leurs états sont décrits par une structure en bande à température nulle. Dans la HDM et la WDM, *les atomes, les ions et les électrons ont des comportements intrinsèquement liés au plasma.*

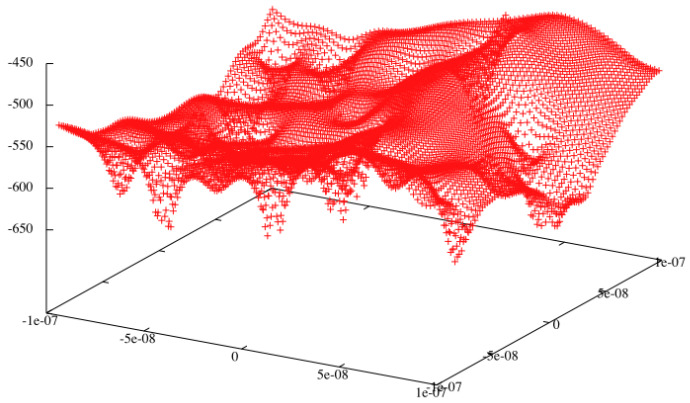

FIGURE 3.2 – Potentiel vu par un électron se déplaçant dans un plasma de béryllium couplé.

Par exemple, la figure 3.2 représente un instantané du potentiel ionique ressenti par un électron se déplaçant sur une surface. La simulation est effectuée dans le

cas d'un plasma de béryllium à $N_e = 10^{23}\ cm^{-3}$, $T_e = 100\ eV$ et $T_i = 10eV$. À chaque point de la surface, l'énergie potentielle est mesurée en tenant compte des interactions entre tous les ions de la boîte de simulation (les conditions aux limites périodiques sont appliquées). On voit clairement que les charges évoluent dans un potentiel complexe qui fluctue quand les ions bougent. Une des conséquences est que la structure atomique des ions présents dans le plasma peut être influencée par ces forts couplages : des états liés peuvent disparaître dans le continuum. En d'autres termes, le potentiel d'ionisation d'un ion plongé dans ce type de plasma peut être réduit à cause des interactions entre toutes les charges. La prise en compte de l'*abaissement du potentiel d'ionisation* ou IPD (pour Ionization Potential Depression) dû aux effets du plasma est un problème de longue date, [18, 19, 20] mais qui est rémanent. Les expériences faites récemment au *Linac Coherent Light Source* (LCLS) ravivent les discussions sur la modélisation de l'IPD dans les plasmas chauds et denses, [21, 22, 23, 24, 25], comme on le verra dans la suite.

3.2 Implémentation d'un processus d'ionisation/recombinaison collisionnelle dans la DM-TCP → *Annexe A*

Les modèles d'ionisation/recombinaison collisionnelle généralement utilisés dans les plasmas supposent que les électrons suivent des trajectoires définies par leurs paramètres d'impact et leurs vitesses. Des taux d'ionisation et de recombinaison sont alors calculés et permettent d'obtenir les distributions de charges à l'équilibre, [26]. Dans les plasmas denses, où plusieurs charges interagissent simultanément, une telle approche n'est plus pertinente car la notion de collisions binaires entre un ion et un électron n'est plus appropriée. La trajectoire et l'énergie de l'électron impliqué dans le processus collisionnel varient de manière non linéaires en fonction des charges environnantes. Afin de décrire les processus collisionnels à plusieurs corps dans ces plasmas, nous avons développé un modèle adapté à notre technique de simulation DM-TCP, [27].

Il implique la capture et la délivrance des électrons par les ions. La notion de couche est introduite pour caractériser le plasma environnant les ions. La couche d'un ion particulier est constituée de ses deux électrons plus proches voisins : le premier plus proche électron étant noté (FNe) et le second plus proche électron (SNe). Suivant la configuration locale du plasma et de l'énergie totale des deux électrons voisins impliqués, cette coquille sera étiquetée chaude, froide ou inactive. Ici, le critère sur l'énergie totale tient compte de la complexité de l'état de surface de l'énergie potentielle autour de l'ion ainsi que de l'abaissement du potentiel d'ionisation au niveau local dû aux charges environnantes.

Le processus d'ionisation démarre lorsque l'ion i est entouré d'une couche

chaude c'est-à-dire lorsque à l'instant t_i, l'énergie totale des deux électrons plus proches voisins est positive. La charge de l'ion Z_i augmente d'une unité et un nouvel électron est créé sur l'ion avec l'énergie potentielle minimum. À cause des interactions de ce nouvel électron avec toutes les autres charges de la simulation (et en autre avec l'électron FNe), celui-ci est accéléré et voit son énergie potentielle augmenter. Afin de tenir compte d'une incertitude sur le démarrage du processus d'ionisation, aucun autre événement sur cet ion n'est autorisé pendant un temps qui correspond au temps de traversée par un électron d'une distance égale à la longueur d'onde de de Broglie. Ensuite, l'électron créé aura suffisamment d'énergie pour se libérer de l'ion ou pas.

Le processus de recombinaison est défini à l'inverse : il démarre lorsque l'ion i est entouré d'une couche froide c'est-à-dire l'énergie totale des deux électrons plus proches voisins est négative. Alors l'électron FN_e disparaît, la charge de l'ion Z_i est diminuée d'une unité. L'énergie perdue par l'électron recombiné est transférée à l'électron SNe qui redistribue celle-ci à toutes les charges environnantes par le jeu des interactions.

Dans tous les cas la neutralité du plasma est conservée, mais, vue la forme particulière de nos potentiels d'interaction (cf. eq.(2.10) et eq.(2.12)), l'énergie totale n'est pas conservée au cours du processus d'ionisation/recombinaison. Ceci implique une dérive de l'énergie non négligeable au cours de la phase d'équilibrage de la simulation. Un thermostat est appliqué et aucune mesure n'est faite jusqu'à l'obtention d'un état d'équilibre. Ce dernier est atteint lorsque les taux d'ionisation et de recombinaison s'égalisent et les fluctuations d'énergie deviennent très faibles.

Ainsi, le processus d'ionisation/recombinaison ajouté à notre simulation de DM-TCP a deux fonctions fondamentales : i) il permet l'évolution des états de charges (et donc de la densité électronique) vers un état stationnaire qui dépendra de la température, de la densité de charges et de la composition du plasma ; ii) il permet de traiter la population d'électrons piégés temporairement dans le puits de potentiel de l'ion. La notion des états d'énergie discrets de l'ion est remplacé par son équivalent continu. Par contre, à la différence du code de DM classique développé par Glosli et co-auteurs, [28, 29], notre modèle ne tient pas compte du couplage avec le rayonnement.

Plusieurs comparaisons ont contribué à la validation de ce modèle et notamment les comparaisons entre les abondances ioniques obtenus par la DM-TCP avec les résultats de nombreux codes de cinétiques des plasmas regroupés dans la base de données du NIST [1], [27, 30]. Dans l'*Annexe A*, la dynamique des électrons et les abondances ioniques sont discutées pour des plasmas de carbone et d'aluminium.

1. Yu. Ralchenko, *Nist SAHA Plasma Kinetics Database (version 1.0)*, National Institute of Standards and Technology, Gaithersburg, MD, (2006). Available from : http ://nlte.nist.gov/SAHA.

Nous montrons qu'il est possible d'étudier les durées de relaxation entre deux états d'équilibre ce qui donne des informations précieuses sur la dynamiques des électrons dans les plasmas couplés. D'autre part, les comparaisons des abondances ioniques avec les modèles existants montrent que le modèle d'ionisation/recombinaison que nous proposons donne des résultats raisonnables.

Ce modèle couplé à la DM-TCP offre ainsi un nouveau point de vue pour l'analyse des plasmas couplés. Comme nous allons le voir dans la suite, le placement instantané de l'électron créé au cours du processus d'ionisation donne accès par exemple à la mesure de l'abaissement du potentiel d'ionisation dû aux effets des charges environnantes.

3.3 Estimation de l'abaissement du potentiel d'ionisation par la DM → *Annexe B et C*

Le potentiel d'ionisation d'un ion plongé dans un plasma est diminué par rapport à celui d'un ion isolé, à cause des interactions entre toutes les particules (ions et électrons) qui interagissent avec celui-ci. L'étude de l'abaissement du potentiel d'ionisation (IPD) dû aux effets du plasma date des années 30 et deux modèles proposés dans les années 60, perdurent, [19, 20]. Cependant leur validité a été récemment remise en cause par deux expériences dédiées à la génération de plasmas de haute énergie, une utilisant un XFEL (LCLS, [21, 22, 31]) et l'autre utilisant un laser optique de grande puissance (Orion, [24, 23]). Alors que les résultats obtenus sur un plasma d'aluminium avec le XFEL montrent un large désaccord avec le modèle de Stewart and Pyatt (SP), [20], ceux obtenus sur un plasma d'aluminium plus chaud et plus dense avec le laser Orion, montrent un désaccord avec le modèle de Ecker and Kröll (EK), [19]. Cette controverse relance les études théoriques sur l'IPD, car ses effets sont d'une importance cruciale dans la modélisation des processus atomiques dans les plasmas denses.

Avec le processus d'ionisation/recombinaison implémenté dans notre technique de simulation, la mesure des effets du plasma sur le potentiel d'ionisation d'un ion donné est directe. La méthode consiste à évaluer l'énergie potentielle de l'électron localisé sur l'ion au cours du processus d'ionisation. L'amplitude de cette énergie potentielle correspond à la quantité d'énergie cinétique qu'il faudrait à l'électron pour rejoindre les électrons libres. Or l'énergie potentielle de cet électron résulte de la somme de toutes les interactions de celui-ci avec toutes les charges du plasma. En échantillonnant les énergies potentielles des électrons localisés sur les ions de même état de charge, on mesure l'énergie moyenne d'ionisation correspondant à cet état de charge. La différence avec l'énergie d'ionisation de l'ion isolé est alors interprétée comme la mesure de l'abaissement du potentiel d'ionisation due aux effets du plasma.

Dans l'*annexe B*, l'étude de l'IPD par la DM-TCP classique est illustrée et

discutée pour un plasma d'aluminium pour deux densités et pour une gamme de températures allant de 50 eV à 190 eV. Les premiers résultats montrent que les valeurs de l'IPD mesurées par notre technique purement classique se situent entre les valeurs calculées par les modèles EK et SP. Par contre elles se comparent bien aux valeurs obtenues dans la limite des couplages forts du modèle SP à haute densité et basse température ; ce qui est un résultat en soi. Nous montrons aussi que l'IPD dépend de la température : l'IPD décroît quand la température augmente. Cette tendance est reproduite par le modèle SP mais pas par le modèle EK qui ne dépend de T qu'à travers la valeur de la densité critique, i.e. $n_{cr} = \frac{3}{4\pi}(\frac{k_B T}{Z_N^2 e^2})^3$ où Z_N est la charge du noyau et T la température du plasma, et de sa charge moyenne $\overline{Z}$.

Par contre, ces simulations réalisées à l'équilibre, ne permettent pas de se comparer directement aux expériences. Afin de nous rapprocher des conditions expérimentales de Ciricosta, [22], une série de simulations avec des ions à température ambiante a été entreprise.

L'*annexe C* regroupe les résultats de l'IPD dans le cas d'un plasma d'aluminium hors équilibre. Ici la question soulevée est : est-ce que la façon de générer le plasma agit sur l'IPD et comment ? En effet, dans les expériences dédiées à cette étude le XFEL chauffe la cible solide d'aluminium pendant 80 fs avec des photons d'énergie dans la gamme $1540 - 1830$ eV (proche de la couche K de l'aluminium froid) et avec une intensité aux alentours des 10^{17} W/cm^2. À ces intensités les électrons sont arrachés par photo-ionisation à la cible. Il s'en suit une désexcitation Auger qui se traduit par une thermalisation des électrons à des températures allant de 70 à 180 eV. Par contre le transfert d'énergie entre les électrons et les ions ne permettent pas de chauffer ces derniers en si peu de temps. Nous avons simulé deux systèmes idéaux : i) un plasma à l'équilibre thermodynamique dans lequel le processus d'ionisation/recombinaison collisionnel permet d'atteindre l'équilibre avec des ions et des électrons à la même température ; ii) un plasma hors équilibre dans lequel les ions à température ambiante (300 K) s'arrangent sur une structure quasi-cristalline alors que les électrons sont portés à des températures plus hautes. Il en résulte que l'IPD augmente lorsque les ions sont figés. La structure ionique du plasma agit donc sur l'IPD. D'autre part, les simulations montrent un effet de température électronique sur l'IPD que l'on explique par un arrangement différent des électrons autour des ions et un degré d'ionisation différent dans le plasma.

Par contre, les résultats de la simulation avec les ions figés, sensée se rapprocher des conditions expérimentales, montrent un comportement différent de ceux des points mesurés. Ceci peut s'expliquer par la façon d'ioniser le plasma. Alors que dans les expériences l'ionisation résulte de la photo-ionisation, dans nos simulations, ce sont des processus purement collisionnels qui ionisent le plasma.

Les résultats présentés ici sont préliminaires mais soulignent la complexité d'une telle étude.

3.4 Étude de la lumière diffusée par les électrons libres : diagnostics par diffusion Thomson X → *Annexe D*

L'avantage de la DM-TCP dotée du protocole d'ionisation/recombinaison est de pouvoir décrire, d'une part, les effets de couplage entre les charges dans un plasma dont l'état d'ionisation est atteint au cours de la simulation et, d'autre part, le comportement collectif des électrons libres du plasma. Elle permet notamment d'étudier les propriétés dynamiques des électrons sous l'influence des différents états de charges, sans découpler ces derniers des ions (pas d'approximation de Born-Oppenheimer) et en utilisant un minimum de mécanismes microscopiques qui rendent compte de la complexité du problème à N-corps dépendant du temps.

Dans les plasmas denses, la dynamique des électrons est étudiée par diffusion Thomson X (DTX) à des fins de diagnostic en densité et en température. L'utilisation de cette technique comme outil diagnostic dans ce type de plasma n'est plus à démontrer. Elle est largement utilisée depuis une dizaine d'années pour mesurer les propriétés thermodynamiques des plasmas créés par laser, (voir [13] et les références internes), des plasmas de z-pinch, [32], et plus récemment de la matière tiède et dense, [33, 34, 35, 36]. Cette technique est l'analogue de la diffusion Thomson dans le domaine optique, [37], et permet de sonder la matière dense opaque au rayonnement visible.

L'utilisation de la DTX comme diagnostic des plasmas non idéaux requiert donc, non seulement des sources X bien caractérisées mais aussi des modèles théoriques appropriés pour décrire les facteurs de structure dynamique (DSF), ingrédient principal de l'interprétation des spectres, [38].

Dans le cas de la matière tiède et dense, ni les modèles issus de la physique des plasmas classiques ni ceux issus de la physique des solides ne permettent une description satisfaisante des facteurs de structure dynamique des électrons. C'est dans ce contexte que nous avons proposé d'étudier les effets de couplages sur les propriétés dynamiques des électrons libres en utilisant notre technique de dynamique moléculaire classique [2].

Brièvement, le principe d'une expérience idéale de diffusion Thomson X consiste à irradier le plasma par un rayonnement monochromatique (de vecteur d'onde k_0 et

2. Le calcul des facteurs de structure dynamique dans le cadre des plasmas d'hydrogène a fait l'objet du travail de stage de M2 RES de Dony Rifardo, *Étude de la matière tiède et dense par simulation de dynamique moléculaire classique*, 2013

de longueur d'onde λ_0) et d'observer le rayonnement diffusé (de vecteur d'onde $\vec{k}_s$ tel que $|\vec{k}_s| \approx |\vec{k}_0|$) sous un angle θ tel que :

$$k = |\vec{k}| = \frac{4\pi}{\lambda_0} sin(\theta/2). \tag{3.2}$$

Dans la simulation DM-TCP, à cause des conditions aux limites périodiques, le nombre d'onde k doit satisfaire la condition :

$$k_{x,y,z} = n_{x,y,z} \frac{2\pi}{c}, \tag{3.3}$$

où c est la taille de la boite de simulation (cf. eq. (2.4)) et $n_{x,y,z}$ un nombre entier. Cette condition contraint donc le nombre de particules N dans la boîte et la plus petite valeur de k atteinte dans la simulation est déterminée par le plus grand nombre de particules simulables dans des temps raisonnables.

Du fait du rapport de masse entre les ions et les électrons, on peut considérer que ce sont essentiellement les électrons qui diffusent. Le spectre observé présente une structure qui caractérise donc les fluctuations de la densité électronique. Suivant la longueur d'onde de diffusion, $\lambda_s = \frac{\lambda_0}{2sin(\theta/2)}$, on a accès aux effets collectifs ou individuels des électrons. Plus précisément, on caractérise le régime de diffusion Thomson par le paramètre α défini par le rapport :

$$\alpha = \frac{\text{longueur caractéristique de la sonde}}{\text{longueur caractéristique de l'écran}} = \frac{\lambda_s}{\lambda_e}, \tag{3.4}$$

avec λ_e la longueur de l'écran dans le plasma. Dans le cas des plasmas non dégénérés, la longueur d'écran est la longueur de Debye (cf. eq.(2.6)). Dans le cas des plasmas dégénérés, on considère la longueur d'onde de Thomas-Fermi comme longueur d'écran : $\lambda_e \sim \lambda_{TF} = \sqrt{\frac{3k_B T_F}{8\pi n_e e^2}}$.

Lorsque $\alpha > 1$, la forme du spectre diffusé est déterminée essentiellement par les effets collectifs. Il présente deux composantes (plasmons) situées de manière symétrique de part et d'autre du pic central (pic Rayleigh). Ce dernier correspond à la diffusion élastique des électrons liés aux ions. C'est la basse fréquence des fluctuations de la densité électronique. La mesure de la largeur de ce pic nous renseigne sur les interactions ions-électrons. La position des plasmons, très dépendante des couplages, nous donne accès à une mesure de la densité électronique, alors que le rapport de leur intensité nous renseigne sur la température électronique par le biais de la balance détaillée, [39]. Enfin, la largeur du plasmon est liée aux interactions entre les diverses charges du plasma.

Lorsque $\alpha < 1$, le spectre du rayonnement diffusé résulte de la superposition des effets individuels associés au mouvement thermique des électrons. Il est déplacé par rapport à la fréquence du rayonnement incident d'une valeur $\omega = -\hbar k^2/2m_e \pm k v_{th}$ où v_{th} est la vitesse thermale des électrons. C'est la diffusion Compton. Dans le cas

des plasmas dégénérés, la largeur du spectre est liée à la température de Fermi et donc à la densité électronique, tandis que dans le cas des plasmas non-dégénérés, la largeur du spectre est liée à la température électronique via la distribution de Maxwell-Boltzmann.

Formellement dans la simulation DM-TCP, si on identifie l'opérateur d'Heisenberg $\vec{r}_i(t)$ à la position de la $i^{\text{ème}}$ particule et que l'on suppose que les effets quantiques sont essentiellement dus à la balance détaillée, il est possible de mesurer les fluctuations de la densité électronique données par le facteur de structure dynamique :

$$S_{ee}(\vec{k},\omega) = \frac{1}{2\pi N}\int_{-\infty}^{+\infty} e^{i\omega t} < \rho(\vec{k},t)\rho(-\vec{k},t) > dt, \tag{3.5}$$

où $< ... >$ dénote une moyenne d'ensemble et

$$\rho(\vec{k},t) = \sum_{i=1}^{N} e^{i\vec{k}\cdot\vec{r}_i(t)}, \tag{3.6}$$

est la transformée de Fourier de la distribution de densité totale des électrons, avec $\vec{r}_i(t)$ le vecteur position à un instant t donné du $i^{\text{ème}}$ électrons.

Récemment, nous avons appliquée la DM-TCP à l'étude des facteurs de structure dynamique dans des conditions correspondant à deux expériences sur du béryllium dédiées à l'étude de la WDM, [33, 34]. L'*Annexe D* regroupe les résultats. L'objectif de ce travail est de vérifier si la TCP-MD contient suffisamment de physique pour explorer le comportement de la WDM par comparaison aux modèles existants et de montrer les effets de corrélations entre les particules sur les formes et le déplacement des composantes des DSF.

Les calculs présentés dans cette publication ont été effectués avec 220 atomes de béryllium. Le nombre d'électrons varie au cours de la simulation à cause du processus d'ionisation-recombinaison : les simulations démarrent avec une densité électronique correspondant à une charge moyenne $\overline{Z} = 2$. Après une phase de préparation du système imposant une température de $T_e = 12\ eV$ où de nombreux processus d'ionisation-recombinaison font varier les états de charges du béryllium, le système atteint un état d'équilibre avec une densité électronique et une charge moyenne que nous avons mesurées et comparées aux valeurs diagnostiquées par ailleurs.

Les résultats sont comparés à ceux obtenus dans l'approche RPA (Random Phase Approximation) dans laquelle la fonction diélectrique (reliée au facteur de structure dynamique par le théorème de fluctuation-dissipation) est calculée pour un plasma à une composante (OCP) sans interaction entre les électrons (plasma idéal), [40]. Dans les cas où la longueur d'onde de diffusion est telle que ce sont les effets collectifs des électrons qui sont mis en évidence, nos résultats montrent

l'effet de couplage entre les particules sur la position du plasmon. Par contre, dans les cas où la longueur d'onde de diffusion est telle que ce sont les effets individuels qui apparaissent dans les DSF, nos résultats sont en désaccord avec ceux de la RPA à cause des effets de dégénérescence des électrons. Une comparaison avec l'approche RPA développée dans la limite classique corrobore cette explication. Néanmoins, afin d'étendre le domaine d'application de notre technique, nous proposons une modification de nos résultats qui tient compte des effets de dégénérescence.

3.5 L'effet des corrélations entre les charges sur les propriétés statistiques des microchamps → *Annexe E*

Les raies spectrales émises par les atomes ou les ions dans un plasma sont sensibles à leur environnement et lui sont couplées par l'intermédiaire de l'interaction dipolaire avec le microchamp électrique total du plasma. Du fait des déplacements des charges, ce microchamp fluctue. À cause de la différence de masse entre les ions et les électrons du plasma, on considère généralement de manière séparée l'effet Stark dû à la composante *basse fréquence* ionique du microchamp de celui dû à la composante *haute fréquence* électronique. L'effet Stark ionique est ainsi traité par un modèle en champ statique tandis que l'effet Stark électronique est décrit par un processus dynamique. Dans les plasmas non-idéaux, les corrélations entre les charges du plasma ont un effet non négligeable sur les propriétés statistiques des microchamps et donc sur les profils de raies. Aussi, depuis les travaux de Baranger et Mozer, [41], puis de Hooper, [42] et d'Iglesias et co-auteurs, [43], une attention particulière a été portée sur les fonctions de distribution des champs électriques avec notamment une distinction entre sur les fonctions de distributions des microchamps hautes et basses fréquences. Mais cette distinction est nécessairement liée au processus physique pour lesquels ces microchamps sont étudiés et, comme le soulignent Baranger et Mozer, ne peut pas simplement se baser sur la contribution séparée des électrons et des ions au microchamp total, i.e. $\vec{F}(t) = \vec{F}_e(t) + \vec{F}_i(t)$, avec $\vec{F}_e(t)$ et $\vec{F}_i(t)$ les microchamps électronique et ionique, respectivement. À cause des interactions entre les charges, les ions voient leur potentiel momentanément écranté par un ensemble d'électrons. Le potentiel attractif entre les ions et les électrons produit un effet moyen des électrons sur le champ ionique. Une partie du microchamp électronique doit être enlevée de la composante hautes fréquences et ajoutée à la composante basses fréquences. La question de comment définir la composante basses fréquences du microchamp total ici se pose.

La simulation DM-TCP permet de générer des histoires de microchamps qui tiennent compte de toutes les interactions entre les particules chargées. Elle offre donc la possibilité de discuter les différents modèles. Dans l'article de l'*Annexe E*, la discussion se base sur l'analyse statistique des microchamps, mesurés sur un point neutre ou chargé, à partir de leurs fonctions de distribution statique et de

leur fonction de corrélation. Le plasma étudié est un plasma d'hydrogène dans des conditions de couplages modérés, pour lesquelles plusieurs mesures expérimentales des raies H$-\alpha$ et H$-\beta$ existent, [44, 45, 46, 47, 48] et des études des effets de corrélations sur ces profils de raies ont été proposées, [49] et *Annexe H*.

Dans les conditions de l'étude, les effets de couplages sont tels que le microchamp électronique apparaît comme la somme d'une composante hautes fréquences associée aux mouvements des électrons et d'une composante basses fréquences associée aux électrons couplés aux ions, comme le montre la figure 3.3(a), qui représente un bout d'histoire des microchamps ioniques (en bleu) et électroniques (en rouge). Le champ ressenti par l'émetteur neutre est la somme de ces deux microchamps (en noir). Les fonctions de corrélations associées à ces champs montrent cette dépendance statistique entre les ions et les électrons. On remarque sur la figure 3.3(b) que, d'une part la fonction de corrélation ion-electron présente une anti-corrélation entre $\vec{F}_e(t)$ et $\vec{F}_i(t)$, et, d'autre part, que la fonction de corrélation du microchamp électronique ne tend vers zéro que sur une échelle de temps correspondant au temps τ_i de corrélation ionique [3].

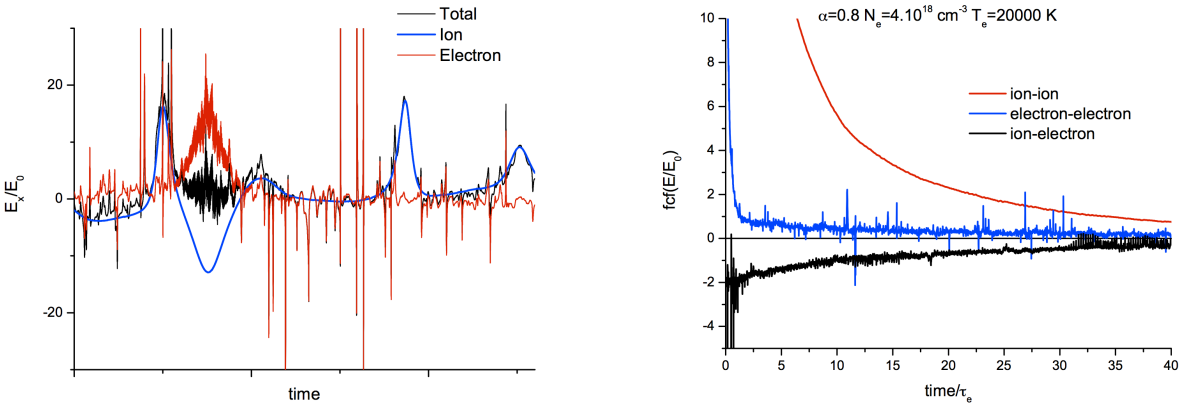

FIGURE 3.3 – *(a) à gauche :* Exemple de microchamp électrique vu par un émetteur neutre. *(b) à droite :* Fonction de corrélation des microchamps électriques.

Ces observations nous ont amenés à redéfinir le champ total en une somme de composantes hautes, $\vec{F}_F(t)$, et basses, $\vec{F}_S(t)$ fréquences : $\vec{F}(t) = \vec{F}_F(t) + \vec{F}_S(t)$ telles que ces composantes soient statistiquement indépendantes (ou du moins faiblement corrélées). Elles sont définies par une moyenne temporelle sur un intervalle de temps

3. le temps de corrélation ionique τ_i est défini comme le temps nécessaire pour un ion de traverser la distance moyenne ion-ion r_0 à la vitesse thermale v_{th}. Le temps de corrélation électronique τ_e est défini de manière analogue.

Δt compris entre les temps de corrélation électronique et ionique :

$$\overline{\vec{F}}(t)_{S,\Delta t} = \frac{1}{\Delta t}\int_{-\Delta t/2}^{\Delta t/2}[\vec{F}_e(t+t') + \vec{F}_i(t+t')]dt' \text{ et } \overline{\vec{F}}(t)_{F,\Delta t} = \vec{F}(t) - \overline{\vec{F}}(t)_{S,\Delta t} \quad (3.7)$$

L'objectif ici est de comparer les fonctions de distribution statique de la composante basses fréquences, obtenues pour différents temps d'intégration, avec celles obtenues par des modèles où les ions sont vus comme des particules chargées autour desquelles les électrons s'ajustent instantanément. Les simulations montrent que même en considérant des temps d'intégration longs ($\Delta t \simeq 10\tau_e$), il n'est pas possible de reproduire la fonction de distribution de la basses fréquences issue d'un modèle d'ions écrantés. Par contre, pour des temps d'intégration supérieurs à quelques dizaines de τ_e, on commence à moyenner sur les microchamps ioniques, jusqu'à obtenir un champ globalement nul pour des temps très longs, ce qui change totalement la fonction de distribution de champ et l'objectif recherché. Récemment, cette étude a été reprise et complétée par Hau-Riege et Weisheit sur des plasmas mixtes de carbone et d'hydrogène, [50]. Les fonctions de distribution statique des microchamps basses fréquences sont simulées de manière analogue à la notre pour différents types de plasmas de carbone. En définissant un intervalle de temps sur lequel ces fonctions de distribution statique varient très peu, les auteurs proposent une méthode pour extraire des simulations la composante basses fréquences du microchamp total.

Bibliographie

[1] R.C Davidson *et al.*, *Frontiers in high energy density physics : the X-games of contemporary science*, The National Academies Press, Washington D.C.

[2] V.E. Fortov, I.T. Iakubov and A.G. Khrapak, *Physics of strongly coupled plasma*, Clarendon Press, Oxford, ISBN 0–19–929980–3 (2006).

[3] R. W. Lee, et al., *Plasma-based studies with intense x-ray and particle beam sources*, Laser and Particle Beams **20**, 527 (2002).

[4] R.W. Lee, et al., *Finite temperature dense matter studies on next-generation light sources* J. Opt. Soc. Am. B **20**, 770 (2003).

[5] R.P. Feynman et al., *Equations of state of elements based on the generalized Fermi-Thomas theory*, Phys. Rev. **75**, 1561 (1949).

[6] B. Holst, R. Redmer and M. Desjarlais, *Thermophysical properties of warm dense hydrogen using quantum molecular dynamics simulations*, Phys. Rev. B **77**, 184201 (2008).

[7] F.B. Rosmej et al., *Strongly coupled laser produced plasmas : investigation of hollow ion formation and line shape analysis*, JQSRT **81**, 395 (2003).

[8] E. Galtier et al., *Interference effects and Stark broadening XUV intrashell transitions in aluminum under conditions of intense XUV free-electron-laser irradiation*, Phys. Rev. A **87**, 033422 (2013).

[9] M. Benfatto et al., *Multiple-scattering regime and higher-order correlations in x-ray-absorption spectra of liquid solutions*, Phys. Rev. B **34**, 5774-5781 (1986).

[10] A. Lévy et al., *X-ray absorption for the study of warm dense matter*, Plasma Physics and Controlled Fusion **51**, 124021 (2009).

[11] B.I. Cho et al., *Electronic Structure of Warm Dense Copper Studied by Ultrafast X-Ray Absorption Spectroscopy*, Phys. Rev. Lett. **106**, 167601 (2011).

[12] J.-P. Geindre et al., *Frequency-domain interferometer for measuring the phase and amplitude of a femtosecond pulse probing a laser-produced plasma*, Optics Letters **19**, 1997 (1994).

[13] Glenzer S.H. and R. Redmer, *X-ray Thomson scattering in high energy density plasmas*, Review of Modern Physics **81**, 1625 (2009).

[14] H. Minoo, M.M Gombert, C. Deutsch, *Temperature-dependent Coulomb interactions in hydrogenic systems*, Phys. Rev. A **23**, 924-943 (1981).

[15] F. J. Rogers, *Analytic electron-ion effective potentials for* $Z \leqslant 55$, Phys. Rev. A **23**, 1008-1014 (1981).

[16] C.S. Jones and M. S. Murillo, *Analysis of semi-classical potentials for molecular dynamics and Monte Carlo simulations of warm dense matter*, High Energy Density Physics **3**, 379 (2007).

[17] C. Dorso, S. Duarte and J. Randrup, *Classical simulation of the Fermi gas*, Phys. Lett. B **188**, 287 (1987).

[18] D.R. Inglis and E. Teller, *Ionic Depression of Series Limits in Cne-Electron Spectra.*, Astrophys. J. **90**, 439 (1939).

[19] G. Ecker and W. Kröll, *Lowering of the Ionization Energy for a Plasma in Thermodynamic Equilibrium*, Phys. Fluids **6**, 62 (1963).

[20] J.C. Stewart and K.D. Pyatt Jr, *Lowering of Ionization Potentials in Plasmas*, Astrophys. J. **144**, 1203 (1966).

[21] S.M. Vinko et al., *Creation and diagnosis of a solid-density plasma with an X-ray free-electron laser*, Nature **482** 59 (2012).

[22] O. Ciricosta et al., *Direct measurements of the ionization potential depression in a dense plasma*, Phys. Rev. Lett. **109**, 065002 (2012).

[23] T. R. Preston et al., *The effects of ionization potential depression on the spectra emitted by hot dense aluminium plasmas*, High Energy Density Physics **9** 258 (2013).

[24] D.J. Hoarty *et al.*, *Observations of the Effect of Ionization-Potential Depression in Hot Dense Plasma*, Physical Review Letters **110**, 265003 (2013).

[25] C.A. Iglesias, *A plea for a reexamination of ionization potential depression measurements*, High Energy Density Physics **12**, 5-11 (2014).

[26] I.I. Sobelman, L.A. Vainstein, E.A. Yukov, *Excitation of Atoms and Broadening of Spectral Lines*, Springer Series in Chemical Physics 7, ed. V.I. Goldanskii et al., Springer-Verlag Berlin Heidenberg New-York (1981).

[27] A. Calisti, T. del Río Gaztelurrutia, B. Talin, *Classical molecular dynamics model for two component plasmas*, High Energy Density Physics **3**, 52 (2007).

[28] J. Glosli et al.,*Molecular dynamic simulations with radiation*, J. Phys. A : Math Theor. **42**, 11214030 (2009).

[29] R. More et al., *Radiation in particle simulations*, High Energy Density Phys. **6**, 29-38 (2010).

[30] A. Calisti et al., *Microfields in hot dense hydrogen plasmas*, High Energy Density Phys. **7**, 197-202 (2011).

[31] B.I. Cho et al., *Resonant Kα Spectroscopy of Solid-Density Aluminum Plasmas*, Phys. Rev. Lett. **109**, 245003 (2012).

[32] J.E. Bailey et al., *X-Ray Thomson Scattering Measurements of Warm Dense Matter*, Sandia Report, **SAND2012-7998** (2012).

[33] S.H. Glenzer et al., *Observations of Plasmons in Warm Dense Matter*, Phys. Rev. Lett. **98**, 065002 (2009).

[34] H.J. Lee et al., *X-Ray Thomson-Scattering Measurements of Density and Temperature in Shock-Compressed Beryllium*, Phys. Rev. Lett. **102**,115001 (2009).

[35] R.R. Fäustlin et al., *Observation of Ultrafast Nonequilibrium Collective Dynamics in Warm Dense Hydrogen*, Phys. Rev. Lett. **104**, 125002 (2010).

[36] L.B. Fletcher et al., *Observations of Continuum Depression in Warm Dense Matter with X-Ray Thomson Scattering*, Phys. Rev. Lett.**112**,145004 (2014).

[37] D.E. Evans and J. Katzenstein, *Laser light scattering in laboratory plasmas*, Rep. Prog. Phys.**32**, 207 (2009).

[38] G. Gregori et al., *Theoretical model of x-ray scattering as a dense matter probe*, Phys. Rev. E **67**, 026412 (2003).

[39] A. Höll et al., *Thomson scattering from near-solid density plasmas using soft X-ray free electron lasers*, High Energy Density Physics **3**, 120 (2007).

[40] N.R. Arista and W. Brandt, *Dielectric response of quantum plasmas in thermal equilibrium*, Phys. Rev. A **29**, 1471 (1984).

[41] M. Baranger and B. Mozer, *Electric Field Distributions in an Ionized Gas*, Phys. Rev. **115**, 521-525 (1959) ; B. Mozer and M. Baranger, *Electric Field Distributions in an Ionized Gas. II* Phys. Rev. **118**, 626-631 (1960).

[42] C.F. Hooper, *Electric Microfield Distributions in Plasmas*, Phys. Rev. **149**, 77 (1966).

[43] C.A. Iglesias et al. *Electric microfield distributions in strongly coupled plasmas*, Phys. Rev. A **28**, 1667-1672 (1983).

[44] Y. Vitel, *Experimental study of H−α broadening and shift in dense argon plasmas*, J. Phys. B **20**, 2327 (1987).

[45] S. Böddeker et al., *Shift and width of the H−α line of hydrogen in dense plasmas*, Phys. Rev. E **47**, 2785 (1993).

[46] S. Büscher et al., *The Stark width and shift of the hydrogen H−α line*, J. Phys. B **35**, 2889 (2002).

[47] S. Flih et al., *Comparison of the Stark widths and shifts of the H−α line measured in a flash tube plasma with theoretical results.*, J. Phys. B **36**, 283 (2003).

[48] C.G. Parigger et al., *Balmer series H−β measurements in a laser-induced hydrogen plasma.*, Appl. Optics **30**, 5992 (2003).

[49] E. Stambulchik et al., *Correlation effects and their influence on line broadening in plasmas : Application to H−α*, High Energy Density Phys. **3**, 272 (2007).

[50] S. Hau-Riege and J. Weisheit, *Electric microfield in dense carbon-hydrogen plasmas*, Phys. Rev. E **91**, 033106 (2015).

Chapitre 4

Simulation des profils de raies dans les plasmas

Le rayonnement émis par un plasma est généralement la seule quantité observable qui permet d'obtenir des informations sur le milieu. Les informations contenues dans le spectre sont reliées à la physique atomique de l'atome ou de l'ion émetteur et à la physique du plasma environnant. L'analyse de ces spectres peut fournir des renseignements sur l'état d'ionisation, les densités, les températures, etc.. à condition de se donner des modèles de calcul des profils de raies pertinents.

La modélisation des profils de raies dans les plasmas est un problème faussement élémentaire. Différents mécanismes d'élargissement influent sur la forme des profils de raies. L'élargissement Doppler produit par le mouvement thermique des émetteurs est en général le mécanisme dominant dans les plasmas chauds et relativement denses avec des émetteurs de charge nette Z modérée. Lorsque Z augmente l'émission spontanée augmente fortement en Z^4 et l'élargissement naturel peut devenir prépondérant. Pour des plasmas plus denses, c'est l'élargissement Stark, produit par les microchamps créés par les particules chargées, qui est la cause principale de l'élargissement des raies.

La notion d'*élargissement* est généralement associée à la notion de *fluctuations* et la notion de *processus aléatoire* y est donc essentielle. Par « fluctuations » il faut comprendre ici que les différents atomes ou ions émetteurs dans un plasma ressentent différentes interactions. Ainsi, le caractère aléatoire de la perturbation est une nécessité pour l'élargissement et ce n'est pas spécifique aux plasmas. Par exemple, pour l'élargissement Doppler, il faut évaluer une distribution de vitesse : un émetteur se déplaçant à une vitesse unique implique un déplacement Doppler de la raie émise par cet émetteur et non un élargissement Doppler. Dans le cas de l'élargissement Stark, la difficulté principale est de caractériser proprement l'environnement de l'émetteur. En effet, l'élargissement Stark des raies résulte de l'interaction des degrés de liberté internes de l'émetteur avec les microchamps électriques créés par les ions et les électrons du plasma environnant. Et, à cause du déplacement des charges, ces microchamps fluctuent au cours du processus d'émission du rayonnement. Réaliser des modèles qui tiennent compte de ces fluctuations reste un problème complexe.

Historiquement, [1], le point de vue adopté était que les ions, plus lents que les

électrons, génèrent des microchamps électriques faiblement fluctuants, considérés quasi-statiques mais aléatoires, qui donnent lieu à un élargissement inhomogène des raies. De manière analogue à l'élargissement Doppler, chaque émetteur ressent un microchamp différent qui résulte en un éclatement et un déplacement des raies ; parce que les microchamps sont aléatoires, on considère une distribution de ces déplacements et, une intégration sur ces microchamps (ou de manière équivalente sur ces déplacements) donne lieu à un élargissement du profil de raies. D'un autre côté, l'interaction due aux électrons, plus rapides, était modélisée dans l'approximation d'impact. Les électrons perturbent les émetteurs via des collisions, se traduisant sur le profil par un élargissement homogène. Évidemment ces deux points de vues sont des cas limites et généralement les émetteurs sont sensibles aux fluctuations des microchamps.

Les premières tentatives pour prendre en compte la dynamique des ions dans les modèles théoriques remontent aux années 70, [2, 3, 4, 5] suite aux différences obtenues entre les modèles quasi-statiques et les expériences, [6]. Avec le développement des outils informatiques, les simulations des profils de raies ont vu le jour dans les années 80, [7, 8, 9, 10, 11] et des modèles plus sophistiqués pour des émetteurs neutres ou multi-chargés ont suivi, [12, 13, 14, 15, 16]. Forcément, ces modèles diffèrent dans leur champ d'application, leur précision et leur facilité de mise en œuvre mais très peu de comparaisons existent, comme il l'est discuté dans l'annexe G.

Les expériences dédiées à la validation des modèles de calculs de profils de raies sont quasi-inexistantes car elles nécessitent non seulement des spectroscopes de très bonne résolution, mais aussi un diagnostic indépendant des paramètres plasmas. On peut citer tout de même quelques expériences qui ont contribué à la mise en évidence de la dynamique des ions et la validation de certains modèles, [17, 18, 19, 20]. Une autre voie de validation est la comparaison avec les profils obtenus par les simulations numériques. La simulation numérique des profils de raies dans les plasmas est basée sur un schéma type représenté sur la figure 1 de la ref. [21] et reproduite ici sur la figure 4.1. Les calculs sont divisés en deux grands blocs indépendants. Le premier consiste à simuler le plasma c'est-à-dire à simuler les trajectoires des particules chargées du plasma. Le microchamp électrique $\vec{E}_l(t)$ qu'elles produisent est mesuré sur l'émetteur à chaque pas de temps et est enregistré pour être utilisé dans le second bloc de la simulation. Le second bloc consiste à calculer les profils de raies : l'équation d'évolution de l'émetteur est intégrée pas à pas et le résultat est moyenné sur un très grand nombre de configurations l. Le profil est obtenu par transformée de Fourier et les effets d'élargissement additionnel (effet Doppler, largeur instrumentale,...) sont ajoutés postérieurement. Comme les fluctuations des microchamps sont prises en compte naturellement dans les simulations, les profils simulés sont généralement considérés comme référence au même titre que les résultats expérimentaux.

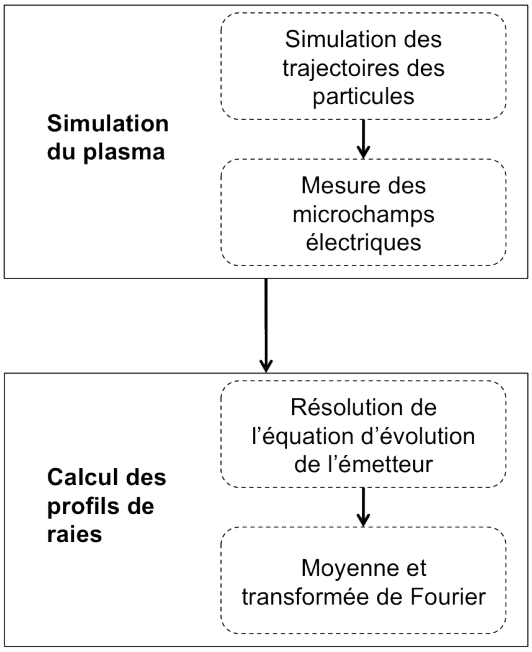

FIGURE 4.1 – Schéma du déroulement d'une simulation numérique pour le calcul des profils de raies.

Bien que les codes de simulation numérique des profils de raies dans les plasmas reposent sur le schéma général de la figure 4.1, ils diffèrent les uns des autres à cause des modèles utilisés (voir [21] et les références incluses). Par exemple, dans les premières simulations développées par Stamm et Voslamber, [7], seuls les ions étaient simulés via un modèle de quasi-particules (OCP-Yukawa). Les électrons restaient modélisés par la théorie collisionnelle. De plus les ions étaient supposés ne pas interagir entre eux, se déplaçant ainsi sur des trajectoires rectilignes (les effets d'écrans étaient modélisée par un potentiel de Debye lors du calcul des champs électriques). Les interactions entre ions n'ont été prises en compte que plus tard, [22]. Puis, avec le développement des capacités de calcul, les simulations de plasmas plus « réalistes » où les interactions entre les ions et les électrons sont prises en compte ont vu le jour, [24, 25, 26, 27, 28].

Dans la suite de ce Chapitre, nous montrons comment notre technique de simulation par Dynamique Moléculaire a été utilisée dans le cadre de la validation des modèles développés pour le calcul des profils de raies dans différents types de plasmas. On verra par exemple, combien elle a été un support omniprésent dans le développement du modèle de fluctuation de fréquence dédié à la dynamique des ions. De part sa structure, l'ajout de champs extérieurs constants ou dépendants du temps est facilement réalisable dans les simulations. Aussi, elle a permis l'extension du FFM au calcul des profils de raies dans les plasmas magnétisés. Finalement, elle a été utilisée dans l'étude des effets de corrélations sur les profils de raies élargies

par effet Stark et Doppler.

4.1 Formalisme

Dans notre étude, le problème de base est de modéliser la forme des profils de raies spectrales émises par un émetteur quelconque plongé dans un bain de perturbateurs. Dans les plasmas, les perturbateurs sont des ions et des électrons. Ceux-ci créent un champ électrique $\vec{E}(t)$ (appelé microchamp) qui est à l'origine de l'élargissement des raies par effet Stark.

Le point de départ du formalisme des profils de raies est l'expression de la fonction d'autocorrélation du moment dipolaire de l'émetteur. Elle s'exprime sous la forme d'une trace sur les états du système, [29] :

$$C(t) = Tr\big\{\vec{d}(0) \cdot \vec{d}(t)\rho_0^s\big\}, \tag{4.1}$$

où $\vec{d}$ est l'opérateur moment dipolaire et ρ_0^s est la matrice densité à l'équilibre. La transformée de Laplace de $C(t)$ donne l'expression du profil de raies :

$$I(\omega) = \frac{1}{\pi}\Re \int_0^\infty dt\ e^{i\omega t}C(t). \tag{4.2}$$

Le problème dans sa forme générale est complexe et ne peut pas être résolu analytiquement. Il est donc nécessaire de faire un certain nombre d'hypothèses et d'approximations :

- on suppose que le système local est composé de deux sous-systèmes : le système actif composé d'une seule particule émettrice et le système perturbatif composé du bain thermique formé de toutes les autres particules,
- on suppose que l'émetteur ne modifie pas le bain. Ceci implique que la matrice densité du système, ρ_0^s, peut être factorisée : $\rho_0^s = \rho_0^r \otimes \rho_0^p$ avec ρ_0^r et ρ_0^p représentant les états du système émetteur (**r***adiator*) et le bain (**p***erturbers*), respectivement, (dans la suite on notera ρ_0 la matrice densité de l'émetteur)
- on attribue une trajectoire classique aux perturbateurs tandis que les états de l'émetteur sont traités quantiquement (méthode semi-classique).

Le problème revient donc à trouver l'évolution de temporelle de l'opérateur dipolaire de l'émetteur isolé $\vec{d}$ moyenné sur un ensemble statistique représentant le bain de perturbateurs. La fonction $C(t)$ s'écrit donc :

$$C(t) = Tr_r\big\{\big\langle\vec{d}(0) \cdot \vec{d}(t)\big\rangle_p\rho_0\big\}, \tag{4.3}$$

avec $Tr_r\{...\}$ la trace sur les états de l'émetteur et $\langle...\rangle_p$ la moyenne sur le bain.

Dans la plupart des cas, on considère que les perturbateurs n'induisent pas de transition entre les états excités et les états d'énergie moindre sur lesquels l'atome

se désexcite. C'est l'approximation du « *no quenching* ». Dans ce cas, le calcul de la moyenne sur le bain est simplifié. On travaille dans la représentation de Liouville, [30], où l'opérateur de Liouville $L = \frac{1}{\hbar}(HI^\dagger - IH^\dagger)$ est construit à partir de l'Hamiltonien, H, avec I l'opérateur identité et $H^\dagger$ l'adjoint de H. Ainsi, les valeurs propres de L sont les fréquences propres ω_{ab} du système entre deux états propres a et b. Cette représentation permet une formulation compacte de $C(t)$:

$$C(t) = \ll \vec{d}^\dagger | U(t) | \vec{d}\rho_0 \gg, \tag{4.4}$$

où $U(t) = \left\langle U_l(t) \right\rangle_{l\in\{F\}}$ est l'opérateur d'évolution moyen de l'émetteur, l appartenant à l'ensemble des fonctionnelles $\{F\}$. Le problème revient donc à

- trouver l'opérateur d'évolution $U_l(t)$ pour une configuration de microchamps donnée, ce qui revient à résoudre l'équation suivante :

$$\frac{dU_l(t)}{dt} = -iL_l(t)U_l(t), \quad U_l(0) = \mathbf{1}, \tag{4.5}$$

  avec $L_l(t) = L_0 - \vec{d}\cdot\vec{E}_l(t)$ où L_0 est le Liouvillien de l'émetteur isolé et $\vec{d}\cdot\vec{E}_l(t)$ la perturbation due à l'effet Stark qui relie le dipôle de l'émetteur au microchamp $\vec{E}_l(t)$,

- et à moyenner sur un ensemble statistique de microchamps $\{\ \}_{l\in F}$.

Du fait du caractère aléatoire de la perturbation, il n'existe pas de solution analytique à cette équation. Cependant, comme on le verra dans la suite, $U(t)$ peut être obtenu, soit par simulation numérique en intégrant l'équation stochastique (4.5) sur un échantillon simulé de microchamps, soit par des méthodes alternatives.

Par exemple, dans *les méthodes standards*, [31], le calcul du profil de raies est basée sur la séparation des contributions des ions et des électrons en raison des propriétés dynamiques très différentes des microchamps qu'ils génèrent. En effet, la fréquence typique de fluctuation du microchamp créé par des perturbateurs p de densité n_p se déplaçant à la vitesse thermique v_p relativement à l'émetteur, est définie par :

$$\nu_p = v_p/r_p, \tag{4.6}$$

où $r_p = (3/4\pi n_p)^{1/3}$ est la distance moyenne entre les particules. Si l'on suppose des températures ioniques et électronique égales, alors, le rapport entre la fréquence de fluctuation du microchamp électronique et la fréquence de fluctuation du microchamp ionique est proportionnel à :

$$\frac{\nu_e}{\nu_i} \sim \left(\frac{\mu_i}{\mu_e}\right)^{1/2} Z_i^{1/3}. \tag{4.7}$$

Par conséquent, la perturbation due aux électrons (de masse réduite μ_e) est au moins de deux ordres de grandeur plus rapide que celle due aux ions (de masse réduite μ_i

et de charge Z_i). Ceci permet donc de prendre la moyenne sur les électrons et sur les ions séparément dans l'équation Eq.(4.3) :

$$\langle ... \rangle_p = \langle \langle ... \rangle_{\text{électrons}} \rangle_{\text{ions}} \tag{4.8}$$

Le microchamp ionique est supposé fluctuer très lentement (approximation quasi-statique pour les ions) alors que l'aspect collisionnel est mis en avant pour décrire l'effet du microchamp électronique (approximation d'impact pour les électrons). Dans cette approximation, l'effet Stark dû aux ions décompose chaque transition radiative en un certain nombre de composantes (élargissement inhomogène des raies) et les collisions dues aux électrons rapides élargissent chacune des composantes de manière homogène. Pour que l'approche collisionnelle soit justifiée il faut que les durées typiques des processus « courts » d'interaction avec le bain soient négligeables devant les échelles de temps relatives à la décorrélation du dipôle.

Les microchamps dans le plasma sont caractérisés par une densité de probabilité $Q(\vec{E}) =< \delta(\vec{E} - \vec{E_p}) >$ de trouver un microchamp $\vec{E}$ égal à $\vec{E_p}$ mesuré sur la particule p. Pour les plasmas isotropes, on utilise la fonction de distribution $W(E) = 4\pi E^2 Q(\vec{E})$. Elle peut être obtenue analytiquement dans le cas des plasmas idéaux, [32] ou par des modèles qui tiennent compte des corrélations entre les charges, [33]. Une moyenne sur la distribution des microchamps ioniques est donc effectuée.

Le profil de raies dans l'approximation quasi-statique s'écrit :

$$I_s(\omega) = \frac{1}{\pi} Re \langle \langle \vec{d}^{\dagger} | \int \mathrm{d}E W(E) \int_0^{\infty} dt \ \mathrm{e}^{i\omega t} \mathrm{e}^{-i(L_0 - dE - i\phi)} | \vec{d}\rho_0 \rangle \rangle. \tag{4.9}$$

L'opérateur $\phi = \phi^e + \gamma^s$ représente les effets d'élargissements homogènes électronique ϕ^{el} et naturel γ^s.

Ces deux approximations constituent deux limites très utiles pour lesquelles la résolution de l'équation stochastique est maîtrisée. Cependant, certaines conditions de plasma ne permettent pas l'utilisation de cette approche standard.

C'est le cas par exemple lorsque les microchamps ioniques fluctuent pendant une échelle de temps correspondant à l'inverse de la demi-largeur de la raie. Il est alors nécessaire de tenir compte de la dynamique des ions dans l'évaluation de l'opérateur d'évolution. On reviendra sur ce problème dans la section suivante.

C'est le cas aussi des raies de l'hydrogène (ou de ses isotopes) à nombre quantique principal élevé ($n \geqslant 8$) observées dans les plasmas de divertor ou de bords de tokamak, [34], ou des raies de l'hydrogène émises dans les plasmas tièdes et denses, [35]. Dans ces conditions l'approximation d'impact pour les électrons n'est plus valable [1]. La perturbation électronique est alors traitée par une méthode appropriée au régime intermédiaire entre le collisionnel et le statique, [34, 35].

1. Cette étude a fait l'objet de mon travail de thèse : *Modélisation non collisionnelle des effets d'élargissement électronique des raies de l'hydrogène dans les plasmas, (1999)*

4.2 Intégration numérique de l'équation stochastique

La simulation des profils de raies dans les plasmas, que nous proposons, consiste à résoudre numériquement l'équation stochastique (4.5) dans laquelle le microchamp $\vec{E}_l(t)$ est obtenu par la dynamique moléculaire et à moyenner sur un grand nombre de configurations l. Cette intégration s'effectue sur un domaine fini, divisé en plusieurs pas de temps Δt. Ce dernier doit être choisi de manière à rendre compte en détail de la décroissance de la fonction d'autocorrélation du dipôle $C_{dd}(t)$. Une des difficultés de la simulation est donc l'optimisation des échelles de temps : δt pour résoudre les équations du mouvement et $\Delta t = k\delta t$ (avec k entier) pour intégrer numériquement l'équation d'évolution.

Plusieurs méthodes existent pour intégrer numériquement les équations différentielles, [36, 37]. Nous utilisons l'algorithme très stable, [36], donnant la valeur de $U_l(t)$ à un instant donnée en fonction de sa valeur à l'instant précédent :

$$\frac{U_l(t+\Delta t) - U_l(t)}{\Delta t} = -i\frac{L_l(t+\Delta t)U_l(t+\Delta t) + L_l(t)U_l(t)}{2}, \tag{4.10}$$

où $L_l(t) = L_0 - \vec{d}\cdot\vec{E}_l(t)$, $\vec{E}_l(t)$ étant le microchamp créé soit par les ions, soit par les électrons ou les ions et les électrons du plasma. Tout dépend du modèle de plasma choisi.

Après arrangements, cette équation s'écrit :

$$U_l(t+\Delta t) = \left(1 + i\frac{\Delta t}{2}L_l(t+\Delta t)\right)^{-1}\left(1 - i\frac{\Delta t}{2}L_l(t)\right)U_l(t), \tag{4.11}$$

avec la condition initiale : $U(0) = \mathbf{1}$. L'erreur ici est en $\mathcal{O}(\Delta t^3)$.

Ainsi, les valeurs de $U_l(t)$ sont calculées de proche en proche sur un intervalle de temps compris entre la valeur initiale et une valeur $t_{max} = n\Delta t$ (n entier). Pour obtenir des profils de raies précis il faut que ce temps soit bien supérieur à l'inverse de la largeur de la raie, notée w : $t_{max} >> w^{-1}$. D'autre part, il faut choisir un pas de temps Δt qui doit être au moins inférieur à la fréquence typique des fluctuations du microchamp (cf. eq.(4.6)) (correspondant au perturbateur le plus léger), c'est-à-dire : $\Delta t << \nu_e$ dans le cas d'une simulation TCP par exemple.

À l'opérateur $U_l(t)$ de la $l^{\text{ième}}$ réalisation $\vec{E}_l(t)$ du microchamp, correspond donc une fonction d'autocorrélation du moment dipolaire électrique $C^{(l)}(t)$. La fonction d'autocorrélation totale est obtenue en effectuant une moyenne d'ensemble sur toutes les réalisations du microchamp :

$$C(t) = \frac{1}{n_r}\sum_{i=1}^{n_r} C^{(i)}(t). \tag{4.12}$$

Finalement, le profil de raie $I(\omega)$ est obtenu en prenant la partie réelle de la transformé de Fourier de $C(t)$.

Il n'existe pas de limitation formelle à cette technique si ce n'est le coût en temps de calcul. Le calcul de $U_l(t)$ et donc de $C(t)$ nécessite des inversions et des multiplications de matrice dont le rang est d'autant plus grand que les nombres quantiques principaux des niveaux sont élevés : pour simuler un système quantique défini par n_e niveaux supérieurs et n_g niveaux inférieurs, la matrice L a pour dimension $n_g n_e \times n_g n_e$. Pour un plasma de température et de densité données, la simulation peut s'effectuer sur des centaines de milliers de pas de temps (et ce nombre sera d'autant plus grand que la raie est étroite) et sur un très grand nombre de réalisations (de l'ordre de 10^4). Cette méthode est donc lente et ne peut pas être appliquée à n'importe quel système atomique, malgré les progrès réalisés dans les moyens informatiques. C'est pourquoi il est apparu indispensable, ne serait-ce que pour les diagnostics, de développer des modèles de calculs de profils de raies rapides et performants.

Remarque : Dans le cadre de la simulation des profils de raies émises par l'atome d'hydrogène ou des ions hydrogénoïdes, il existe une méthode efficace basée sur la symétrie $SO(4)$ de l'atome d'hydrogène, [38, 39, 40]. Cette méthode est beaucoup plus rapide car quel que soit le nombre quantique principal de la raie calculée, la taille des matrices est de 4×4. Elle est cependant limitée aux calculs sans structure fine mais adaptée à l'introduction d'un champ magnétique extérieur (cf. *Annexe I*).

En revanche, la simulation numérique des profils de raies présente certains avantages :

— Les interactions entre les particules étant prises en compte dans la DM, il est possible avec cette technique d'étudier les effets de couplage entre les particules sur les profils de raies. Par exemple, la technique de dynamique moléculaire a été utilisée pour simuler une impureté ionique dans un gaz d'électrons afin d'étudier les effets de corrélation de charges au niveau de l'élargissement Stark électronique [26].

— Les effets de dynamique des particules apparaissent naturellement sur les profils simulés. Ces derniers sont utilisés comme profils de référence dans les comparaisons avec les modèles (cf. *Annexes F, G, H* et *I*).

— Par construction, il est aussi possible d'introduire des champs électriques ou magnétiques extérieurs dépendant ou pas du temps. Comme nous le verrons dans la suite, la DM a été utilisée pour calculer les profils de raies élargies par effet Stark et Zeeman dans le cadre de l'étude des plasmas magnétisés. Une étude sur les effets de champs électriques oscillants a aussi été menée grâce à cette technique, [41, 42, 43].

4.3 La DM comme outil de validation des modèles

4.3.1 La dynamique des ions → *Annexes F et G*

La prise en compte de la dynamique des ions dans les modèles est un problème de longue date. Les premières tentatives datent des années 70 avec les simulations de Stamm et Voslamber, [7]. Depuis, plusieurs modèles basés sur des approches stochastiques ou collisionnelles ont été développées en parallèles avec les simulations numériques, (voir [21] et les références citées). Parmi ces modèles on peut citer la méthode du microchamp modèle (MMM) [44] développée pour les émetteurs neutres, le modèle de Boerker Iglesias et Dufty (BID), [12], qui est une extension du MMM applicable aux ions multichargés ou encore le modèle de fluctuation de fréquence (FFM), et le code de calcul de profils de raies PPP associé, qui ont été développés dans l'équipe, [14].

L'effet de dynamique des ions nécessite la prise en compte des fluctuations temporelles du microchamp et se traduit par une re-homogénéisation du profil calculé dans l'approximation statique. La difficulté principale dans la modélisation d'un tel effet est de fournir une solution de l'équation stochastique suffisamment précise en supposant un processus stochastique ou collisionnel idéalisé qui conserve les propriétés de l'interaction « réelle » entre le microchamp et le système émetteur.

Le MMM et le BID reposent sur un modèle stochastique du microchamp dans lequel ce dernier est constant dans un intervalle de temps donné puis saute à une autre valeur de manière aléatoire. Les deux contraintes étant i) les amplitudes des microchamps qui constituent une séquence doivent être cohérentes avec les propriétés statiques des microchamps, ii) la fréquence des sauts doit être choisie de manière à reproduire proprement les propriétés dynamiques des microchamps.

Le FFM repose sur une représentation différente de ces processus stochastiques : le système quantique perturbé par un champ électrique fluctuant réagit comme un ensemble de transitions à deux niveaux habillés, sujet à un processus de mélange de type collisionnel.

Ainsi, contrairement à la simulation numérique et aux modèles MMM et BID, le modèle de fluctuation de fréquence ne traite pas directement l'influence des fluctuations du microchamp mais part de l'hypothèse clé selon laquelle ces dernières entraînent, à travers l'opérateur d'évolution, des fluctuations aléatoires de la fréquence du rayonnement émis. Sa mise en œuvre se fait en deux étapes principales, [45, 14] :

1. *Construction des transitions Stark habillées dans l'approximation quasi-statique*
   L'effet du microchamp ionique se traduit par un éclatement des niveaux d'énergie par effet Stark linéaire ou quadratique. Chaque transition radia-

tive initiale se décompose en plusieurs composantes Stark dont la largeur homogène agit comme un filtre de bruit. L'intégrale sur le microchamp de l'équation (4.9) peut-être remplacée par une somme pondérée de n_f termes représentant la distribution statique de microchamp :

$$I_s(\omega) = \frac{1}{\pi} Re\langle\langle \vec{d}^{\dagger}| \sum_{f=1}^{n_f} W_f \int_0^{\infty} dt\ \mathrm{e}^{i\omega t} \mathrm{e}^{-i(L_0 - dE_f - i\phi)} |\vec{d}\rho_0\rangle\rangle. \tag{4.13}$$

W_f est le poids associé au champ électrique constant E_f.

Pour chaque champ, il existe une matrice complexe de changement de base M_f permettant d'écrire l'exposant sous forme d'une matrice diagonale : $\mathrm{L}_d = M_f^{-1}(L_0 - dE_f - i\phi)M_f$. En portant cet opérateur dans l'équation (4.13) et après un peu d'algèbre, le profil quasi-statique s'écrit comme une somme de n_c fractions rationnelles :

$$I_s(\omega) = \sum_{k=1}^{n_c} \frac{c_k(\omega - f_k) + a_k\gamma_k}{(\omega^2 - f_k^2) + \gamma_k^2}, \tag{4.14}$$

où les paramètres $f_k + i\gamma_k$ sont les fréquences propres généralisées et $a_k + ic_k$ les amplitudes propres généralisées, [46].

L'ensemble des paramètres $(f_k, \gamma_k, a_k, c_k)$ constituent toute l'information nécessaire au calcul du profil de raies dans l'approximation quasi-statique. On notera ici que l'information sur la polarisation est volontairement négligée mais, comme on le verra dans l'application du FFM au calcul des profils de raies dans les plasmas magnétisés, il est tout à fait possible de la conserver lors de cette étape.

Formellement, chaque état propre a une contribution au processus d'émission qui peut être interprétée comme la contribution d'un système élémentaire à deux niveaux dont le rayonnement est caractérisé par les fréquences et les amplitudes propres généralisées. Nous appelons ces systèmes des canaux radiatifs ou des *Stark Dressed Transitions* (SDT). Ainsi chaque transition radiative participant à la formation du spectre est associée à un ensemble S de SDT et résulte de la somme de ces contributions élémentaires. On peut alors travailler dans un nouvel espace dans lequel on définit un dipôle effectif D_j et une probabilité instantanée p_j liés à la j$^{\text{ème}}$ SDT tels que :

$$p_j = a_j/r, \tag{4.15}$$

$$D_j = r\sqrt{1 + ic_j/a_j}, \tag{4.16}$$

avec $r^2 = \sum_{k \in S} a_k$ l'intensité totale de la transition radiative considérée.

Le profil de raie associé s'écrit dans la base des SDT :

$$I(\omega) = \frac{1}{\pi}\Re\sum_{k,j} i \ll D_k|G^s(\omega)|D_j \gg p_j, \tag{4.17}$$

en définissant le propagateur quasi-statique :

$$G^s(\omega) = (\omega\mathbf{1} - \mathrm{L}_d)^{-1}, \tag{4.18}$$

où L_d est le Liouvillien dont les états propres forment la nouvelle base.

2. *Mélange stochastique des SDT pour tenir compte de la dynamique des ions :* Les fluctuations du champ associées au mouvement des ions se traduisent par un mélange des n_c canaux radiatifs appartenant à l'ensemble S lors du processus d'émission. Le profil dynamique (en référence à la dynamique des ions perturbateurs) est alors obtenu en incluant dans l'opérateur d'évolution du système un processus stochastique de mélange des canaux radiatifs, [14]. Ce mélange est modélisé par un processus de Markov stationnaire paramétré par un taux ν caractéristique des fluctuations du microchamp ionique.

   Un processus de Markov stationnaire de n états est entièrement défini par les probabilités instantanées des états, $p_1, p_2, ..., p_n$, et les taux de transitions entre ces états, $W_{i,j}$ avec $i, j = 1, ..., n$. Ici, les états sont les canaux radiatifs caractérisés par leur probabilité d'émission $p_j = a_j/r$. Le mécanisme d'échange entre les canaux est caractérisé par les coefficients de la matrice des taux de transition W définis par :

$$W_{i,j} = -\nu p_i, \ i \neq j, \tag{4.19}$$
$$W_{i,i} = \nu(1 - p_i). \tag{4.20}$$

   Ces coefficients obéissent à des règles de somme qui assurent la stationnarité du processus :

$$\sum_i W_{i,j} = 0 \text{ et } \sum_j W_{i,j}p_j = 0. \tag{4.21}$$

   Le profil dynamique associé à la raie correspondant à l'ensemble S s'écrit :

$$I(\omega) = \frac{1}{\pi}\Re\sum_{k,j} i \ll D_k|G^d(\omega)|D_j \gg p_j, \tag{4.22}$$

   avec le propagateur dynamique :

$$G^d(\omega) = (\omega\mathbf{1} - \mathrm{L}_0 + iW)^{-1}. \tag{4.23}$$

Chacune de ces deux étapes n'est pas unique et font l'objet de procédures d'optimisation. La résolution de l'équation (4.22) nécessite la diagonalisation et l'inversion de matrices dont la taille est liée au nombre de canaux radiatifs.

Ce nombre, correspondant au nombre de valeurs propres de L^d multiplié par le nombre de microchamps n_f peut s'avérer très grand pour des émetteurs complexes et constitue le facteur limitant des calculs. Dans la version originale du FFM, un processus de renormalisation des canaux a été mis au point pour réduire le nombre de composantes (voir [14]). Les canaux de l'ensemble S de fréquences et de largeurs voisines sont regroupées en une seule entité définissant un canal radiatif avec de nouveaux paramètres $(f_k, \gamma_k, a_k, c_k)$. L'algorithme statistique sous-jacent est mis en œuvre avec la contrainte que la compression des données ne doit pas (ou peu) modifier le profil statique. Bien que ce processus ait prouvé son efficacité à plusieurs reprises, il introduit une approximation supplémentaire et a montré ses limites pour des cas très complexes, [47]. Récemment, une nouvelle formulation du modèle ne nécessitant pas d'inversion de matrice a été proposée.

Nouvelle formulation du FFM, (cf. *Annexe F*)

En distinguant les éléments diagonaux des éléments non-diagonaux de la matrice des taux de transition, le propagateur dynamique s'écrit :

$$G^d(\omega) = (\omega \mathbf{1} - \mathrm{L}_0 - i\Gamma + i\,W)^{-1}, \tag{4.24}$$

où Γ est une matrice diagonale correspondant à l'inverse des durée de vie des SDT telle que $\Gamma_{i,j} = \nu\delta_{i,j}$ et W est une matrice non diagonale correspondant aux taux de transitions entre les SDT, $W_{i,j} = \nu p_j$.

On défini un propagateur quasi-statique :

$$G^s(\omega) = (\omega \mathbf{1} - \mathrm{L}_0 + i\Gamma)^{-1} \tag{4.25}$$

qui ne présente que des éléments de matrice diagonaux, le propagateur dynamique de l'équation (4.24) peut s'écrire sous la forme :

$$G^d(\omega) = G^s(\omega) - iG^s(\omega) \cdot W \cdot G^d(\omega). \tag{4.26}$$

En introduisant cette expression dans l'équation (4.22), on obtient l'expression du profil dynamique associé à une raie donnée de n composantes :

$$I_d(\omega) = \frac{r^2}{\pi} \Re \frac{\sum\limits_k \frac{(a_k + ic_k)/r^2}{i(\omega-\omega_k)+\gamma_k+\nu}}{1 - \nu \sum\limits_k \frac{a_k/r^2}{i(\omega-\omega_k)+\gamma_k+\nu}}, \tag{4.27}$$

où on rappelle que $r^2 = \sum\limits_{k\in S} a_k$ est l'intensité totale de la raie.

Ainsi, l'ensemble des paramètres $(f_k, \gamma_k, a_k, c_k)$ obtenu dans l'approximation quasi-statique **et** le taux de fluctuation du microchamp ionique constitue toute l'information nécessaire au calcul du profil de raies incluant la dynamique des ions.

L'implémentation de la nouvelle formulation dans le code de calcul de profils de raies PPP ouvre de nouvelles possibilités. Elle permet en effet d'effectuer des calculs pour des transitions radiatives hors de portée des méthodes de simulation numériques et difficilement réalisable avec le FFM dans sa forme originale (voir les exemples dans l'*Annexe F* et [48]).

De plus, comme l'expression du profil dynamique n'est fonction que de la distribution statique des fréquences et du taux de fluctuation du microchamp, la partie principale du travail numérique revient à calculer le profil statique ; la prise en compte de la dynamique des ions se faisant alors en *post-processing* d'autres méthodes.

Pour l'hydrogène et les ions hydrogénoïdes, il existe des modèles analytiques permettant de calculer la distribution statique des fréquences, basés par exemple sur la description de l'effet Stark dans le système de coordonnées paraboliques, [49, 50, 21].

Pour les ions multichargés, des codes aussi sophistiqués que PPP sont développés comme MERL (*Multi-Electron-Radiator Line shape code*), [13] ou encore le récent code MELS (*Multi Electron Line Shape*) basé sur un algorithme très performant, [51]. Récemment, le FFM a été appliqué au modèle *Quasi-Contiguous* (QC), [52, 53], pour améliorer le calcul des raies d'atomes ou d'ions hautement excités par la prise en compte de la dynamique des ions. Il a été aussi couplé à la *Frequency Separation Technique* (FST), dans laquelle les fluctuations rapides du microchamp créé par les ions et les électrons du plasma sont modélisées par la théorie d'impact et les fluctuations lentes (essentiellement dues aux ions) sont modélisées par le FFM, [15, 16].

***Validation du modèle (cf.** Annexes F et G)*

Le FFM a donc été développé dans le but de fournir des calculs rapides et précis des profils de raies dans les plasmas pour une large gamme de densités et températures et pour des émetteurs complexes. La simulation numérique étant un moyen d'obtenir des profils de référence, son utilisation est omniprésente dans le développement et la validation de ce modèle, [45, 46, 14, 54, 18, 35] et annexes F et G. Les comparaisons avec les simulations sur différents types de raies et de conditions de plasmas liés aux expériences montrent un accord satisfaisant (cf. annexes F et G, [55]).

Néanmoins, comme l'effet de la dynamique des ions est généralement faible par rapport aux élargissements électroniques et Doppler dans les conditions communément observées, ces comparaisons sont utiles mais insuffisantes pour évaluer de manière critique le FFM et lui apporter des améliorations si nécessaire. Récemment, une série de comparaisons entre différents codes de calculs de profils de raies a été effectuée sur un large panel de cas test, [56]. Une étude spécifique des modèles traitant la dynamique des ions a été menée sur une série de raies dans

des conditions de densités et températures couvrant les limites impact et statique, (*Annexe G*). La plus grande dispersion des résultats s'est vue sur la raie la plus simple du point de vue de sa physique atomique : la raie Lyman$-\alpha$ de l'hydrogène. Alors que les simulations numériques donnent des résultats similaires, le MMM et le FFM donnent une largeur de raie beaucoup plus faible que l'ensemble des résultats.

Afin de comprendre les raisons de ces différences importantes, une étude sur les effets de changement de direction et de magnitude des microchamps a été menée, [57]. Les simulations numériques, qu'elles tiennent compte directement des interactions entre les ions ou qu'elles utilisent un modèle de pseudo-particules écrantées, s'accordent. Elles ont donc été utilisées comme référence dans cette étude. Il en ressort que les modèles stochastiques ne reproduisent pas correctement les effets de rotation. Sur les raies présentant une composante centrale, comme la raie Lyman$-\alpha$ par exemple, le profil statique est formé de trois composantes Stark : une non-déplacée et deux latérales. Lorsque la direction du microchamp varie, les profils simulés montrent que les trois composantes sont affectées par le changement de direction. Au fur et mesure que l'effet de dynamique augmente (en augmentant la température par exemple), les composantes s'élargissent et collapsent vers le centre de gravité de la raie. Les modèles stochastiques sont incapables de reproduire cet effet même en changeant artificiellement la valeur du taux de fluctuation. Une piste, encore non exploitée, serait d'utiliser un taux de fluctuation dépendant de la fréquence ou d'utiliser un modèle de diffusion comme il l'a été proposé pour modéliser le rétrécissement Dicke sur les profils Doppler, [58]. On retrouvera ce modèle dans la suite.

L'étude de la dynamique des ions sur les raies He$-\alpha$ et $-\beta$ de l'argon fait apparaître des conclusions similaires, [48] et *Annexe G*. Les modèles stochastiques et les simulations présentent des profils dynamiques différents. Ces différences ne sont pas dues au choix du taux de fluctuation dans les modèles. Aucun taux de fluctuation ne permet de reproduire les profils simulés dans leur totalité. Néanmoins, il semblerait que différentes valeurs de ce taux permettent de reproduire différentes portions du spectre. Nous l'expliquons par le fait que ce raies étant affectées par de l'effet Stark linéaire et quadratique, un taux dépendant du champ ou de la fréquence est nécessaire pour reproduire les effets des champs faibles (effet Stark linéaire) et l'effet des champs forts visibles sur l'effet Stark quadratique.

4.3.2 Les effets non-binaires dans l'élargissement électronique → *Annexes H*

L'élargissement Stark des raies de l'hydrogène est un sujet étudié de longue date mais qui continue d'évoluer encore aujourd'hui. La détermination des densités électroniques à partir des largeurs des raies de Balmer-α de l'hydrogène (H-α) est un moyen de diagnostic établi. C'est une des raies spectrales les plus étudiées tant

sur le plan théorique qu'expérimental. Des mesures sont disponibles sur plusieurs ordre de grandeurs de densité (de 10^8 à 10^{19} cm^{-3}). Outre l'aspect diagnostic, ce large spectre de conditions plasmas offre aux théories un précieux banc d'essai.

L'investigation des plasmas couplés à haute densité et faible température a fait apparaître des désaccords importants entre les théories standards et l'expérience. Lors de mon travail de thèse[2], il a été montré que certains désaccords sont dus au fait qu'un opérateur de collision électronique usuel n'est pas adapté dans ces conditions pour décrire correctement le profil de raies. Cette situation se produit lorsque l'élargissement électronique est le mécanisme prépondérant d'élargissement des raies et quand les effets non-binaires sont importants. La figure 4.2 représente les largeurs à mi-hauteur de la raie H-α sur plus de 4 ordres de grandeurs en densité. Les mesures expérimentales proviennent de différentes expériences, [59, 60, 61, 62], dont le point commun est la température électronique proche de 1 eV. Ces résultats expérimentaux sont comparés aux largeurs obtenues par les théories standards, par le modèle FFM où les ions sont dynamiques et les électrons impacts et par la technique de simulation DM-TCP où les ions et les électrons sont simulés simultanément, (cf. fig. 4.2). La différence dans les largeurs à basse densité s'explique par la négligence de la structure fine dans les calculs. Contrairement aux théories standards, on montre que le modèle FFM est en accord avec les expériences et les simulations, validant le fait que la dynamique des ions est bien reproduite par ce modèle sur cette raie. Par contre, aux hautes densités, le FFM surestime les largeurs d'environ 40% . Cette différence est expliquée par l'impossibilité d'utiliser l'approximation d'impact pour les électrons à ces densités. Les effets de corrélations entre les électrons ne sont plus négligeables.

→ L'approche alternative que nous proposons est d'utiliser le FFM pour décrire les deux composantes (ioniques et électroniques) du plasma (*Annexe H*).

Les électrons étant traités classiquement, leur effet sur l'émetteur est similaire à celui des ions ; la seule différence étant les échelles de temps. Ainsi, toute solution développée pour traiter la dynamique des ions devrait être applicable aux électrons. La simulation de dynamique moléculaire TCP constituée de protons et d'électrons a été utilisée dans un premier temps pour discuter les effets de corrélations sur les microchamps, par comparaison aux fonctions de distribution statique calculées dans un modèle OCP purement électronique. Dans un second temps, la simulation DM-TCP a fourni des profils de raies qui tiennent compte de toutes interactions entre les particules chargées du plasma. Les comparaisons des quatre premières raies de la série de Balmer de l'hydrogène avec les résultats de la simulation DM-TCP montrent que l'utilisation du FFM pour décrire l'élargissement électronique en remplacement des modèles collisionnels binaires standards améliore les résultats.

2. Modélisation non collisionnelle des effets d'élargissement électronique des raies de l'hydrogène dans les plasmas, Sandrine Ferri, Thèse de Doctorat, Université de Provence (juin 1999).

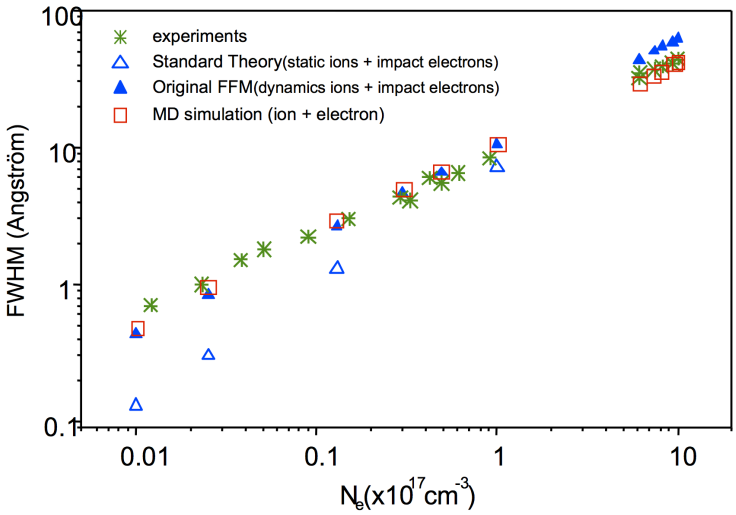

FIGURE 4.2 – Comparaisons de la largeur à mi-hauteur (FWHM) de la raie H-α obtenue expérimentalement (étoiles), avec la simulation (carrés), avec les théories standards (ions statiques et électron impacts) (triangles) et avec le FFM appliqué aux ions, les électrons étant impact) (triangles pleins).

Cependant des différences subsistent entre le FFM et la simulation. Les différences observées sur les raies à composantes centrales peuvent être en partie expliquées par les lacunes du FFM pour prendre en compte les effets de rotations des microchamps (cf. section précédente). Une autre raison plausible est l'hypothèse selon laquelle les effets de corrélations entre les ions et les électrons sont négligeables et l'utilisation de modèle OCP avec un potentiel écranté n'est pas valable dans ces conditions tièdes et denses (cf. Chapitre 3).

Remarque sur les limites du FFM :

L'objectif de la publication en *Annexe H* était aussi de montrer que le FFM est capable de décrire l'élargissement électronique de la limite impact jusqu'à la limite statique. Le terme « impact » est inapproprié pour le FFM. En effet, alors que ce modèle possède bien la limite statique ($\nu = 0$ dans l'équation (4.27)), il ne possède pas la limite impact mais la limite des fluctuations rapides (cf. *Annexe F*) et [48]. Lorsque le taux de fluctuation augmente, les composantes se mélangent, le profil devient plus étroit tend vers la limite des fluctuations rapides, qui correspond à $\nu \to \infty$. La limite du FFM près du centre de la raie est donnée par :

$$\lim_{\nu\to\infty} I_d(\omega) \approx \frac{\Gamma/\pi}{\omega^2 + \Gamma^2}, \tag{4.28}$$

avec $\Gamma \sim 1/\nu$ et ν donné par l'équation (4.6). Ce résultat est en contradiction avec la dépendance en N_p et T attendue dans la limite impact, [1]. Un modèle empirique,

basé sur un changement du taux de fluctuation suivant si l'on décrit le centre de la raie ou les ailes, a été proposé dans le cadre de l'application du FFM au modèle QC, [52].

4.3.3 Prise en compte de l'effet Stark-Zeeman dans les plasmas magnétisés → *Annexes I et J*

La présence de champs magnétiques dans les plasmas de laboratoire (Tokamak, X- et Z- Pinches, plasmas créés par implosion ou impact laser, etc.) et dans les plasmas astrophysiques ravive l'intérêt de la modélisation des profils de raies élargies simultanément par effets Stark et Zeeman. Bénéficiant de la souplesse des techniques utilisées, le code de simulation numérique des profils de raies, dans un premier temps, puis le code PPP basé sur le FFM dans sa nouvelle formulation, dans un deuxième temps, ont été étendus à l'étude des plasmas magnétisés.

La modélisation des effets Stark et Zeeman simultanés est un problème compliqué qui nécessite une bonne description de la physique atomique et des propriétés statistiques des plasmas. Un champ magnétique a trois effets sur les profils de raies élargies par effet Stark : 1) la polarisation partielle du rayonnement émis, 2) un éclatement des niveaux d'énergie dû à l'effet Zeeman et 3) les trajectoires en hélice des particules chargées du plasma autour d'une ligne de champ magnétique. Il résulte donc en une structure supplémentaire du profil de raies.

au niveau de la simulation numérique...

La simulation DM a été modifiée afin de tenir compte de ces effets. Les trajectoires des particules chargées en présence d'un champ magnétique sont calculées dans la simulation à l'aide d'un algorithme de Verlet Vitesse qui tient compte d'un champ magnétique homogène et statique, [63]. Les équations du mouvement sont re-écrites avec une force mesurée sur la particule i à l'instant t :

$$\vec{F}_i(t) = \vec{F}_C(t) + \vec{F}_L(t), \tag{4.29}$$

où $\vec{F}_C(t)$ est la force due au champ électrique coulombien et $\vec{F}_L(t) = Z_i e\ \vec{v}(t) \times \vec{B}$ est la force de Lorentz. Ici on oriente le champ magnétique dans la direction z. Cet algorithme a l'avantage d'avoir un pas de temps δt indépendant de la durée des oscillations de Larmor générées par le champ magnétique.

La position et la vitesse de chaque particule sont connues à chaque pas de temps et le microchamp électrique en présence d'un champ magnétique est alors mesuré sur l'émetteur de la même manière que précédemment. Les distributions statiques des microchamps obtenus ont été comparées aux résultats de Murillo, [64].

La modification de la physique atomique due à l'effet Zeeman est prise en compte

en même temps que celle due à l'effet Stark. Le Liouvillien s'écrit :

$$L_l(t) = L_0 - \vec{d}\cdot\vec{E}(t) + \frac{\mu_B}{\hbar}\vec{B}\cdot[\vec{J} + (g_s - 1)\vec{S}], \tag{4.30}$$

avec $\mu_B = 5.7883817555(79) \times 10^{-5}\ eVT^{-1}$ le magnéton de Bohr, $g_s \simeq 2.0023$ le facteur de Landé, $\vec{J}$ et $\vec{S}$ les moments angulaires et de spin, respectivement. Ici, on suppose que le terme diagmagnétique, proportionnel à B^2 est négligeable.
L'équation d'évolution (4.5) est résolue numériquement en présence des champs électrique fluctuant et du champ magnétique.

La particularité dans ce problème est que la direction du champ magnétique impose un axe de quantification et le rayonnement émis est polarisé. Le profil de raie observé dépend donc de l'angle entre la direction d'observation et la direction du champ $\vec{B}$:

$$I(\omega, \alpha) = I_{\parallel} cos^2\alpha + I_{\perp} sin^2\alpha, \tag{4.31}$$

où les composantes parallèles, $I_{\parallel}$, et transverses, $I_{\perp}$, des profiles s'expriment en terme d'émission polarisée comme :

$$I_{\parallel} = I_+(\omega) + I_-(\omega), \tag{4.32}$$

$$I_{\perp} = \frac{1}{2}\big(I_+(\omega) + I_-(\omega)\big) + I_0(\omega), \tag{4.33}$$

avec $0, \pm 1$ liés aux règles de sélection $\Delta M = 0$ pour la composante π et $\Delta M = \pm 1$ pour les composantes σ. La fonction d'autocorrélation $C(t)$ est donc calculée pour les trois directions $q = 0, \pm 1$.

Un exemple de profils simulés comparés aux profils expérimentaux est donné sur la figure 4.3, [65]

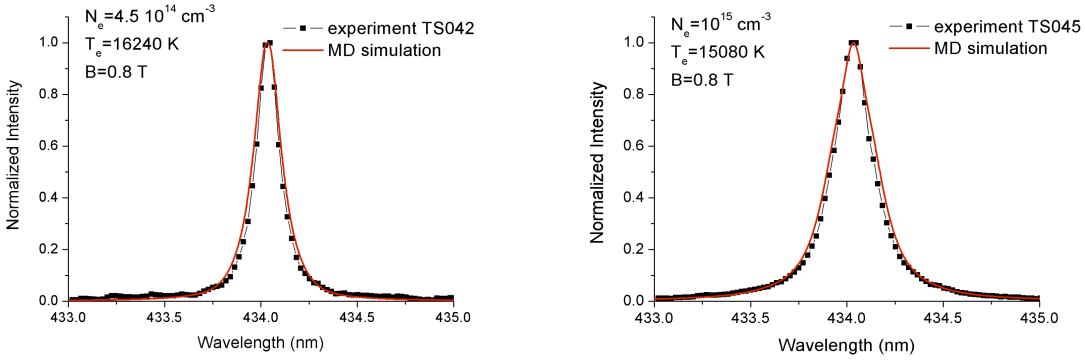

FIGURE 4.3 – Profils Stark-Zeeman de la raie H-γ observés expérimentalement (carrés) et comparés aux profils obtenus par simulation numérique (traits rouge) pour deux densités.

Les profils des raies de la série de Balmer, jusqu'à $n = 5$ (H-γ) ont été observées dans le Pilot-PSI du FOM-Institute for Plasma Physics (Pays-Bas) pour des densités allant jusqu'à 2×10^{15} cm^{-3}, des températures de l'ordre de 2 eV et des champs magnétiques atteignant les 2 Teslas. Ces conditions de plasma ont été diagnostiquées de manière indépendantes par diffusion Thomson. Les comparaisons entre les simulations et les profils expérimentaux montrent un très bon accord pour toute la gamme de densités étudiées comme le montre la figure 4.3 représentant les profils de la raie H-γ pour deux densités. Cependant, dans ces conditions et pour la raie étudiée l'effet Zeeman est masqué par l'effet Stark, ce qui ne permet pas vraiment de contraindre nos simulations [3].

Remarque : Le formalisme de la simulation permet de prendre en compte des perturbations extérieures aux plasmas. Ces perturbations peuvent être dues à un champ magnétique statique comme nous venons de le voir, mais aussi à un champ magnétique ou électrique dépendant du temps. C'est le cas par exemple de l'étude menée sur les profils de la raie Lyman$-\alpha$ de l'aluminium hydrogénoïde soumis à un champ laser. Les profils obtenus par nos simulations de DM incluant un champ électrique harmonique extérieur se comparent très bien avec les modèles existants, [66, 67, 41].

au niveau du FFM... *(Annexe I)*

La souplesse et la rapidité dues à la nouvelle formulation du FFM a permis d'étendre les compétences de notre code de calcul PPP aux calculs des profils de raies élargies par effet Stark-Zeeman en tenant compte non seulement du champ magnétique mais aussi de la dynamique des ions.

L'effet du champ magnétique est introduit dans la physique atomique de l'émetteur. Dans une première étape, le profil de raies élargies par effet Stark-Zeeman est calculé dans l'approximation quasi-statique pour les ions (les électrons sont modélisés dans l'approximation d'impact) (cf. éq. (4.14)). La polarisation du rayonnement est prise en compte dans ce formalisme en découplant le calcul pour chaque état de polarisation de chacune des transitions. De plus, la direction du champ magnétique imposant l'axe de quantification, la moyenne sur les microchamps (cf. éq.(4.13)) doit s'effectuer sur les trois directions du microchamps. On obtient alors un jeu de fréquences et intensités généralisées $(f_{q,k}, \gamma_{q,k}, a_{q,k}, c_{q,k})$ et, dans une deuxième étape, le profil Stark-Zeeman dynamique est calculé par le biais de la nouvelle formulation du FFM :

$$I_q(\omega) = \frac{r_q^2}{\pi} Re \frac{\sum_k \frac{(a_{q,k}+ic_{q,k})/r_q^2}{i(\omega-\omega_{q,k})+\gamma_{q,k}+\nu}}{1-\nu\sum_k \frac{a_{q,k}/r_q^2}{i(\omega-\omega_{q,k})+\gamma_{q,k}+\nu}}. \tag{4.34}$$

3. Ce travail a fait l'objet d'une communication par poster au 16$^{\text{th}}$ International Conference on Spectral Line Shapes, Valladolid (Espagne), juin 2008

Le profil observé dans une direction donnée est obtenu en utilisant l'équation 4.31.

Les comparaisons avec des simulations sur les raies de l'hydrogène et sur des systèmes atomiques plus compliqués comme la raie Lyman$-\alpha$ avec structure fine de l'argon hydrogénoïde ont validé cette méthode, comme il l'est décrit dans l'Annexe I. Nous avons montré que ce formalisme d'une grande efficacité permet d'obtenir des profils de raies pour différents types d'émetteurs neutres ou chargés et pour une grande variété de densités, températures et valeurs de champ magnétique, ce qui est d'une importance extrême en physique des plasmas et en astrophysique. Grâce à la rapidité du code, les rapports d'intensité des composantes polarisées sont générés et utilisés, par exemple, comme outil de diagnostic de densité ou de champ magnétique dans les plasmas de fusion thermonucléaire. Nous avons aussi réalisé une étude de la raie Lyman-α de l'argon hydrogénoïde, émise dans le domaine du rayonnement X par des plasmas de fusion inertielle. Dans ce type de plasmas chauds et denses, des champs magnétiques supérieurs à 100 MG sont mesurés et les raies de structure fine de l'argon sont non seulement affectées par l'effet Stark (les ions sont dynamiques) mais aussi par l'effet Zeeman. Le modèle est excellent accord avec les profils simulés en utilisant la méthode développée par M. Gigosos et collègues, [40] ainsi qu'avec le code MELS couplé au BID, [68]

Ce travail a été utilisé récemment pour le calcul des profils de raies émises par du carbone dans les plasmas d'ablation de glaçons dans les Tokamak, [69]. Les comparaisons avec les simulations numériques développées par E. Stambulchik, [11] ne sont, par contre, pas très satisfaisantes. Le modèle que nous avons développé permet de calculer l'effet Zeeman soit dans l'approximation du champ fort (dans ce cas le champ magnétique est traitée comme une perturbation sur les états exprimés dans la base $|n, l, m_l >$), soit dans l'approximation du champ faible (dans ce cas le champ magnétique est traité comme une perturbation des états de structure fine dans la base $|n, j, m_j >$). Or dans les conditions de l'étude, l'effet du champ magnétique est du même ordre de grandeur que le déplacement des niveaux d'énergie dû à la structure fine. Ces deux effets doivent être traités simultanément dans la résolution de l'équation d'évolution. L'extension du modèle à une résolution plus universelle est à l'étude.

4.4 Étude des effets de corrélations dans le développement des lasers XUV → *Annexe K*

Depuis une dizaine d'années, le développement des sources XUV cohérentes n'a cessée de croître. Couvrant le domaine spectral entre 0.2 nm et 50 nm, de tels lasers peuvent s'avérer d'une grande utilité de la médecine à la physique du solide. Trois principales techniques sont utilisées pour générer des sources XUV cohérentes : la génération d'harmoniques d'ordre élevé, [70], les lasers à électrons libres, [71], et les

lasers générés dans des plasmas de cibles solides, [72] . Ce sont ces derniers qui nous intéressent dans cette étude.
Les lasers XUV générés dans les plasmas chauds et denses sont des sources intenses caractérisées par une émission extrêmement monochromatique. La mesure de leur largeur spectrale, typiquement $\Delta\lambda/\lambda \simeq 10^{-5}$, représente un challenge expérimental car elle se situe à la limite de résolution des spectromètres les plus performants dans ce domaine, [73]. Aussi, le degré de cohérence temporelle est un paramètre important qu'il est nécessaire de maîtriser pour les applications. Actuellement, la durée des impulsions de ces lasers XUV est limitée à une picoseconde, [74]. En effet le profil de raie très étroit des plasmas utilisés limite cette impulsion à une durée minimale donnée par la limite de Fourier :

$$\tau_{FL} = \frac{0.44\lambda}{c}\frac{\lambda}{\Delta\lambda}, \tag{4.35}$$

où λ est la longueur d'onde du laser et $\Delta\lambda$ est la largeur spectrale. Cette dernière dépend non seulement de la largeur intrinsèque de la raie lasante, mais aussi des effets de gain et de saturation dans le processus d'amplification.

Or pour de nombreuses applications telles que la production de plasmas dans le régime WDM, il faut générer des lasers X de courte durée de pulse, pratiquement en dessous de la picoseconde voire même de la femtoseconde. Ceci est réalisable si le laser X fonctionne en mode injecté, mais seulement si sa bande spectrale est élargie d'un facteur 3 ou plus, [74]. Ainsi la connaissance des propriétés spectrales des raies laser est un enjeu important dans la compréhension et l'amélioration de ces sources.

Comme nous l'avons vu précédemment les propriétés spectrales des raies dépendent intimement des conditions locales du plasma. Le profil des raies émises par un atome ou un ion émetteur est affecté par de nombreux mécanismes d'élargissement. L'élargissement Doppler produit par le mouvement thermique des émetteurs est en général le mécanisme dominant dans les plasmas chauds et relativement denses avec des émetteurs de charge nette Z modérée. Il faut y ajouter l'élargissement naturel ainsi que l'effet Stark lorsque Z et la densité augmentent. Ces différents mécanismes d'élargissement influent sur la forme intrinsèque des profils de raies et de ce fait sur la forme du profil de gain qui caractérise une source X. L'élargissement spectral de la raie lasante contrôle la cohérence temporelle de la source et la contribution relative des élargissements homogènes / inhomogènes contrôle l'existence d'un re-élargissement de la raie lasante dans le régime de saturation.

La raie étudiée dans ce travail correspond à la transition $4d - 4p$ $(J = 0 - 1)$ de l'argent nickeloïde à $\lambda = 13.9\ nm$. Laser à cette longueur d'onde est réalisable sur une large gamme de densités $(5 \times 10^{19} \leqslant n_e \leqslant 8 \times 10^{20}\ cm^{-3})$ et de températures comprises entre 200 et 700 eV pour la température électronique et entre 20 et

200 eV pour la température ionique. Les conditions de plasma dépendent du schéma de pompage qui est utilisé pour obtenir l'inversion de population entre les niveaux qui participent à l'effet laser. Les contributions relatives de l'élargissement Doppler et Stark (électronique et ionique) du profil intrinsèque sont ici étudiées dans le régime transitoire où $T_i = 20\ eV$ et $T_e = 200\ eV$ et le régime quasi-stationnaire (QSS) où $T_i = T_e = 200\ eV$.

Dans cette gamme de densités et températures le plasma est moyennement jusqu'à fortement couplé ($0.6 \leqslant \Gamma \leqslant 14$). La question se pose quant au calcul standard de l'effet Doppler dans lequel les charges du plasma sont supposées se déplacer sur des trajectoires rectilignes à vitesse constante. Nous avons donc étudié l'effet des corrélations sur l'élargissement Doppler de la raie à $\lambda = 13.9\ nm$ par le biais de la dynamique moléculaire. Si l'on tient compte du mouvement de l'émetteur au cours du rayonnement, l'expression du profil de raies donné par l'éq. (4.2) apparaît comme la transformée de Fourier du produit de deux fonction de corrélation :

$$I(\omega) = \frac{1}{\pi}\Re \int_0^\infty dt\ e^{i\omega t} S_s(\vec{k}, t) C(t), \tag{4.36}$$

avec C(t) la fonction de corrélation du dipôle (cf. éq. 4.1) et

$$S_s(\vec{k}, t) = < e^{\vec{k}\cdot\vec{r}(t) - \vec{k}\cdot\vec{r}(0)} > \tag{4.37}$$

le facteur d'autostructure où <> dénote la moyenne sur les états du bain. Ici, nous avons ignoré les corrélations entre le moment dipolaire de l'émetteur $\vec{d}(t)$ et son mouvement $\vec{r}(t)$. L'expression du facteur d'autostructure est bien connue dans la limite des particules libres : $S_s(k,t) = e^{-k^2t^2/2\beta m_i}$ avec $\beta = 1/k_B T_i$ et m_i la masse de l'ion émetteur.

Les comparaisons des profils simulés aux profils Doppler standards montrent que les effets de corrélations entre les charges ne peuvent pas être ignorées dans la gamme de températures et densités étudiée, même si ces effets sont finalement masqués par les élargissements Stark et naturel de la raie. Un profil purement Doppler présente un élargissement inhomogène Gaussien : à chaque classe de vitesses décrivant la distribution de Maxwell, correspond un déplacement en fréquence. Or si, à cause des interactions (ou collisions entre les ions), la vitesse change en module et en direction au cours du rayonnement, il n'est plus possible de considérer des trajectoires rectilignes. Le profil se re-homogénéise et devient plus étroit ; cet effet est connu sous le nom de rétrécissement Dicke, [75]. Il est similaire à l'effet de dynamique des ions sur les profils de raies élargies par effet Stark. La prise en compte de cette re-homogénéisation est incontournable dans l'évaluation du profil de gain et de saturation des lasers X. Une piste envisagée est d'utiliser un modèle de mouvement Brownien, [76] dans lequel une expression du facteur d'autostructure est donnée en fonction d'un taux de fluctuation des vitesses. Dans ce travail, ce dernier est obtenu par un ajustement des fonctions de corrélation des

vitesses[4]. L'insertion de cette redistribution collisionnelle dans le calcul du gain reste à faire.

4. Cette étude a fait l'objet du travail de stage de M1 Physique de Mathieu Collombon, *Effets des corrélations sur l'élargissement Doppler des profils de raies dans les plasmas*, (2013).

Bibliographie

[1] H.R. Griem, *Spectral line broadening by plasmas* Academic Press, New York (1974).

[2] J. Dufty, *Ion motion in plasma line broadening*, Phys. Rev. A **2**, 534(1970).

[3] U. Frish and A. Brissaud, *Theory of Strak broadening : Exact line profile with model microfield*, J. Quant. Spectrosc. Radiat. Transfer. **11**, 1767 (1971).

[4] J.D. Hey and H.R. Griem, *Central structure of low-n Balmer lines in dense plasmas*, Phys. Rev. A **12**, 169 (1975).

[5] A.V. Demura, V.S. Lisitsa and G.V. Sholin, *Effet of reduced mass in Stark broadening of hydrogen lines*, JETP **46**, 209 (1977).

[6] D.E. Kelleher and W.L. Wiese, *Observation of ion motion in hydrogen Stark profiles*, Phys. Rev. Lett. **31**, 1431 (1973).

[7] R. Stamm and D. Voslamber, *On the role of ion dynamics in the Stark broadening of hydrogen lines*, J. Quant. Spectrosc. Radiat. Transfer. **22**, 599 (1979).

[8] J. Seidel, *Effects of radiator motion on plasma-broadened hydrogen Lyman$-\beta$*, J. Quant. Spectrosc. Radiat. Transfer **27**, 499 (1982).

[9] G.C Hegerfeldt and V. Kesting, *Collision-time simulation technique for pressure-broadened spectral lines with applications to Ly$-\alpha$*, Phys. Rev. A **37**, 1488 (1988).

[10] V. Cardeñoso and M.A. Gigosos, *Computer-simulation technique applied to the study of hydrogen Stark broadening by plasmas*, Phys. Rev. A **39**, 5258 (1989).

[11] E. Stambulchik and Y. Maron, *A study of ion-dynamics and correlations effects for spectral line broadening in plasma : K-shell lines*, J.Q.S.R.T **99**, 730 (2006).

[12] D.B. Boercker, C.A. Iglesias and J.W. Dufty, *Radiative and transport properties on ions in strongly coupled plasmas*, Phys. Rev. A **36**, 2254 (1987).

[13] R.C. Mancini et al., *Calculational aspects of the Stark line broadening of multielectron ions in plasmas*, Comput. Phys. Commun. **63**, 314 (1991).

[14] B. Talin et al., *Frequency-fluctuation model for line-shape calculations in plasma spectroscopy*, Phys. Rev. A **51**, 1918 (1995).

[15] S. Alexiou, *Implementation of the Frequency Separation Technique in general lineshape codes*, High Energy Density Physics **9**, 375 (2013).

[16] S. Alexiou, *The use of extrapolation concepts to augment the Frequency Separation Technique*, High Energy Density Physics **14**, 47 (2015).

[17] N. Woolsey et al., *Spectroscopy of compressed high energy density matter*, Phys. Rev. E **53**, 6396 (1996).

[18] L. Godbert-Mouret et al., *Accuracy of Stark broadening calculations for ionic emitters.*, Phys. Rev. Lett. **81**, 5568 (1998).

[19] Th. Wrubel et al., *Balmer-α transition of He II : measurements and calculations.*, J. Phys. B : At Mol. Opt. Phys. **34**, 461 (2001).

[20] S. Büscher et al., *The Stark width and shift of the hydrogen Hα line.*, J. Phys. B : At Mol. Opt. Phys. **35**, 2889 (2002).

[21] E. Stambulchik and Y. Maron, *Stark effect of high-n hydrogen-like transitions : quasi-contiguous approximation*, J. Phys. B : At. Mol. Opt. Phys.**41**, 095703 (2009).

[22] R. Stamm et al., *Ion-dynamic effects on the line shapes of hydrogenic emitters in plasmas*, Phys. Rev. A **34**, 4144 (1986).

[23] J.P. Hansen and I.R. McDonald, *Microscopic simulation od a strongly coupled hydrogen plasma*, Phys. Rev. A **23**, 2041 (1981).

[24] D.V. Fisher, Y. Maron, *Statistics of inter-particle distances and angles in plasmas*, Eur. Phys. J. D **14**, 349 (2001).

[25] B. Talin, et al., *Molecular dynamics simulation for modelling plasma spectroscopy*, J. Phys. A : Math. Gen. **36**, 6049 (2003).

[26] E. Dufour, et al., *Charge-charge coupling effects on dipole emitter relaxation within a classical electron-ion plasma description*, Phys. Rev. E **71**, 066409 (2005).

[27] H. B. Nersisyan, C. Toepffer, G. Zwicknagel, *Microfield distributions in strongly coupled two-component plasmas*, Phys. Rev. E **72**, 036403 (2005).

[28] E. Stambulchik et al., *Correlation effects and their influence on line broadening in plasmas : Application to H$-\alpha$*, High Energy Density Phys. **3**, 272 (2007).

[29] M. Baranger, *Problem of Overlapping Lines in the Theory of Pressure Broadening*, Phys. Rev. **111**, 494 (1958).

[30] A. Ben Reuven, *Spectral Line Shapes in Gases in the Binary-Collision Approximation*, Advances in Chemical Physics **33**, 235 (1975).

[31] H.R. Griem, *Principles of Plasma Spectroscopy* (Cambridge University Press, Cambridge, UK, 1997).

[32] J. Holtsmark, *Über die Verbreiterung von Spektrallinien.* Ann. Phys. **58**, 577 (1919).

[33] C.A. Iglesias et al., *Electric field distributions in strongly coupled plasmas*, Phys. Rev. A **31**, 1681 (1985).

[34] S. Ferri, et al., *Electronic broadening for high-n Balmer line profiles*, Phys. Rev. E **58**, R6943 (1998).

[35] A. Calisti, et al. *Discussion of the validity if binary collision models for electron broadening in plasmas*, J.Q.S.R.T **65**, 109 (2000).

[36] S.E. Koonin, *Computational Physics*, Academic :Addison-Wesley Publishing Company (1986).

[37] C. Moler and C.V. Loan, *Nineteen dubious way to compute the exponential of a matrix, twenty-five years later*, SIAM Rev. **45**, 3 (2003).

[38] M.A. Gigosos and V. Cardeñoso, *Stark-broadening simulation in hydrogen - Study of the binary and complete binary collision hypotheses*, J. Phys. B **19**, 3027 (1986).

[39] M.A. Gigosos and V. Cardenoso, *Study of the effects of ion dynamics on Stark profiles of Balmer−α and −β lines using simulation techniques*, J. Phys. B**20**, 6005 (1987).

[40] M.A. Gigosos and V. Cardenoso, *New plasma diagnosis tables of hydrogen Stark broadening including ion dynamics*, J. Phys. B **29**, 4795 (1996).

[41] S. Ferri, *Al XIII Lyman-α line under an external harmonic perturbation*, 2^{nd} Spectral Line Shape in Plasmas Workshop, Vienne (Autriche), non publié (2013).

[42] S. Ferri, *Extension of the BinGo and PPP codes to external macro-field studies*, 3^{rd} Spectral Line Shape in Plasmas Workshop, Marseille (France), non publié (2015).

[43] S. Ferri, *External macro-field studies : C VI Lyman−α line in presence of strong magnetic field and Ar XVIII Lyman−α line under external harmonic perturbations*, 3^{rd} Spectral Line Shape in Plasmas Workshop, Marseille (France), non publié (2015).

[44] A. Brissaud and U. Frisch, *Theory of Stark broadening - II. Exact line profile with model microfield*, J. Quant. Spectrosc. Radiat. Transfer **11**, 1767 (1971) ; *Solving linear stochastic differential equations*, J. Math. Phys. **15**, 524 (1974).

[45] A. Calisti, et al., *Model for the line shapes of complex ions in hot and dense plasmas*, Phys. Rev. A **42**, 5433 (1990).

[46] A. Calisti et al., *Fast numerical methods for line shape studies in hot and dense plasmas*, J. Quant. Spectrosc. Radiat. Transfer **51**, 59 (1994).

[47] E. Galtier et al., *Interference effects and Stark broadening in XUV intrashell transitions in aluminum under conditions of intense XUV free-electron-laser irradiation*, Phys. Rev. A **87**, 033422 (2013).

[48] C. Iglesias, *Efficient algorithms for stochastic Stark-profile calculations*, HEDP **9**, 209 (2013).

[49] L.A. Bureyeva and V.S. Lisitsa, *A perturbed atom in "Astrophys. and. Space Phys. Reviews"* (R.A. Sunyaev, ed.) Hardwood Academic Publisher, (2000).

[50] C. Mossé et al., *A universal approach to Rydberg spectral line shapes in plasmas*, J. Phys. B : At. Mol. Opt. Phys. **37**, 1343 (2004).

[51] C.A. Iglesias, V. Sonnad, *Robust algorithm for computing quasi-static Strak broadening of spectral lines*, HEDP **6**, 399 (2010).

[52] E. Stambulchik and Y. Maron, *Quasi-contiguous approximation for line-shape modeling in plasmas*, AIP Conf. Proc. **1438**, 203 (2012).

[53] E. Stambulchik, E. Maron, *Quasicontiguous frequency-fluctuation model for calculation of hydrogen and hydogen-like Stark-broadened line shapes in plasmas*, Phys. Rev. E **87**, 053108 (2013).

[54] B. Talin, et al., *Ground work supporting the codes based upon the frequency fluctuation model*, J. Quant. Spectrosc. Radiat. Transfer **58**, 953 (1997).

[55] R.C. Mancini et al., *The effect of improved line satellite line shapes on the argon Heβ spectral feature*, HEDP **9**, 731 (2013).

[56] E. Stambulchik, *Review of the first spectral line shapes in plasmas code comparison workshop*, HEDP **9**, 528 (2013).

[57] A. Calisti et al., *Influence of microfield directionality in line shapes*, Atoms **2**, 259 (2014).

[58] S.G Rautian and I.I. Sobelman, *Reviews of Topical Problems : the Effect of Collisions on the Doppler Broadening of Spectral Lines*, Sov. Phys. Usp. **9**, 701 (1967).

[59] W. L. Wiese, D.E. Kellher and D. R. Paquette, *Detailed Study of the Stark Broadening of Balmer Lines in a High-Density Plasma*, Phys. Rev. A **6**, 1132 (1972).

[60] H. Ehrich and H.J. Kusch, *Untersuchungen an stromstarken Kapillarentladungen. Teil III : Spektroskopische Messungen / Investigations on High Current Capillary-Discharges. Part 111 : Spectroscopic Measurements*, Z. Naturforsch **28a**, 1132 (1972).

[61] H. Ehrich and . D.E. Kelleher, *Experimental investigation of plasma-broadened hydrogen Balmer lines at low electron densities*, Phys. Rev. A **21**, 319 (1980).

[62] Y. Vitel, *Experimental study of H−α broadening and shift in dense argon plasmas*, J. Phys. B **20**, 2327 (1987).

[63] Q. Spreiter and M. Walter, *lassical Molecular Dynamics Simulation with the Velocity Verlet Algorithm at Strong External Magnetic Fields*, J. Comput. Phys. **152**, 102 (1999).

[64] M.S. Murillo, M.E. Cox and S.M. Carr, *Magnetized plasma microfield studies by molecular dynamics simulation*, J.Q.S.R.T **58**, 811 (1997).

[65] S. Ferri et al., *Emission spectroscopy of hydrogen lines in magnetized plasmas : Application to PSI studies under conditions foreseen in ITER*, AIP Conf. Proc. **1058**, 216 (2008).

[66] O. Peyrusse, *Spectral line shape calculations for mulctielectron ions in hot plasmas submitted to a strong oscillating electric field*, Phys. Rev. A **79**, 013411 (2009).

[67] P. Sauvan and E. Dalimier, *Floquet-Liouville approach for calculating Stark profiles in plasmas in the presence of a strong oscillating field*, Phys. Rev. E **79**, 036405 (2009).

[68] C.A. Iglesias, *Efficient algorithms for Stark-Zeeman spectral line shape calculations*, HEDP **9**, 737 (2013).

[69] M. Koubiti et al., *Line-shape code comparison through modeling and fitting of experimental spectra of the C II 723-nm line emitted by the ablation cloud of carbon pellet*, Atoms **2**, 319 (2014).

[70] Y. Wang et al. , *Phase-coherent, injection-seeded, table-top soft-X-ray lasers at 18.9 nm and 13.9 nm*, Nat Photon, **2**, 94 (2008).

[71] B. McNeil, *Free electron lasers : First light from hard x-ray laser*, Nat Photon, **3**, 375 (2009).

[72] D. L. Matthews et al., *Demonstration of a soft x-ray amplifier*, Phys. Rev. Lett., **54**, 110 (1985).

[73] A. Klinick et al., *Demonstration of a 2-ps transient x-ray laser*, Phys. Rev. A **65**, 033810 (2002).

[74] Y. Wang et al., *Measurement of 1-ps soft-x-ray laser pulses from an injection-seeded plasma amplifier*, Phys. Rev. A **79**, 023810 (2009).

[75] R.H. Dicke, *The Effect of Collisions upon the Doppler Width of Spectral Lines*, Phys. Rev. **89**, 472 (1953).

[76] J.P. Hansen and I.R. McDonald, *Theory of simple liquids*, Academic Press, London (1976).

Chapitre 5

Conclusion et perspectives

Les travaux présentés dans ce document de synthèse donnent un aperçu de la richesse des mesures accessibles par la technique de dynamique moléculaire classique pour l'étude des propriétés radiatives des plasmas. Basée sur un modèle où chaque particule est caractérisée par un ensemble de grandeurs physiques (masse, charge, position, vitesse, etc.) et où l'évolution de l'ensemble du système est déterminée, à chaque instant, par les lois de forces entre les particules, cette méthode s'avère être un outil puissant et versatile pour l'étude des systèmes complexes à N-corps. Les trajectoires des particules, obtenues dans l'espace des phases, constituent les données brutes à partir desquelles les propriétés thermodynamiques d'intérêt (température, énergie totale, etc) et les propriétés statistiques statiques (fonction de distribution) et dynamiques (fonctions de corrélation) sont calculées. Initialement développée en support des modèles pour le calcul des profils de raies dans les plasmas, elle n'a cessé d'évoluer au gré des études poursuivies dans l'équipe.

Ses premières utilisations étaient dédiées à l'étude de la dynamique des microchamps électriques autour de points neutres ou chargés, [1, 2]. Afin d'étudier les effets de corrélations et les mécanismes d'écrantage entre les ions et les électrons du plasma, des simulations à deux composantes (DM-TCP) ont été ensuite développées, [3]. Ce travail nous a amené naturellement à l'étude des plasmas non-idéaux dans lesquels les effets de couplage entre les charges sont importants. Les premières simulations réalisées dans ce cadre ont fait apparaître la nécessité d'implémenter dans la DM un protocole d'ionisation et de recombinaison à trois corps, [4]. Du fait du potentiel attractif entre les ions et les électrons, des électrons se retrouvent piégés autour d'un ion. Ce mécanisme de piégeage, réversible dans le temps grâce aux interactions avec toutes les autres particules du plasma, peut être interprété comme un mécanisme d'ionisation-recombinaison collisionnel. La DM-TCP dotée de ce protocole permet donc d'une part de traiter la population d'électrons piégés temporairement dans le puits de potentiel de l'ion et d'autre part de suivre l'évolution des états de charges vers un état stationnaire qui dépendra de la température, de la densité de charges et de la composition du plasma. Par contre, nous ne tenons pas compte des processus radiatifs, tels que l'absorption ou l'émission d'un photon, [5].

Un net avantage de cette méthode par rapport aux simulations de dynamique moléculaire quantique, est qu'elle donne accès aux propriétés dynamiques des électrons libres du plasma. Elle permet, par exemple, de calculer les facteurs de

structure dynamique en tenant compte de toutes les interactions entre les charges. Un modèle théorique précis pour le calcul de ces fonctions est primordial dans l'utilisation de la diffusion du rayonnement X pour le diagnostic des plasmas denses. Aussi, dans le cas de la matière tiède et dense, ni les modèles issus de la physique des plasmas classiques, ni ceux issus de la physique des solides ne permettent une description satisfaisante de ces facteurs de structure dynamique. Nous avons démontré la faisabilité d'utiliser la DM-TCP pour ce type de calcul sur des plasmas de béryllium lorsque les effets de dégénérescence des électrons sont négligeables, [6]. Ce dernier point est une limite de notre technique de simulation lorsqu'elle est appliquée aux plasmas tièdes et denses. Les effets de corrélations entre les charges sont tels que les propriétés quantiques sont mal reproduites par nos pseudo-potentiels binaires : dépendant seulement des coordonnées spatiales, ils conduisent à la fonction de distribution de Maxwell. Nous envisageons donc d'utiliser d'autres formes de potentiels effectifs. Par exemple, pour modéliser les fonctions de distribution d'un gaz d'électrons soumis à la statistique de Fermi, une solution serait d'ajouter un terme d'interaction dépendant des moments, [7].

Très récemment, nous avons tiré avantage du protocole d'ionisation/recombinaison implémenté dans la DM-TCP pour étudier l'abaissement du potentiel d'ionisation (IPD), [8]. Suivant les conditions, le potentiel d'ionisation d'un ion du plasma peut être diminué à cause des interactions de cet ion avec toutes les autres charges du plasmas (ioniques et électroniques). Les électrons liés, qui sont supposés occuper les états d'énergie hautement excités de cet ion, ne le sont plus et deviennent des électrons libres. La connaissance de l'IPD est primordiale dans la modélisation des propriétés radiatives des atomes et des ions dans un plasma car il affecte non seulement la forme des profils de raies mais aussi les populations. Ce problème est étudié de longue date, [9, 10], mais des expériences récentes dédiées à la mesure direct de l'IPD in situ ravivent les discussions sur sa modélisation, [11, 12]. Grâce à notre modèle spécifique d'ionisation/recombinaison, il est possible de mesurer le potentiel d'un ion en tenant compte de l'influence des électrons libres et des ions environnants. En comparant ce potentiel à celui du potentiel d'un ion isolé, nous mesurons l'abaissement du potentiel dû aux effets du plasma. Les premiers résultats que nous avons obtenus montrent que notre technique de simulation est un outil précieux pour alimenter cette discussion. Ce travail est en cours et un sujet de thèse a été déposé.

Une autre perspective dans l'application de la DM-TCP aux plasmas non-idéaux est l'étude de la dynamique de mélange de deux plasmas à l'interface dans les plasmas de fusion par confinement inertiel (FCI). La FCI consiste à produire des réactions de fusion à partir d'un mélange de deutérium et de tritium, contenu dans une micro-capsule. Pour y arriver, il faut chauffer et comprimer ce mélange en un temps très court. On utilise des lasers intenses qui déposent leur énergie à la surface de la micro-capsule. La surface extérieure explose, produisant une force de réaction sur le reste de la cible qui se comprime. La capsule est

conçue de telle sorte qu'une onde de choc se propage jusqu'au combustible pour initier la réaction de fusion. L'étape cruciale réside au moment de l'impact du matériau ablateur sur le combustible : les imperfections de l'interface peuvent générer des instabilités hydrodynamiques qui peuvent compromettre la réaction de fusion. Cette situation arrive lorsque les matériaux comprimés ont une densité de l'ordre de la densité du solide et la température de l'ordre de quelques dizaines d'électron-volts. Ils sont à l'état de matière tiède et dense. Pour comprendre la dynamique de l'interface dans ce régime, il est donc nécessaire de bien comprendre le mélange à l'interface de l'ablateur avec le combustible. Plusieurs propriétés microscopiques telles que la conductivité thermique des électrons, la viscosité, la diffusion jouent un rôle essentiel dans le contrôle des instabilités. Ces propriétés sont généralement déterminées à partir de simulations à l'équilibre alors que l'interface est dans un état nettement hors-équilibre. La modélisation hors-équilibre d'un tel phénomène dans les conditions de la WDM est compliquée tant sur le point théorique que numérique, mais notre technique de simulation permet d'envisager l'étude de la dynamique de l'interpénétration de deux plasmas par la mesure, par exemple, du coefficient de diffusion, [13]. Un sujet de thèse a été déposé.

Finalement, concernant l'utilisation de notre technique de Dynamique Moléculaire à des fins de validation des modèles de calculs de profils de raies dans les plasmas, cette technique permet de générer des profils de raies qualifiés de référence car les interactions entre les particules du plasma et l'atome ou l'ion émetteur sont naturellement prises en compte. Par exemple, la simulation du plasma nous donne accès aux champs électriques que générèrent les particules chargées sur un atome ou ion émetteur. Ces microchamps électriques, fluctuant au cours du temps, sont à l'origine de l'élargissement Stark des raies. La simulation des profils de raies consiste alors à utiliser ces microchamps électriques pour résoudre numériquement l'équation d'évolution de l'émetteur. Cependant, la prise en compte de ces fluctuations dans les modèles de calcul de profils de raies reste un problème compliqué du fait du caractère aléatoire de la perturbation, mais nécessaire à résoudre si nous voulons proposer un outil de calcul performant et universel à des fins de diagnostics par spectroscopie des plasmas. Nous avons donc systématiquement utilisé les profils de référence simulés pour accompagner le développement et l'amélioration de notre code de calculs de profils de raies, basé sur le Modèle de Fluctuation de Fréquence, [14, 15]. Ce dernier, avec le code MERL développé par R. Mancini, [16] et le code MELS développé par C. Iglesias, [17], sont les seuls, à notre connaissance, à être capables de produire des profils de raies d'ions multichargés (de structure atomique complexe) en tenant compte de la dynamique des microchamps ioniques et des termes d'interférence dans l'élargissement électroniques, comme le montre l'étude des profils des raies des satellites de recombinaison diélectronique de l'argon observées dans les plasmas de FCI, [18] et l'étude des raies intra couche de l'aluminium observées dans les plasmas tièdes et denses obtenus avec les lasers à électrons libres (FEL), [19]. Les résultats obtenus sur ces raies suggèrent la possibilité d'étudier pour la première fois les

effets d'interférence quantique non linéaire via les profils de raies XUV observés. Pour mener à bien le travail théorique accompagnant les expériences, il faudrait adapter les codes déjà existants de structure atomique, de profils de raies et de cinétique de population pour tenir compte des effets de corrélations entre les charges et des électrons dégénérés. La simulation numérique aurait encore ici un rôle à jouer.

Bibliographie

[1] A. Calisti, R. Stamm, B. Talin, *The BINGO Manual : the molecular dynamics method*, Rapport interne, Université de Provence (1995).

[2] M. Berkowsky et al., *Nonlinear response of electric fields at neutral points*, Phys. Rev E **51**, 4917 (1995) ; *Electric field dynamics et a charged point*, Phys. Rev. E **54**, 4087 (1996).

[3] B. Talin et al., Molecular dynamics simulation for modelling plasma spectroscopy, J. Phys. A **36**, 6049 (2003).

[4] A. Calisti, S. Ferri and B. Talin, Classical molecular dynamics model for coupled two component plasmas, High Energy Density Physics **5**, 307 (2009).

[5] J. Glosli et al., *Molecular dynamic simulations with radiation*, J. Phys. A : Math. Theor. **42**, 214030 (2009).

[6] A. Calisti et al., Warm dense matter through classical molecular dynamics, High Energy Density Physics **13**, 1 (2014).

[7] C. Dorso, S. Duarte and J. Randrup, *Classical simulation of the Fermi gas*, Phys. Lett. B **188**, 287 (1987).

[8] A. Calisti, S. Ferri and B. Talin, *Ionization potential depression in hot dense plasmas through a pure classical model*, à paraître dans Contribution to Plasma Physics

[9] G. Ecker and W. Kröll, *Lowering of Ionization Potential Energy for a Plasma in Thermodynamics Equilibrium*, Physics of Fluids **6**, 62 (1963).

[10] J.C. Stewart and K.D. Pyatt, *Lowering of Ionization Potentials in Plasmas*, Astrophysical Journal **144**, 1203 (1966).

[11] O. Ciricosta et al., *Direct Measurements of the Ionization Potential Depression in a Dense Plasma*, Phys. Rev. Lett. **105**, 065002 (2012).

[12] D.J. Hoarty et al., *Observation of the effect of ionization potential depression in hot dense plasma*, Phys. Rev. Lett. **110**, 265003 (2013).

[13] C. Ticknor et al, *First principles nonequilibrium plasma mixing*, Phys. Rev. E **89**, 013108 (2014).

[14] B. Talin et al., *Frequency-fluctuation model for line-shape calculations in plasma spectroscopy*, Phys. Rev. E **51**, 1918 (1995).

[15] A. Calisti et al., *Dynamic Stark broadening as the Dicke narrowing effect*, Phys. Rev. E **81**, 016406 (2010).

[16] R. Mancini et al., *Calculational aspects of the Stark line broadening of multielectron ions in plasmas*, Computer Phys. Comm. **63**, 314 (1991).

[17] C. Iglesias, *Efficient algorithms for stochastic Stark-profile calculations*, High Energy Density Physics **9**, 209 (2013).

[18] R. Mancini et al., *The effect of improved satellite line shapes on the argon Heβ spectral feature*, High Energy Density Physics **9**, 731 (2013).

[19] E. Galtier et al., *Interference effects and Stark broadening in XUV intrashell transitions in aluminum under conditions of intense XUV free-electron-laser irradiation*, Phys. Rev. A **87**, 033424 (2013).

Appendices

Annexe A

Classical molecular dynamics model for coupled two component plasmas

High Energy Density Physics 5 (2009) 307–311

Contents lists available at ScienceDirect

High Energy Density Physics

journal homepage: www.elsevier.com/locate/hedp

Classical molecular dynamics model for coupled two component plasmas

A. Calisti*, S. Ferri, B. Talin

UMR6633, CNRS, Université de Provence, Centre Saint Jérôme, 13397 Marseille Cedex 20, France

ARTICLE INFO

Article history:
Received 27 April 2009
Accepted 27 April 2009
Available online 9 May 2009

PACS:
52.65.-y
52.65.Yy

Keywords:
Classical molecular dynamics
Regularized Coulomb potential
Collisional ionization
Ion balance

ABSTRACT

This work is an improved continuation of a previous attempt to use classical molecular dynamics (MD) as a tool for the investigation of hot and dense "real" plasmas. "Real" in this context refers to ions and electrons interacting through Coulomb forces and undergoing ionization/recombination. The objective of designing such a non standard approach to plasma equilibrium is to explore a new way to discuss warm and dense matter with a method able to deal with the whole complexity of a N-body system of ions and electrons. Plasma relaxation times can be investigated up to a picosecond. The resulting equilibrium ion populations, built self consistently, are comparable to those found in literature and, potentially validate access to all the statistical data usually derived from MD simulations.

1. Introduction

Herein we report an attempt to answer the following question, "is it possible to use classical molecular dynamics (MD) to simulate the physics of coupled plasmas in the hot and dense domain?". This attempt follows a preliminary series of MD simulations on the same subject [1] involving a mechanism of ionization/recombination. A new molecular dynamics model with ionization/recombination has been developed and its behavior studied in order to decide, through comparisons with available data, to what extent it is appropriate to mimic a real plasma. If this is feasible, the method could be useful to complement other models for example those based on population kinetics. The advantages of MD are known:

1) Interactions between all particles that contribute to the motion of electrons and ions are accounted for.
2) Infinite systems are reduced using simple and effective periodic boundary conditions.
3) Collective behaviors appear in a natural way.
4) Mechanisms depending on time can be investigated.
5) MD can provide microfield sequences for ions or neutrals and sampling of their statistical properties.
6) Selected quantum features like ionization energies or ion radii can be accounted for as external parameters.
7) MD and statistical models use distinct sets of approximations (e.g., average potential can be avoided in MD) leading to helpful comparisons and benchmarks.

Classical mechanics for ions and electrons involves some specific mechanisms. Electrons move in a space with ions at random positions. The system is neutral. The ionic potential wells, based on soft ion–electron potentials (i.e., Coulomb-like potentials finite at short distance) give rise to strong exchanges between the kinetic and potential energies of electrons which, in turn, mediate information on energy from one ion to another [2,3]. In order to take advantage of known quantum data, e.g., ionization energies of ion stages, it appears necessary to implement a self consistent ionization/recombination process in MD. In this way, the ion charge distribution can be obtained for thermal equilibrium conditions and compared to data from literature. Contrary to standard rate equations electrons involved in a ionization or recombination event are recycled into the simulation, partly as trapped electrons belonging to "excited" ions and partly as "free" electrons. Time dependent plasma properties of interest are available with MD; e.g., the relaxation time of the electron velocity distribution function can be "measured". Discussions of these relaxation times appear as one of the important issues of this work.

Two component plasma (TCP) MD simulations involve some specific difficulties. The mass ratio between ions and electrons enforces a very small timestep appropriate for the description of electron motion around ions while, ions must move significantly in order to self consistently attain their spatial structure. This results

* Corresponding author.
E-mail address: annette.calisti@univ-provence.fr (A. Calisti).

1574-1818/$ – see front matter © 2009 Elsevier B.V. All rights reserved.
doi:10.1016/j.hedp.2009.04.011

in expensive simulations. Trapped electron trajectories occur due to multiple electron collisions around an ion. They can be de-trapped by collisions as the process is reversible. However, the lifetime of quasi-bound electron states can be long, depending on the potential depth and the plasma conditions. The occurrence of such classical metastable electron states suggests that pairs composed of one ion of charge Z surrounded by a trapped electron might be considered as an ion of charge $Z-1$, i.e., as the classical equivalent of a nucleus of charge Z with an optical electron in a bound excited state. This behavior can be extended by assuming that an electron upon an ion (same position and velocity) has a potential energy equivalent to the ionization energy of the ion specie in the ion stage $Z-1$. This assumption underlies the implementation of an ionization/recombination process in TCP simulations presented hereafter. Applications to carbon and aluminum plasmas are reported.

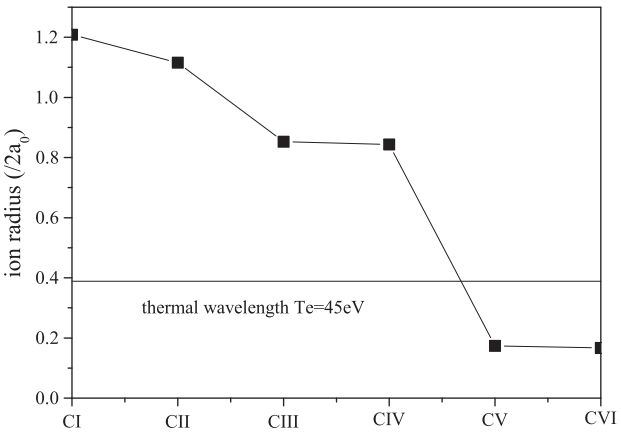

Fig. 2. Regularization distances, δ_Z, for carbon ion stages a_0: Bohr radius.

2. Plasma modeling

The first step in modeling is the definition of potentials between particles. Their derivatives give the binary forces for Newton's equations. In order to agree with the periodic boundary conditions implemented in MD the potentials are screened at a distance λ in accordance with the cubic cell size c. As the interactions among charges introduce a physical screening length λ_d the condition $c \gg \lambda_d$ allows collective screenings to take place in a natural way.

Contrary to earlier works [4–6], in order to properly describe the different ion stages of a given atom, a soft ion–electron potential is defined for each ion stage with the constraint that the potential of an electron upon an ion of charge $Z+1$ is bound by a negative energy equal to the ionization energy E_Z of the ion of charge Z. Following this classical approach for an isolated ion, the kinetic energy of an unbound electron must be larger than E_Z. A standard form of regularized ion–electron potential is given by [7]:

$$V_{ie}(r) = -Ze^2\left(1-e^{-r/\delta}\right)e^{-r/\lambda}/r \tag{1}$$

where δ is a short range regularization parameter. Here, for each E_Z, δ is defined by $\delta=\delta_Z=-Ze^2/E_Z$. As an example in Figs. 1 and 2 are plotted the ionization energies of the ion stages of carbon [8] and the corresponding short range parameters δ_Z respectively. Here after, δ_Z will be used also to define an exclusion sphere around ions and referred as ion stage radius.

The ion–ion and electron–electron interactions are taken to be Coulombic

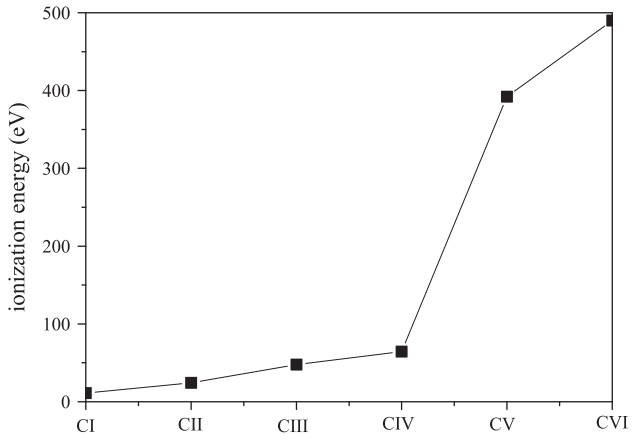

Fig. 1. Ionization energies of carbon ion stages.

$$V_{12}(r) = Z_1Z_2e^{-r/\lambda}/r \tag{2}$$

where Z_1Z_2 is positive.

Other parameters of interest are the average electron–electron distance, $r_0=(3/4\pi N_e)^{1/3}$, defined in terms of the electron density N_e, the electron thermal velocity $v_0=(k_BT_e/m_e)^{1/2}$, the electron coupling constant $\Gamma=e^2/r_0k_BT_e$, the thermal de Broglie wavelength $W_{th}=\hbar/(m_ek_BT_e)^{1/2}$ and the Debye length $\lambda_D=(kT_e/4\pi N_ee^2)^{1/2}$. Molecular dynamics simulations of two component plasmas were carried out using N electrons and N/Z_i ions. Particle motion in MD simulations is achieved using a Verlet's velocity algorithm. The simulations are carried out with the constraint that both the total energy and the plasma composition i.e., the average ionic charge and the electron density, are stationary during the system evolution. Stationarity is obtained by a careful preparation of the initial plasma cell. Indeed, stationarity does not mean that temperature and energy stay constant as they necessarily fluctuate but that their drift is small (a few percent) when the time average of a given quantity is performed.

2.1. Ionization/recombination protocol

The plasma model is completed with a ionization/recombination process. The most striking point here, for the densities considered, $N_e \sim 10^{22}\,cm^{-3}$ is the inadequacy of the concept of isolated ion. As an illustration, in Fig. 3 one can see a typical ionic potential energy of an electron on a plane section of the simulation cell of a carbon plasma. For each node of the surface, a potential energy is obtained, according to the periodic boundary conditions, accounting for all ions inside the simulation cell centered on the node. Clearly, the plasma electrons move into a fluctuating complex attractive potential that is much more complex and fluctuating more rapidly with all the electrons taken into account. Considering the design of an ionization/recombination process, with this observation it becomes difficult, to accept the conceptualization of an ion impurity in an electron plasma undergoing electron collisions. Owing to the capability of classical MD to overcome such a complexity, an alternative approach compatible appears useful. Empirical ionization and recombination mechanisms based on the electronic environment of ions are proposed as an attempt to deal with the complex ion potential structure. There is no trivial way for choosing such an empirical process; the rules proposed hereafter are not unique. As a result, the calculations and comparisons shown below are not to be considered as benchmarks but as a validation of the method.

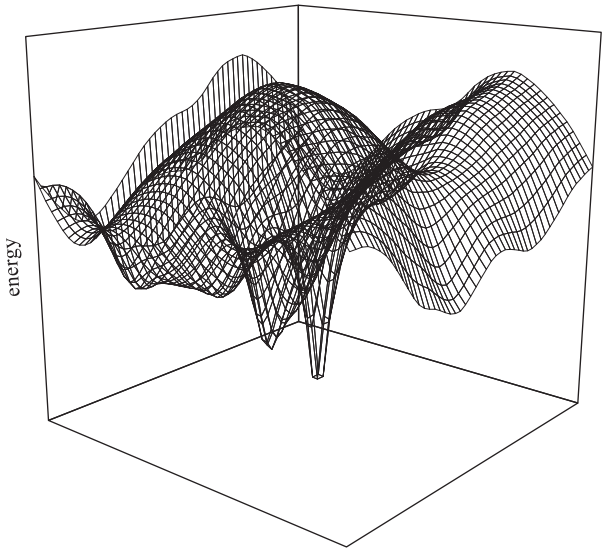

Fig. 3. Ionic potential seen by an electron moving on a plane.

The ionization/recombination protocol implemented in MD allows the ion charge to increase or decrease by amounts of 1 with the release or capture of an electron with ionic charge Z, $Z_N \geq Z \geq 1$, where Z_N is the charge of the bare nucleus. This protocol rests on a few definitions. If for an ion labeled ζ_i, a mutual nearest neighbor (NN_i) electron is found, it plays a major role ("mutual" means that both particles are the nearest neighbor from each other). When the total energy ϵ of the NN_i, i.e., the sum of the potential energies accounting for all ions and electrons and its kinetic energy, is negative, ζ_i is defined as an excited ion with the net charge $Z_i - 1$. Conversely, when $\epsilon > 0$, ζ_i is considered as ionized with the charge Z_i. A shell noted S_i, formed with the NN_i and the second nearest neighbor electron, SN_i, is defined as the nearest environment of ζ_i. This definition holds when the NN_i, is at a distance d_i of ζ_i such that $\delta_i < d_i < \sqrt{2}\delta_i$ where δ_i is the ion stage radius.

A ionization process occurs for ζ_i when it is surrounded by a hot shell, i.e., when the total energy θ_i of S_i is positive. Z_i is increased by 1 while an electron appears upon the ion with the minimum potential energy. Then the ionization process follows, resulting from an increase of the kinetic energy of the released electron interacting with the previous *NN* and all the positive and negative charges involved in the simulation. This mechanism excludes any other event until the new *NN* is able to belong to a new shell when its distance to the ion becomes larger than the ion sphere radius. During this process the total energy of the particle set is conserved.

The reverse capture process follows the same energy conservation rules. Recombination of ζ_i starts when there is a cold shell, $\theta_i < 0$, around ζ_i. Then, the *NN* electron disappears, the ion charge is decreased by 1 and the kinetic energy of the *SN* electron is increased to account for energy conservation. In all other circumstances both the ion charges and the number of free electrons do not change.

Note that the preparation process, intended to reach a stationary state before starting statistics, particularly the adjustment and the slow relaxation of the initial unique ion charge, is an empirical process. An incorrect estimate of this charge given to all the ions would result, at the end of the preparation phase, in an electron density different from that fixed at simulation start. Indeed, the number of free electrons in the constant simulation volume increases (decreases) if the average charge has been underestimated (overestimated). Fluctuations of the plasma conditions are inevitable but should be small enough to allow interpretation of simulation results.

3. Results

Investigations available with MD are not limited to the study of the statistical properties of complex systems in thermal equilibrium. The possible analysis of relaxation time between two well defined equilibrium states is able to provide useful information on, e.g., electron dynamics in plasmas.

3.1. Electron dynamics

Molecular dynamics simulations have the following typical characteristic times illustrated here for a carbon plasma with $N_e = 10^{22}$ cm^{-3} and $T_e = 45$ eV. The shortest time-scale is the time step $\sim 10^{-19}$ s. The time for an electron to cross the average distance r_0 follows, $\sim 10^{-16}$ s. The relaxation time of the electron velocity distribution is three orders-of-magnitude larger $\sim 10^{-13}$ s. Longer still is the time required for the ion charge distribution to reach equilibrium.

A first example is given by the relaxation of the electron energy distribution between two equilibrium states. A numerical experiment intended to observe the evolution of a two component plasma in a state *A* towards an other equilibrium state *B* is performed under the following conditions. The initial state *A* is the superposition, without ion–electron interaction, of a one component plasma (OCP) of ions and an electronic OCP. Both OCPs are in thermal equilibrium at the same temperature and the whole system is neutral. In state *A* the electron energy distribution is peaked at about 200 eV as the repulsive forces of the electron OCP result in a positive potential energy for individual electrons. At time $t = 0$, the ion–electron interactions are switched on without ionization recombination. Electrons start to be attracted by ions and exchanges between the negative potential energy associated with the ion wells and electron kinetic energy take place. This relaxation can be analyzed with the energy distribution of electrons obtained by sampling the sum of kinetic energy and potential energy of each electron. At $t = 0$ there are no negative energy states. These states then start to be populated due to the multiple collisions undergone by the electrons. To illustrate a hydrogen-like carbon plasma at $T_e = 45$ eV and $N_e = 10^{22}$ cm^{-3} is chosen for its specificity. As will be shown below the equilibrium charge distribution resulting from the model with ionization recombination, is peaked at $\sim 98\%$ $Z = 4$ and is therefore useful for discussion and analysis of the model. In

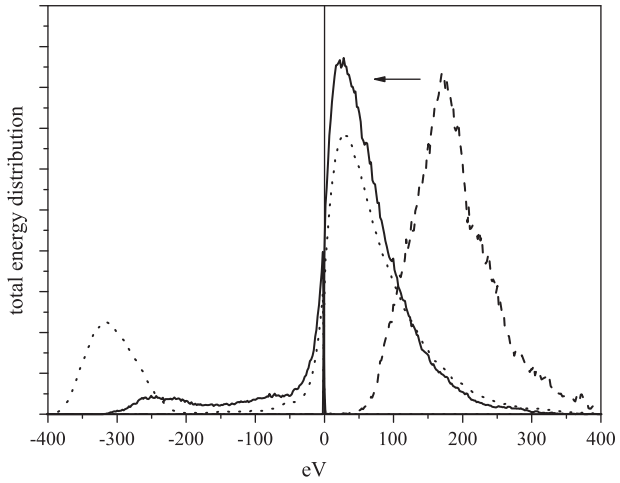

Fig. 4. Electron energy distribution relaxation for a carbon hydrogen-like plasma at $N_e = 10^{22}$ cm^{-3} and $T_e = 45$ eV (dash: $t = 0$, solid: $t \sim 10^{-12}$ s) compared to the distribution at equilibrium (dots).

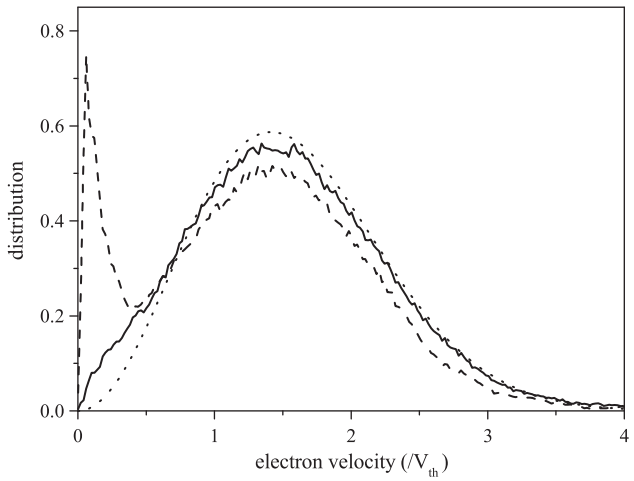

Fig. 5. Electron velocity distribution relaxation for an aluminum plasma at $N_e = 10^{22}$ cm^{-3} and $T_e = 50$ eV (dash: $t = 0$, solid: $t = 2.5 \times 10^{-13}$ s) compared to the Maxwell distribution (dots).

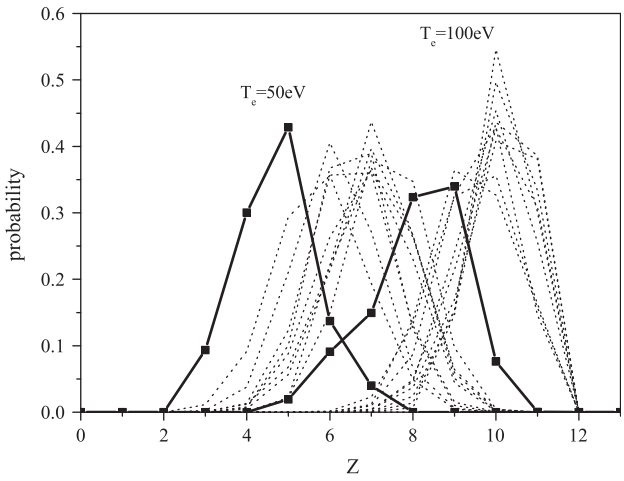

Fig. 7. Ion abundance versus temperature for aluminum at $N_e = 10^{22}$ cm^{-3}, (dots: NIST data, black: this work).

Fig. 4, the electron energy distribution has been plotted at two times, $t = 0$ and $t \sim 10^{-12}$ s. A simulation thermostat has been employed. The evolution shown results from the relaxation of the system approaching a new equilibrium state. There is a large difference between the time-evolved energy distribution function and the distribution obtained at equilibrium with ionization/recombination. Two reasons can explain this difference:

1) The ionization/recombination process favors the population of non thermal electrons trapped in a metastable state. The contribution of these electrons corresponds to the well separated bump peaked at ~ -315 eV where the helium like ionization energy is -393.1 eV. There are about 20% trapped electrons among the whole population. Therefore, 98% of the ions can be considered as helium-like *excited* electron–nucleus pairs.
2) Without ionization/recombination electrons possess thermal (Maxwellian) velocity distribution. Multiple collisions allow thermal electrons to descend deeply into ion wells, it is a very slow process not yet completed after 1 ps of system evolution.

In general, several ion stages coexist in the plasma. This complicates an analysis of the model based on the electron energy distribution. Nevertheless this remains useful and feasible. Inclusion of metastable states population results necessary in order to reach equilibrium. This mechanism is accomplished by the ionization/recombination process implemented in the simulation model. The point here is to allow clear identification of both members of ion–electron metastable pairs and as a result, which charges have to be included to calculate microfields in such highly coupled plasmas.

To complement the previous illustration a second example concerns the electron velocity distribution. Again the evolution between two states *A* and *B* in thermodynamical equilibrium is followed. *A* is chosen as an aluminum plasma at $N_e = 10^{22}$ cm^{-3} and $T_e = 50$ eV with a ionic balance obtained at equilibrium, accounting for ionization/recombination. At the start, the ionization/recombination is switched off. At positive times the system evolves freely resulting in changes in the electron velocity distribution function. In Fig. 5, the initial velocity distribution function is non-Maxwellian as ionization/recombination permanently generates excited electrons with non thermal velocities represented by the low velocity

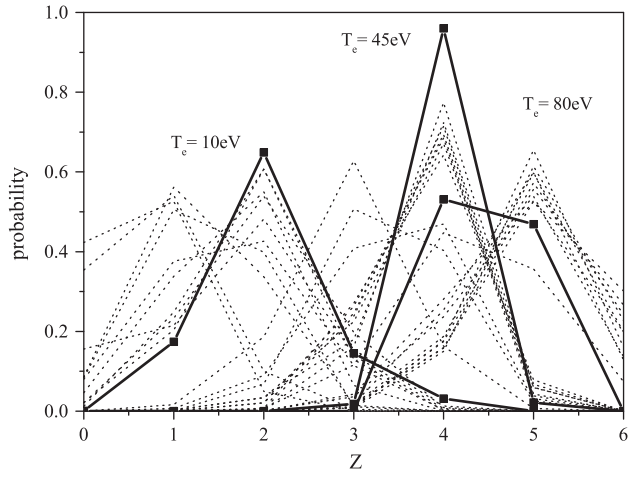

Fig. 6. Ion abundance versus temperature for carbon at $N_e = 10^{22}$ cm^{-3}, (dots: NIST data, black: this work).

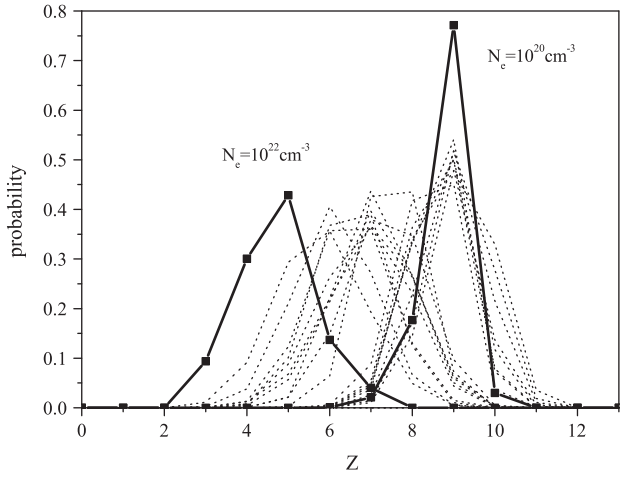

Fig. 8. Ion abundance versus density for aluminum at $T_e = 50$ eV, (dots: NIST data, black: this work).

peak. Multiple collisions occurring after switching off the ionization/recombination process induce a slow thermalization of the excited electrons as shown by the solid curve on Fig. 5 which tends towards the Maxwellian. Here again, this thermalization time $t \sim 3 \times 10^{-12}$ s can be useful for the estimation of the electron population time evolution in laser plasmas.

3.2. Ionization balance

Ion abundances versus temperature, deduced from the present simulations, are shown in Fig. 6 and compared to data provided by the NIST Saha database [9]. Results obtained for carbon at three temperatures $T_e = 10$, 45, 80 eV at $N_e = 10^{22}$ cm^{-3} are plotted with the corresponding NIST data. Comparisons of the same kind for aluminum are plotted in Fig. 7. Inherently to simulation fluctuations remain for the ion stage populations once a quasi-stationary state has been reached. As a result, all the probabilities shown have to be considered with error bars of a few percent.

In Fig. 8, the dependency on density for aluminum at $T_e = 50$ eV is shown to be in relative agreement with the NIST results. It is worthwhile to note in Fig. 7 the dispersion of the NIST data and a shift of the present results towards smaller charges. This shift is decreased for higher temperatures and disappears at low density as shown on Fig. 8 while it looks negligible for carbon in Fig. 6. Such a different behavior for increasing coupling conditions, not yet understood, suggests further questions, particularly, because the self consistent treatment of potential lowering in the simulation model.

4. Conclusion

Classical MD is a powerful and versatile tool for the investigation of complex many-body systems. A possible way to improve its capabilities in plasma modeling is to use known quantum data as external parameters. Ionization energies of ion stages appear essential as they control storage and exchange of negative potential energy with electrons. Ionization energies necessarily come with the implementation of ionization and recombination mechanisms allowing equilibration of ion populations self consistently. Because of the empirical characteristic of the model and the possible influence of the neglect of any radiative processes in the system evolution, the present results cannot be considered as benchmarks but contribute to the validation of the method.

MD applied to ions and electrons involves inherent difficulties. As shown in the present work it is possible to effectively overcome quite well these difficulties for highly coupled conditions, including the possibility of following the plasma evolution, over a long period of time. Simulations are illustrated here with carbon and aluminum plasmas. Weakly coupled plasma conditions which require more expensive MD calculations are neither readily available nor useful in comparison with standard approaches. Implicitly, MD is able to take into account dynamically for all the complexity of the potential for charge motion including ion potential lowering, charge-exchange, many-body collisions, collective behaviors, and non-Maxwellian velocity distributions. As shown above, beside the usual mean statistical quantities and microfields, MD is appropriate to provide information on electron dynamics up to a few picoseconds. In this way the evolution time between a well defined initial state of the system to an other equilibrium state can be estimated through the development of the velocity distribution or the electron energy distribution.

The plasma model chosen for ionization and recombination mechanisms associated with the molecular dynamics approach, behaves similarly to models found elsewhere. Hopefully, this work opens a non standard point of view for coupled plasma analysis.

References

[1] A. Calisti, T. del Río Gaztelurrutia, B. Talin, HEDP 3 (2007) 52.
[2] B. Talin, A. Calisti, J.W. Dufty, Phys. Rev. E 65 (2002) 056406;
B. Talin, A. Calisti, E. Dufour, J. Dufty, J. Quant. Spectrosc. Radiat. Transf. 71 (2001) 729.
[3] T. Pschiwul, G. Zwicknagel, J. Phys. A 36 (2003) 6251.
[4] G. Kelbg, Ann. Phys. 12 (1963) 219 13 (1964) 354; 14 (1964) 394.
[5] W. Ebeling, Ann. Phys. 19 (1967) 104;
W. Ebeling, B. Miltzer, F. Schautz, Contrib. Plasma Phys. 37 (1997) 137.
[6] F.J. Rogers, J. Chem. Phys. 73 (1980) 6272;
Phys. Rev. A 29 (1984) 868.
[7] H. Minoo, M.M. Gombert, C. Deutsch, Phys. Rev. A 23 (1981) 924.
[8] R.D. Cowan, The Theory of Atomic Structure and Spectra, University of California Press, Berkeley and Los Angeles, California, 1981.
[9] Yu. Ralchenko, Nist SAHA Plasma Kinetics Database (version 1.0), National Institute of Standards and Technology, Gaithersburg, MD, 2006, Available from: http://nlte.nist.gov/SAHA.

Annexe B

Ionization potential depression in hot and dense plasmas through a pure classical model

Contrib. Plasma Phys. **55**, No. 5, 360 – 365 (2015) / **DOI** 10.1002/ctpp.201400087

Ionization Potential Depression in Hot Dense Plasmas Through a Pure Classical Model

A. Calisti*, **S. Ferri,** and **B. Talin**

Aix Marseille Université, CNRS, PIIM UMR 7345 13397, Marseille, France

Received 27 October 2014, revised 23 January 2015, accepted 23 January 2015
Published online 17 February 2015

Key words Classical molecular dynamics, ionization potential depression, multi component plasma

The ionization potential of an ion embedded in a plasma, lowered due to the whole of the charged particles (ions and electrons) interacting with this ion, is the so-called plasma effect. A numerical plasma model based on classical molecular dynamics has been developed recently. It is capable to describe a neutral plasma at equilibrium involving ions of various charge states of the same atom together with electrons. This code is used here to investigate the ionization potential depression (IPD). The study of the IPD is illustrated and discussed for aluminum plasmas at mid and solid density and electron temperatures varying from 50eV to 190eV. The method relies on a sampling of the total potential energy of the electron located at an ion being ionized. The potential energy of such electron results from all of the interacting charged particles interacting with it.

1 Introduction

The radiative properties of an atom or an ion surrounded by a plasma are modified through various mechanisms. For instance, the line shapes of radiation emitted by bound-bound transitions are broadened and therefore carry informations useful for plasma diagnostics. Depending on plasma conditions, the electrons supposedly occupying the upper quantum levels of radiators no longer exist as they belong to the plasma free electron population. All the charges present in the radiator environment, electrons and ions, contribute to the lowering of the energy required to free a bound electron. This mechanism is known as ionization potential depression (IPD). The knowledge of IPD is useful as it affects both the radiative properties of the various ionic states and their populations. Its evaluation requires dealing with highly complex n-body coupled systems, involving particles with different dynamics and attractive ion-electron forces. A few recent experiments [1, 2] leading to IPD measurements in situ renew interest for this issue, see for instance [3–7]. Some approximate models allow a general discussion of these experiments as they provide a scaling for the IPD. Our will to contribute to the discussion on IPD has motivated the development of a distinct approach. The work on IPD described here is carried out using a classical molecular dynamics (MD) code, the BINGO-TCP code [8], developed recently to simulate neutral multi-component (various charge state ions and electrons) plasmas. Our simulations involve the mechanism of collisional ionization/recombination necessary to simulate stationary plasmas with a definite temperature and equilibrated populations of ions of various charge states. The code which is particularly robust and versatile is an efficient tool able to provide approximate reference data available by sampling, once a stationary state of the plasma has been reached. All the advantages of classical MD techniques are a benefit in the present approach which relies on a reduced set of postulates involving mainly an ion-electron potential depending on the ion charge state and an ionization-recombination protocol which controls the plasma ion charge distribution in the plasma and the trapping of electrons in the ion wells.

Our study focuses on aluminum plasmas for two ionic densities and several temperatures in order to explore the IPD for different plasma coupling conditions.

* Corresponding author. E-mail: annette.calisti@univ-amu.fr

2 Model summary

2.1 Theoretical models

The IPD has been formulated in the sixties following two slightly distinct paths. First, Stewart and Pyatt [9] proposed a model using the finite-temperature Thomas-Fermi potential for the average electrostatic potential near nuclei of the plasma particles. The bound electrons are considered as part of the unperturbed ion. The plasma free electrons are described by Fermi-Dirac statistics and ions by Maxwell-Boltzmann statistics. Note that in this model, the bound electrons do not contribute to the reduction of the ionization energy. The reduction of the ionization energy is given by:

$$\Delta U_{SP}(Z) = \frac{3Ze^2}{2r_0}\left\{\left[1+(\frac{\lambda_D}{r_0})^3\right]^{2/3} - (\frac{\lambda_D}{r_0})^2\right\} \tag{1}$$

$$\lambda_D = \sqrt{\frac{kT}{4\pi(n_i+n_e)e^2}},\ \frac{4\pi n_i r_0^3}{3} = 1 \tag{2}$$

where Z is the charge state of the atom (or ion) after the ionization occurrence, i.e. $Z = 1$ for neutrals, λ_D is a generalized Debye length and r_0 the average inter-ionic distance for the average ion charge $\overline{Z}$. n_i is the corresponding ion density and n_e the electron density. In the high density or low temperature limit, the IPD becomes:

$$\Delta U_{SP}(Z) = \frac{3Ze^2}{2r_0} \tag{3}$$

Second, Ecker-Kröll [10] formulated a generalized Saha equation as a function of the chemical potential of the plasma. This model assumes two functional forms for the IPD depending on the particle (ions plus electrons) density:

$$\Delta U_{EK}(Z) = Ze^2\begin{cases} 1/\lambda_D & n_{cr} \geq n_i(1+\overline{Z}) \\ C\times(1+\overline{Z})^{1/3}/r_0 & n_{cr} < n_i(1+\overline{Z}) \end{cases} \tag{4}$$

where

$$n_{cr} = \frac{3}{4\pi}\left(\frac{kT}{Z_N^2 e^2}\right)^3 \tag{5}$$

is the critical density which includes both ion and free electron densities, Z_N being the nuclear charge and T the plasma temperature. The constant C is determined by imposing the continuity of the IPD at the critical density:

$$C = \left(\frac{r_0}{(1+\overline{Z})^{1/3}\lambda_D}\right)_{n_{cr}}. \tag{6}$$

Recent experimental results [1] have shown discrepancies with the SP model which is the most widely used among the IPD models and, shown good agreement with the EK model in which C has been set to 1 according to experimental considerations. In contrast, other experimental results [2] obtained independently have corroborated the SP model. In the following, we will compare our simulation results with both models SP and EK with $C = 1$.

2.2 Molecular dynamics, potentials and ionization/recombination protocol

The BINGO-TCP code is based on standard MD techniques. The particle motions in the simulation box are ruled by a Verlet velocity algorithm [11] associated with periodic boundary conditions. The whole of the interactions between charges contribute to the motion of the individual electrons and ions. The time step is chosen for an accurate description of electron motion. The total charge in the box is zero. The Born-Oppenheimer approximation is not useful and collective behaviors naturally appear. The BINGO-TCP code involves two major features intended to achieve realistic simulations of plasmas, with ion charge distributions adjusting with temperature and

density conditions. First, a regularized electron/ion potential, i.e., finite at short distances, that depends on the ion charge Z_i is defined to be:

$$V_{ie}(r) = -Z_i e^2 e^{-r/\lambda}(1 - e^{-r/\delta(Z_i)})/r \tag{7}$$

where the regularization distance $\delta(Z_i)$ is function of the ionization energy E_i of an ion of charge Z_i. An electron located at an ion ($r = 0$) occupies the fundamental state of the ion whose charge is Z_i with a core charge $Z_i + 1$ such that

$$\delta(Z_i) = Z_i e^2/E_i \tag{8}$$

Ion-ion and electron-electron potentials are taken to be screened Coulomb potentials

$$V_{ii,ee} = Z_{i,e}^2 e^2 e^{-r/\lambda}/r \tag{9}$$

The screening factor present in these potentials $e^{-r/\lambda}$ where λ is half the simulation box size, helps to smooth the small fluctuations of forces arising with the periodic boundary conditions. It doesn't affect the mechanisms controlling the particle motion in the simulation box.

The second major feature is that the collisional ionization/recombination process implemented in the code has two fundamental functions. On the one hand, it allows the evolution of the charge state population towards a stationary state depending on temperature, density and composition of the plasma. On the second hand, it favors the creation of a population of electrons temporary trapped in the ion wells. Briefly, the local conditions for the ionization of an ion of charge Z_i are controlled by the total energy E and the location, inside a shell around the ion, of the two nearest neighbor electrons of that ion. If $E > 0$, Z_i is replaced by $Z_i + 1$ and an electron appears at the same location as the ion being ionized. This electron-ion pair stands for the fundamental state of Z_i. The effective ionization, i.e., the heating of the supplementary electron is a long term process resulting from the multiple interactions in the simulation box. An analogous process occurs for the collisional recombination of an electron when $E < 0$. The sign of the total energy of individual electrons provides a simple way to separate the electron population into trapped (negative energy) and free (positive energy) electrons. Electron temperature and density are obtained on the basis of the free electron population.

The present work uses the instantaneous placement of one supplementary electron at an ion to start an ionization process. The ionization protocol guarantees that there is no other electron at short distance from the ion undergoing an ionization. The magnitude of the supplementary electron potential energy represents the opposite amount of kinetic energy required by the electron to join the free electron population. Such events are rather seldom but sufficient to perform a statistical study of these energies for each kind of ion. Their average for each ionic charge state is interpreted as the corresponding IPD.

3 Results

The study of the IPD is illustrated and discussed for aluminum plasmas at two different densities ($\rho = 0.34$ g/cm^3 and $\rho = 2.7$ g/cm^3) and plasma temperatures varying from 50 eV to 190 eV. TCP-MD simulations have been performed with 80 atoms of aluminum. We started the simulations with an electronic density corresponding to a mean charge $\overline{Z} = 8$. After an equilibration step controlled by imposing the temperature, we ensure that an equilibrium state has been reached by checking the stationarity of the total energy and the charge distribution.

The analysis of the electron energy distribution function permits the inference of the electronic density and consequently of the mean charge value $\overline{Z}$. The distribution function of negative energies is associated with trapped electrons. As the total number of electrons in the simulation box is known, this function allows us to estimate the density of free electrons in our simulations. The variation of the mean charge value as a function of the temperature has been plotted in fig. 1 and compared with the FLYCHK code [12] results. It can be observed that, except at the highest temperature, the mean charge value obtained by TCP-MD simulation is smaller than the one obtained by FLYCHK. Nevertheless, the agreement is good with an overall difference of less than 6.5 %. At the solid density, it has been found that the mean ionization of the simulated plasmas was larger than that inferred by FLYCHK and that the overall difference was about 20 %.

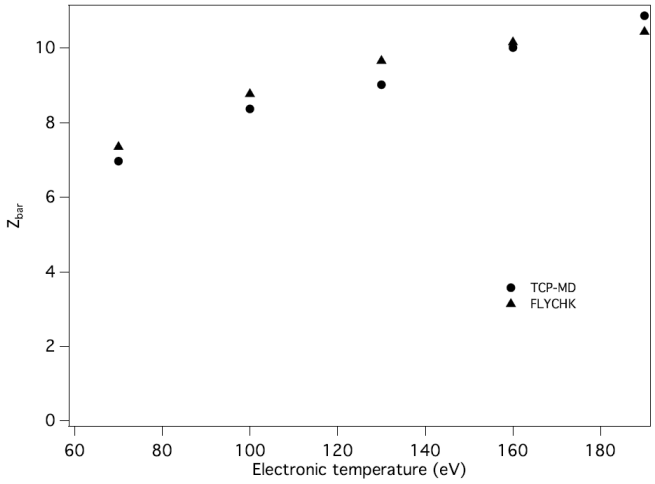

Fig. 1 Mean charge value versus temperature at $\rho = 0.34$ g/cm^3.

By sampling the total potential energies of the electrons located at ions being ionized while they are in the same ionization charge state (cf. fig. 2(a)), we have access to their corresponding average ionization energy. The difference as compared to the ionization energy of the isolated ions can be interpreted as the corresponding IPD. The IPD of the different ion charge states present in the simulated plasma has been measured for five cases of temperature at $\rho = 0.34$ g/cm^3. The results are plotted in fig. 2(b). It can be noticed that the statistics on the ionization events did not permit the measurement of the IPD for Z lower than 8. The IPD decreases as the temperature increases. The SP model presents a similar behavior but not the modified EK one which depends on the temperature only through the value of $\overline{Z}$.

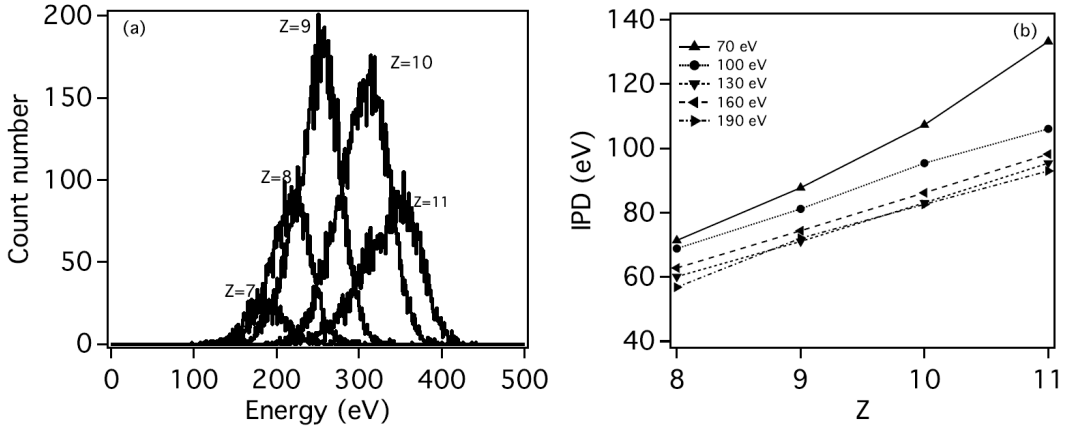

Fig. 2 (a) Distribution of the total potential energy of an electron located at different charge state ions at 100 eV and $\rho = 0.34$ g/cm^3. (b) Evolution of the IPD with the temperature at $\rho = 0.34$ g/cm^3.

Figure 3 and 4 show the comparisons of the TCP-MD results with the SP and EK models at $\rho = 0.34$ g/cm^3 and $T_i = T_e = 100$ eV, and $\rho = 2.7$ g/cm^3 and $T_i = T_e = 50$ eV, respectively. As expected, the IPD is greater for the highest density and lowest temperature and it corresponds to a ionization energy 40% lower than the corresponding energy of the isolated ions. With $C = 1$ and the chosen conditions, the modified EK model gives IPD values greater than the SP predictions. For both cases, the simulated IPDs fall in between the two models. It can be seen in fig. 4 that the IPD compares well with the SP strong coupling limit. However, the good agreement observed does not allow to conclude because the SP strong coupling limit does not depend on temperature contrary to our calculation performed at $T_i = T_e = 50$ eV.

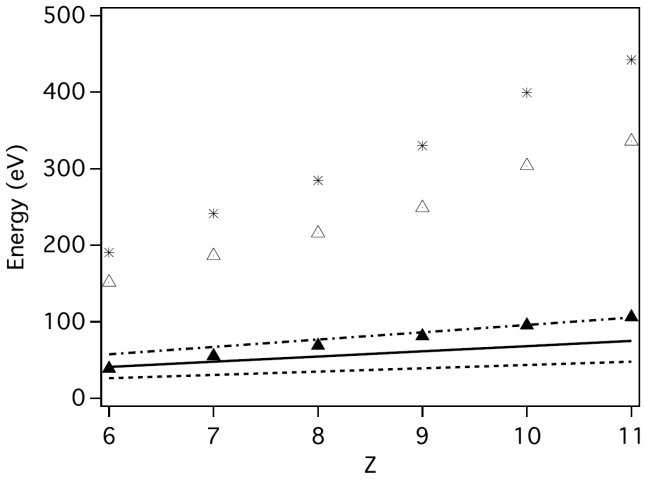

Fig. 3 Comparison of the simulation results at 100 eV and $\rho = 0.34$ g/cm^3 with the SP and EK models. (stars): ionization energy of the isolated ion, (triangles): simulated ionization energy, (black triangles): simulated ionization potential depression, (dash-dotted line): modified EK model, (full line): SP strong coupling limit, (dashed line): SP model.

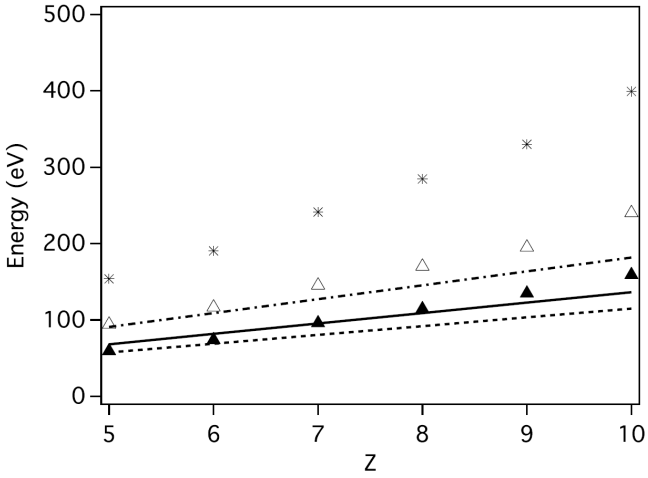

Fig. 4 Comparison of the simulation results at 50 eV and $\rho = 2.7$ g/cm^3 with the SP and EK models. Same code as fig. 3.

4 Conclusion

The ionization potential depression in a dense aluminum plasma has been simulated via a pure classical model based on classical molecular dynamics simulation method adapted to follow the evolution of plasmas involving ions of various charge states. Due to the specific implementation of the ionization/recombination model, our classical MD method gives access to the ionization potential of an ion accounting for the influence of the free electrons and neighboring ions. By comparison with the ionization potential of the equivalent isolated ions, the ionization potential depression can be estimated.

Both the regularized ion electron potential design and the ionization/recombination protocol result in a ion charge distribution which depends on density and temperature. The equilibrium particle configurations are adjustments, at a given temperature, of slow ions represented by wells with depths depending on the ion charge and fast electrons either trapped or free. Such a behavior, based on energy exchange mechanisms between particles, appears to be quite independent of the potential well shapes and the details of the ionization/recombination protocol. Concomitantly with the development of the BINGO-TCP code, a model to account for quantum processes in classical MD has been developed based on different but similar idea to model atomic processes in dense non equilibrium plasmas [13]. Comparisons between both methods are still to be done.

Calculations have been performed at two ionic densities, $\rho = 0.34$ g/cm^3 and $\rho = 2.7$ g/cm^3 and for temperatures varying from 50 to 190 eV. First, It has been shown that the IPD depends on the temperature. Second, the results obtained with our TCP-MD simulation code have been compared with different semiclassical models, the SP model and the associated strong coupling limit which are widely used in astrophysical and laser plasma

simulations, and the EK model which has been modified accordingly with Ciricosta et al. experimental results. It has been shown that the simulated IPD falls in between the SP and EK model results and compares well with the SP strong coupling limit for the highest density and lowest temperature. These first results are very encouraging. Owing to the fact that a bad estimation of the IPD in laser plasma simulations have consequences for the estimation of the ionization degree, the equation of state etc., the model proposed in this work appears as an important tool to provide data for further discussion on IPD models. The present results being obtained for stationary plasmas at equilibrium, the next step will be to simulate plasmas with cold ions in order to compare with Ciricosta et al. experimental results.

References

[1] O. Ciricosta et al., Phys. Rev. Lett. **105**, 065002 (2012).
[2] D.J. Hoarty et al., Phys. Rev. Lett. **110**, 265003 (2013).
[3] S.M. Vinko et al., Nat. Commun. **5**, 3533 (2014).
[4] B.J.B. Crowley, HEDP **13**, 84 (2014).
[5] C.A. Iglesias, HEDP **12**, 5 (2014).
[6] S.K. Son et al., Phys. Rev. X **4**, 0311004 (2014).
[7] L.B. Fletcher et al., Phys. Rev. Lett. **112**, 145004 (2014).
[8] A. Calisti, B. Talin, CPP **51**, 6, 524-528 (2011); A. Calisti et al., HEDP **5**, 307 (2009).
[9] J.C. Stewart, K.D. Pyatt, Astrophys. J. **144**, 1203 (1966).
[10] G. Ecker, W. Kröll, Phys. Fluids **6**, 62 (1963).
[11] L. Verlet, Phys. Rev. **159**, 98 (1967).
[12] H.-K. Chung et al., HEDP **1**, 3 (2005).
[13] S.P. Hau-Riege et al., New J. Phys. **15**, 015011 (2013).

Annexe C

Ionization Potential Depression for non equilibrated aluminum plasmas.

Ionization potential depression for non equilibrated aluminum plasmas

A. Calisti, S. Ferri and B. Talin

Aix Marseille Universite, CNRS, PIIM UMR 7345, 13397, Marseille, France

E-mail: annette.calisti@univ-amu.fr

March 2015

Abstract. A classical Molecular Dynamics simulation model, designed to simulate neutral plasmas with various charge states of a given atom together with electrons, is used to investigate the ionization potential depression (IPD) in dense plasmas. The IPD is discussed for aluminum plasma at and out of equilibrium. The simulation results are compared with those of earlier theoretical models and with experimental data obtained in the framework of x-ray free-electron laser experiments. The model proposed in this work appears as an important tool to provide data for further discussion on IPD models.

PACS numbers: 52.65.Yy, 52.25.b, 52.27.Gr

Keywords: Ionization Potential Depression, Classical Molecular Dynamics Simulations, Multi Component Plasma Simulations

1. Introduction

The ionization potential depression (IPD) of an ion in a dense plasma is somehow an average quantity characterizing the global effect of the plasma on that ion. Quantum properties, e.g., the ionization potential of an ion are modified due to the interactions of the valence electron with the whole of the surrounding charges. Essentially two distinct theoretical models, the Stewart-Pyatt (SP) [1] and Ecker-Kröll (EK) [2] models have been developed and used to describe the IPD. Recently, their validity has been discussed in the framework of two experiments, one using an x-ray free-electron laser [3] and the other one using a high-power optical laser [4] to create the dense plasma. It seems that neither the SP model nor the EK model be able to explain both experiments. This has initiated a renewed interest for the problem of the ionization potential depression in dense plasmas, see for instance [5, 6, 7, 8, 9].

In a previous study of the IPD [10], we considered an aluminum plasma in equilibrium, i.e. with equal ion and electron temperature. Such conditions are quite academic in regard of the true experimental process of generation of plasmas for IPD

studies by impact of a short radiation pulse on a solid target [11, 3]. In these experiments, the electrons within the target are heated, within 80 fs, to temperature between 70 eV and 180 eV depending on the photon energy of the irradiation. Moreover, the $K-shell$ fluorescence, on which the interpretation of the experiment is based, only occurs while the target is irradiated (80 fs). On this time scale, the ion motion is negligible and emission occurs in a plasma where the ion density n_i is the solid-density and where the electron density is given by $n_e = \overline{Z} n_i$, with $\overline{Z}$ the ionization amount. To get closer of these conditions one can use MD to simulate a two component plasma of ions at room temperature and solid density, and electrons in pseudo equilibrium with the cold ion population. The argument here is that the electron adjustment to the ions can occur in a time that does not allow the ion population to be heated by the electrons. The code BINGO-TCP [12, 13] has been used to match approximately these conditions, with typically the ion temperature, $T_i = 300K$ and two electron temperatures, $T_e = 50eV$ or $T_e = 160eV$. The purpose of this work is the evaluation of the differences induced on the IPD by these two kinds of plasmas at and out of equilibrium.

The real question that arises here, is : does the generation process of the plasma can affect the IPD measurement?

2. Model summary

In the vicinity of an isolated ion, i.e., a point charge an electron moves into an attractive spherical potential. If there are several ions, an electron moves into a complex potential resulting from the sum of the individual ion potentials which overlap and the electron potentials. In average the plasma is neutral and the electrons provide a negative blurred imprint of the ion structure. This is clearly connected to the kinetic energy required to extract a trapped electron from a local minimum energy attached to an ion of charge Z. In average these energy are interpreted as the ionization potential of ions of charge Z in the plasma. In the following, semi classical models developed elsewhere to solve this N-body problem will be used.

Both the theoretical and simulation models have been recalled elsewhere [10]. Their following mention is limited to a few guidelines.

2.1. Theoretical models

Two theoretical models formulated in the sixties for plasmas in equilibrium will be used in the following for discussions. These models are of importance as they are commonly used for dense plasma modeling.

The Stewart and Pyatt model [1] is based on the finite-temperature Thomas-Fermi potential for the average electrostatic potential near nuclei of the plasma particles. The bound electrons are considered as part of the unperturbed ion and do not contribute to the reduction of the ionization energy. The plasma free electrons are described by Fermi-Dirac statistics and ions by Maxwell-Boltzmann statistics. The SP model relates

the IPD of an ion of charge Z to the generalized Debye length λ_D:

$$\Delta U_{SP}(Z) = \frac{3Ze^2}{2r_0}\left\{ \left[1 + (\frac{\lambda_D}{r_0})^3\right]^{2/3} - (\frac{\lambda_D}{r_0})^2 \right\} \tag{1}$$

$$\lambda_D = \sqrt{\frac{kT}{4\pi(n_i + n_e)e^2}},\ \frac{4\pi n_i r_0^3}{3} = 1 \tag{2}$$

where Z is the charge state of the atom (or ion) after the ionization occurrence ($Z = 1$ for neutrals), r_0 the average inter-ionic distance for the average ion charge $\overline{Z}$. n_i is the corresponding ion density and n_e the electron density. In the high density or low temperature limit, the IPD becomes:

$$\Delta U_{SP}(Z) = \frac{3Ze^2}{2r_0} \tag{3}$$

Second the Ecker-Kröll model [2] reads

$$\Delta U_{EK}(Z) = Ze^2 \begin{cases} 1/\lambda_D & n_{cr} \geq n_i(1+\overline{Z}) \\ C \times (1+\overline{Z})^{1/3}/r_0 & n_{cr} < n_i(1+\overline{Z}) \end{cases} \tag{4}$$

where

$$n_{cr} = \frac{3}{4\pi}\left(\frac{kT}{Z_N^2 e^2}\right)^3 \tag{5}$$

is the critical density which includes both ion and free electron densities, Z_N being the nuclear charge ($Z_N = 13$ for Al) and T the plasma temperature. The constant C is determined by imposing the continuity of the IPD at the critical density:

$$C = \left(\frac{r_0}{(1+\overline{Z})^{1/3}\lambda_D}\right)_{n_{cr}}. \tag{6}$$

None of these two models allows ionic and electronic distinct temperature. In the following, we will compare our simulation results with both models SP and modified EK with C = 1 according to experimental considerations [3].

2.2. Molecular dynamics, potentials and ionization / recombination protocol

The BINGO-TCP simulation code described in [12, 13] involves two major specificities.

First, an ion / electron regularized potential which avoids Coulomb collapse has been implemented in the simulation. The choice of the potential is guided by the study of the evolution of ion charge populations. For this purpose, the potential depends on the ion charge Z_i through the characteristic length $\delta(Z_i)$ in order to fit the ionization energies of the various ion stages.

$$V_{ie}(r) = -Z_i e^2 e^{-r/\lambda}(1 - e^{-r/\delta(Z_i)})/r. \tag{7}$$

This choice implies that an electron located at an ion ($r = 0$) occupies the fundamental state of the ion whose charge is Z_i with a core charge $Z_i + 1$ and with the expected ionization potential for that ion

$$E_i = Z_i e^2/\delta(Z_i) \tag{8}$$

where E_i is the ionization energy of the unperturbed ion of charge Z_i. It would not be suitable for electron temperatures much higher than the highest ionization energy, leading to a plasma of fully ionized ions and electrons.

The screening parameter λ reminds that in our simulations the forces between particles are effectively screened by the simulation box. This helps to smooth the small fluctuations of forces arising with the periodic boundary conditions. It doesn't affect the mechanisms controlling the particle motion in the simulation box.

Second the collisional ionization / recombination process implemented in the code relies on the knowledge of position and velocity of individual particles at each time step. The main idea is to extract from these data an information about a local characteristic of the plasma around an ion "A". For that purpose notions of hot shell and cold shell of an ion have been introduced. They correspond to the location of the two nearest neighbor electrons and the sign of their total energy used to evaluate if locally the plasma, at one step of its evolution, is favorable to an ionization (positive energy) or a recombination (negative energy) of ion "A". This test results into a pre-ionization, i.e., an increase by 1 of the ion charge and one more electron or a recombination, i.e., a decrease by 1 of the ion charge while the nearest neighbor electron is removed. This local discontinuity over one time step is then accounted for by the whole system through a normal evolution. The pre-ionized state, i.e., an ion with a trapped electron can be converted into an ionized state through multiple collisions. The actual ionization or recombination of an ion lasts until a new ionization or a recombination becomes allowed.

The collisional ionization / recombination process allows a fast joint equilibration of the electron population with the ionic charge state population. "Equilibration of ions and electrons"refers to the necessary preparation phase of the particle set (into the simulation box) before extracting any sampling from simulations. At start, the ion-electron interaction potentials are switched-on inducing a non equilibrium state of the ion-electron plasma obtained by mixing electrons with ions of the same kind. Due to the pairwise exchange of kinetic and potential energy, this non equilibrium state, would evolve towards a state far from the density-temperature conditions expected regarding the objective of the simulation. The electron temperature is constrained by velocity rescaling while the ionization recombination process broadens the charge distribution. During this short phase no significant change of ion temperature and positions can occur. At the end of the preparation phase the system follows a quasi stable evolution with stationary trapped and free electron populations. The system evolution is considered as stationary, when the ionization events compensate the recombinations and the total energy fluctuations of the simulated particles remain small.

During the stationary evolution of the simulation cells, each ionization event of an ion starts with the placement of an electron at the ion. This placement means that the valence electron is in its fundamental state and has a vanishingly small kinetic energy. The total energy of this electron takes into account the whole complexity of the potential energy surface around the ion including the ionization energy lowering at a local level due to the surrounding charges. The ionization potential of ions with a given charge

in the plasma is obtained as the average of the corresponding instantaneous ionization potentials and the IPD results from the difference with the ionization potential of the corresponding isolated ion.

Classical molecular dynamics is designed to solve ideal N-body problems. Here, ideal, means that the system under study relies on the simplest hypothesis. One of the main interest to use MD is to fully account for electron dynamics and for the structure of ion configurations. In the previous work reported, [10], the ideal system was defined as a stationary aluminum plasma at solid density and equal ion and electron temperature $T_e = T_i$. This choice is quite academic as we do not know if the generation of such a plasmas can be practically done. Another type of ideal system, composed with aluminum ions at room temperature, imbedded into hot electrons e.g., a few tens of eV, can be considered. This second ideal experiment corresponds to the conditions that could be obtained by a short radiation pulse on solid aluminum. In our MD simulation the only mechanism of temperature equilibration of two kinds of interacting particles e.g., ions and electrons, is a collisional mechanism. Coulomb explosion is not allowed as the system is infinite and there is no hot electron. The mass difference between aluminum ions and electrons ensures the coherence of the two temperature model because the necessary ion / electron equilibration phase can take place with a negligible heating of the ion component.

3. Results and discussion

Both the electrons and ions are responsible for the IPD, however, in the framework of our ion-electron MD simulations, their respective effect cannot be considered separately. With MD, the electron-ion interaction is not represented by a potential screened by the electrons themselves but accounts for all the surrounding electrons through binary interactions. Contrary to MD, theoretical models link the IPD to the electron plus ion Debye screening of ions with the average charge and the average ion-ion distance (SP model) or connect the IPD to the average static electric micro-field (EK model) generated by ions and electrons. Both these approaches based on an approximate ion effect, could provide some insight on the specific electron contribution to the IPD. In our model, electrons adjust dynamically to ions to compensate the ionic charge. Therefore, the electron plasma structure gives an approximate negative imprint of the ion structure. Here, ions are practically motionless over a typical time of interest ($\sim$100 fs) while electrons behave more or less like a fluid. A series of simulations with different temperature and ionic density will help the understanding of the main mechanisms giving rise to the IPD.

The study of the IPD is illustrated and discussed for two aluminum plasmas: one with ions at room temperature with hot free electrons and one at equal ion / electron temperature. The difference between the two plasmas appears in the ion-ion pair correlation function.

For ions at room temperature a quasi crystalline ion configuration results into a

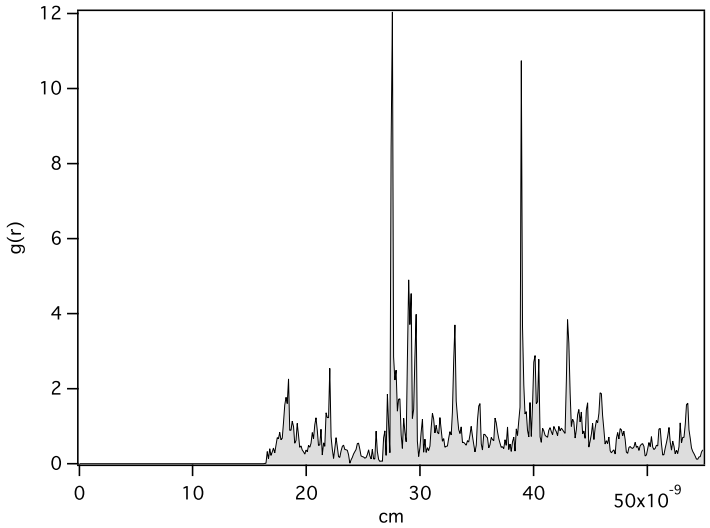

Figure 1. ion/ion pair correlation function at room temperature

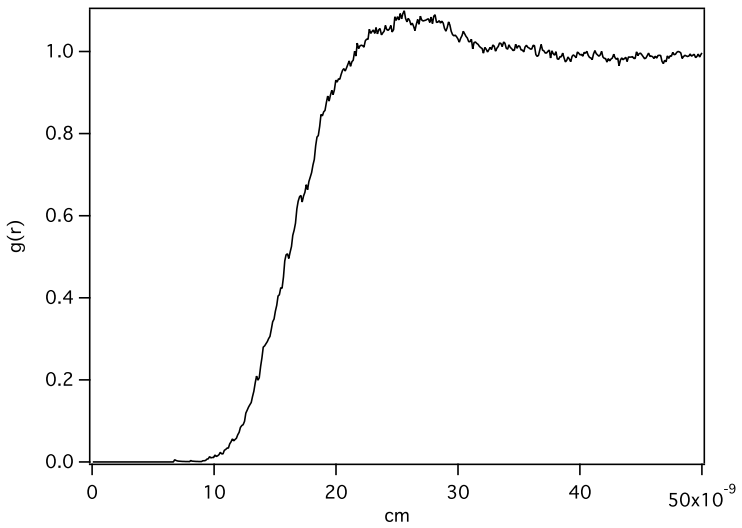

Figure 2. ion/ion pair correlation function at $T_e = T_i = 50eV$

series of peaks in the $g(r)$ plotted in fig. 1 while in fig. 2, at equal ion / electron temperature a smooth ordered structure is revealed only by a bump. The term "quasi-crystalline" refers to our calculation process carried out on a set of independent initial ion configurations at room temperature prepared at random but not at all like a perfect crystalline structure. Even though, the pair correlation function in fig. 1 is fairly noisy, this does not affect the IPD measurements.

The influence of the ionic structure on the IPD is shown in fig. 3 together with the comparison with the different models. Simulations show that there is an increase of the IPD for the case with ions at room temperature. An interpretation of this result

associates the overlapping of the ion wells which depends on their short distance ordering to an increase of the IPD. At room temperature the quasi crystalline ordering results into a lowering of the energy required to free an electron from the ion configurations. Comparisons with theoretical models show that our simulation results fall in between both models.

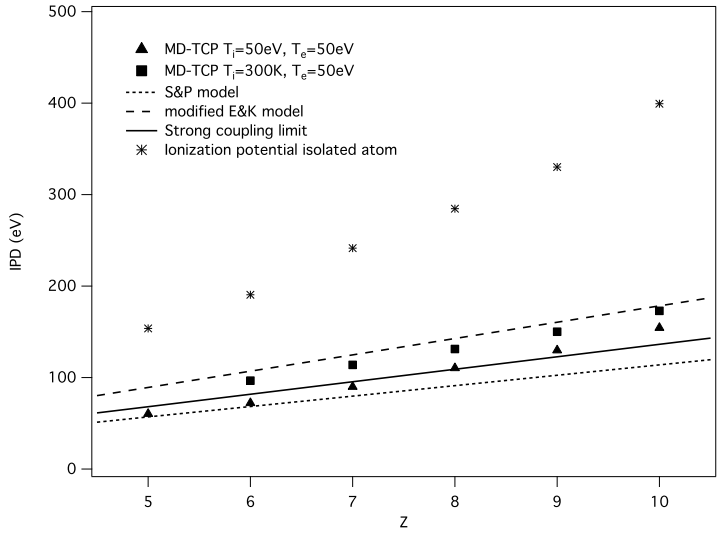

Figure 3. Influence of the ionic structure on the ionization potential depression (IPD).

The ion well overlapping mechanism which strongly depends on the ionic structure appears to be fundamental in the IPD formation. A compression of the plasma at a ionic density greater than solid density, $n_i = 8 \times 10^{22} cm^{-3}$, increases this overlapping inducing an increase of the IPD as can be shown in fig. 4.

Comparisons with theoretical models show here again that our simulation results fall in between both models and that the density variation is qualitatively well reproduced by both models even though our simulations predict an IPD increase twice less large than the theoretical models. Analyzing fig. 3 and 4, it appears that the IPD corresponding to a simulated system with ions at room temperature would be better represented by the EK model.

This model describes the lowering of the ionization potential as being due to the presence of an electric microfield and the ionization potential is defined as the difference between the ground state energy of the ion of charge Z and that of the ion of charge $Z + 1$. The IPD EK-model only depends on the total density (ion plus electron) and thus depends on the ionization amount. In our simulation model, the ionization amount is deduced from the total energy distribution of the electrons associated to the total number of electrons in the simulation box. For $T_e = 50eV$, we have obtained $\overline{Z} = 7.09$ for the ions at room temperature and $\overline{Z} = 6.56$ at equilibrium. These results are consistent with the IPD increase at room temperature. We recall that in our model, the ionization / recombination process is a pure collisional process. In order to compare, our

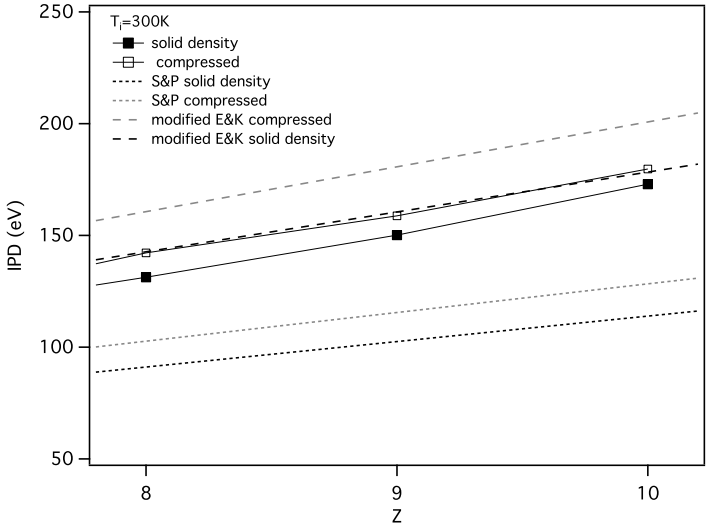

Figure 4. IPD simulation and theoretical model results for $T_e = 50eV$. empty squares: compressed; black squares: solid density.

results with the models for different ionization amounts, a calculation at $T_e = 160eV$ has been performed in both cases $T_i = 300K$ and $T_i = 160eV$ corresponding to $\overline{Z} = 9.55$ and $\overline{Z} = 8.99$, respectively. The results are presented in fig. 5.

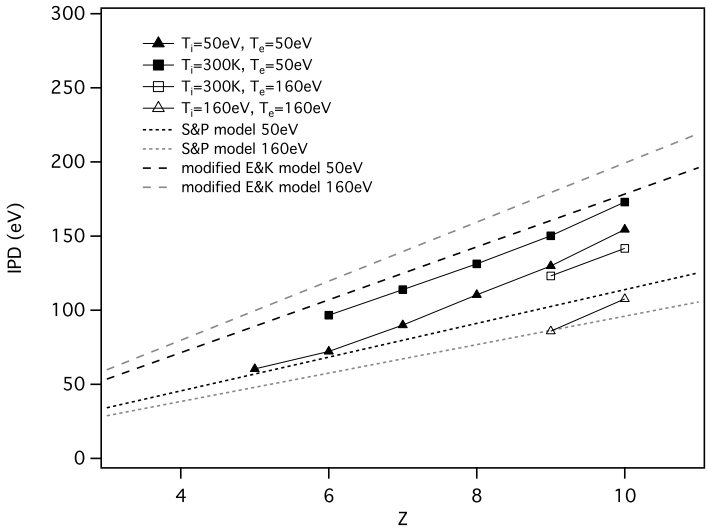

Figure 5. Comparisons of IPD simulation results with models for two different electronic temperatures.

When the electron temperature increases to $T_e = 160eV$ two points have to be considered. First, the plasma composition is modified as confirmed by the increasing $\bar{Z}$. $Z = 9$ and $Z = 10$ are the only data available through sampling of the IPD. For simplicity, the helium-like and hydrogen-like charge state are not considered in our

model. The corresponding ionization energies are greater than $2000eV$, i.e., more than one order of magnitude than the electron energy. A population of ions reduced to the highest charges has certainly a consequence on the overlapping of the ion wells. However, it should be noted that there is no practical way to determine the ion charge distribution because there is no mean to neatly separate an excited ion, i.e., an ion with a trapped electron, from a bare ion of the same charge. One can only assert that bare ions with $Z < 9$ are almost absent with $T_e = 160eV$. Second, the negative image of the ion structure given by the electrons is blurred in comparison with the case at $T_e = 50eV$. The resulting effect is a net decrease of the IPD as shown in fig. 5. In the same figure one can see that at the highest temperature the increase of the IPD for ions at room temperature is larger than for $T_e = 50eV$. A tentative interpretation of the effect due to faster electrons seems to be a reduced influence of the electrons on ions or in terms of electron screening present in the theoretical models, an increasing of the Debye length λ_D. According to this, it can be noticed that the variation with the temperature is better represented by the SP model than the EK model in which the temperature increase only appears in the value of the $\overline{Z}$.

The electron contributions to the IPD can be analyzed in terms of the electron total energy distributions.

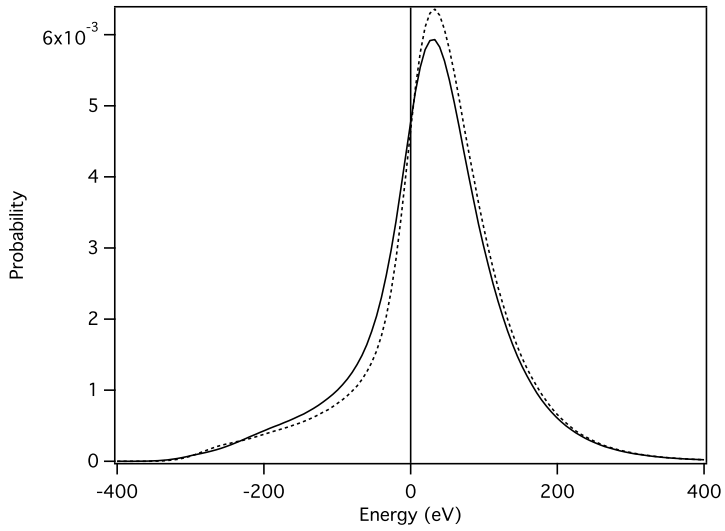

Figure 6. Electron total energy spectra. Continuous line: $T_i = T_e = 50eV$, dotted line: $T_i = 300K$

These distributions roughly measure the population of trapped electrons with negative energy versus the free electron population with positive energy. They allow to estimate the free electron population and therefore the average ion charge $\bar{Z}$. In fig. 6, the energy distributions for the two kinds of plasmas are slightly different. The transfer of a small amount of negative energy electron population to the positive energy region confirms that the ionization is made easier for the plasma with cold ions.

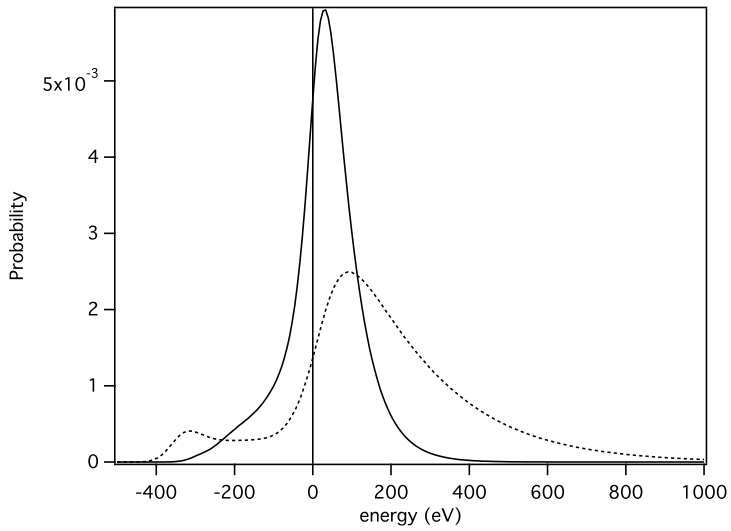

Figure 7. Electron total energy spectra. Continuous line: $T_i = T_e = 50eV$, dotted line: $T_i = T_e = 160eV$

In fig. 7, the electron total energy distribution functions are plotted for both equilibrium cases, $T_i = T_e = 50eV$ and $T_i = T_e = 160eV$. The bump in the negative energy region means that there is a small population of electrons deeply trapped around the highest charge state present at $T_e = 160eV$ around $-350eV$. Within our approach these electrons are the classical equivalent of excited states below ionization occurring for ions with a net charge $Z - 1$. The proportion of positive energy electrons is neatly increased at $160eV$ compared to $50eV$. At the same time, the total electron number in the simulation box itself is also increased in relation with the increase of the mean charge $\bar{Z}$.

Finally in fig. 8, we compare our simulation results with experimental data [3]. Even though considering ions at room temperature improves greatly the comparisons with experiment, some discrepancies remains. In the experiment, the ionization process is dominated by photoionization followed by KLL Auger decay, so, it will only take place in a given ion if the photon energy of the pump lies above that ion's K edge. As a consequence, each experimental point in fig. 8, corresponds to a different pump photon energy and thus to different plasma conditions. In our simulation models, the ionization process is a pure collisional process and each series of points is the result of a unique numerical experiment (all values of the IPD are measured in the same simulated plasma).

4. Conclusion

In this paper, a classical molecular dynamics simulation code, BINGO-TCP, has been used to infer the ionization potential depression in dense plasma at and out of

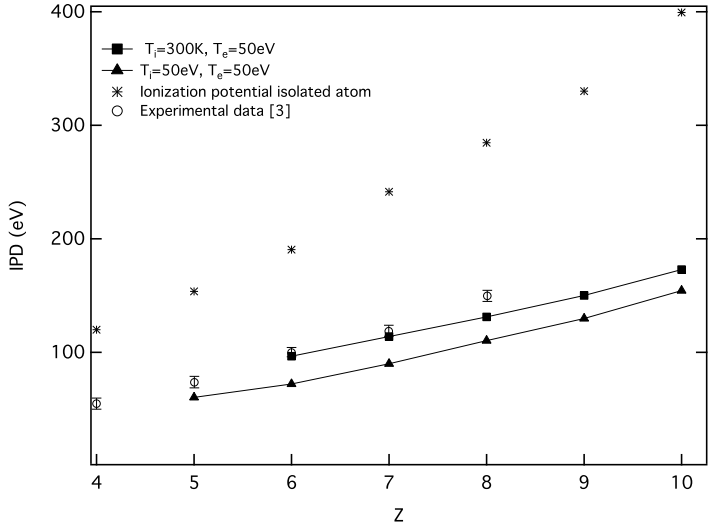

Figure 8. Comparisons with experimental data [3].

equilibrium accounting for the influence of the free electrons and neighboring ions. Thanks to a ionization / recombination process associated to an ad-hoc ion-electron regularized potential, this code developed a few years ago, allows us to simulate neutral systems involving different charge state ions and electrons.

Calculations have been performed at two ionic densities, $n_i = 6 \times 10^{22} cm^{-3}$ and $n_i = 8 \times 10^{22} cm^{-3}$ and two different electronic temperatures, $T_e = 50eV$ and $T_e = 160eV$. Two types of plasmas have been considered, at equilibrium with $T_i = T_e$ and out of equilibrium with $T_i = 300K$.

Our conclusion about the IPD inside an aluminum plasma at solid density reflects the complexity of the problem. For some aspects our study should be considered as preliminary. Our simulations tend to show that the IPD depends not only on the average ion charge but on the relative placement of the ions. This attributes an important role to the ion temperature and suggests that overlapping of the ion wells is a major mechanism in the calculation of the IPD in plasmas.

An electron temperature change induces both a change in the electron adaptation to the ions and a change in the ion charges present in the plasma which in turn plays a role in the ion well overlapping mechanism.

Comparisons with the theoretical models, show that neither Stewart and Pyatt nor the modified Ecker and Kröll (with C taken equals to 1) models are able to reproduced simulations results even though the modified EK model seems to be in better agreement with our results for ions at room temperature. The EK model has been developed for strong coupling plasmas and the SP model provides an answer to the IPD which yields the ion-sphere and the Debye-Hückel results as approximate limits. None of them had been designed to be used in non-equilibrium conditions. As a consequence, nothing in this study allows us to conclude that one or the other of the two models is better or not.

Even though, the simulated plasmas cannot be considered as being exactly in the same conditions as the experimental plasmas, the ionization process being purely collisional, comparisons with experimental data show an overall good agreement.

The model proposed in this work appears as an important tool to provide data for further discussion on IPD models.

references

[1] Stewart J C and Pyatt K D 1966 *Astrophys. J.* **144** 1203.
[2] Ecker G and Kröll W 1963 *Phys. Fluids* **6** 62.
[3] Ciricosta O et al. 2012 *Phys. Rev. Lett.* **105** 065002.
[4] Hoarty D J et al. 2013 *Phys. Rev. Lett.* **110** 265003.
[5] Vinko S M et al. 2014 *Nat. Commun.* **5** 3533.
[6] Crowley B J B 2014 *HEDP* **13** 84-102.
[7] Iglesias C A 2014 *HEDP* **12** 5-11.
[8] Son S K et al. 2014 *Phys. Rev. X* **4** 0311004.
[9] Fletcher L B et al. 2014 *Phys. Rev. Lett.* **112** 145004.
[10] Calisti A, Ferri S and Talin B 2015 *CPP* DOI 10.1002/ctpp.201400087
[11] Vinko S et al. 2012 *Nature* **482** 59-62
[12] Calisti A and Talin B 2011 *CPP* **51** vol 6 524-8
[13] Calisti A et al. 2009 *HEDP* **5** 307.

Annexe D

Warm Dense Matter through Classical Molecular Dynamics.

High Energy Density Physics 13 (2014) 1–8

Contents lists available at ScienceDirect

High Energy Density Physics

journal homepage: www.elsevier.com/locate/hedp

Warm dense matter through classical molecular dynamics

A. Calisti [a, *], S. Ferri [a], M. Marciante [b], B. Talin [a]

[a] Aix-Marseille Université, CNRS, PIIM, UMR7345, Campus Saint Jérôme, 13397 Marseille Cedex 20, France
[b] LASIM, UMR 5579 CNRS/UCBL, Domaine Scientifique de la Doua, Université Claude Bernard Lyon 1, 69622 Villeurbanne Cedex, France

ARTICLE INFO

Article history:
Received 4 July 2014
Accepted 21 July 2014
Available online 30 July 2014

Keywords:
Warm dense matter
Classical molecular dynamics
Dynamic structure factors

ABSTRACT

A classical Molecular Dynamics code has been developed to simulate dense plasmas i.e. neutral systems of interacting ions and electrons. Our goal is to design a tool that relies on a reduced set of microscopic mechanisms in order to obtain solutions of complex time dependent N-body problems and to allow an efficient description of the plasma states between classical high temperature systems to strongly coupled plasmas. Our present objective is an attempt to explore the behavior of such a classical approach for typical conditions of warm dense matter. We calculate the dynamic structure factor in warm dense beryllium by means of our molecular dynamics simulations. The results are then compared with those obtained within the framework of the random phase approximation (RPA).

1. Introduction

The purpose of this work is to investigate the dynamical properties of electrons in warm dense plasmas using classical molecular dynamics techniques. In dense plasmas, electron dynamics is revealed in X-ray Thomson scattering experiments developed to diagnose electron temperature and density, see Ref. [1] and references therein. Schematically, a monochromatic incident X-rays, which can penetrate dense and/or compressed matter, couples to electron density fluctuations and the scattered spectrum shows a central peak surrounded by wings mainly related to the free electron dynamics characteristics. If the length scale of the electron density fluctuations measured in the scattering experiment is larger or shorter than the screening length of the interaction potential of the electrons, the collective or individual behavior of the electrons will be accessed, respectively. Using Thomson scattering as a diagnostic requires a proper theoretical treatment of the dynamic structure factor (DSF) for the interpretation of spectra. There is still ongoing research for cases where the warm dense matter (WDM) occurs, which is a complicated state of matter: electron degeneracy and strong ion–ion coupling mean that neither classical plasma nor solid matter formulations that use the usual approximations satisfactorily apply. In this context, simulation is a reasonable way to predict the scattering spectra.

As other approaches to complexity, e.g., quantum molecular dynamics (QMD), classical molecular dynamics (MD) for two component plasmas (TCP) has to be developed within a framework of constraints and approximations either grounded in theoretical formulations or for the sake of computational feasibility. TCP-MD proposed in this work [2,3], does not make use of the Born–Oppenheimer approximation and relies on a minimum set of microscopic mechanisms implemented into a numerical code designed to obtain numerical solutions of complex time-dependent N-body problems.

The advantage of MD is to allow an efficient description of the transition between classical high temperature systems and strongly coupled plasmas. Conditions at which quantum effects would prevail are not neatly defined. Bellow we choose to explore the transition between classical and partially degenerate plasmas by comparing TCP-MD results with those provided by other numerical and theoretical methods. For this purpose it is necessary to use the same simulation model over the whole density range. For TCP-MD, all the particles considered are point particles, thus the main constraint is the need to choose potentials that avoid the short range collapse of ion–electron pairs. The first advantage of this choice is taken to introduce known ad hoc quantum characteristics of isolated ions, e.g., the ionization energy or the diffusive properties of an ion for colliding electrons. The second advantage is that one gains the ability to describe the ion–electron coupling accounting for mixtures of ions undergoing changes of their ionization stages. Note that the coupling of electrons with radiation is ignored. Within this classical scheme the energy of electrons is continuous. The lowest energy of an electron depends on all the

* Corresponding author.
E-mail addresses: annette.calisti@univ-amu.fr, annettecalisti@gmail.com (A. Calisti).

http://dx.doi.org/10.1016/j.hedp.2014.07.002
1574-1818/

charges including the closest ion. The notion of discrete energy for the ionic excited states is here replaced by its continuous equivalent. Depending on its total energy and its nearest neighbor ion, an electron is either trapped or free.

One postulates that molecular dynamics of a neutral system of ions and electrons with soft potentials, has stable solutions. Ignoring possible numerical drifts, stable here means that inside the simulation cell, temperature and potential energy fluctuate around averages. The way to drive the system into such a state, i.e., to reach a suitable phase space trajectory, is in itself a major problem. The simplest method is to initiate the system into an unequilibrated state then use an empirical procedure that constrains its evolution to approach an equilibrium state. The possibility of using such a procedure takes advantage of TCP-MD, which is designed to follow the evolution of a system of ions and electrons out of equilibrium.

Below the following points will be discussed: First, the simulation model based on approximate charge–charge potentials together with a three-body collisional ionization/recombination mechanism is presented. Second, the technique used to obtain the collective behavior of the free electrons from the TCP-MD is described. Finally, the model and techniques are illustrated for the case of warm dense beryllium.

2. Two component plasma molecular dynamics simulations

Classical molecular dynamics for two component plasmas, i.e., for mixture of interacting ions and electrons has proven useful, see for example [4–6]. It complements QMD to span the whole domain of dense plasmas, from solid to high energy matter. The specificity of the present model relies on the choice of the charge–charge potentials and a mechanism of ionization/recombination allowing one to model systems with ions in variable ionization states. The MD simulations reported below are standard in the sense that a finite number of particles is considered in a cubic cell. The velocity-Verlet algorithm is used to propagate the dynamics. The time step has to be chosen to be sufficiently small enough to allow a proper description of electron motion. This requirement leads to a technical difficulty since the total simulated time necessary to obtain relevant statistics is governed by the mobility of ions of the system. Here we apply periodic boundary conditions to the cubic simulation cell together with the minimal image convention to simulate an infinite system. In the following, several useful statistical data are sampled when the system is considered in a stationary state.

2.1. Soft potentials

The ion–ion and electron–electron interactions are taken to be

$$V_{12}(r) = Z_1 Z_2 e^2 e^{-r/\lambda} \Big/ r \tag{1}$$

where Z_1Z_2 is positive. For practical purposes, the Coulomb interactions have been screened at a distance $\lambda \simeq L/2$, of the order of the cubic cell size L. This screening is compatible with the usual periodic boundary conditions in the MD simulation and given that the interactions between charges introduce a physical screening at much shorter distances, it does not affect any of the properties considered in this work. This point has been checked numerically by increasing the box size. The electron–electron potential does not account for degeneracy. The choice of a repulsive potential that excludes short distance location of particles of the same sign is required to guarantee the exchange of the mechanical energy between positive and negative charges. The electron dynamics investigated is not that of a jellium model [7,8] and, thus, has to account for the ion potential wells.

In contrast, electron-ion interactions are attractive and therefore configurations involving electron-ion distances of the order of the de Broglie wavelength or shorter have to be considered. At such distances, the Coulomb interaction must be regularized. A standard regularized potential is as follow [9],

$$V_{\mathrm{ie}}(r) = -Z_{\mathrm{i}} e^2 \left(1 - \mathrm{e}^{-r/\delta}\right) \mathrm{e}^{-r/\lambda} \Big/ r \tag{2}$$

where δ is the short range regularization parameter. Regularization provides well-defined classical physics for opposite sign charge systems, and allows application of the N-body methods of classical statistical mechanics.

A great deal of work on plasmas has been performed with the help of pseudo potentials [9–11]. Owing to the temperature and density domain considered in the present work, the choice of a potential is guided by the study of the evolution of ion charge populations. For this purpose, δ depends on the instantaneous ionization state in order to fit the ionization energies of the various ion stages. This choice would not be suitable for electron temperatures much higher than the highest ionization energy, leading to a plasma of fully ionized ions and electrons. In a potential given by Eq. (2) the minimum energy of an electron located at the same position as an ion of charge Z is Ze^2/δ. In what follows, the kinetic energy required to overcome this minimum potential energy, i.e. Ze^2/δ, will be considered as the ionization energy for an electron trapped by an ion of charge Z. In this model, the zero temperature limit is defined as a state where each ion has a unit charge and possesses a single electron located at the bottom of its potential well without relative velocity with respect to the ion.

Other parameters of interest are the average charge–charge distance, $r_0 = (3/4\pi n)^{1/3}$, defined in terms of the charge density n, the electron thermal velocity $v_0 = (k_{\mathrm{B}}T_{\mathrm{e}}/m_{\mathrm{e}})^{1/2}$, the ion coupling constant $\Gamma = <Z>^2 e^2/r_0 k_{\mathrm{B}}T$ where $<\ >$ is an ensemble average, the thermal de Broglie wavelength $\Lambda_{\mathrm{e}} = h/(2\pi m_{\mathrm{e}} k_{\mathrm{B}} T_{\mathrm{e}})^{1/2}$, the Debye length $\lambda_{\mathrm{D}} = (k_{\mathrm{B}}T_{\mathrm{e}}/4\pi n_{\mathrm{e}} e^2)^{1/2}$ and the electron degeneracy parameter $\Theta_{\mathrm{e}} = 2m_{\mathrm{e}}k_{\mathrm{B}}T_{\mathrm{e}}/\hbar^2(3\pi^2 n_{\mathrm{e}})^{-2/3}$. Molecular dynamics simulations of two component plasmas (TCP-MD) are carried out using N electrons and N/Z_{i} ions. The chosen simulation protocol implies that the electronic density is a fluctuating quantity.

2.2. Collisional ionization recombination protocol in classical MD

Usual collisional models [12] for ionization/recombination in plasmas assume that electrons follow well-defined trajectories given by their impact parameter and their velocity. Averages are performed to calculate the ionization and recombination rates and the resulting equilibrium ion charge distributions. This approximation cannot be considered as relevant for dense plasmas for which the notion of binary electron–ion collision becomes inappropriate. On average, for a neutral plasma there are Z_{i} electrons per ion and both the trajectory and the energy of an electron are nonlinear functions of all surrounding charges. In an attempt to describe multi-collisional processes in dense plasmas, we recently developed more suitable concepts practical to MD simulations. The notion of a shell has been introduced to characterize the near plasma environment of ions. The shell belonging to a particular ion is composed of its two nearest neighbor electrons, denoted first nearest (*FNe*) and second nearest (*SNe*) electron. During a time step $[t_{\mathrm{i}}, t_{\mathrm{i}} + \delta t]$, depending on the local configuration space of the plasma (mutual nearest neighbors criterion between the ion and its *FNe*) and on the total energy of the two neighbor electrons, the shell is labeled hot, cold or inactive. The electron total energy criterion

takes into account the whole complexity of the potential energy surface around the ion including the ionization energy lowering at a local level due to the surrounding charges.

A hot shell around one ion starts an ionization process of this ion while for a cold shell a recombination of the *FNe* electron occurs. This means that during the time step $[t_i, t_i + \delta t]$, an electron appears or disappears and the ion charge increases or decreases by one unit. After this instantaneous event all the involved particles continue evolving according to dynamics of the simulation. In this way an electron appearing at the same place as the ion at the time of an ionization process, is progressively accelerated by its surrounding environment, increasing during this time its potential energy. Another discontinuous event applied to the same ion is prohibited for the time it takes for an electron to cross a distance equal to the de Broglie wavelength. This delay is intended to account for time uncertainty of the ionization process beginning. The recombination process follows the same scheme, i.e., an instantaneous event where an electron disappears and the ion charge decreases by one. The kinetic energy loss of the recombining electron is transferred to the *SNe*. Then, the process is completed by an energy redistribution among the remaining charges within the normal simulation process. The actual ionization or recombination of an ion lasts until a new ionization or a recombination becomes allowed.

Two remarks have to be made: First, the particular forms of the chosen interaction potentials do not allow the conservation of the total energy during the collisional ionization/recombination process. This leads to non-negligible energy drift during the equilibration step of the simulation, when all thermodynamic properties, as well as the mean ion charge, are far from equilibrium. During this initial step the system is driven toward equilibrium using a thermostat and is not supposed to be used for any measurements. Once the system has reached an equilibrium state, the ionization and recombination rates become equals and the effect of the process reduces to small residual energy fluctuations. At the same time, the happening of the process become far less frequent than it was in the equilibration step. Second, this imperfect mechanism allows an efficient evolution of the initial non equilibrated ion–electron system towards equilibrium.

2.3. Statistical data

In order to extract statistical information from the simulated system a few distributions and time-dependent functions are calculated. These data allow one to check the system behavior as well.

The pair correlation functions carry information about the system structure, i.e., the way charges are statistically located with respect to the other ions. These functions are often interpreted in terms of screening mechanisms as an ionic system built with screened forces between ions can have a similar structure than the one obtained from TCP simulation. Hereafter, the ionic pair correlation functions are compared to those provided by finite-temperature density functional theory molecular dynamics (FT-DFT-MD) simulations [13] and by screened Coulomb one component plasma (Yukawa OCP) simulations. FT-DFT-MD simulations, or ab initio simulations, aim to describe fully interacting quantum systems. They include ionic correlations as well as the quantum behavior for the electrons. In the Yukawa model, only the ions are explicitly considered, and the electrons are treated as a polarizable background. The Yukawa potential is then given by:

$$V_{ii}(r) = \frac{Z_i^2 e^2}{r} \mathrm{e}^{-\kappa r} \tag{3}$$

To describe the partially degenerate electrons in WDM, the inverse screening length κ should be calculated by $\kappa^2 = (4e^2 m_e/\pi\hbar^3) \times \int dp f_e(p)$ with $f_e(p)$ the Fermi distribution. With this definition, the Thomas–Fermi screening length is given by $\lambda_{TF} = \sqrt{k_B T_F/6\pi n_e e^2}$ with $T_F = \hbar^2(3\pi^2 n_e)^{2/3}/2k_B m_e$. In the following, the two limiting cases corresponding to the classical Debye–Hückel law and Thomas–Fermi screening are presented.

It can be seen in Fig. 1 that our model reproduces rather well the interparticle spacing and the maximum in the distribution. The Yukawa model, which treats the electrons within linear response, underestimates ion–ion repulsion at small distances. It can be also noticed that our model reproduces qualitatively the results obtained with "FT-DFT-MD". The remaining differences, which appear to be of the same order as the differences between the two OCP models, could be attributed to the fact that we neglect any electron degeneracy effects.

The velocity distribution functions of each kind of particles in a pure classical TCP without ionization/recombination protocol is Maxwellian. In this work, the electron velocity distribution function is non-Maxwellian as ionization/recombination generates excited electrons with non-thermal velocities. When the electronic temperature decreases, it would be necessary to take into account the Pauli exclusion principle that gives rise to a Fermi-Dirac distribution instead of a Maxwell–Boltzmann one. This is not done here and the consequences will be commented on in Sec. 3. The electron energy distribution function is plotted in Fig. 2. The distribution function of negative energies is associated with trapped or free slow electrons. Associated to the knowledge of total number of electrons in the simulation box, this function allows us to estimate the density of free electrons in our simulations. Moreover, the formation of the negative wing helps to follow the evolution of the TCP system towards stability.

Considering a binary system reduced to a single electron bounded in the potential well of an ion i of charge Z_i, the minimum electron potential energy is the ionization energy parameter E_i of the model. If a second ion j of charge Z_j is added to this system, provided the inter-ion distance is small enough, the energy barrier seen by the electron to escape the potential of ion i will be significantly lowered in the direction of ion j. Similar reasoning holds if one adds an electron instead of an ion to the binary system, and this leads to a lowering of the potential well seen by the bound electron in the opposite direction of the additional electron. In this way, the model naturally describes the ionization energy as a function of the local configuration of charges, which statistically results in an ionization potential lowering.

The dynamic behavior of the free electrons can be investigated through the density–density dynamic structure factor (DSF). It is given by:

$$S\left(\vec{k},\omega\right) = \frac{1}{2\pi N} \int_{-\infty}^{+\infty} e^{i\omega t} < \rho\left(\vec{k},t\right)\rho\left(-\vec{k},0\right) > \mathrm{d}t \tag{4}$$

$$\rho\left(\vec{k},t\right) = \sum_{i=1}^{N} e^{i\,\vec{k}\cdot\vec{r}_i(t)} \tag{5}$$

The DSF is related to the dielectric function $\varepsilon(\vec{k},\omega)$ via the fluctuation–dissipation theorem (FDT):

$$S\left(\vec{k},\omega\right) = \frac{\hbar k^2 \mathrm{Im}\varepsilon^{-1}\left(\vec{k},\omega\right)}{n4\pi^2 e^2\left[1-e^{-\beta\hbar\omega}\right]} \tag{6}$$

This function does not possess any symmetry and satisfies the detailed balance relation, $S(-\vec{k},-\omega) = e^{-\beta\hbar\omega} S(\vec{k},\omega)$.

In classical MD simulations, identifying the Heisenberg operator $\vec{r}_i(t)$ with the position of the ith particle, we get:

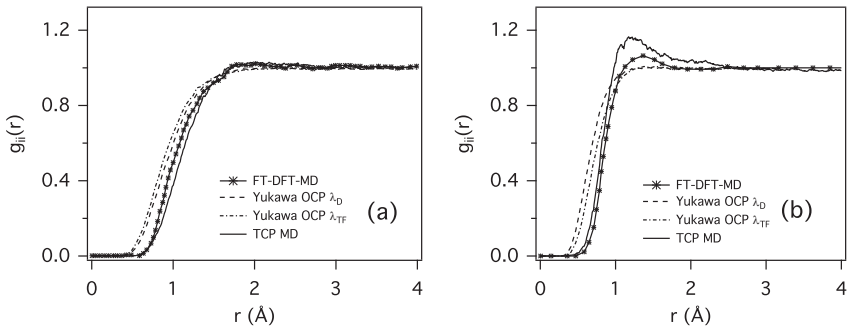

Fig. 1. Ion–ion pair distribution functions in warm dense beryllium at (a): $\rho_0 = 1.85$ g/cm^{-3} and $T_e = T_i = 12$ eV and (b): $\rho_0 = 5.5$ g/cm^{-3} and $T_e = T_i = 13$ eV. The ion charge states (for the Yukawa OCP simulation) are $Z = 2.17$ and $Z = 2.24$ for (a) and (b), respectively.

$$R\left(\vec{k},\omega\right) = \frac{k^2}{n4\pi^2 e^2 \beta\omega}\mathrm{Im}\varepsilon^{-1}\left(\vec{k},\omega\right) \tag{7}$$

This function reveals the electron density fluctuations on a length scale given by $\lambda_{scat} = 2\pi/k$ with $k = \left|\vec{k}\right|$.

The dimensionless scattering parameter, $\alpha = 1/k\lambda_s$ which compares λ_{scat} with the screening length λ_s is defined to characterize the scattering regime. At $\alpha > 1$, in the collective scattering regime, the density fluctuations at a scale larger than the screening length are probed, while at $\alpha < 1$, in the non-collective scattering regime, the density fluctuations of individual electrons are resolved. Depending on the scattering regime, the scattered spectra show Compton or plasmon features that are related to individual or collective charge properties, respectively.

As an example, we have plotted in Fig. 3, the R function corresponding to the density fluctuation of the free electrons in a Be plasma at $\rho_0 = 1.85$ g/cm^{-3} and $T_e = T_i = 12$ eV. It can be seen that the behavior of the R function versus α reproduces correctly the description given in Ref. [14]. For $\alpha > 1$ the function presents two symmetric well pronounced maxima and as α decreases, the dip between the two maxima is progressively filled to reach a Gaussian shape at $\alpha = 0$.

The DSF, $S(\vec{k},\omega)$, (see Fig. 4) is related to the R function by:

$$S\left(\vec{k},\omega\right) = \frac{\hbar\beta\omega}{1-\mathrm{e}^{-\hbar\beta\omega}}R\left(\vec{k},\omega\right) \tag{8}$$

which approximates Eq. (6) assuming that the main quantum effects are due to the detailed balance.

The DSF as the basic input for the Thomson scattering cross-section is directly related to the spectrally resolved X-ray Thomson scattering measurements [1] which are widely used as diagnostics to infer dense plasma parameters such as electronic density and temperature. A more detailed analysis of our results is provided in Sec. 3 for conditions corresponding to two recent experiments performed on beryllium [15,16].

3. Application to beryllium

For a few years, the behavior of warm dense beryllium has been an issue of interest from both a theoretical and experimental point of view [15–20,13]. The recent possibility to carry out comparisons with different approaches motivates our interest to develop a pure classical investigation based on classical MD. TCP MD provides straightforward access to electron dynamics and the possibility to observe free electron plasmons for the interpretation of Thomson scattering experiments. Two WDM conditions have been investigated so far, labeled in literature as the un-compressed and compressed beryllium with the density and temperature conditions; $\rho_0 = 1.85$ g/cm^{-3} and $T_e = T_i = 12$ eV and $\rho_0 = 5.5$ g/cm^{-3} and $T_e = T_i = 13$ eV, respectively. The comparisons rely on the dynamic structure factor of free electrons $S_{ee}(\vec{k},\omega)$.

Warm dense matter conditions result in a de Broglie wavelength of the order of the average distance between particles. This often motivates the implementation of a regularized electron–electron potential intended to represent electron–electron exchange in numerical simulations. With our ionization/recombination protocol, this model leads to unphysical results. With a large regularization length all the electrons become uncoupled. The strong ion–electron coupling is no longer in competition with the electron–electron coupling for those electrons falling into the ion

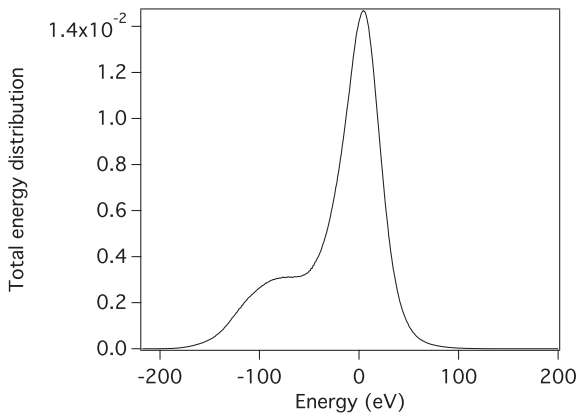

Fig. 2. Electron energy distribution for a beryllium plasma at $\rho_0 = 1.85$ g/cm^{-3} and $T_e = T_i = 12$ eV.

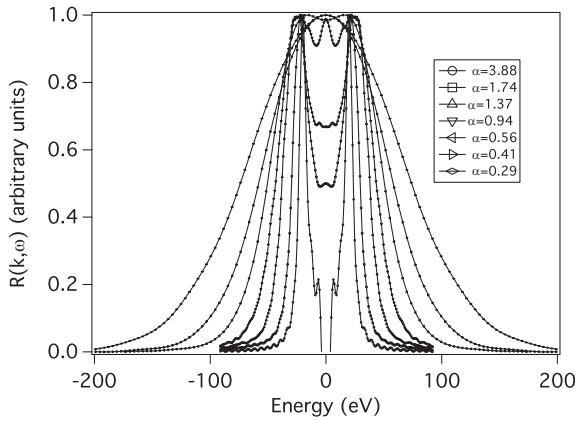

Fig. 3. R Function for different values of the scattering parameter and for the same conditions as Fig. 2.

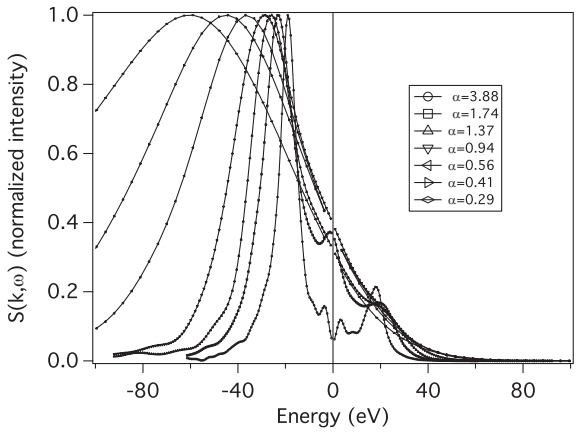

Fig. 4. Structure factor, S, for different values of the scattering parameter and for the same conditions as Fig. 2.

potential wells. Charge coupling insures the mechanism of energy exchange between particles and leads to plasma simulations that reach equilibration to a stable state.

3.1. Un-compressed beryllium

Here, the TCP MD results are presented for plasma conditions corresponding to those of the first observation of plasmons in solid-density plasmas [15]. The mass density is $\rho_0 = 1.85$ g/cm^{-3} and the temperature is set to 12 eV in accordance with the theoretical best-fit of the experimental data provided by authors. The experiment was designed to observe collective x-ray forward scattering spectra at an average scattering angle of $\theta = 40^\circ$ with the probe wavelength $\lambda_0 = 0.42$ nm. In the nonrelativistic limit and for small momentum transfers, the wave vector $\vec{k}$ is related to the scattering angle through:

$$k = \left|\vec{k}\right| = \frac{4\pi}{\lambda_0}\sin(\theta/2) \tag{9}$$

where λ_0 is the wavelength of the incident wave. For MD simulations performed in a cubic box of side L, due to periodic boundary conditions, $\vec{k}$ must satisfy:

$$k_{x,y,z} = n_{x,y,z}\frac{2\pi}{L} \tag{10}$$

where $n_{x,y,z}$ is an integer number. In this work, the DSF has been calculated for different values of k in order to span the values of $\alpha = 1/k\lambda_D$ from 0.2 to 3.88, from non collective to collective scattering regimes. The smallest value of k reachable in our simulation is determined by the highest number of simulated particles N (constraining L through the plasma mean density N/L^3) allowing one to keep the simulations performed to a reasonable time.

According to these constraints, TCP-MD simulations have been performed with 220 atoms of beryllium. We started the simulations with an electronic density corresponding to a mean charge $Z_b = 2$. After an equilibration step controlled by imposing a temperature of 12 eV, we ensure that an equilibrium state has been reached by checking the stationarity of the total energy and charge distributions. The equilibrium state is reached for $n_e = 2.68 \times 10^{23}$ cm^{-3} and $Z_b = 2.17$. This corresponds to charge coupling parameters $\Gamma_e = 1.25$ and $\Gamma_i = 4.53$ for electrons and ions respectively, and a degeneracy parameter $\Theta_e = 0.79$. These values, $\Gamma_{i,e} > 1$ and $\Theta_e < 1$ indicate that the plasma statistical data should show strong correlation and degeneracy effects. The free electron DSF obtained by TCP-MD is plotted in Fig. 5(a) and (b) for $\alpha = 3.88$ and $\alpha = 0.65$ respectively. They are compared with those obtained in the same way by OCP MD simulations in which only interacting electrons are considered and with the random phase approximation (RPA) calculations in which the dielectric function is calculated for a one component plasma of free electrons without interactions [21]. As the TCP-MD simulations are classical simulations, the RPA results in the classical limit are also plotted for comparisons. The DSF plotted in Fig. 5(a) corresponds to free electron density fluctuations in the collective scattering regime and is mainly affected by correlations and collective effects. It can be seen that the plasmon peak obtained by TCP-MD is much wider and shifted to slightly lower frequencies than those obtained by RPA. At this value of α, degeneracy effects are negligible (the differences between RPA and RPA in the classical limit results are small). The main differences between the RPA calculations and MD simulations concern interactions between charges which results in a broadening and shift toward the low frequencies of the plasmon peak. These effects concern the electron–electron interactions (compare RPA results with interacting electron OCP simulation) and are strongly enhanced accounting for ion–electron interactions (TCP-MD results). Similar results have already been obtained previously in Ref. [13].

In contrast, for $\alpha = 0.65$, the DSF displayed in Fig. 5(b) is measured in the non-collective scattering regime and accesses the properties of individual electrons as the shape of the DSF reflects the velocities of the electrons in the direction of the scattering vector $\vec{k}$. This will permit one to evaluate the importance of the electron degeneracy effects. It can be seen that our result differs from the RPA calculation due to the presence of degenerate electrons. The RPA calculation in the classical limit agrees very well with our results. The effects of interactions between charges begin to be negligible.

3.2. Compressed beryllium

The results presented in this section correspond to observations of both the inelastic Compton and plasmon scattering spectra from shock-compressed dense matter [16]. The mass density is $\rho_0 = 5.5$ g/cm^{-3} and the temperature is 13 eV. In the experiment, two scattering angles were chosen to probe the density fluctuations in both scattering regimes, i.e., the collective regime with $\theta = 25^\circ$ and non-collective regime with $\theta = 90^\circ$. The probe wavelength here is 0.2 nm.

In order to fulfill Eqs. (9) and (10) with small enough values of k, the TCP-MD simulations have been performed with 200 atoms of beryllium. We started the simulations with a temperature of 13 eV and an electronic density corresponding to a mean charge $Z_b = 3$. After the equilibration phase, we reached an equilibrium state with the parameters: $n_e = 8.21 \times 10^{23}$ cm^{-3} and $Z_b = 2.24$. This corresponds to charge coupling parameters $\Gamma_e = 1.67$ and $\Gamma_i = 6.41$ for electrons and ions, respectively, and a degeneracy parameter $\Theta_e = 0.41$.

Here again, it can be seen in Fig. 6(a) that the plasmon peak location and width are modified by the density effects. Fig. 6(b) clearly demonstrates that the electron are mainly degenerate and thus our model is not appropriate to simulate this case with $\Theta_e = 0.41$ and $\alpha < 1$.

4. Discussion

For a better understanding of the different results, an analysis of the maximum position ΔE of $S_{ee}(k,\omega)$ as a function of k has been performed.

We recall that for $\alpha < 1$, the density fluctuations of individual electrons are resolved and the Compton down-shifted spectrum is

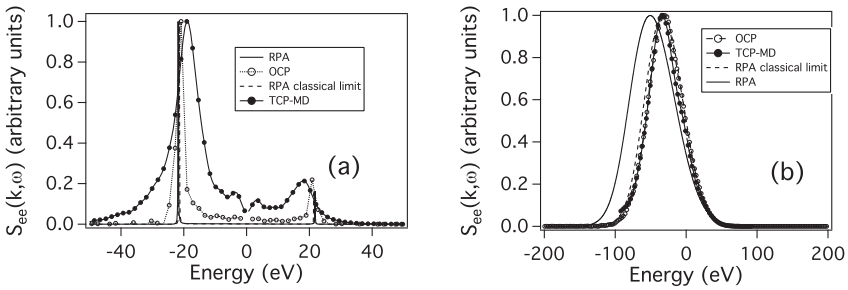

Fig. 5. Dynamic structure factor for (a): $\alpha = 3.88$ and (b): $\alpha = 0.65$ plotted for $n_e = 2.68 \times 10^{23}$ cm^{-3} and $T_e = 12$ eV.

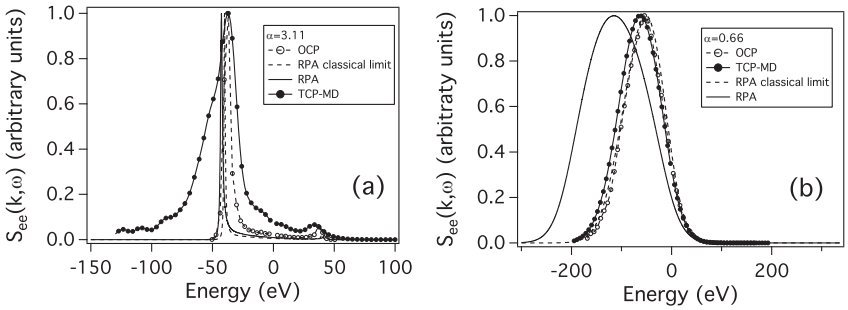

Fig. 6. Dynamic structure factor for (a): $\alpha = 3.11$ and (b): $\alpha = 0.66$ plotted for $n_e = 8.21 \times 10^{23}$ cm^{-3} and $T_e = 13$ eV.

observed. In a nondegenerate plasma, the Compton scattering spectrum will reflect a Maxwell–Boltzmann distribution, providing a measure of the electron temperature whereas for degenerate plasma, the Compton spectrum will reflect a Fermi distribution.

For $\alpha > 1$, one has access to the collective regime and to the plasmon scattering features. For a classical collisionless plasma an expression for the plasmon dispersion has been given by Bohm and Gross [22]:

$$\omega_{BG}^2 = \omega_{pe}^2 + \frac{3k_B T_e}{m_e} k^2, \tag{11}$$

with $\omega_{pe} = \sqrt{4\pi n_e e^2/m_e}$, the electronic plasma frequency. This relation has been obtained by expanding the dielectric function to second order in k for a classical Maxwell–Boltzmann ideal plasma. In order to extend the range of applicability to higher wave numbers and higher densities (or lower temperatures), a modified Bohm–Gross dispersion relation including electron quantum diffraction effects has been proposed [17]:

$$\omega_{BGmod}^2 = \omega_{pe}^2 + \frac{3k_B T_e}{m_e} k^2 \left(1 + 0.088 n_e \Lambda_e^3\right) + \left(\frac{\hbar k^2}{2m_e}\right)^2. \tag{12}$$

These relations do not account for particle interactions. Their range of applicability is restricted to small k where the interactions between particles are predominant. In our model, all the interactions between particles are taken into account but as noted in the previous section, degeneracy effects are missing. Using the same idea as for the modification of ω_{BG} and assuming that the differences between the RPA and RPA in classical limit are all due to degeneracy effects, we propose a modification of our pure classical results obtained with TCP-MD that combines the consideration of interactions between all particles and the effects of degeneracy. In practical terms, the difference between the two curves representing the maximum position of $S_{ee}(k,\omega)$ calculated in the RPA and the RPA in the classical limit models has been fitted by a polynomial function, $P(k)$, of the variable k. This polynomial function thus captures the effects of electron degeneracy, and the TCP-MD results have been modified as follows:

$$\Delta E_{TCP-MDmod}^2 = \Delta E_{TCP-MD}^2 + P(k)^2. \tag{13}$$

Comparisons of the results obtained by TCP-MD with RPA and RPA in the classical limit results and pure electron OCP simulations are plotted in Fig. 7 and in Fig. 8 for un-compressed and compressed cases, respectively.

Comparing the results obtained with pure classical models, it can be seen in Fig. 7 that the positions of the plasmon peaks in the TCP-MD and in the OCP are shifted towards lower frequencies relative to the RPA in the classical limit due to interactions between particles. For large k (small α), both RPA and simulations yield almost the same location for the maximum peak of the Compton spectrum. Here the non-collective regime has been reached and the Compton spectrum reflects the thermal electronic motion.

When the degeneracy effects are accounting for, RPA (empty triangles and long dashes) and modified TCP-MD (black squares and full line) differ at low k due to the strong influence of particle interactions, but they give similar results as soon as $1/k\lambda_{TF} < 1$.

Finally, for sake of completeness, we have plotted in Fig. 7 the maximum position of the plasmon peak (diamond) measured in the un-compressed beryllium experiment [15].

Similar results have been obtained for the compressed beryllium conditions. The results are plotted in Fig. 8. Owing to the fact that the parameter α does not span exactly the same range of values as previously, similar behavior is observed comparing the different results obtained with pure classical models. The maximum peak values obtained with the modified TCP-MD compare very well with the data points measured in the compressed beryllium experiment [16] plotted again for completeness.

To summarize, a two-component plasma classical molecular dynamics simulation code has been applied to calculate free electron dynamic structure factors for beryllium in warm dense matter conditions. The ionic structure properties compare well with results obtained with finite temperature density functional theory

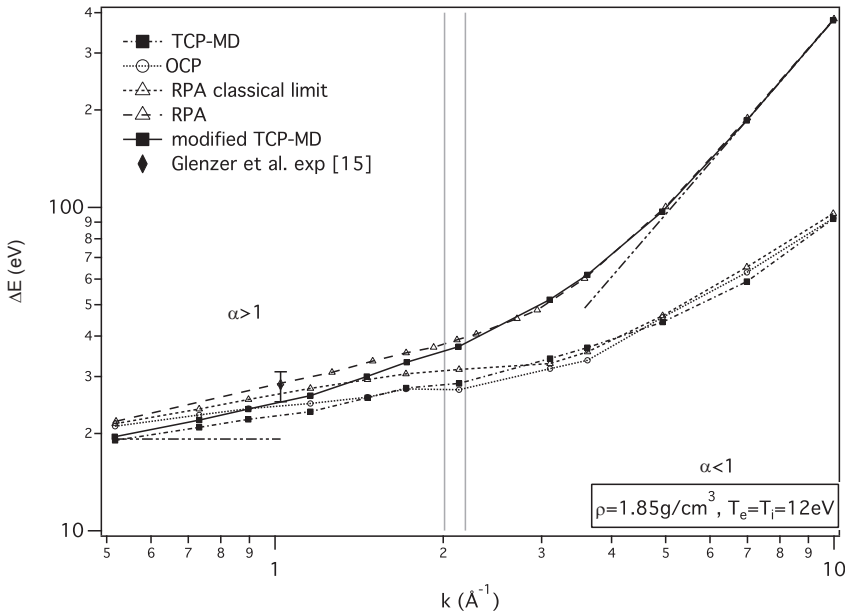

Fig. 7. Maximum position ΔE of $S_{ee}(k,\omega)$ as a function of k for the un-compressed case conditions. The vertical gray lines show from the left to the right, the positions of the inverse of λ_D and λ_{TF}, respectively. The two dash-double dot lines at small and large k show the two asymptotes.

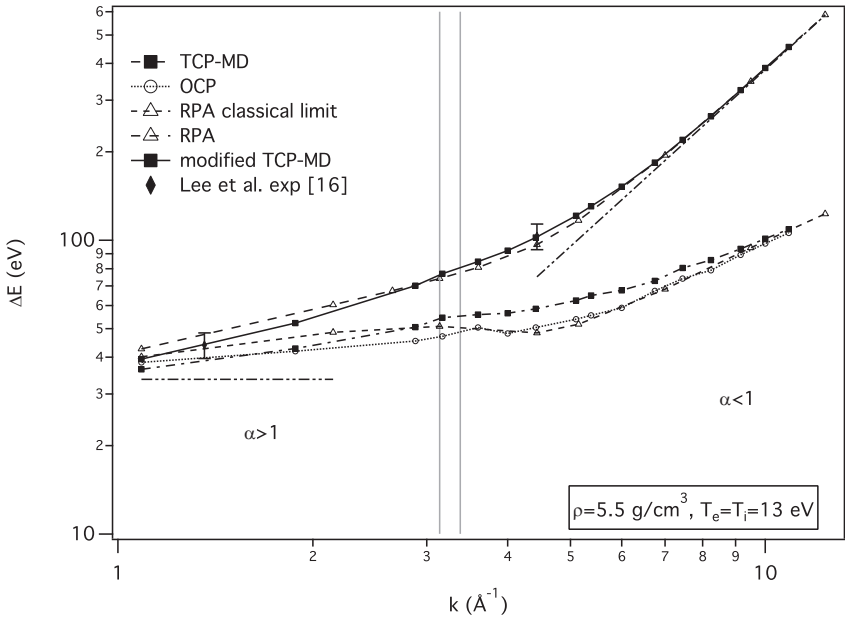

Fig. 8. Same as Fig. 7 for the compressed case conditions.

molecular dynamics and also compare well with the ionic mean charge and thus the electronic density. Concerning the electron dynamic properties, to neglect the degeneracy effects is a weakness of this model. When the scattering wavelength is such that the α parameter is much larger than unity, the electron degeneracy effects are negligible and our results are useful to investigate the role of interactions between particles and how these affect the position of the plasmon peak and the broadening of the structure factor. In order to extend the range of applicability of our results, a modification of the relation that gives the position of the maximum peak of the DSF has been proposed to keep the benefit of the classical MD while including the effects of electron degeneracy, which is important as estimates for the peak position are useful for plasma diagnostics.

References

[1] S.H. Glenzer, R. Redmer, Rev. Mod. Phys. 81 (2009) 1625 (39).
[2] A. Calisti, S. Ferri, B. Talin, HEDP 5 (2009) 307.
[3] A. Calisti, B. Talin, Contrib. Plasma Phys. 51 (6) (2011) 524–528.
[4] J.P. Hansen, I.R. McDonald, Phys. Rev. A 23 (1981) 2041.
[5] A.V. Filinov, et al., Phys. Rev. E 70 (2004) 046411.
[6] A. Calisti, et al., HEDP 7 (2011) 197–202.
[7] W.D. Kraeft, D. Kremp, W. Ebeling, R. Röpke, Quantum Statistics of Charged Particle Systems, Akademie-Verlag, Berlin, 1986.
[8] S. Ichimaru, Statistical Plasma Physics: I. Basic Principles, Addison-Wesley, Reading, 1992. Statistical Plasma Physics II: Condensed Plasmas, Addison-Wesley, Reading, 1994.
[9] H. Minoo, M.M. Gombert, C. Deutsch, Phys. Rev. A 23 (1981) 924.
[10] F.J. Rogers, Phys. Rev. A 23 (1981) 1008–1014.
[11] C.S. Jones, M.S. Murillo, HEDP 3 (2007) 379–394.
[12] I.I. Sobelman, L.A. Vainstein, E.A. Yukov, Excitation of atoms and broadening of spectral lines, in: V.I. Goldanskii, et al. (Eds.), Springer Series in

Chemical Physics, vol. 7, Springer-Verlag Berlin Heidelberg, New-York, 1981.
[13] K.U. Plagemann, et al., New J. Phys. 14 (2012) 055020.
[14] E.E. Salpeter, Phys. Rev. 120 (1960) 1528.
[15] S.H. Glenzer, et al., Phys. Rev. Lett. 98 (2007) 065002.
[16] H.J. Lee, et al., Phys. Rev. Lett. 102 (2009) 115001.
[17] R. Thiele, et al., Phys. Rev. E 78 (2008) 026411.
[18] K. Wünsch, J. Vorberger, D.O. Gericke, Phys. Rev. E 79 (2009) 010201(R).
[19] V. Schwarz, et al., HEDP 6 (2010) 305.
[20] J. Ye, B. Zhao, J. Zheng, Phys. Plasmas 18 (2011) 032701.
[21] N.R. Arista, W. Brandt, Phys. Rev. A 29 (1984) 1471.
[22] D. Bohm, E.P. Gross, Phys. Rev. 75 (1949) 1851.

Annexe E

Microfields in hot and dense hydrogen plasmas

High Energy Density Physics 7 (2011) 197–202

Contents lists available at ScienceDirect

High Energy Density Physics

journal homepage: www.elsevier.com/locate/hedp

Microfields in hot dense hydrogen plasmas

A. Calisti [a,*], S. Ferri [a], C. Mossé [a], B. Talin [a], M.A. Gigosos [b], M.Á. González [b]

[a] PIIM, Université de Provence, CNRS, Centre Saint Jérôme, 13397 Marseille Cedex 20, France
[b] Departamento de Óptica y Física Aplicada, Facultad de Ciencias, Universidad de Valladolid, 47071 Valladolid, Spain

ARTICLE INFO

Article history:
Received 13 April 2011
Accepted 13 April 2011
Available online 22 April 2011

Keywords:
Hydrogen plasmas
Two component molecular dynamics simulation
Screened potential
Electric microfield

ABSTRACT

We present a study of statistical static and dynamic properties of local electric fields in moderately coupled hydrogen plasmas. In this regime new molecular dynamics simulations of neutral hydrogen, protons and electrons are now well controlled. They provide new insight into the statistical properties of the microfield. Taking advantage of such careful MD simulations this work focuses on a new analysis of concepts for the high and low frequency components introduced in the past in several seminal works.

1. Introduction

Study of classical plasmas composed of ions and electrons is a complex N-body problem. In a first approach ions are replaced by quasi-particles (quasi-ions) dressed by electrons so that the original two component plasma (TCP) is reduced to a one-component plasma (OCP) for which the ion–ion forces are modified by the electrons. The ion–electron interaction is approximated by a screening term in the potential resulting from the assumption that *electrons instantaneously adjust about ions* [1]. This efficient simplification is illustrated by several approaches for microfield-property modeling [2–7]. The second approach is based on classical molecular dynamics (MD) designed to account for the entire system of interacting ions and electrons. Comparisons between the two methods gives one the opportunity to discuss the mechanisms of electron screening of ions within the context of an MD simulation and exposes where unphysical effects arise due to the approximation of the TCP by an OCP. The question of screening leads to a discussion concerning the statistical properties of the local microfields where temporal aspects play a crucial role.

This role derives from the necessity to introduce a physical response time for the interpretation of the local field dynamics in terms of fast and slow fluctuations. For its efficiency and its capability to provide temporal analysis, the following discussion will be based on MD techniques. MD is able to treat ions and electrons on the same footing and has been widely used to benchmark models. As a prerequisite it is assumed that MD provides relevant static and dynamic statistical results (See Appendix). Hereafter, the plasma parameter domain will be restricted to the moderately coupled conditions for which MD works well. This study investigates hydrogen plasmas which is the focus of a great deal of interest in various domains of physics: spectroscopy, warm dense matter, high energy physics and nuclear reactions. Further, we note that the "small" proton–electron mass ratio results in a favorable situation for MD simulations.

For TCP simulations, the ion–electron potential must be finite (regularized) at short distances as the Coulomb potential for opposite charges may induce numerical infinities. Several effective semi-classical potentials including quantum corrections have been derived to account for diffraction and symmetry effects in an approximate way [8–11]. However, the potential behavior at short distances has no essential consequences with regard to the conclusions of this work. Once such a regularization is postulated, cf. Eq. (A.1), some inherent features sensitive to the potential depth $V_{ie}(0)$ result, e.g., electrons with temporary negative energy and long-living trapped electron states. Moreover, the regime characterized by a moderate plasma coupling parameter $\Gamma < 1$ is considered and the study focuses on electron density, $N_e \sim 10^{18}$ cm^{-3}, relevant for plasma spectroscopy. An additional high density case, $N_e \sim 10^{26}$ cm^{-3}, corresponding to solar interior is also commented as a generalization to the classical hydrogen plasma. The condition, $\Gamma < 1$, guarantees a small number of long-lived trapped electrons making the interpretation of the simulations more straightforward (See A.3).

* Corresponding author.
E-mail address: annette.calisti@univ-provence.fr (A. Calisti).

1574-1818/$ – see front matter © 2011 Elsevier B.V. All rights reserved.
doi:10.1016/j.hedp.2011.04.003

The discussion below will be based on a statistical analysis of microfields at neutrals or charged points in terms of field distribution and field correlation functions, characterizing the contributions of ions or electrons or both (total). At first we estimate the convergence time θ necessary to reach the statistical average of a stochastic quantity, e.g., the average ionic potential. This will lead to a tentative definition of screening of ions by electrons connected to time. In the second step, the dynamic and static properties of the ionic and the electronic constituents will be used separately to discuss the signature of screening mechanisms in hydrogen plasmas. Finally, the use of a simple filtering technique, accounting for a given response time, intended to get ride of the mixing of the fast and the slow stochastic processes that compose the total microfield, will lead to the conclusive remarks.

2. Statistical averages

Molecular dynamics is designed to obtain time sequences of quantities, e.g., the total electric field at neutral or charged points. These continuous time sequences are attached to individual particles. The plasma, as described by MD, is invariant in time so, the notion of time makes sense only at a local level. First, we carry out an ideal numerical experiment. It is intended to provide some examples of time averaging performed with MD techniques and provides guidelines for further discussion. A fixed positively charged impurity (infinite mass limit) imbedded into an electron plasma is placed at the point P_0. The total electric field $E(t) = E_i + E_e(t)$ at a distinct fixed point P_1 is a function of time accounting for all charges present in the simulation cell. Statistical analysis of the field at P_1 is performed using $E(t)$ supposedly known on $[0,\infty]$. For instance the time average

$$< E > \lim_{T\to\infty} \frac{1}{T}\int_0^T E(t)\mathrm{d}t \equiv \lim_{T\to\infty} \overline{E}(T) \qquad (1)$$

is a non null vector in the direction $P_0 \to P_1$. A study of the convergence of the temporal average (actually a discrete sum based on time steps) allows one to estimate what field history length is required to reach a given precision in Eq. (1). There are some simple features and definitions associated with the modeling of statistical data. Static averages, e.g., $< E >$ at P_1 can be obtained using a Monte Carlo simulation while time properties are necessarily investigated through statistical sampling of local time histories. The average electric field in Eq. (1) versus the distance of P_0 to P_1 is usually approximated by the derivative of a screened Coulomb potential. Collective charge couplings are often referred to in terms of screening effects.

If P_0 and P_1 are free to move in the plasma, $< E >$ vanishes. Non null partial time averages of $E(t)$ will be useful to separate the slow variation induced by the relative motion of P_0 and P_1 from the fast one due to electrons. Such limited time average taken on a test particle will be called, for practical purposes, a local average. A statistical average, hereafter noted $< .. >$, exploiting the whole field history measured at P_1 will be referred to as a statistical or global average. For instance, the field modulus distribution at P_1 or the pair correlation function are available by sampling the whole system evolution using a set of statistically independent data extracted from the field history. In the same way, time properties, e.g., field correlation functions or velocity correlation functions are investigated by averaging functions of time defined on finite time intervals. In Eq. (1) the statistical average is written as the limit of local averages, for times going to infinity. For MD, samplings based on a unique neutral or charged test point are difficult to deal with. When N independent measurement points can be used, e.g., in two component plasmas, the numerical cost to obtain statistical properties decreases by a factor N.

3. Moderate density regime

The moderate density regime corresponds to astrophysical or laboratory hydrogen plasmas mainly observed by spectroscopic means. The density temperature domain considered here is close to warm dense matter regime. The conditions of the present study are appropriate for molecular dynamics investigations.

3.1. Characteristic lengths

For the density condition considered hereafter, $N_e = 4\times10^{18}$ cm^{-3} and $T_e = 20000$ K, the plasma coupling parameter $\Gamma = e^2/r_0 k_B T_e$ equals 0.2 where r_0 is the mean electron–electron distance $r_0 = (3/4\pi N_e)^{1/3}$. The usual Debye length $\lambda_D = \sqrt{k_B T_e/4\pi N_e e^2}$ is $\lambda_D \sim 1.25 r_0$, the potential regularization length associated with 1 Rydberg (see the second approach in A.1) is $\delta = 0.027 r_0$ and the regularization length of the first approach Eq. (A.2) is $\delta' = 0.021 r_0$. Thus, for these plasma conditions both approaches are similar.

3.2. Characteristic times

A useful dynamic timescale $\tau_e = r_0/v_{th}$ is the time spent by an electron with the thermal velocity $v_{th} = (k_B T_e/m_e)^{1/2}$ to cross over the average electron–electron distance r_0. It is interpreted as the average time for the electron system to lose correlation with an initial electron configuration. For the present simulations, the time step $dt = 2\times10^{-18}$ s is taken to be: $dt \sim 0.001\tau_e$. The equivalent of τ_e for protons, $\tau_i \sim 40\tau_e$ provides the scaling of the evolution times for the ion motion.

Besides these times associated to the plasma, the interval of time T in Eq. (1), is a physical time of interest characterizing the response time of a measurement device imbedded in the plasma. The global average convergence of Eq. (1) is checked for the case of one fixed ion with charge e. Here, the test particle P_1 is considered as a measurement device with an infinite response time. The evolution versus time in units of τ_e plotted in Fig. 1 for three independent runs of $\overline{E_e}(T)\cdot E_i/E_0^2$, E_0 being the average field produced by a charge e at the average distance r_0, leads to the following qualitative interpretation. For the infinite mass limit all the independent runs, as expected, tend towards the same plateau. The mean electron field and the ion field are opposite. This defines what can be called a screening effect of ions by electrons. The

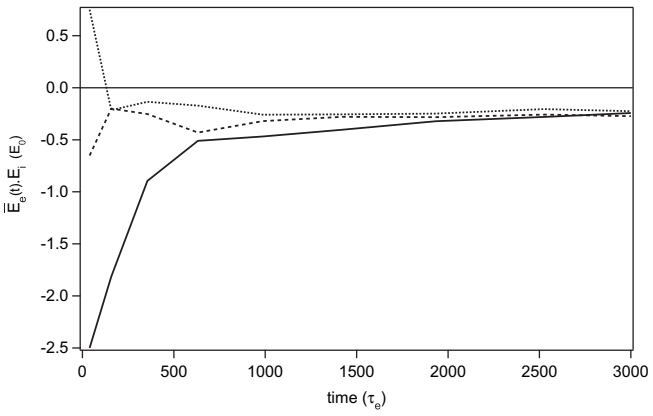

Fig. 1. Three independent runs of the evolution of the scalar product of the ionic field with the average electron field at a neutral test particle located at a distance r_0.

fluctuation of the local average field before reaching the plateau depends on the initial configuration that starts each field history considered in these simulations. The electron field at P_1 can be in any direction with a magnitude larger than E_0. Despite a lack of precision a rough estimate of the convergence time θ necessary to reach the plateau gives $\theta >> \tau_i$. That is, θ is much longer than any relevant response times each of which cannot exceed the lifetime of ionic configurations τ_i. θ should not be confused with the average lifetime of electronic configurations τ_e, it is rather connected to the time necessary for the electron system trajectory to fill the phase space. A more refined study of the mean field convergence versus time, e.g., through a statistical study of the dispersion of data versus time, is mainly academic, difficult and too expensive to be carried out with fixed impurities. Thus, a more realistic approach based on TCP MD simulations i.e., with neutrals, protons and electrons moving, will be used.

On the other hand, an estimate of the mean field can be obtained with a set of fixed neutral test points located at various distances from the fixed ion impurity. In Fig. 2 the average total field is fitted with a Coulomb field whose corresponding screened potential $V_s(r)$ is given by

$$V_s(r) = -e^2 e^{-r/\rho}/r \tag{2}$$

where $\rho \sim r_0 = 0.8 \times \lambda_D$. The use of protons as test points instead of neutral atoms leads to the same average potential estimate. There is no noticeable effect associated with the change of symmetry occurring with the replacement of a neutral–proton pair by a proton–proton pair in the electron plasma. Below, the mean proton–proton potential will be used to carry out OCP simulations.

3.3. Electron proton TCP MD simulation

According to the previous discussions, when all protons and electrons are moving, the response time of interest, Δt, for local averaging is limited by τ_i, $\Delta t < \tau_i$. For longer times, ionic configurations lose their correlation and the local average of the total field goes to 0 with increasing Δt. The gap between the convergence time θ and τ_i makes impossible the convergence of electron averages before destruction of ionic configurations. τ_i being an upper bound for response times, the assumption that electrons adjust instantaneously around ions is invalidated for protons. For heavier particles with the same charge the hypothesis could become reasonable. This motivates a discussion of the approximation of a TCP by an OCP based on screened potentials and indicates another approximation. The following is based on a careful statistical analysis by TCP simulations of both the plasma structure implicit in the pair correlation functions and the field distribution functions at neutrals.

Information on the average static ion structure is involved in the proton pair correlation function $g_{ii}(r)$. The first we look at results from a TCP simulation of $g_{ii}(r)$ that is fit to the results of an OCP with a screened potential according to Eq. (2). Note that the ionic and the electronic pair correlation functions should be identical as the potential energy per proton and per electron are the same. The screening-length best fit, i.e., $\rho = 0.9 \times r_0$ is slightly smaller than previously found, i.e., $\rho = r_0$ from the static neutrals and one proton in an electron gas. The TCP $g_{ii}(r)$ and its best fit are plotted in Fig. 3 together with the result for protons in a neutralizing background for comparison. The fact that a system of charges with screened interactions has a structure that mimics a TCP does not allow one to conclude that binary proton–proton forces are screened. When the uniform continuous neutralizing background set up in a pure proton case is replaced by electrons, due to attractive forces leading to terms with opposite sign in binary sums, the potential energy per proton decreases and changes in the proton $g_{ii}(r)$ occur. With the same kinetic energy, protons with a smaller potential energy can get closer from each other. Note that the three calculations plotted on Fig. 3 can be performed analytically with the hypernetted chain (HNC) technique (see also the A.3). To some extent, this validates the MD calculations of statistical averages.

The consequences of the ion–electron forces at a dynamical level can be summarized as follows. The total field at neutral particles results from a superposition of fast and slow fluctuations with electronic and ionic time characteristics. Due to attractive forces, the electron field itself follows this behavior. As shown in Fig. 4, the simulated electron field autocorrelation function $< E_e(0).E_e(t) >$ begins by a fast de-correlation followed by a slower one, that correspond to the electron and proton dynamical time constants τ_e and τ_i respectively. In Fig. 4, as expected, the cross correlation function $< E_i(0).E_e(t) >$ of the ion field and the electron field is located in the negative plane. Here again there is no straightforward argument leading to conclude that protons can be replaced by screened charges even if the electron field dynamical behavior clearly results from the increased probability density of electron around protons.

The discussions of the statistical properties of fields are necessarily related to the physical process for which they are

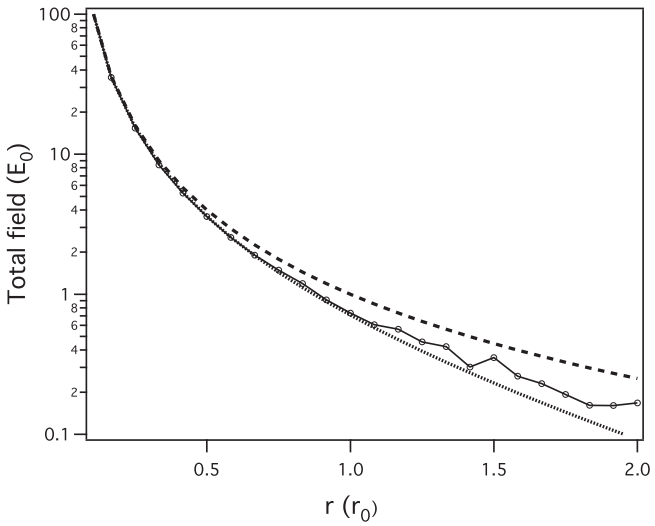

Fig. 2. Average field versus distance at neutral test particles; Coulomb (dash), simulation (black dots), best fit (Eq. (2)) (solid).

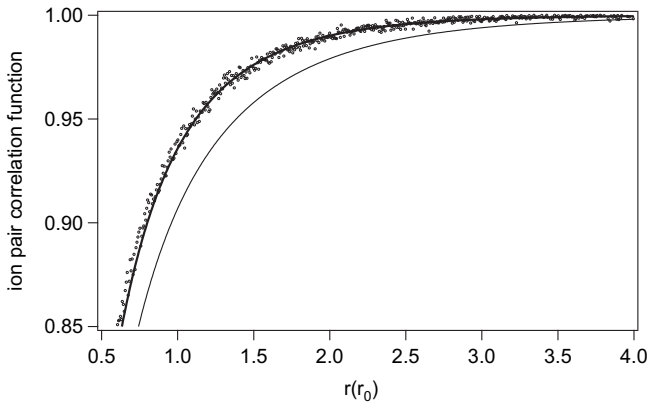

Fig. 3. Proton–proton pair correlation function; screened ion–ion interactions (thick line); no screening (thin line); TCP (circles).

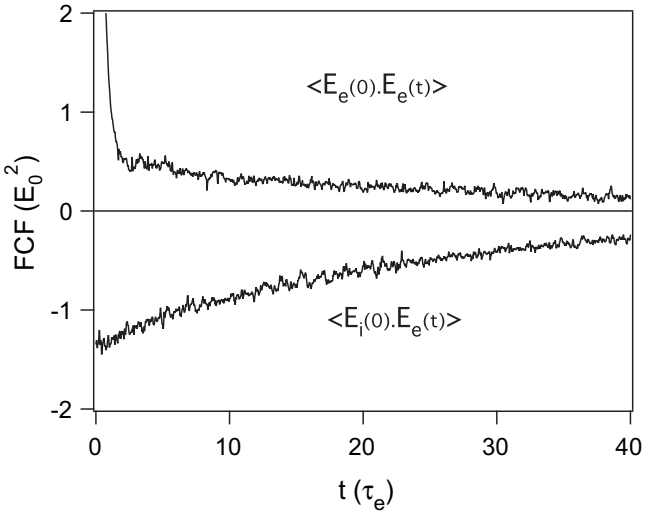

Fig. 4. Electron field autocorrelation function (upper curve) and ion–electron field anti correlation function (lower curve).

investigated. Indeed, an investigation makes sense for response times such as $\Delta t<\tau_i$ and simple method that makes use of a decomposition of each local field into a sum of fast (F) and slow (S) components, is useful.

$$E(t) = E_e(t) + E_i(t) = E_S(t) + E_F(t) \tag{3}$$

The components are subject to the following constraints: 1) their sum must be the total field, 2) they must be statistically independent or at least weakly correlated. The slow component is defined as a local average of the total field,

$$\overline{E}(t)_{S,\Delta t} = \frac{1}{\Delta t}\int_{-\Delta t/2}^{\Delta t/2} (E_e(t+t') + E_i(t+t'))\mathrm{d}t' \tag{4}$$

the fast component is the remainder $\overline{E}_{F,\Delta t}(t) = E(t) - \overline{E}_{S,\Delta t}(t)$.

Global averages of local averages for times Δt, providing the distribution and correlation functions of both the slow and the fast components, are performed in the limit $\tau_e<\Delta t<\tau_i$. A few field distribution functions (FDF) of the slow component have been plotted in Fig. 5 for $\Delta t = 0,2,5,10\tau_e$. The objective of this is the comparison of an FDF of the slow component provided by an OCP of ions seen by neutrals as charges screened by electrons with FDF's of slow total field components obtained by varying the integration time Δt. None of the slow component FDF compares with the screened FDF but, when Δt increases, it does tend towards the FDF obtained with the TCP protons seen as unscreened charges at neutrals. This confirms the previous interpretation leading to one to the observation that it is impossible to have effective screening of protons by electrons. This observation suggests that a good approximation for slow field components consistent with response times such as $\tau_e<\Delta t<\tau_i$ can be obtained in a simple OCP with proton–proton forces resulting from screened potentials to get the right $g_{ii}(r)$, but measuring the unscreened field at neutrals as protons are not seen as screened charges. In a similar manner, the fast component FDF is the same as that can be obtained by an OCP of electrons.

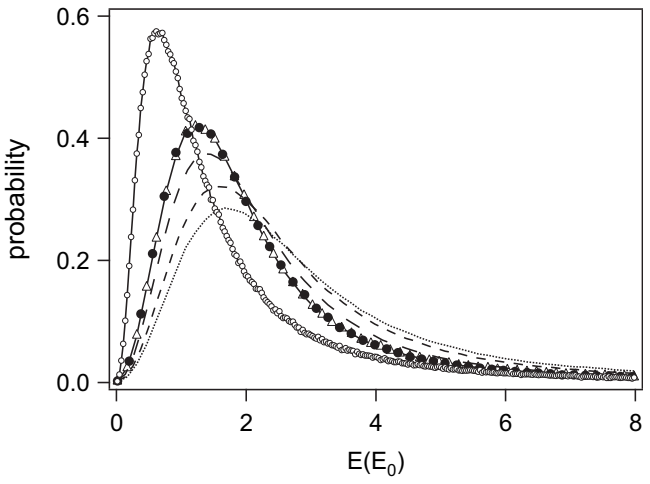

Fig. 5. Slow field distribution components at neutrals, dots $\Delta t = 0$ (total field), short dash $\Delta t = 2\tau_e$, dash $\Delta t = 5\tau_e$, black dots $\Delta t = 10\tau_e$, triangles ion field, circles screened ion field.

4. Discussion

For the case of a static ionic impurity, an analysis of the time required to obtain average fields leads one to suspect the practical difficulty within a TCP for ions to be seen as screened charges. For TCP simulations, the proton plasma structure given by the proton–proton pair correlation function is well represented with an OCP based on binary forces deriving from a screened potential. However, this is not a proof of screening but a consequence of the change in the pair correlation function occurring when the uniform continuous neutralizing background is replaced by negative charges. Confirmation that ions behave as unscreened charges is obtained by an analysis of local field dynamics at neutral test particles (hydrogen atoms) moving freely in a TCP plasma. The simplified OCP system in which electrons have been removed and replaced by mean fields leads to the standard definition of the slow field component. On the other hand, slow components extracted dynamically from the total local field in TCP fail to match the OCP result. It can be concluded that electric fields slow/fast component of the TCP are much better approximated by a simple OCP of protons/electrons seen as unscreened charges at neutrals. Other calculations not reported here, performed for different plasma conditions in the moderate density regime (e.g., for smaller plasma coupling) lead to the same conclusion.

Similar arguments can be used for totally different plasma conditions, the high density and temperature found in sun interior, commented here for illustration. The screening of the proton–proton forces by electrons have been suggested as a possible key ingredient for the proton–proton chain $p + p \rightarrow {}^2H + \nu + \beta^+$ reaction rate calculation [12–14]. Although the model itself is not the purpose of this discussion, a few simulations have been performed for the solar interior plasma conditions. As in the previous part, the differences between θ and τ_i that prevent the formation of screening charges around ions, is another argument against screened charge models. At typical electron density $N_e = 10^{26}$ cm^{-3}, length scales are about 1000 times shorter than those of the average density regime. The regularization length previously associated to 1 *Rydberg* is inappropriate for the electron energies in sun interior. An approach with a regularization length depending on temperature leads to a more physically realistic model. For simplicity an approximate Deutsch potential (see Eq. (A.2) in A.1) can be chosen. The corresponding regularization length leads to a minimum energy of ~ -400 eV with protons represented by potential wells of such a depth. For a hydrogen plasma at $N_e = 10^{26}$ cm^{-3} and $T_e = 10^7$ K the plasma coupling parameter is $\Gamma \sim 0.1$ and quite similar to the plasma coupling of the previous density conditions. The time duration hierarchy is based on the

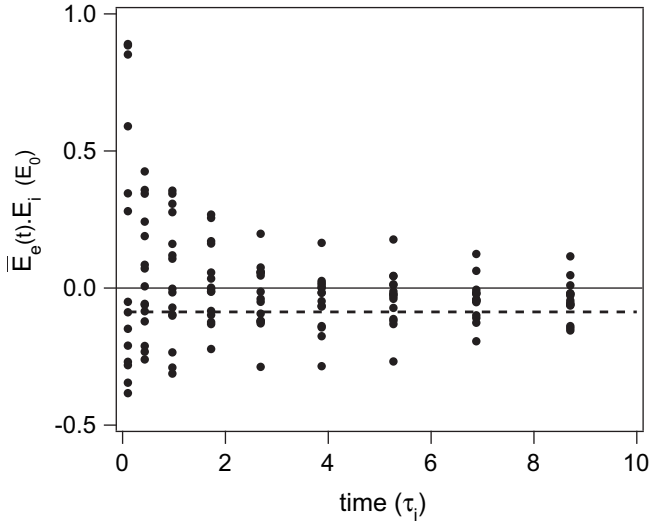

Fig. 6. Typical dispersion of local averages versus time for a static pair of protons at a distance r_0 (dots); mean field (dashed line).

time step dt that is given by $dt = 10^{-21}$ s $\sim 0.001\tau_e$. Here, as neutral hydrogen does not exist, an equivalent static model for time estimates is composed of proton pairs imbedded into an electron gas. For the same reasons as before (large gap between convergence time and time of interest see Fig. 6) the effective screening of proton–proton binary forces by electrons results ineffective.

Finally, the present work does not allow one to extrapolate the general conclusions found for hydrogen plasmas, where protons cannot be seen as screened charges, to other plasmas that contain ions with larger charge and mass. However, if approximate models have to be used, similar questions should be considered in relation with the magnitude of the physical response time in comparison with τ_e, τ_i and θ.

Acknowledgments

The work of M.A.G. and M.Á.G. was partially supported by the Spanish Ministerio de Educación y Ciencia through grant ENE2010-19542/FTN and by the Junta de Castilla y León through grant VA00709.

Appendix A. Two component plasma molecular dynamics

Molecular dynamics is well known however it is worth clarifying some specific features arising with attractive forces. Here, we discuss MD models for an infinite two component ion and electron plasmas in thermodynamical equilibrium with periodic conditions on a cubic box.

A.1. Ion–electron potentials

The ion–electron soft potential used in this work is given by

$$V_{ie}(r) = -Ze^2\left(1 - e^{-r/\delta}\right)e^{-r/\lambda}/r \tag{A.1}$$

At large distance it is a screened Coulomb potential and at short distances has a lower bound: $Ze^2/\delta = -V_{ie}(0) \leq -V_{ie}(r)$. For simplicity, the Ewald sum technique is not implemented, thus, the Coulomb potential is cutoff at a distance corresponding to the cubic simulation cell. This large distance cutoff, replaced by a screening to guarantee continuous potentials, does not appreciably affect the short range dynamical properties investigated in this work.

Different approaches have been used in Eq. (A.1). The first one accounts for quantum diffraction effects and depends on temperature. Such an ion–electron potential is obtained using the de Broglie wavelength as regularization distance.

$$\delta = \hbar/(2\pi m_e k_B T_0)^{1/2} \tag{A.2}$$

The second approach does not depend on temperature and assumes that the minimum potential energy is the ionization energy E_Z of an ion of charge $Z-1$

$$\delta = Ze^2/E_Z \tag{A.3}$$

For the proton–electron plasma at moderate density considered in this work, the regularization distance is chosen to be the Rydberg energy.

A.2. System setting

A simulation procedure starts with a preparation phase intended to get as close as possible of an equilibrium state with definite temperature. By construction, MD maintains a constant density. The goal is to use one or several time periods where the system remains stable in order to extract the desired statistical data. It is understood that during these periods the system is isolated and does not have a temperature correction mechanism, i.e., it is without a thermostat and at the end, the relative total energy drift must be small. For a TCP, the natural way to reach an equilibrium state is to first run a preparation phase for the ions alone in the simulation cell, then, add the electrons at random, switch on the ion–electron potential and finally allow this non-equilibrated system to evolve towards equilibrium adjusting temperature when necessary, which is considered the thermostat. Observations of temperature and total energy drifts indicate whether the whole system is in a quasi-equilibrium state. This method is empirical but in many cases of interest leads to the expected useful stationary evolution of the system. The time it takes to achieve this quasi-equilibrium can be very long depending on the magnitude of $V_{ie}(0)$ and the ion–electron mass ratio. However, the setting up of the positions and velocities of particles of a system that has reached a quasi-stationary state takes place once and then, is maintained dynamically.

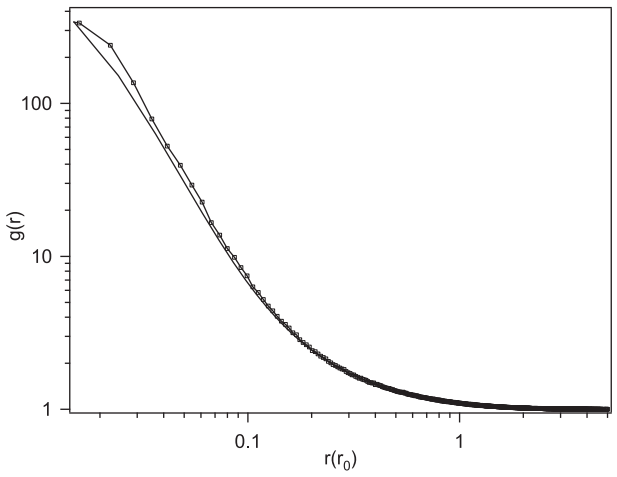

Fig. A.7. Ion–electron pair correlation function for the moderate density conditions; HNC (solid line), MD (circles).

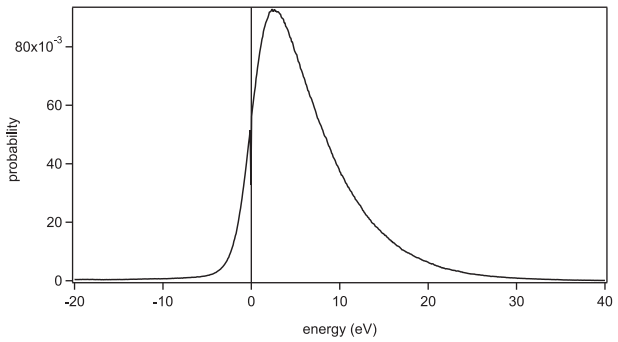

Fig. A.8. Electron energy distribution function for the moderate density conditions.

A.3. Electron trapping

The average response of electrons to positive charges, i.e., to ion attraction, is an increased electron density probability around ions. This effect appears in the ion–electron pair correlation function $g_{ie}(r)$ peaked at $r = 0$. A typical shape of this function, obtained for the moderate density case, is shown in Fig. A.7.

The electron behavior appears also in the total energy distribution, i.e., a sampling of the sum of the kinetic energy and the potential energy for each electron. When the ion–electron interaction is switched on, the sum accounts for terms with opposite sign and the electron total energy distribution $f(\epsilon)$ is shifted towards smaller energies. According to the chosen potential and the plasma conditions, a more or less noticeable negative wing can appear. Among the negative energy states a few result from temporary trapping of electrons by ions through multiple electron collisions quite similar to the collisional three-body recombination mechanisms. In Fig. A.8 both the negative and the positive components of the electron energy distribution are plotted.

The occurrence of trapped electrons depends on potential depth and plasma coupling. In the present work, conditions leading to a small amount of long-living electron–ion pairs have been chosen. When trapped electrons do exist they play the role of classical excited atomic states and increase the number of neutral hydrogen atoms.

References

[1] S. Galam, J.P. Hansen, Phys. Rev. A14 (1976) 816.
[2] M. Baranger, B. Mozer, Phys. Rev. 115 (1959) 521.
[3] B. Mozer, M. Baranger, Phys. Rev. 118 (1960) 626.
[4] C.F. Hooper Jr., Phys. Rev. 149 (1966) 77.
[5] C.F. Hooper Jr., Phys. Rev. 165 (1968) 215.
[6] C.A. Iglesias, J.L. Lebowitz, D. MacGowan, Phys. Rev. A28 (1983) 1667.
[7] C.A. Iglesias, H.E. DeWitt, J.L. Lebowitz, D. MacGowan, W.B. Hubbard, Phys. Rev. A31 (1985) 1698.
[8] G. Kelbg, Ann. Phys. (Leipzig) 12 (1963) 219.
[9] T. Dunn, A.A. Broyles, Phys. Rev. 157 (1967) 156.
[10] G.E. Norman, A.A. Valuev, Plasma Phys. 21 (1979) 531.
[11] H. Minoo, M.M. Gombert, C. Deutsch, Phys. Rev. A23 (1981) 924.
[12] G. Shaviv, N.J. Shaviv, Phys. Rep. 311 (1999) 99.
[13] N.J. Shaviv, G. Shaviv, Astrophys. J. 558 (2001) 925.
[14] D. Mao, K. Mussack, W. Däppen, Astrophys. J. 701 (2009) 1204.

Annexe F

Dynamic Stark broadening as Dicke narrowing effect

Dynamic Stark broadening as the Dicke narrowing effect

A. Calisti,[1,*] C. Mossé,[1] S. Ferri,[1] B. Talin,[1] F. Rosmej,[2,†] L. A. Bureyeva,[3] and V. S. Lisitsa[4]
[1]*PIIM, UMR6633, Centre Saint Jérôme, Université de Provence–CNRS, Case 232, 13397 Marseille Cedex 20, France*
[2]*UMR 7605, LULI, Université Pierre et Marie Curie, Case 128, 4 Place Jussieu, 75252 Paris Cedex 05, France*
[3]*Institute of Spectroscopy, Troitsk, Moscow Region 142190, Russia*
[4]*Russian Research Center, "Kurchatov Institute," Moscow 123182, Russia*
(Received 24 August 2009; published 26 January 2010)

A very fast method to account for charged particle dynamics effects in calculations of spectral line shape emitted by plasmas is presented. This method is based on a formulation of the frequency fluctuation model (FFM), which provides an expression of the dynamic line shape as a functional of the static distribution of frequencies. Thus, the main numerical work rests on the calculation of the quasistatic Stark profile. This method for taking into account ion dynamics allows a very fast and accurate calculation of Stark broadening of atomic hydrogen high-n series emission lines. It is not limited to hydrogen spectra. Results on helium-β and Lyman-α lines emitted by argon in microballoon implosion experiment conditions compared with experimental data and simulation results are also presented. The present approach reduces the computer time by more than 2 orders of magnitude as compared with the original FFM with an improvement of the calculation precision, and it opens broad possibilities for its application in spectral line-shape codes.

DOI: 10.1103/PhysRevE.81.016406 PACS number(s): 52.20.−j, 52.25.−b, 32.70.Jz, 32.60.+i

I. INTRODUCTION

The emitted radiation is usually one of the few observable physical quantities available to obtain information on the underlying physical processes involved in line formation in plasmas. Modeling broadening due to Stark effect of transitions from neutral or charged emitters is a complicated problem that involves a complex combination of atomic physics data, statistical mechanics, and detailed plasma physics [1]. The most difficult part of a line-broadening problem is to properly and completely identify the environment of the emitter. In particular, accounting for the fluctuations of electric fields produced at emitters, by moving electrons and ions, has been of constant interest for both the experimental and theoretical points of view since the 1960s [2]. Different methods have been developed among which the model microfield method (MMM) [3,4] and numerical simulations [5–9] and kinetic theory models such as those developed by Boerker, Iglesias, and Dufty (BID) [10] and frequency fluctuation model (FFM) [11] have proven to be the most successful. Recently, with the advances in computer technology, two-component ion plus electron plasma molecular dynamics (MD) simulations have been applied in studies devoted to spectral line shapes [12–14]. The simulations numerically solve the Schrödinger equation describing the time evolution of the emitter wave functions in the time-dependent field of electrons and ions produced by MD and then average over configurations to obtain the final result. Simulations are used as model laboratory experiments to compare with line shapes calculated by other methods or resulting from experiments. Unfortunately, this technique is time consuming and thus impractical for the modeling of today's highly complex plasma experiments. The FFM has been developed to overcome this difficulty and to permit fast calculations of the radiation emitted by complex or highly charged ions in plasmas. It relies on the hypothesis that the emitter-plasma system behaves approximately like a pseudomolecule embedded into a thermal bath. As a result, the pseudosystem can be considered to have internal states connected to each other by collisions with the bath. This simple starting point has been turned into a powerful renormalization process, called FFM, resulting, a few years ago, in a fast line-shape code called PPP [15] and a code for the computation of radiative redistribution function [16]. The validity of the FFM has been abundantly tested by comparisons with both simulations and, where available, high-precision line-shape measurements [17]. The modern state of the art in radiating plasma physics investigations deals with a complex combination of different theoretical models such as detailed atomic level population kinetics together with radiation transport phenomena in nonuniform plasmas. In this context, the FFM in its original formulation, despite its rapidity, remains too slow and, above all, too difficult to be implemented in the codes used in plasma spectroscopy. The goal of the present paper is to present a more efficient formulation of the FFM to account for dynamic effects of electric fields on atomic spectra in plasmas.

II. METHOD

The line-shape function in the radiative dipole approximation is related to the imaginary part of the Fourier-transformed dipole autocorrelation function. This can be written as a normalized Liouville space-matrix element of the response function,

$$I(\omega) = \mathrm{Im}\langle\langle d^+|G(\omega)|d\rho_0\rangle\rangle, \tag{1}$$

where ρ_0 is the equilibrium density-matrix operator for the active quantum system and d is the dipole operator for the

*annette.calisti@univ-provence.fr
†Also at Ecole Polytechnique, Laboratoire pour Utilisation des Lasers Intenses (LULI), Physique Atomique dans les Plasmas Denses, 91128 Palaiseau Cedex, France.

emitting quantum system. The response function, $G(z)$, is given by the one-sided Fourier transform of the bath-averaged evolution operator of the emitter $U(t,0)$,

$$G(z) = i\int_0^{+\infty} U(t,0)e^{-izt}dt = (z-L)^{-1}. \tag{2}$$

Here, L is the Liouville operator for the emitter evolution alone. If the interaction fluctuations or collisions are random, a stochastic Liouville equation (SLE) must be solved to obtain $G(z)$. In a few well-known cases, the SLE can be solved either exactly or to a good approximation. For example, an analytical solution is obtained for the impact limit in which short and rare binary collisional events occur between emitters and perturbers and the mean time between collisions is much longer than the collision time. The second example concerns the static limit where the perturbing ion microfields, acting on emitters, are constant during the radiative process and are well characterized by a probability density. In most of theoretical models of spectral line shapes in plasmas, the time dependence of the perturbation is eliminated, resulting in a spectral line shape that has pure homogeneous and inhomogeneous contributions and is described by a simple sum of independent electron-impact broadened static components. Although the electron collisions are often well described by the impact approximation, it is well known that a quasistatic treatment of the ion perturbation can lead to large errors for plasma conditions that yield substantial ion-field fluctuations. As an alternative solution, the FFM is based on the premise that a quantum system perturbed by an electric microfield behaves like a set of field dressed two-level transitions, the Stark dressed transitions (SDT). If the microfield is time varying, the transitions are subject to a collision-type mixing process (a Markov process) induced by the field fluctuations.

Suppose the system variables take the values $x_1,x_2,\cdots,x_n$ at times $t_1,t_2,\cdots,t_n$ with probability function $\phi_n(x_n,t_n;\cdots x_1,t_1)$. The changes in $x(t)$ are a Markov process when

$$\phi_n(x_n,t_n;\cdots x_1,t_1) = P(x_nt_n|x_{n-1}t_{n-1})\cdots P(x_2t_2|x_1t_1), \tag{3}$$

where $P(x_2t_2|x_1t_1)$ is the conditional probability that $x(t)$ will have the value x_2 at t_2 when $x(t_1)=x_1$. The conditional or transition-probability function satisfies the Chapman-Kolmogorov equation

$$P(x_2t_2|x_1t_1) = \sum_{x'} P(x_2t_2|x't')P(x't'|x_1t_1), \tag{4}$$

as well as

$$\sum_{x_2} P(x_2t_2|x_1t_1) = 1 \tag{5}$$

and

$$\sum_{x_1} P(x_2t_2|x_1t_1)\Phi_1(x_1,t_1) = \Phi_1(x_2,t_2), \tag{6}$$

where $\Phi_1(x,t)$ is the single-state probability distribution. At this point, it is convenient to introduce a matrix notation. If only stationary Markov processes are considered, Eq. (4) shows that it is possible to define a time-independent matrix of transition rates $\underline{\mathcal{W}}$ such as

$$\underline{P}(t) = e^{\underline{\mathcal{W}}t}. \tag{7}$$

Dividing $\underline{\mathcal{W}}$ into a diagonal matrix of inverse state lifetimes $\underline{\Gamma}$ and an off-diagonal matrix $\underline{W}$ of transition rates between different states,

$$\mathcal{W}_{x_2,x_1} = -\Gamma_{x_1}\delta_{x_2,x_1} + W_{x_2,x_1}, \tag{8}$$

the matrix elements of $\underline{P}(t)$ satisfy

$$\partial_{t_2}P(x_2t_2|x_10) = -\Gamma_{x_2}P(x_2t_2|x_10) + \sum_{x'} W_{x_2,x'}P(x't_2|x_10). \tag{9}$$

Since $P(x_2t_2|x_10)$ satisfies Eq. (5), we have

$$\Gamma_{x_1} = \sum_{x_2} W_{x_2,x_1}. \tag{10}$$

Multiplying Eq. (9) by $\Phi_1(x_1,0)$, summing over x_1, and using Eq. (6) yield a master equation which relates the single-state probability distribution to W_{x_2,x_1},

$$\partial_t\Phi_1(x_2,t) = -\Gamma_{x_2}\Phi_1(x_2,t) + \sum_{x'} W_{x_2,x'}\Phi_1(x',t). \tag{11}$$

The steady-state solution, $P_1(x)$, of this equation is then determined by

$$\Gamma_x P_1(x) = \sum_{x'} W_{x,x'}P_1(x'). \tag{12}$$

Using matrix notation, we can write the one-sided Fourier transform of $\underline{P}(t)$ as

$$\underline{P}(z) = -i(z + i\underline{W} - i\underline{\Gamma})^{-1} \tag{13}$$

so that the propagator is [18]

$$\underline{\mathcal{G}}(z) = (z + i\underline{W} - i\underline{\Gamma} - \underline{L})^{-1}. \tag{14}$$

Assuming that the rate of transitions from state x_1 to state x_2 is independent of x_1, we obtain

$$W_{x_2,x_1} = \Gamma P_1(x_2), \tag{15}$$

where Γ is a constant fluctuation rate. This transition rate matrix is referred to as the strong collision limit for velocity states in Doppler-broadening description [19] or Poisson step process in the model microfield method [3], it suggests that the cause of the change in states is so violent that in its final states, the system has no memory of its initial state. Working in the Liouville space of the dressed two-level radiators in which the basis set of eigenvectors, $\{|e,g;j\rangle\rangle\}$, is labeled by the quantum numbers of the emitters (e,g) and by the SDT label j, the line shape is written as [16]

$$I(\omega) = \mathrm{Re}\frac{1}{\pi}\sum_{kj} i\langle D_k|(\omega - \underline{L} - i\underline{\Gamma} + i\underline{W})^{-1}|D_j\rangle p_j, \tag{16}$$

where $\underline{L}$ is the Liouville operator involving the transition energies of the SDT, D_i are the matrix elements of the dipole moment for the SDT and $p_i=a_i/r^2$ (a_i being the intensity of

the SDT, i, and $r^2=\Sigma_k a_k$) is the instantaneous probability of state i; the probability of quantum radiation at the specific frequency shift due to Stark splitting of energy levels. $\underline{\Gamma}$ is the diagonal matrix of inverse state lifetimes with $\Gamma_{kj}=\Gamma\delta_{kj}=(v_{th}/d)\delta_{kj}$ (where v_{th} is the thermal velocity of perturbers and d is the mean interparticle distance) and $\underline{W}$ is the matrix of transition rates between different states such as $W_{kj}=\Gamma p_k$.

Equation (16) involves a finite matrix inversion whose size can be very large. In the original FFM [11], a renormalization process was proposed to overcome this difficulty. This process introduced an additional approximation and proved insufficient in some very complex cases. Hereafter, a formulation is presented which avoids matrix inversion, thus considerably improving the method. Defining the quasistatic propagator

$$\underline{G^s}(z)=(z-\underline{L}-i\underline{\Gamma})^{-1}, \tag{17}$$

which has only diagonal matrix elements, the total propagator $\mathcal{G}(z)$, from Eq. (14), can be written as

$$\mathcal{G}(z)=\underline{G^s}(z)-i\underline{G^s}(z)\cdot\underline{W}\cdot\mathcal{G}(z). \tag{18}$$

Introducing the previous expression in Eq. (16), we get

$$I(\omega)=\frac{r^2}{\pi}\mathrm{Re}\frac{\sum_k \frac{a_k/r^2}{i(\omega-\omega_k)+\Gamma}}{1-\Gamma\sum_k \frac{a_k/r^2}{i(\omega-\omega_k)+\Gamma}}. \tag{19}$$

All the above results are easily extended to the situation where $x(t)$ belongs to a continuum of values. In this case, the probabilities $P(x_2t_2|x_1t_1)$ and $\Phi(x,t)$, defined for discrete $x(t)$, become probability densities $p(x_2t_2|x_1t_1)$ and $\phi(x,t)$, and all sums are replaced by integrals. In this case, the probability $p_k=a_k/r^2$ is replaced by $W(\omega)d\omega$ the probability to have a radiation at a frequency in the range ω and $\omega+d\omega$ obtained in the static limit. The previous equation is then written as

$$I(\omega)=\frac{r^2}{\pi}\mathrm{Re}\frac{\int \frac{W(\omega')d\omega'}{\Gamma+i(\omega-\omega')}}{1-\Gamma\int \frac{W(\omega')d\omega'}{\Gamma+i(\omega-\omega')}}. \tag{20}$$

With $W(\omega)$ being the normalized static line shape, the main numerical work remains in the calculation of the quasistatic profile.

Note that this expression is similar to that obtained in [19] to describe the Doppler effect in the framework of a strong collision model (Dicke effect [20]),

$$I(\omega)=\frac{1}{\pi}\mathrm{Re}\frac{\int \frac{W(\vec{v})d\vec{v}}{\nu+i(\omega-\vec{k}\,.\,\vec{v})}}{1-\nu\int \frac{W(\vec{v})d\vec{v}}{\nu+i(\omega-\vec{k}\,.\,\vec{v})}}. \tag{21}$$

There, the thermal bath is composed of radiator velocity states $\vec{v}$ with the probability distribution $W(\vec{v})$. The velocity-changing collisions result in an effective jumping from one value of the atomic velocity to one other following a Markov process. The line shape is, then, transformed from nonuniform Gaussian to uniform Lorentzian line shape with the effective line width equal to

$$\gamma_D\propto\frac{\Delta\omega_D^2}{\nu} \tag{22}$$

where $\Delta\omega_D$ is the Doppler width of the line and ν is the velocity-changing collision frequency. We will come back on this analogy in the following section.

As it has been noticed previously, electrons in plasmas are well described by the impact approximation. The quantum-emitter system evolution operator in Eq. (2), then, contains in the Liouville operator a non-Hermitian homogeneous electron-impact broadening contribution, resulting in static Stark components (SDT) characterized by a complex frequency $\omega_k-i\gamma_k$ and intensity a_k+ic_k. The line-shape function for a given transition with n SDT is, then, written as

$$I(\omega)=\frac{r^2}{\pi}\mathrm{Re}\frac{\sum_k \frac{(a_k+ic_k)/r^2}{i(\omega-\omega_k)+\gamma_k+\Gamma}}{1-\Gamma\sum_k \frac{a_k/r^2}{i(\omega-\omega_k)+\gamma_k+\Gamma}}. \tag{23}$$

If the condition $c_k\ll a_k$ is fulfilled and γ_k is weakly k dependent, $\gamma_k=\gamma$. Then, Eq. (23) can be written as

$$I(\omega)=\frac{r^2}{\pi}\mathrm{Re}\frac{\int \frac{W(\omega')d\omega'}{\Gamma+\gamma+i(\omega-\omega')}}{1-\Gamma\int \frac{W(\omega')d\omega'}{\Gamma+\gamma+i(\omega-\omega')}}. \tag{24}$$

As γ does not depend on the frequency of the emitting atom, Eq. (24) can be represented as the convolution of a lorentzian function and function (20) which defines the line contour when $\gamma=0$,

$$I(\omega)=\int d\omega''\frac{\gamma/\pi}{\gamma^2+(\omega-\omega'')^2}\mathrm{Re}\left\{\frac{r^2}{\pi}\frac{\int \frac{W(\omega')d\omega'}{\Gamma+i(\omega''-\omega')}}{1-\Gamma\int \frac{W(\omega')d\omega'}{\Gamma+i(\omega''-\omega')}}\right\}. \tag{25}$$

III. RESULTS AND DISCUSSION

The hydrogenic argon Lyman-α transition, including fine structure, in a weakly coupled proton plasma, is considered first in this section to illustrate the effects of ion dynamics on spectral line shapes and the analogy with Dicke narrowing effect. The quantum system involves the four levels $1S_{1/2}$, $2S_{1/2}$, $2P_{1/2}$, and $2P_{3/2}$. This case is very advantageous because the spectrum involves two patterns resulting from both linear and quadratic Stark splitting associated, respectively, with the two fine-structure components $1S_{1/2}$-$2P_{1/2}$ and $1S_{1/2}$-$2P_{3/2}$.

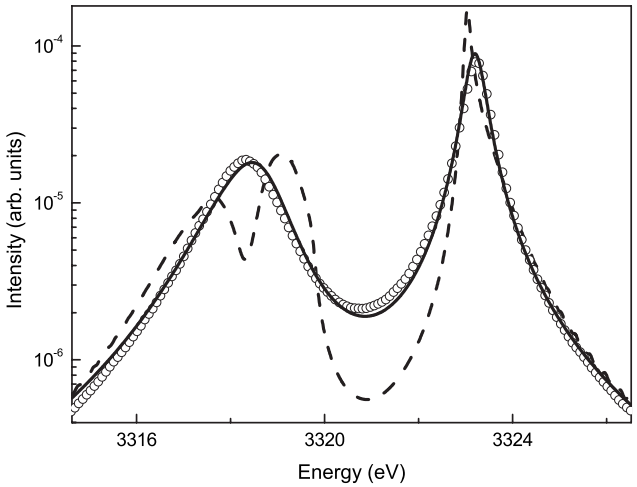

FIG. 1. Lyman-α line with fine structure at $N_e=1.5\times10^{23}$ cm^{-3} and $T_e=10^7$ K. Comparisons between static profile (dash line), dynamic profile (full line) and molecular dynamics simulation calculation (circles).

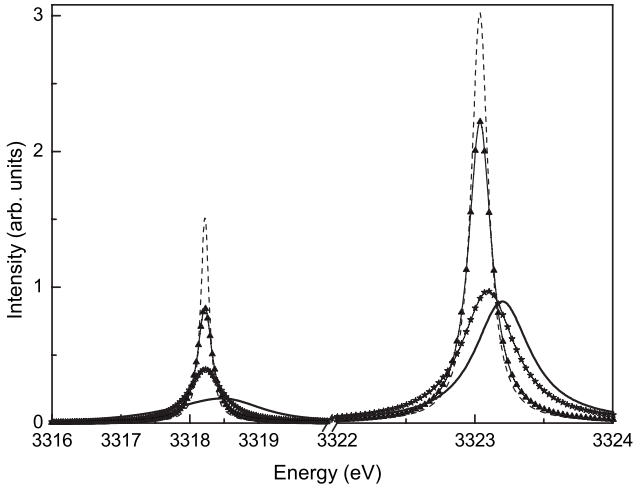

FIG. 2. Lyman-α line with fine structure at $N_e=1.5\times10^{23}$ cm^{-3} and $T_e=10^7$ K. Dynamic profile with different fluctuation rates, Γ (full line: same as Fig. 1 with $\Gamma=1.5$, stars: $\Gamma=10$, and triangles: $\Gamma=100$) compared to unperturbed profile obtained with a zero ionic electric field (dash line).

Figure 1 shows the Lyman-α profile for hydrogenlike argon in protons without Doppler broadening calculated for the plasma conditions $N_e=1.5\times10^{23}$ cm^{-3} and $T_e=10^7$ K. Three different results have been plotted in logarithm scale: the static profile (dash line), the dynamic profile obtained with the new formulation of the FFM (full line) and the simulation result (circles). In these simulations, a representative set of ionic electric-field histories is generated by using molecular dynamics technique, then, the time-depending histories are used in a step-by-step integration of the Schrödinger equation and the final result is obtained averaging over the set of histories. Results from simulations are considered as benchmark, as they rely neither on impact nor static approximation. Comparisons with numerical simulations show a very good agreement. The two fine-structure components show different behaviors. Due to linear Stark effect on the $1S_{1/2}$-$2P_{1/2}$, two resonances appear in the static approximation which are mixed and merged into a single one by ion dynamics. On the $1S_{1/2}$-$2P_{3/2}$ the main feature due to quadratic static Stark effect seems to be enhanced by ion dynamics and the dynamic profile appears broaden and shifted. In all the cases, it can be noticed that, as expected, the wings are well represented by the static profile. The FFM method describes continuously the region between the static limit which corresponds to a zero fluctuation rate and the fast fluctuation limit. In the limit of an infinitely rapid ion micro field fluctuation, the effect of the perturbation disappears and the line components collapse to the center of gravity. This is illustrated in Fig. 2 where the Lyman-α profile is plotted for different values of the fluctuation rate and compared with the unperturbed line corresponding to a zero ionic electric field. As we can see, even though in a first stage the profile is broadened, an increase in the fluctuation rate results in a narrowing of the profile. This effect is the same as Dicke narrowing where the rapid collisionnal mixing of velocity components causes a collapse of the Doppler line shape.

The second example concerns Stark broadening of atomic hydrogen high-n series emission lines which have been used for spectroscopic measurements of plasma density in laboratory experiments [21]. In Ref. [21], a multichannel spectroscopic diagnostic and the corresponding analysis for divertor electron-density measurements using Stark-broadened Balmer and Paschen emission lines originating from $n=7-13$ levels have been developed. It has been shown that the Paschen line profiles are an attractive recombining divertor density diagnostic for a burning plasma experiment. Diagnostics are based on comparisons between experimental data and theoretical results that must be as accurate as possible.

Figure 3 shows the static and dynamic profiles for the Balmer 10–2 and the Paschen 10–3 transitions for an electronic density $N_e=10^{14}$ cm^{-3} and a temperature $T_e=10$ eV corresponding to observations performed in the National Spherical Torus Experiment detached divertor region. These

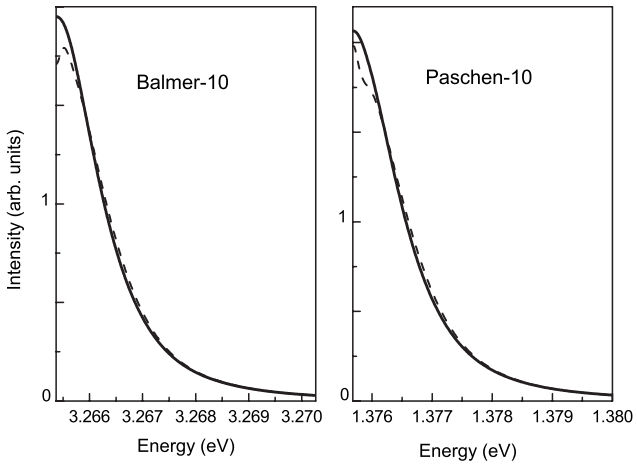

FIG. 3. Balmer 10–2 and Paschen 10–3 lines at $N_e=10^{14}$ cm^{-3} and $T_e=10$ eV. Comparisons between static profile (dash line) and dynamic profile (full line).

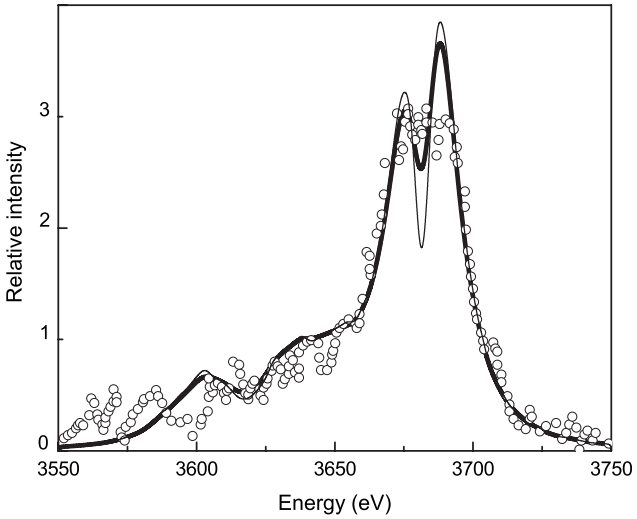

FIG. 4. Ar XVII $1s^2$-$1s3p$ ^1P at $N_e=1.2\times10^{24}$ cm^{-3} and $T_e=700$ eV. Comparison of the full ion dynamics calculation including the Li-like satellites (bold full line) with the experimental data (circles) and the static profile (thin full line).

calculations, which were impracticable or very difficult to perform without approximation, have been done in a few seconds. In addition, as no matrix inversion is required, the results are more accurate.

The method presented here is not limited to hydrogen spectra. It is particularly useful when a Stark-broadened impurity profile is used for plasma diagnostic purposes. This line-shape computation in hot dense plasma conditions can be difficult and very time consuming. This is because the spectra of interest are not limited to the simplest hydrogenlike or heliumlike ionic lines but include also lines radiated by complex three or more electron ions (dielectronic satellites for example).

The third example concerns the Helium-β line of argon, Ar XVII $1s^2$-$1s3p$ ^1P, and the associated lithiumlike dielectronic satellite lines, in deuterium for plasma conditions typical of inertial confinement fusion experiments [22]. In these experiments, rare-gas atoms are introduced in trace amounts as a nonperturbing dopant in the gas fill of the microspheres of the implosion experiments. The profiles of the lines emitted by the rare-gas ions are then used as a diagnostic by comparing the experimental results with theoretical predictions. Figure 4 displays a comparison of the full ion dynamics calculation of the helium-β line including the Li-like $2l3l'$ and $3l3l'$ dielectronic satellite lines for Argon impurities in deuterium at $N_e=1.2\times10^{24}$ cm^{-3} and $T_e=700$ eV with the experimental data [22] and the static profile. It has been shown in Ref. [22] that ion dynamics effects cannot be considered as the unique cause of the filling of the line central feature. Even though, ion dynamics effects improve the comparison with experimental data, some discrepancies remain and their study is not the subject of this paper (for more details see Ref. [22]). Calculations of ion dynamics effects on Li-like satellite lines involve hundred thousands of Stark components, and the calculation with the original FFM was extremely difficult or impracticable. The present FFM formulation permits to get the ion profile in a couple of minutes on a workstation.

IV. CONCLUSION

A very fast method to account for charged particle dynamics effects in calculations of spectral line shapes has been presented and tested by comparisons with numerical simulations. Comparisons with experimental data illustrate the need to calculate ion dynamics effects for line shapes emitted by complex atomic systems.

The method is based on a formulation of the FFM, which provides an expression of the dynamic line profile as a functional of the static frequency distribution and a unique parameter, the fluctuation rate. This expression is similar to that obtained to describe the Doppler effect in the framework of strong collision models (Dicke effect). In this model, a Markovian mixing process of velocities mimics the velocity-changing collision effect, on the Doppler profile, which result in the line-shape transformation from nonuniform Gaussian to uniform Lorentzian line shape when the collision rate increases. The same description of transition from inhomogeneous (static) to homogeneous (Lorentzian or fast fluctuation limit) can be done for Stark profiles. The main numerical work is the calculation of the static profile. It can be obtained by different analytical or numerical methods. Different models [23,24] have been proposed in order to facilitate the calculations of line shapes of highly excited (Rydberg) hydrogen atoms and ions important for many topics in plasma physics and astrophysics. Some very sophisticated code have been developed, PPP-TOTAL code [15] or MERL multielectron-radiator line shape code [25], for example, to calculate spectral line shape emitted by complex multielectronic emitters.

This work opens possibilities for ultra fast calculations of dynamic line shapes for arbitrary values of plasma parameters (densities and temperatures). It is of special importance for strongly nonuniform plasmas where one needs to calculate spectra for a wide domain of plasma parameters. It is the case both for laser driven plasmas and magnetically confined (especially divertor) plasma conditions. Another application concerns Stark-Zeeman profiles for which, ion dynamics calculations are, strongly, facilitated by using this new formulation. These profiles are of great interest for astrophysics and thermonuclear fusion physics.

ACKNOWLEDGMENTS

Authors thank the anonymous referee for his/her very helpful comments and suggestions. The work is partially supported by RFBR Grant No. 08-02-00294-a and Federal Target Program "Academic and Teaching Staff of innovation Russia 2009–2012."

[1] H. Griem, *Spectral Line Broadening by Plasma* (Academic Press, New York, 1974).
[2] H. Griem, *Principles of Plasma Spectroscopy* (Cambridge University Press, Cambridge, 1997).
[3] A. Brissaud and U. Frisch, J. Quant. Spectrosc. Radiat. Transf. **11**, 1767 (1971).
[4] A. Brissaud and H. Frisch, J. Math. Phys. **15**, 524 (1974).
[5] R. Stamm, E. W. Smith, and B. Talin, Phys. Rev. A **30**, 2039 (1984).
[6] R. Stamm, B. Talin, E. L. Pollock, and C. A. Iglesias, Phys. Rev. A **34**, 4144 (1986).
[7] J. Seidel, *Spectral Line Shapes* (Deepack, Hampton, VA, 1987), Vol. 4, p. 57.
[8] G. C. Hegerfeldt and V. Kesting, Phys. Rev. A **37**, 1488 (1988).
[9] V. Cardeñoso and M. A. Gigosos, Phys. Rev. A **39**, 5258 (1989).
[10] D. B. Boercker, C. A. Iglesias, and J. W. Dufty, Phys. Rev. A **36**, 2254 (1987).
[11] B. Talin, A. Calisti, L. Godbert, R. Stamm, R. W. Lee, and L. Klein, Phys. Rev. A **51**, 1918 (1995).
[12] B. Talin, E. Dufour, A. Calisti, M. A. Gigosos, M. A. Gonzalez, T. del Rio Gaztelurrutia, and J. W. Dufty, J. Phys. A **36**, 6049 (2003).
[13] E. Dufour, A. Calisti, B. Talin, M. A. Gigosos, M. A. Gonzalez, and J. W. Dufty, J. Quant. Spectrosc. Radiat. Transf. **81**, 125 (2003).
[14] E. Stambulchik, D. V. Fisher, Y. Maron, H. R. Griem, and S. Alexiou, High Energy Density Phys. **3**, 272 (2007).
[15] A. Calisti, L. Godbert, R. Stamm, and B. Talin, J. Quant. Spectrosc. Radiat. Transf. **51**, 59 (1994).
[16] C. Mossé, A. Calisti, R. Stamm, B. Talin, R. W. Lee, and L. Klein, Phys. Rev. A **60**, 1005 (1999).
[17] L. Godbert-Mouret, T. Meftah, A. Calisti, R. Stamm, B. Talin, M. Gigosos, V. Cardeñoso, S. Alexiou, R. W. Lee, and L. Klein, Phys. Rev. Lett. **81**, 5568 (1998).
[18] B. Talin and L. Klein, Phys. Rev. A **26**, 2717 (1982).
[19] S. G. Rautian and I. I. Sobelman, Sov. Phys. Usp. **9**, 701 (1967).
[20] R. H. Dicke, Phys. Rev. **89**, 472 (1953).
[21] V. A. Soukhanovskii, D. W. Johnson, R. Kaita, and L. Roquemore, Rev. Sci. Instrum. **77**, 10F127 (2006).
[22] N. C. Woolsey, A. Asfaw, B. Hammel, C. Keane, C. A. Back, A. Calisti, C. Mossé, R. Stamm, B. Talin, J. S. Wark, R. W. Lee, and L. Klein, Phys. Rev. E **53**, 6396 (1996).
[23] C. Mossé, A. Calisti, S. Ferri, B. Talin, L. A. Bureyeva, and V. S. Lisitsa, *Spectral Line Shapes: The 19th International Conference on Spectral Line Shapes*, AIP Conf. Proc. No. 1058(AIP, New York, 2008), p. 63.
[24] E. Stambulchik and Y. Maron, J. Phys. B **41**, 095703 (2008).
[25] R. C. Mancini, D. P. Kilcrease, L. A. Woltz, and C. F. Hooper, Jr., Comput. Phys. Commun. **63**, 314 (1991).

Annexe G

Ion dynamics effect on Stark broadened line shapes : a cross comparison of various models

Atoms **2014**, *2*, 299-318; doi:10.3390/atoms2030299

OPEN ACCESS

atoms

ISSN 2218-2004

www.mdpi.com/journal/atoms

Article

Ion Dynamics Effect on Stark-Broadened Line Shapes: A Cross-Comparison of Various Models

Sandrine Ferri [1,*], Annette Calisti [1], Caroline Mossé [1], Joël Rosato [1], Bernard Talin [1], Spiros Alexiou [2], Marco A. Gigosos [3], Manuel A. González [3], Diego González-Herrero [3], Natividad Lara [3], Thomas Gomez [4], Carlos Iglesias [5], Sonja Lorenzen [6], Roberto C. Mancini [7] and Evgeny Stambulchik [8]

[1] Aix-Marseille Université, CNRS, PIIM UMR7345, 13397 Marseille, France;
E-Mails: annette.calisti@univ-amu.fr (A.C.); caroline.mosse@univ-amu.fr (C.M.);
joel.rosato@univ-amu.fr (J.R.); bernard.talin@orange.fr (B.T.)

[2] TETY, University of Crete, 71409 Heraklion, TK 2208, Greece; E-Mail: moka1@otenet.gr (S.A.)

[3] Department de Óptica y Física Applicada, Universidad de Valladolid, Valladolid 47071, Spain;
E-Mails: gigosos@coyanza.opt.cie.uva.es (M.A.G.); manuelgd@termo.uva.es (M.A.G.);
diegohe@opt.uva.es (D.G.-H.); nati@opt.uva.es (N.L.)

[4] Department of Astronomy, University of Texas, Austin, TX 78731, USA;
E-Mail: gomezt@astro.as.utexas.edu (T.G.)

[5] LLNL, Livermore, CA 94550, USA; E-Mail: iglesias1@llnl.gov (C.I.)

[6] Institut für Physik, Universität Rostock, D-18051 Rostock, Germany;
E-Mail: sonja.lorenzen@uni-rostock.de (S.L.)

[7] Physics Dept., University of Nevada, Reno, NV 89557, USA; E-Mail: rcman@unr.edu (R.C.M.)

[8] Faculty of Physics, Weizmann Institute of Science, Rehovot 7610001, Israel;
E-Mail: Evgeny.Stambulchik@weizmann.ac.il (E.S.)

***** Author to whom correspondence should be addressed; E-Mail: sandrine.ferri@univ-amu.fr;
Tel.: +33-49128-8623.

Received: 30 April 2014; in revised form: 10 June 2014 / Accepted: 16 June 2014 /
Published: 4 July 2014

Abstract: Modeling the Stark broadening of spectral lines in plasmas is a complex problem. The problem has a long history, since it plays a crucial role in the interpretation of the observed spectral lines in laboratories and astrophysical plasmas. One difficulty is the characterization of the emitter's environment. Although several models have been proposed over the years, there have been no systematic studies of the results, until now. Here, calculations from stochastic models and numerical simulations are compared for the

Lyman-α and -β lines in neutral hydrogen. Also discussed are results from the Helium-α and -β lines of Ar XVII.

Keywords: Stark broadening; line shapes; plasmas; numerical simulations; models

1. Introduction

Line shape analysis is one of the most important tools for plasma diagnostics, as it provides information on the underlying physical processes involved in the line formation. With the increasing number of applications in different areas of plasma physics, the modeling of line broadening from neutral or charged emitters has been in perpetual development and remains a keystone in plasma spectroscopy [1].

In the formation of a line shape, Stark broadening is the most computationally challenging contribution, since the main difficulty is to properly characterize the emitter environment. It involves a complex combination of atomic physics, statistical mechanics and detailed plasma physics [2]. In particular, it is well known that the quasi-static ion approximation can lead to discrepancies with experimental data near the line center. This happens whenever the electric microfields produced at the emitter by the surrounding ions fluctuate during the inverse half-width at half-maximum (HWHM) time scale. The first attempts to account for ion dynamics in theoretical models were done in the 1970s, followed by experimental proof (see the historic introduction in [3] and the references therein). Since then, several models based on stochastic or collisional approaches have been developed, together with numerical simulations ([4] and the references therein). Necessarily, their limit of applicability, accuracy and, thus, results differ from one another, and up to now, no systematic comparison have existed [5].

The purpose here is to present cross-comparisons of different models that account for the ion dynamics effect. The line shape formalism is briefly recalled in Section 2, which serves to introduce notation. The specifics of the various models and numerical simulations are also presented in this section. We review the simulations Euler–Rodrigues (ER)-simulation [6], HSTRK [7], HSTRK_frequency separation technique (FST) [8], SimU [9,10], Xenomorph [11] and the models QuantST.MMM (MMM—model microfield method) [12], quasicontiguous (QC)-frequency fluctuation model (FFM) [13], multi-electron line-shape (MELS) [14], multi-electron radiator line-shape (MERL) [15,16], PPP [17], ST-PST [18] and UTPP [19] that have been used for the present purpose. The ion dynamics effect on the hydrogen Lyman-α and -β lines is discussed in Section 3.1, demonstrating the difficulty of such modeling even for these well-known lines. In Section 3.2, results on helium-α and -β lines of Ar XVII produced by the two stochastic models (Boerker–Iglesias–Dufty (BID) [20] and FFM [4,21]) are discussed with the help of the numerical simulation (SimU). The reliability of such calculations is of interest in the diagnostics of inertial confinement fusion core plasma conditions. Conclusions are given in Section 4.

2. Theory, Models and Simulations

We recall that the line shape is given by:

$$I(\omega) = \frac{1}{\pi} Re \int_0^\infty dt\, e^{i\omega t} C(t) \tag{1}$$

where $C(t)$ is the autocorrelation function of the radiator dipole operator $\mathbf{d}$, which can be expressed in Liouville space as:

$$C(t) = \ll \mathbf{d}^\dagger | \mathbf{U}(t) | \mathbf{d}\rho_0 \gg \tag{2}$$

where the double bra and ket vectors are defined as usual in Liouville space. Here, ρ_0 is the density operator for the emitter only at the thermodynamical equilibrium and $\mathbf{U}(t) = \{U_l(t)\}_{l \in F}$ is the bath averaged evolution operator of the emitter. l belongs to a measurable functional space, $\{F\}$, which provides a statistical method for the calculation of average quantities. The main problem is to determine $\mathbf{U}(t)$. One has thus:

- to find the time evolution of $U_l(t)$ for a given microfield configuration, which means solving the following equation:
$$\frac{dU_l(t)}{dt} = -i[L_0 - \mathbf{d} \cdot \mathbf{F}_l(t)]\, U_l(t), \quad U_l(0) = 1 \tag{3}$$
where L_0 represents the Liouvillian of the unperturbed radiator and $\mathbf{d} \cdot \mathbf{F}_l(t)$ represents the Stark effect that connects the dipole operator $\mathbf{d}$ to the microfield created by surrounding charged particles $\mathbf{F}_l$ (including ions and electrons),
- and to average it over a statistical ensemble of the microfields $\{\ \}_{l \in F}$.

In its general form, the problem cannot be treated analytically. Nevertheless, $\mathbf{U}(t)$ can be obtained by numerical simulation integrating Equation (3) on simulated sampling of microfield histories. Usually, such a calculation is split into two independent steps [3]. First, the plasma particle trajectories are obtained by a numerical solution of Newton's equations of motion or an alternative method. Knowing the trajectory of each particle, the electric fields at the emitter are evaluated and stored to be used in the second step. Then, the line shape simulation follows: a step-by-step integration of Equation (3) is performed using these field histories. The evolution operator of the emitter is calculated, and the whole procedure is repeated several times in order to average over a representative sample set of independent perturbing field histories $\{f_1, f_2 ... f_N\}$. As a result, $C(t)$ is given by:

$$C(t) = \frac{1}{N} \sum_{i=1}^{N} C_i(t) \tag{4}$$

and the line shape is obtained by a Fourier transform of $C(t)$. Although all line shape simulations are based on the same scheme, we will see in the next section that they can differ slightly depending on the details of the models.

Alternatively, efficient analytical models based on fundamental assumptions and approximations have been developed [1]. In the standard theory (ST), the line shape calculation is based on the separation between the ions and the electrons due to the radically different dynamical properties of the microfields

they create. Indeed, the typical fluctuation rate of the electric field created by perturber species p with a velocity relative to the center of mass v_p and a density n_p is defined by:

$$\nu_p = v_p/d_p \tag{5}$$

where $d_p = (3/4\pi n_p)^{1/3}$ is a typical interparticle distance. Assuming equal temperature for ions and electrons and plasma neutrality, one has [3]:

$$\frac{\nu_e}{\nu_i} \sim \left(\frac{\mu_i}{\mu_e}\right)^{1/2} Z_i^{1/3}. \tag{6}$$

Thus, the perturbation due to the electrons (with reduced mass μ_e) is nearly two orders of magnitude faster than that of ions (with reduced mass μ_i and charge Z_i). This allows for treating the electrons and the ions in a different way. The fast electrons are assumed to perturb the emitter by means of collisions, treated in the impact approximation, and the slow ions are assumed to be quasi-static. This results in a quantum-emitter system perturbation operator $l = -\mathbf{d} \cdot \mathbf{F}_{i,l} + i\phi_e$, containing a non-Hermitian homogeneous electron-impact broadening contribution ϕ_e and the ion microfield interaction $-\mathbf{d} \cdot \mathbf{F}_{i,l}$, which has to be numerically averaged with a static-field probability distribution $Q(\mathbf{F}_i)$, or because of isotropy, with $dW(F_i) = 4\pi F_i^2 Q(\mathbf{F}_i) dF_i$. The later can be calculated numerically in the ideal gas limit for perturbing ions [22] or using more sophisticated models that account for ion correlations [23]. Using the set of above assumptions, the quasi-static line shape is written as:

$$I_s(\omega) = -\frac{1}{\pi} Im \ll \mathbf{d}^\dagger | \int d\mathbf{F}_i \, Q(\mathbf{F}_i) \, G_s(\omega, \mathbf{F}_i) \, | \mathbf{d}\rho_0 \gg \tag{7}$$

in which the resolvent operator is given by:

$$G_s(\omega, \mathbf{F}_i) = (\omega - L_0 + \mathbf{d} \cdot \mathbf{F}_i - i\phi_e)^{-1}. \tag{8}$$

Although the electrons are often well described within the impact approximation, a quasi-static treatment of the ions can lead to large errors for plasma conditions, such as the ion microfields fluctuate during the inverse HWHM time scale. In the next section, we briefly review the simulations and the models that have been developed to account for the ion dynamics effect and that have been used for the present cross-comparisons.

2.1. The Numerical Simulations

The results from four numerical simulation codes based on different models have been submitted. They differ either in the way they model the motions of the plasma particles or in the procedure for the integration of the Schrödinger equation.

In the **ER-simulation**, the simulated plasma is an electrically neutral ensemble of statistically independent charged particles made of N_i ions and N_e electrons moving along straight line trajectories within a spherical volume. An emitter is assumed to be placed at the center of such a box. The temporal evolution of the whole system is measured along a discrete time axis from zero to a definite number of times of a fixed increment. Every temporal state is given by the set of values of the positions and velocities of the particles in the system. At every time step, the electric field produced by ions and

electrons is calculated using Coulomb's law or a Debye-screened field. This electric field is an input to the Schrödinger equation that computes the emitter time evolution operator. For hydrogen and when the no-quenching approximation is considered, the atom state is described with the Euler–Rodrigues parameters [24].

The **HSTRK** and **HSTRK_FST** codes also use the Gigosos–Cardeñoso approach [25]. Both codes rely on the Hegerfeld–Kesting–Seidel method of collision-time statistics [26] and compute $C(t)$. Depending on the appropriate option, HSTRK can do an electron only, ion only or joint simulation, but one can also do combinations, e.g., electron simulation and quasi-static ions or impact electrons and ion simulation. For the Fourier transform, if a long-time exponential behavior is detected for times $t > \tau$, then the contribution to the Fourier transform of the (τ, ∞) region is computed analytically using the detected exponential decay and added to $\int_0^\tau dt C(t) e^{\imath\omega t}$. τ is determined via start-up runs, e.g., a run with a small number of configurations is done to obtain a rough idea of the HWHM and τ is adjusted to cover at least a number of inverse HWHMs. The integral is done by Filon's rule [27].

HSTRK_FST implements the frequency separation technique, which first identifies the "impact" phase space of ion perturbers (e.g., impact parameters and velocities), which produce a width much less (in these runs, "much less" was 10-times less) than the field fluctuation frequency. This meant:

$$HWHM(\Omega) = 0.1\,\Omega \tag{9}$$

where the HWHM is computed by including all ion perturbers with impact parameter ρ and velocity $v > \Omega\rho$. Hence, the calculation is essentially the same, except that only slow ions $v < \Omega\rho$ are included in the simulation. The $C(t)$ obtained from the simulation of these slow ions is then multiplied by $e^{-HWHM(\Omega)t}$, and the Fourier transform is taken as in HSTRK. The use of a pure exponential form for the rapidly fluctuating (impact) part is a consequence of using the complete collision assumption for solving the impact part [28,29] and results in a $C(t)$ that is not correct for very short times. This is manifested in the (far) wing behavior of the HSTRK_FST profiles and can be remedied by using the incomplete collision formulas of the above-cited analytical solutions.

SimU is a combination of two codes: a molecular dynamics (MD) simulation of variable complexity and a solver for the evolution of an atomic system with the MD field history used as a (time-dependent) perturbation. A technical difference from other numerical simulation methods is the way the spectrum is calculated. Instead of employing the dipole autocorrelation function via Equation (1), SimU calculates the Fourier transform of the dipole matrix:

$$\vec{d}(\omega) = \int_0^\infty dt\; e^{-i\omega t} \vec{d}(t) \tag{10}$$

and then uses it directly instead of $C(t)$:

$$I^\lambda(\omega) \propto \frac{1}{2\pi} \sum_i \rho_i \sum_f \omega_{fi}^4 |\vec{e}_\lambda \cdot \langle \vec{d}_{fi}(\omega) \rangle|^2 \tag{11}$$

where $\vec{e}_\lambda$ is the light polarization direction and each initial state i is assigned a population factor ρ_i. Similarly to other methods, this procedure is repeated many times and averaged (*cf.* Equation (4)).

The recently developed code, **Xenomorph**, is based on the models of Gigosos and González [30], where a straight line assumption is made. A general Schrödinger solver described in [31] is used to

obtain the eigenvalues $E_n(t)$ and eigenvectors $|n(t)\rangle$ at every time step of the simulation. The emitter time evolution operator is then evaluated:

$$U_l(t+\Delta t) = \left\{ \sum_n e^{-iE_n(t)\Delta t/\hbar} n(t)\rangle\langle n(t)| \right\} U_l(t) \tag{12}$$

and is used to obtain the dipole matrix. The Fourier transform of the latter is computed to obtain the line shape function, as is done in SimU (*cf.* Equations (10) and (11)).

2.2. The Models

The main difficulty in introducing the ion dynamics in the Stark line shape calculations is to develop a model that provides a sufficiently accurate solution of the evolution Equation (2) assuming an idealized stochastic process that conserves the statistical properties of the "real" interaction between the microfields and the radiating atom.

A successful model developed for neutral emitters—the model microfield method (MMM), due to Brissaud and Frisch [32,33]—involves stochastic fields that are constant in a given time interval and suddenly jump from one value to the next one at random times. The amplitudes of the field sequences are determined in order to be consistent with the static properties of the microfield, *i.e.*, the static-field probability distribution $Q(\mathbf{F})$. The jumping frequency $\nu(\mathbf{F})$ has to be chosen properly in order to reproduce the dynamics properties of the microfields represented by their autocorrelation function $< \mathbf{F}(t) \cdot \mathbf{F}(0) >$. In **QuantSt.MMM**, MMM (for ions) is combined with a quantum-statistical approach to calculate pressure broadening due to plasma electrons. The perturbation by electrons is considered to second order in the potential [34,35].

MELS and **MERL** are based upon the **BID** model. The latter derives from the MMM, but its formulation is based on statistical mechanics [36] and provides a unified description of radiative and transport properties for charged emitters [20]. The stochastic line shape is written as:

$$I_d(\omega) = -\frac{1}{\pi} Im \ll \mathbf{d}^\dagger | \frac{\int d\mathbf{F} Q(\mathbf{F}_i) G_{BID}(\omega, \mathbf{F}_i)}{1 + i\nu(\omega) \int d\mathbf{F} Q(\mathbf{F}_i) G_{BID}(\omega, \mathbf{F}_i)} | \mathbf{d}\rho_0 \gg \tag{13}$$

in which the resolvent is given by:

$$G_{BID}(\omega, \mathbf{F}_i) = \left(\omega - L_0 + \mathbf{d} \cdot \mathbf{F}_i - i\nu(\omega)\right)^{-1} \tag{14}$$

The jumping frequency $\nu(\omega)$ is chosen as:

$$\nu(\omega) = \frac{\nu_0}{1 + i\omega\tau}. \tag{15}$$

where the two parameters ν_0 and τ are defined in this model by the low- and high-frequency limits of the momentum autocorrelation function. Here, τ is assumed to be null.

Another approach is the frequency fluctuation model (**FFM**), on which the **PPP** code and, recently, the **QC-FFM** code rely. The latter is a hybrid model using the quasi-contiguous approximation [37] for H-like transitions and the FFM for modeling the microfield dynamics effect. The FFM relies on a different idealization of the stochastic process than MMM and BID. Here, the quantum system perturbed

by a time-dependent microfield behaves like a set of field-dressed two-level transitions (SDT) subject to a collision-type mixing process. More precisely, the fluctuation mechanism of these SDT obeys a stationary Markov process defined by the instantaneous probability of states $p_j = a_j / \sum_k a_k$ (a_j being the intensity of the SDT, j) and the transition rates between these states $\mathbf{W}_{k,j} = -\Gamma_j \delta_{k,j} + W_{k,j}$, where $\Gamma_{k,j} = \nu \delta_{i,j}$ and $W_{k,j} = \nu p_j$.

The typical fluctuation rate ν_{FFM} of the electric field, given by Equation (5), is used. Working in the Liouville space of the dressed two-level radiators, the line shape is written as [38]:

$$I_d(\omega) = \frac{1}{\pi} Re \sum_{j,k} i \ll D_k | G_{FFM}(\omega) | D_j p_j \gg \tag{16}$$

with the resolvent:

$$G_{FFM}(\omega) = (\omega - \mathbf{L}_\omega + i\mathbf{W})^{-1} \tag{17}$$

where $\mathbf{L}_\omega$ is the Liouville operator involving the transition energies of the SDT (ω_i) and D_i are the matrix elements of the dipole moment for the SDT. Due to the particular form of the matrix of transition rates $\mathbf{W}$, the dynamic line shape is written as [4]:

$$I_d(\omega) = \frac{\sum_k a_k}{\pi} Re \frac{\sum_k \frac{p_k}{\nu + i(\omega - \omega_k)}}{1 - \nu \sum_k \frac{p_k}{\nu + i(\omega - \omega_k)}} \tag{18}$$

Despite the fact that the two stochastic models lead to different functional forms, it follows that both BID and FFM recover the static limit for $\nu_{BID} = 0$ in Equation (14) and for $\nu_{FFM} = 0$ in Equation (18). In the opposite limit, both models recover the fast fluctuation limit ($\nu \to \infty$) that should approximate the "no ions" profile. However, BID recovers the impact limit in the line center whenever ν is large, while the FFM does not (see [39] for a more detailed discussion). We note that QC-FFM uses the FFM approximation for ions and electrons alike. For the latter, correctly approaching the impact approximation in the fast fluctuation limit becomes especially important. To this end, a modification to the effective fluctuation rate was introduced:

$$\tilde{\nu} = \nu + \frac{\nu^2}{\nu_0} \tag{19}$$

where ν_0 is an empirically obtained constant (for details, see [13]).

Two other models based on the collisional approach have been used, too. The **ST-PST** model is based on the standard theory with a number of options. Specifically, apart from the pure ST results, ST-PST can (and by default does) also compute the results of ST with penetrating collisions correctly accounted for analytically [18]. In addition, an **FST-FFM** calculation is also done [8]: first, an Ω is determined, exactly as described above for HSTRK_FST. Next, the FFM is applied to the field that excludes the fast, impact part. Last, the two profiles are convolved. As a result, the impact limit is correctly built in and recovered, hence extending the FFM validity without sacrificing its speed. Note, however, that with the current FST implementation, which uses the completed collision assumption for the impact phase space, the far wings are not accurate, as already discussed.

The **UTPP** code is devoted to the calculation of hydrogen line shapes in regimes where the impact approximation for ions is reasonably accurate. Such a regime is attained for lines with a low principal

quantum number in magnetic fusion experiments in the absence of Doppler broadening (Doppler-free line shape models were required for radiation transport simulations, e.g., [40]). In UTPP, a line shape is calculated using the following formula:

$$I(\omega) = \frac{1}{\pi}\mathrm{Re} \ll \mathbf{d}^{\dagger}|\frac{1}{s + iL_0 + K(s)}|\mathbf{d}\rho_0 \gg \tag{20}$$

where $s = -i\omega$ and $K(s)$ is a collision operator calculated in a framework similar to that used in the Voslamber unified theory (Bogoliubov-Born-Green-Kirkwood-Yvon (BBGKY) hierarchy), but here adapted to ions [19]. The main advance with respect to the unified theory is that the collision operator accounts for the finite lifetime of the atom during each collision; this lifetime yields an effective range for the action of the microfield of the order of $v/\bar{\gamma}$, where $\bar{\gamma}$ is a typical matrix element of the collision operator (see the discussion in [41]). This model (and its adaptation to electrons) does not lead to a divergent collision operator if the Debye length is assumed infinite, which is in contrast to standard hydrogen models (see [42]); this makes it suitable for the presented cases, provided the perturbing species under consideration is strongly dynamic.

3. Comparisons and Discussion

To test the accuracy of the different numerical codes based either on stochastic and collisional models or numerical simulations, calculations for standardized case problems were carried out and analyzed [5]. A preselected set of transitions on a grid of electron densities (n_e) and temperatures ($T = T_e = T_i$) have been proposed, and for each case, the atomic and plasma models have been specified. In this way, various contributions that can affect the Stark broadened line shape, such as the influence of particle correlations on electric microfields, the effects of external fields, the high-n merging with continuum or the satellite broadening, have been investigated. For the present purpose, we will only focus on cases where the ion dynamics effect was studied.

3.1. Hydrogen Lyman-α and Lyman-β Lines

The following examples consider the hydrogen Lyman-α and Lyman-β lines in an ideal plasma consisting of protons for electron densities $n_e = 10^{17} - 10^{19}$ cm^{-3} and temperatures $T = 1 - 100$ eV. These cases are not necessarily practical, but permit basic comparisons to assess the influence of ion dynamics on the line profiles. Here, only pure ionic linear Stark effect is considered ($\Delta n \neq 0$ interactions are ignored) and the fine structure is not taken into account. The concept of ideal plasma means that unscreened particles moving along straight path trajectories are considered in the numerical simulations, and the Holtsmark static-field distribution function [22] is used in the models.

An overall comparison of the results is presented in Figure 1. For each subcase (determined by a combination of (n_e, T)) and for each code, ratios between the full-width at half-maximum (FWHM) and an average of FWHM of all submitted results have been evaluated [5]:

$$R_i = \frac{\mathrm{FWHM}}{< \mathrm{FWHM} >}. \tag{21}$$

The graph is divided in two regions: the left side corresponds to results for the Lyman-α line and the right side to the Lyman-β line. Each region is divided into three sub-regions that correspond to the three densities chosen. Finally, in each sub-region, each set of results corresponds to the temperatures, $T = 1,\ 10,\ 100$ eV, respectively. For the Lyman-α case, the results present a large dispersion, deviating from the average by more than a factor of five in each direction. In contrast, the scatter for the Lyman-β shows a rather good agreement between the codes. In fact, these two lines present a completely different behavior concerning the ion dynamics effect.

Figure 1. Overall comparison of the workshop results of the ion dynamics effect on Lyman-α and -β hydrogen lines. For each subcase, *i.e.*, different pairs of (n_e, T), the scatter of ratios between the different results and an average value is plotted. The different symbols correspond to: (black dot) SimU; (red square) UTPP; (blue triangle) PPP; (blue asterisk) Xenomorph; (cyan open triangle) HSTRK; (cyan triangle) HSTRK_FST; (red diamond) ER-simulation; (green circle) QuantST.MMM; (black cross) QC-FFM.

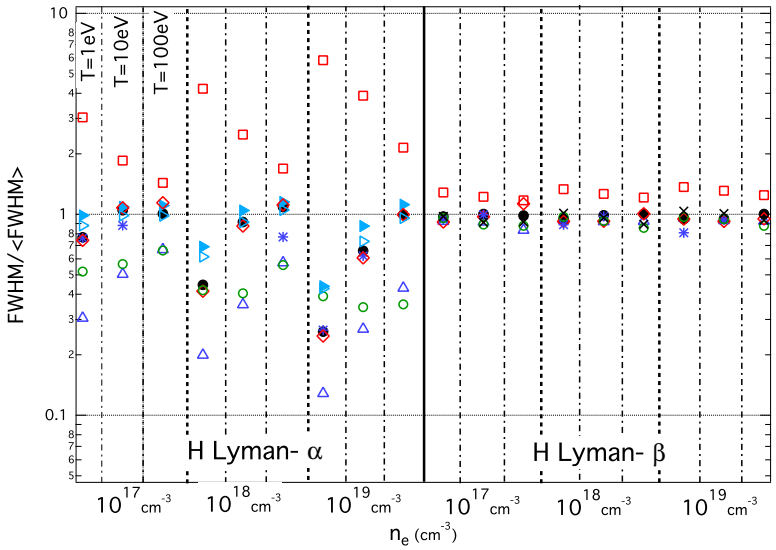

3.1.1. The Lyman-α Line

The static Stark effect of the Lyman-α line (as all the $\Delta n = n - n' = 1$ lines, where n and n' are the principal quantum number of the upper and lower states, respectively) features a strong unshifted component that is highly sensitive to the ion dynamics effect. Thus, even though the Lyman-α line is the simplest case from the atomic structure point of view, it presents a non-trivial Stark-broadening behavior.

In Figure 2, only results from the numerical simulations are plotted for the sake of clarity. One sees that in the range of 1 to 100 eV, the simulations either predict that the width increases when the plasma temperature increases (for the fixed density $n_e = 10^{19}$ cm^{-3}, they present a temperature dependency as $\sim T^{1/3}$) or predict that the width is mostly insensitive to the temperature's rise (for the fixed density $n_e = 10^{17}$ cm^{-3}). Concerning the dependence on the plasma density, the width, which is mainly due to the width of the central component for $T = 1$ eV, increases as $n_e^{1/3}$. For $T = 100$ eV, the results show a $n_e^{2/3}$ dependence, corresponding to the quasi-static behavior of the lateral components [2]. We mention, however, that the cutoff of the Coulomb interaction at a finite box size may not accurately reproduce an ideal plasma [42].

Figure 2. Lyman-α ion FWHMs as a function of (**a**) of T at fixed densities and (**b**) of n_e at fixed temperatures. The ideal, one-component plasma consisting of protons is assumed. Only results from numerical simulations are presented: (red circle) ER-simulation; (blue square) HSTRK; (black dot) SimU; (green asterisk) Xenomorph.

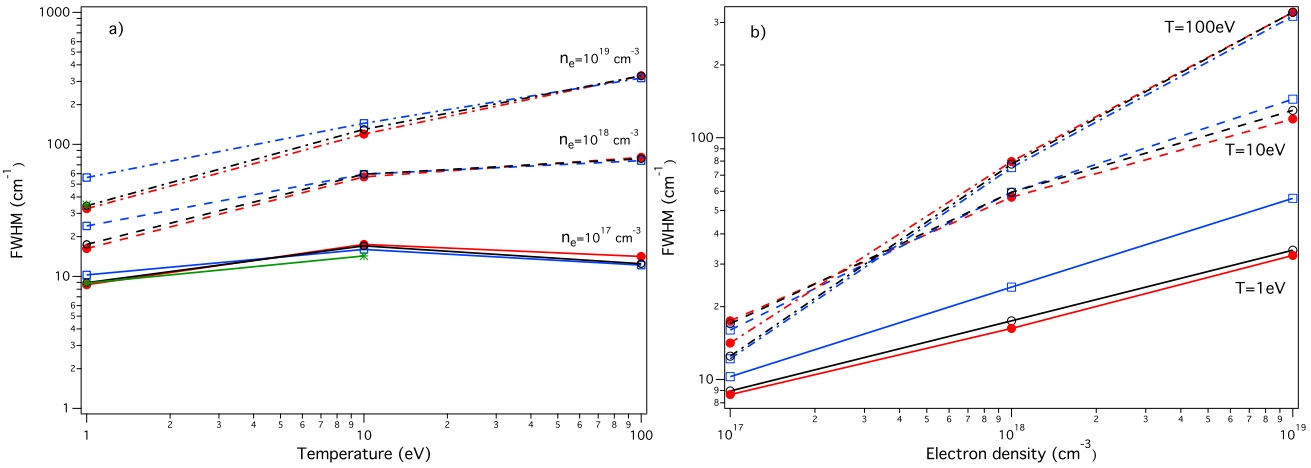

In general, the highest temperature results in the best agreement among simulation codes, for all densities. For lower temperature differences are more discernible, with the most discernible being the appearance of shoulders in ER-simulation and SimU for the highest density and lowest temperature and the lack of such shoulders in HSTRK. This is a general trend at the lowest temperature of 1 eV for all densities, with HSTRK producing significantly larger widths than both ER-simulation and SimU.

The dispersion of the results of the various models demonstrates the difficulties in accurately treating the ion dynamics effect (see Figure 3). In every studied case, the PPP displays a weaker ion dynamics effect on this line, probably due to an incomplete description of this effect on the central component. The FFM mixes the unshifted components with the Stark-shifted components with a unique fluctuation rate. Yet, the unshifted components are not sensitive to the microfield intensity, but only to its rotation, whereas the Stark-shifted components are sensitive to the microfield vibration [43]. A more detailed discussion on the influence of the microfield directionality in the line shape is presented in a separate study [44].

Concerning the description of the ion dynamics effect in terms of microfields mixing, the QuantST.MMM results compare less favorably to the simulations, especially in the far wings.

As already discussed, the far wings of HSTRK_FST are not reliable in this version, due to the complete collision assumption used in the computation of the impact part. This is an artifact of this assumption rather than an inherent limitation of the method.

The UTPP code yields a line width systematically larger than the results obtained from other codes or models and, in particular, the results from numerical simulations. If the latter give reference profiles, this result is expected in general, because the plasma conditions are such that static effects with simultaneous strong collisions are important. However, the application of the UTPP to the electron broadening (not presented here) also indicates a significant discrepancy, with an overestimate of the numerical simulation results by a factor of two. It has been suggested that this discrepancy stems from the fact that the simulations that use a box actually miss a significant contribution to the line broadening, due to the far perturbers, namely, those inside the $v/\bar{\gamma}$ sphere, but outside the simulation box. It is quite difficult to test

this argument by enlarging the simulation box up to $v/\bar{\gamma}$, because this would imply a very large number of particles (up to several billions). An adaptation of UTPP able to account for a plasma of finite size has been performed and has led to a line shape in good agreement with the simulations [42]. This could suggest that an artificial setting of an infinite Debye length in the numerical simulations able to work with an infinite Debye length requires a careful interpretation of the results.

Figure 3. Lyman-α line shape in ideal ionic one component plasma (OCP) calculated for (**a**) the more dynamical regime ($n_e = 10^{17}$ cm^{-3} and $T = 100$ eV) and (**b**) the more static regime ($n_e = 10^{19}$ cm^{-3} and $T = 1$ eV): SimU (black dash); ER-simulation (red dash); HSTRK_FST (blue dot-dash); PPP (solid cyan); QuantST.MMM (solid purple); UTPP (solid green).

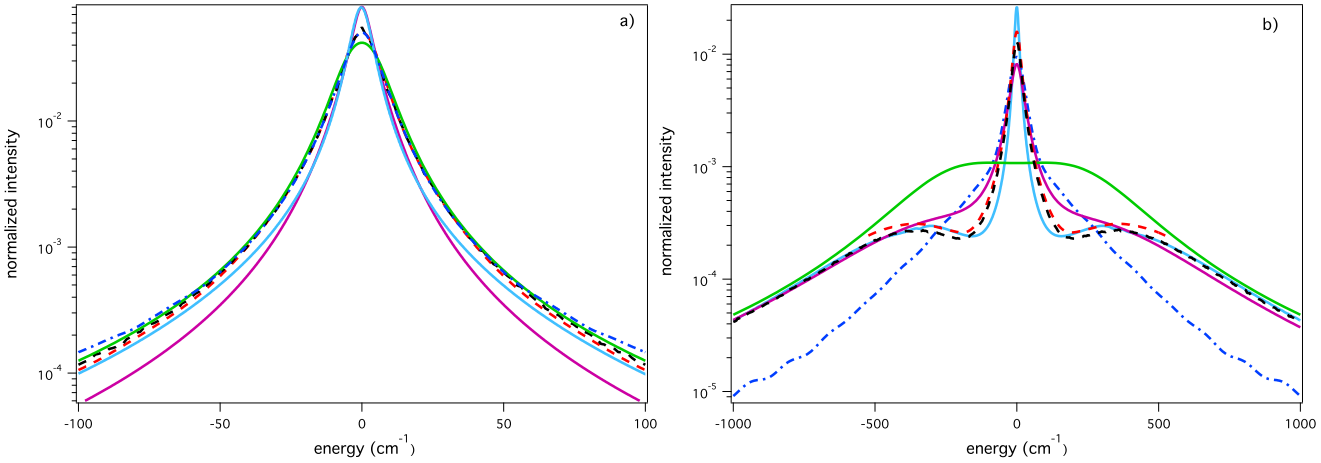

3.1.2. The Lyman-β Line

The static profile of the Lyman-β line (as all of the $\Delta n = 2$ lines) normally shows a dip at the line center. One sees in Figure 4 that, due to the ion dynamics effect, the simulations fill this dip, and the width increases with increasing temperature. This trend is seen for plasma conditions that correspond to typical microfield fluctuation rate values (see Equation (5)) smaller than the splitting of the two Stark components measured in the static case. Here, for $n_e = 10^{17}$ cm^{-3}, the Stark splitting of the static line shape is equal to 5.9×10^{-3} eV, and the typical fluctuation rate is equal to $\hbar\nu = 6.8 \times 10^{-4}$ eV and $\hbar\nu = 2.5 \times 10^{-3}$ eV for $T = 1$ eV and $T = 10$ eV, respectively. For $T = 100$ eV, $\hbar\nu = 2.2 \times 10^{-2}$ eV, *i.e.*, three-times greater that the Stark splitting in the static case. The two components merge, leading to a line shape that is narrower than the one calculated for $T = 10$ eV, as is seen in Figure 4a. Note that for an infinite fluctuation rate, the line shape becomes the Dirac δ-function.

The agreement between the Lyman-β FWHM results of different codes is much better than that for Lyman-α, as is shown in Figure 1. Nevertheless, the concept of FWHM is not really adequate for such a line with a dip in the center. A better way to discuss the ion dynamics effect on a Lyman-β line would be the measure of the relative dip given by:

$$D_{dip} = \frac{I_{max} - I_{\omega_0}}{I_{max}} \tag{22}$$

where I_{max} and I_{ω_0} are the maximum intensity and the intensity at the center of the line, respectively. Table 1 shows the relative dip from the different codes for $n_e = 10^{17}$ cm^{-3}, while the line shapes are shown in Figure 5.

Obviously, the QC approximation, and, hence, the QC-FFM method, is inherently unable to reproduce the central structure (a peak or a dip) of a low-n spectral line. However, the wings of such lines, as well as entire profiles of higher-n transitions, show a very good agreement with numerical simulations [13].

Figure 4. The ion dynamics effect on the Lyman-β line for different values of T obtained by SimU: (solid red $T = 1$ eV; (green dash) $T = 10$ eV and (blue dot-dash) $T = 100$ eV at a fixed (**a**) $n_e = 10^{17}$ cm^{-3} and (**b**) $n_e = 10^{19}$ cm^{-3}. The ideal one-component plasma consisting of protons is assumed.

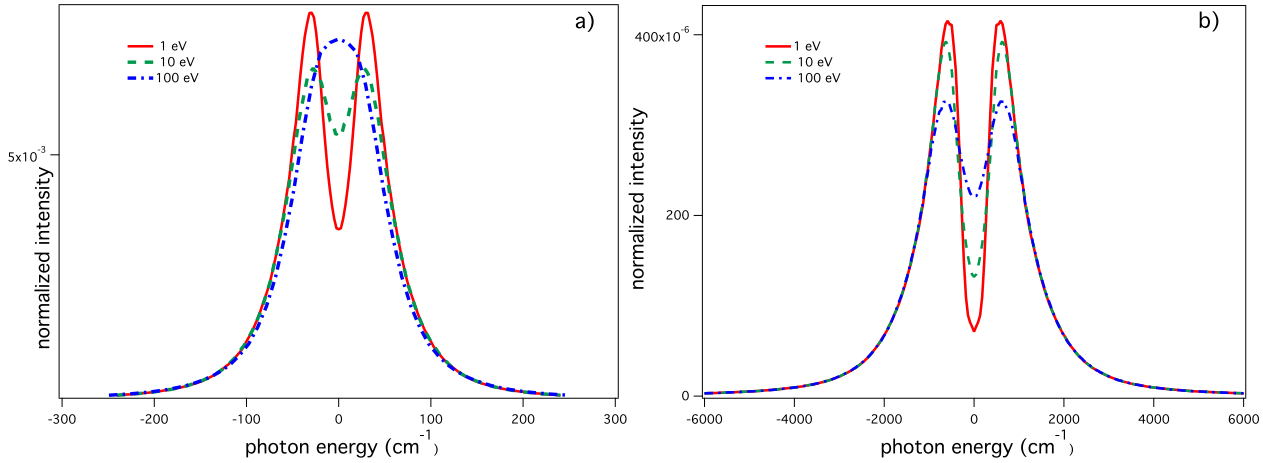

Figure 5. Lyman-β line for $n_e = 10^{17}$ cm^{-3} and $T = 10$ eV: SimU (black dash); ER-simulation (red dash); Xenomorph (blue dot-dash); PPP (solid cyan); QC-FFM (solid orange); QuantST. MMM (solid purple); UTPP (solid green).

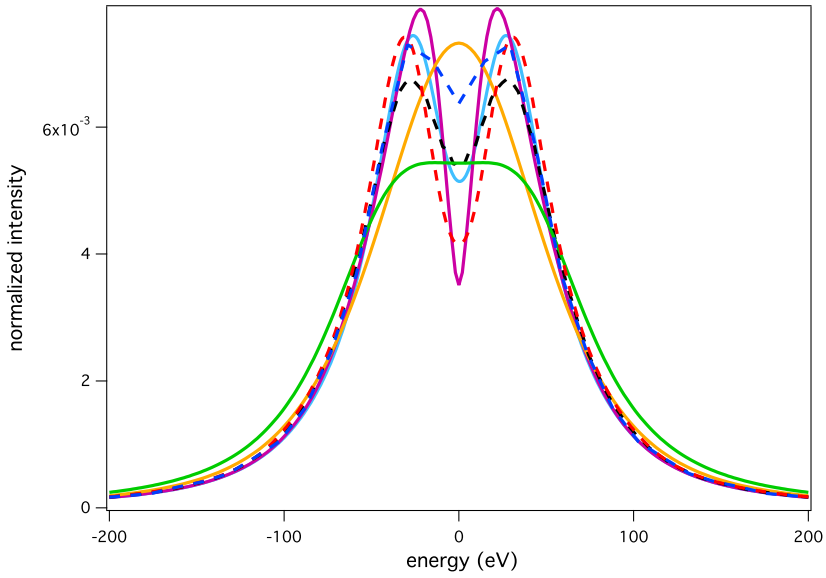

Table 1. The relative dip (%) measured on the Lyman-β line from the different codes for $n_e = 10^{17}$ cm^{-3}.

T (eV) =	1	10	100
ER-simulation	75	44	10
SimU	56	19	0
Xenomorph	56	14	/
PPP	70	31	0
QuantSt.MMM	71	55	32
UTPP	0.6	0.6	0

3.2. Argon He-α and He-β Lines

The argon H- and He-like lines are observed in inertial confinement fusion implosion core plasmas when a tracer amount of argon is added to the deuterium gas fill to diagnose the plasma conditions [45]. Such a diagnostic relies on the temperature sensitivity of the satellite line;s relative intensity to the resonance one and the density dependence in the Stark broadening of both satellite and resonance line profiles [46]. Moreover, they are sensitive to the ion dynamics effects and present a challenge for theoretical models [47]. We only focus here on the He-α and He-β lines. A specific study of the effect of satellite line shapes on the He-β line can be found elsewhere [48].

Two electron densities, $n_e = 5 \times 10^{23}$ cm^{-3} and $n_e = 2 \times 10^{24}$ cm^{-3}, and a plasma temperature of $T = 1$ keV were selected for this comparison. Plasma ions are deuterons with 0.1% Argon XVII. The MELS and MERL (BID) and the PPP (FFM) models submitted results, and the numerical simulation, SimU, was recently extended to describe such lines. Here, the simulation accounts for all interactions; no artificial cutoff arises as for the ideal case conditions. We consider it as a reference.

Figure 6 displays the He-α profiles calculated with the PPP code within the quasi-static approximation. For clarity, results from MELS are not plotted here, but the agreement between the two codes is very good. The small differences observed between both codes are explained by the difference in the electron broadening treatment (the impact approximation is used in PPP, while a frequency dependent collision operator is used in MELS). The quasi-static profile is the superimposition of a strong intensity component, which corresponds to the $1s2p\ ^1P_1 - 1s^2\ ^1S_0$ resonance transition, and a weak intensity component, which corresponds to the $1s2p\ ^3P_1 - 1s^2\ ^1S_0$ intercombination transition. The pure electron broadened profiles are plotted for each component for a better understanding of the ionic Stark effect on the line shapes. Both components display a pronounced quadratic Stark effect in their "blue" wing, and forbidden lines appear on top of their "red" wing.

Concerning the ion dynamics effect, BID and FFM show a different behavior. BID profiles present a more pronounced deviation relative to the static calculation than the FFM. Figures 7 and 8 illustrate this for the two densities. These discrepancies cannot be explained by the use of a different fluctuation rate in both models. A specific study using the same fluctuation rate for both models shows that the BID and FFM are in good agreement for varying values of this parameter for the resonance line, but not for the

intercombination line [39]. Figure 9 shows this difference using both models with the same fluctuation rate. The difference seen on the forbidden component of the intercombination line might be due to a numerical inaccuracy, because of the very weak value of its intensity.

Moreover, numerical simulation results from the SimU code do not discriminate between the stochastic models. For example, in Figure 9, both models agree with the simulation on the allowed transitions, but not on the forbidden transitions. This might be due to a different dynamics between strong microfields, which are emphasized by the quadratic Stark effect of the allowed transitions, and weak microfields, which are the cause of the linear Stark effect of the forbidden transitions.

Figure 6. The He-α line calculated within the quasi-static approximation for $T = 1$ keV and $n_e = 2 \times 10^{24}$ cm^{-3}. (Black line) the entire profile; (blue line) resonant line profile; (red line) intercombination line profile. The pure electron-broadened profiles are plotted in dashed lines for each component.

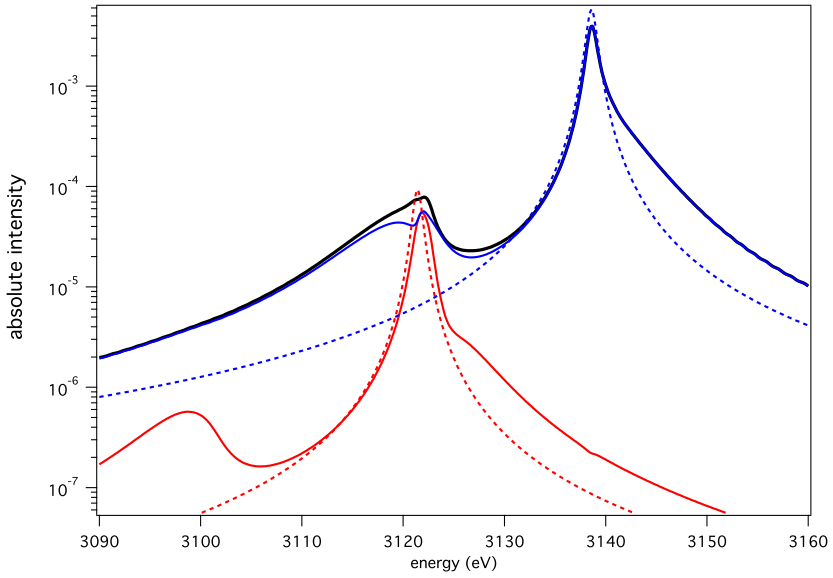

Figure 7. The He-α line for $T = 1$ keV and $n_e = 5 \times 10^{23}$ cm^{-3}: static ions MELS (grey dash); ion dynamics BID (solid red); FFM (solid blue) and SimU (black dot).

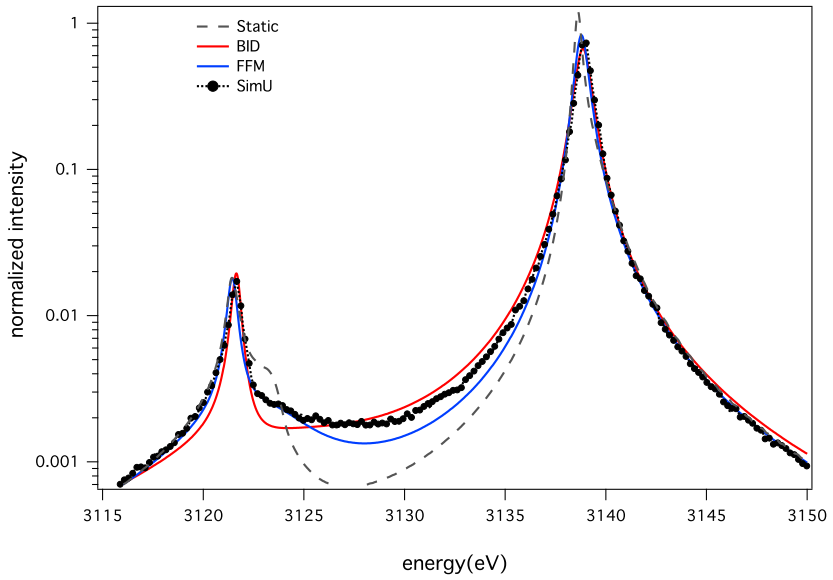

Figure 8. The He-α line for $T = 1$ keV and $n_e = 2 \times 10^{24}$ cm^{-3}: static ions (grey dash); ion dynamics BID (solid red); FFM (solid blue); and SimU (black dot).

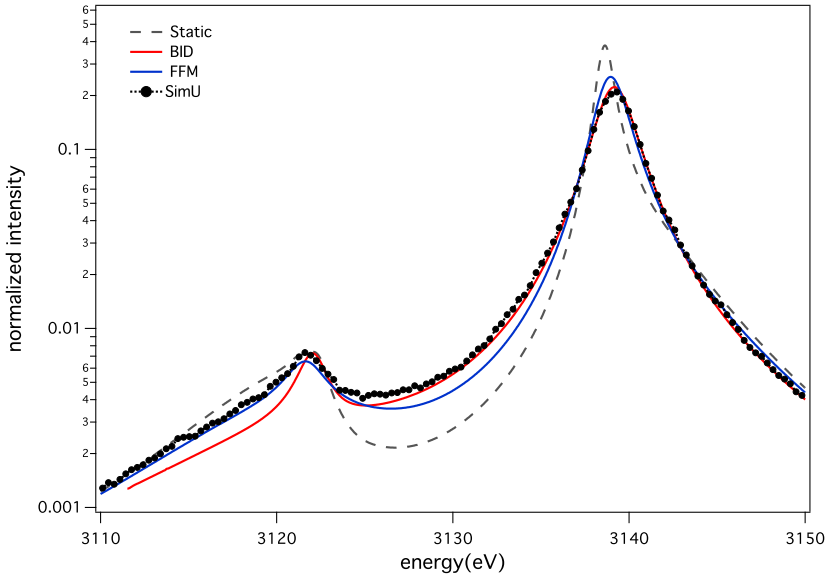

Figure 9. The He-α line for $T = 1$ keV and $n_e = 2 \times 10^{24}$ cm^{-3}: (**a**) resonance line and (**b**) intercombination line. Static ions MELS (red dash) and PPP (blue dash); ion dynamics BID (solid red); FFM (solid blue); and SimU (black dot).

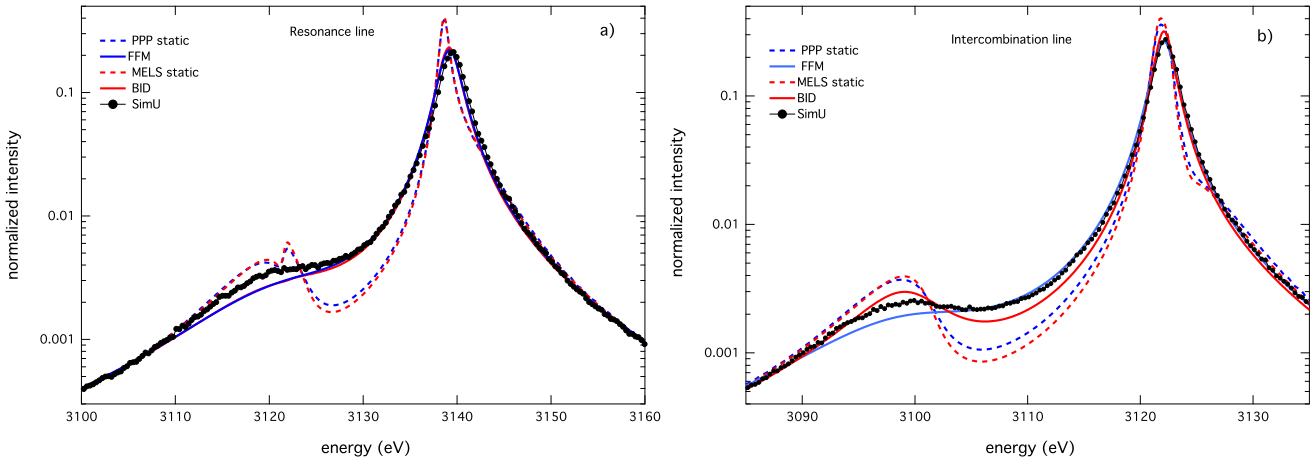

In order to explain these differences, a specific study on the pure ion-broadened profiles was carried out. As both resonance and intercombination lines present similar atomic systems, we will only focus the discussion of the resonance line. Figure 10 shows FFM profiles for different fluctuation rates and the SimU profile. It seems that different values of ν are needed to reproduce different portions of the simulated profile. A lower fluctuation rate has to be used to fit the forbidden component, whereas a higher ν is needed to reproduce the allowed component. This can be interpreted as weak and strong microfields not producing the same dynamics effect on the line shape.

Figure 10. The He-α line, the strong component for $T = 1$ keV and $n_e = 5 \times 10^{23}$ cm^{-3}: SimU (black circles); FFM with $\nu = 3$ eV (solid blue); $\nu = 5.62$ eV (solid red); and $\nu = 8$ eV (solid black).

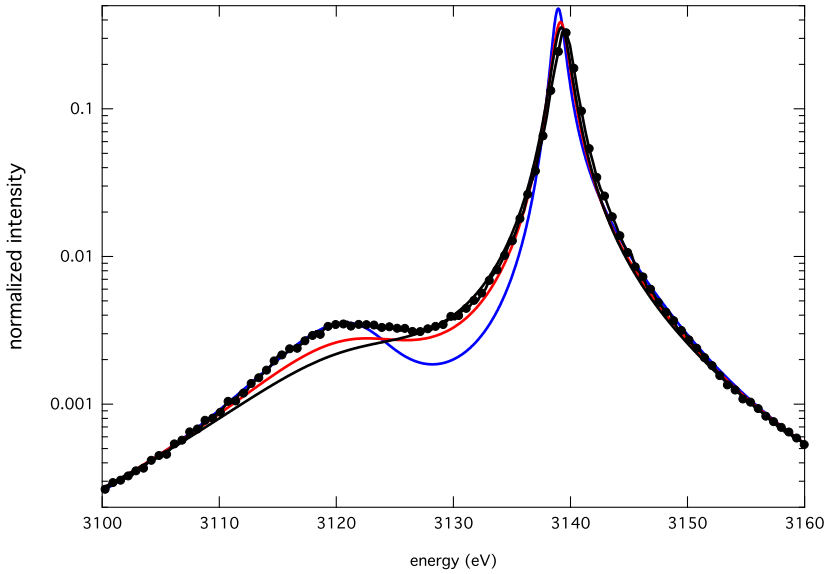

Finally, the He-β line is presented in Figure 11. At the chosen plasma conditions, as the Stark splitting of the He-β quasi-static line shape is greater than the fluctuation rate and the electron width is larger, the ion dynamics effect is less pronounced than on the He-α. Figure 11 shows SimU, BID and FFM in rather good agreement relative to the discrepancies of their quasi-static profiles. The measure of the dynamics-to-static relative depth is defined by:

$$D_{d-s} = \frac{I_{dyn}(\omega_0) - I_{stat}(\omega_0)}{I_{dyn}(\omega_0)} \tag{23}$$

There is a fairly good agreement between the BID and the FFM (see Table 2).

Figure 11. The He-β line for $T = 1$ keV and (**a**) $n_e = 5 \times 10^{23}$ cm^{-3}; (**b**) $n_e = 2 \times 10^{24}$ cm^{-3}. Static ions: MERL (red dot), PPP (blue dot); SimU (black dot); BID (solid red); FFM (solid blue).

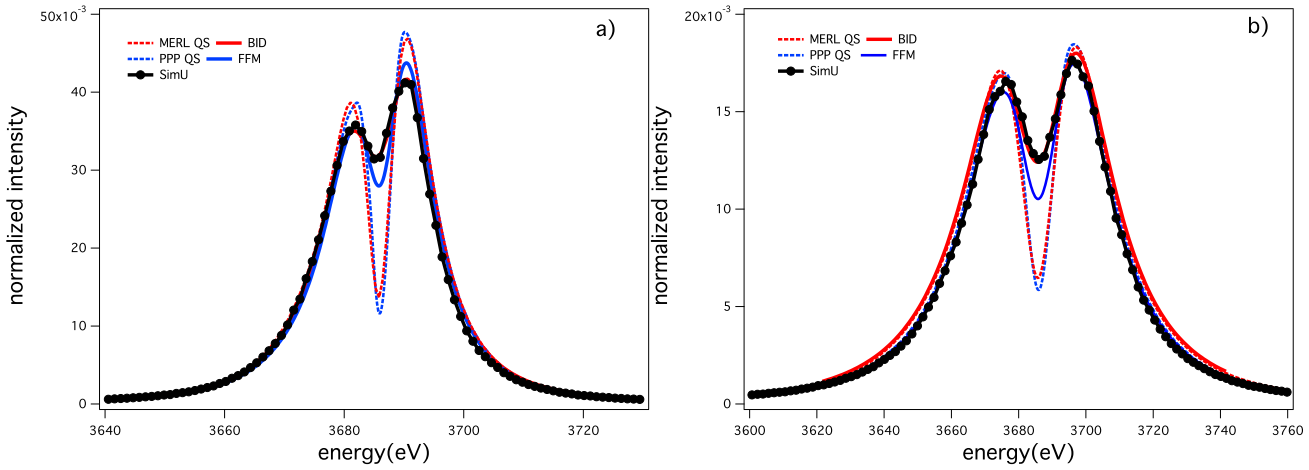

Table 2. Dynamics-to-static relative dip (%) measured on the argon He-β line for $T = 1$ keV.

Models	BID	FFM
$N_e = 5 \times 10^{23}$ cm^{-3}	58	57
$N_e = 1 \times 10^{24}$ cm^{-3}	50	51
$N_e = 2 \times 10^{24}$ cm^{-3}	47	48

4. Conclusions

Line shape calculations from different numerical codes that account for the ion dynamics effect were presented. To test the accuracy of the different codes, standardized case problems have been chosen and a systematic cross-comparison has been done. Results from four numerical simulations based on different algorithms and seven models relying on either stochastic or collisional processes, have been then submitted.

Surprisingly, the results obtained on the hydrogen Lyman-α line in an ideal OCP plasma consisting of protons presents a large dispersion. While the numerical simulations show a relatively good agreement between each other, the FFM and MMM models systematically display a weaker width than the averaged results. This can be explained by an incomplete description of the ion dynamics effect on the central component of this line. The detailed study on the influence of the microfields directionality in the line shape presented in this volume, [44] or other methods discussed here can help improve the modeling of lines with unshifted components. The overestimate of the UTPP code based on a collisional approach is explained by an incomplete description of ion static effects. The results obtained on the H Lyman-β line present a better agreement between all codes.

Concerning the ion dynamics effect on the argon He-α and -β lines, BID and FFM show a different behavior that has been attributed, up to now, to numerical inaccuracies, due to the very weak value of the line intensities. The recently developed numerical simulation code, SimU, could not help discriminate between the two models, but highlighted another problem: it seems that different values of fluctuation rates have to be used to reproduce different portions of the simulated profile. As both the linear and quadratic Stark effect, which are linked to the weak and strong values of microfields, respectively, are involved in producing the shape of this line, one can wonder if a frequency- (or field-) dependent fluctuation rate is needed to give a better description of ion dynamics on this line.

Acknowledgments

The authors would like to acknowledge the International Atomic Energy Agency B.J. Braams and H.-K. Chung for the organizational and financial support of this workshop.

Author Contributions

The present work is based on codes developed by all authors, who also participated in all aspects of this work.

Conflicts of Interest

The authors declare no conflicts of interest.

References

1. Griem, H.R. *Principles of Plasma Spectroscopy*; Cambridge University Press: Cambridge, UK, 1997.
2. Griem, H.R. *Spectral Line Broadening by Plasmas*; Academic Press: New York, NY, USA, 1974; ISBN:0-12-302850-7.
3. Stambulchik, E.; Maron, Y. Plasma line broadening and computer simulations: A mini-review. *High Energy Density Phys.* **2010**, *6*, 9–14.
4. Calisti, A.; Mossé, C.; Ferri, S.; Talin, B.; Rosmej, F.; Bureyeva, L.A.; Lisitsa, V.S. Dynamic Stark broadening as the Dicke narrowing effect. *Phys. Rev. E Stat. Nonlin. Soft Matter Phys.* **2010**, *81*, 016406, doi:10.1103/PhysRevE.81.016406.
5. Stambulchik, E. Review of the 1st Spectral Line Shapes in Plasmas code comparison workshop. *High Energy Density Phys.* **2013**, *9*, 528–534.
6. Gigosos, M.A.; Gonzalez, M.A. Comment on "A study of ion-dynamics and correlation effects for spectral line broadening in plasmas: K-shell lines". *J. Quant. Spectrosc. Radiat. Transf.* **2007**, *105*, 533–535.
7. Alexiou, S. Stark broadening of hydrogen lines in dense plasmas: Analysis of recent experiments. *Phys. Rev. E Stat. Nonlin. Soft Matter Phys.* **2005**, *71*, 066403, doi:10.1103/PhysRevE.71.066403.
8. Alexiou, S. Implementation of the Frequency Separation Technique in general lineshape codes. *High Energy Density Phys.* **2013**, *9*, 375–384.
9. Stambulchik, E.; Maron, Y. A study of ion-dynamics and correlation effects for spectral line broadening in plasma: K-shell lines. *J. Quant. Spectrosc. Radiat. Transf.* **2006**, *99*, 730–749.
10. Stambulchik, E.; Alexiou, S.; Griem, H.R.; Kepple, P.C. Stark broadening of high principal quantum number hydrogen Balmer lines in low-density laboratory plasmas. *Phys. Rev. E Stat. Nonlin. Soft Matter Phys.* **2007**, *75*, 016401, doi:10.1103/PhysRevE.75.016401.
11. Gomez, T.A.; Mancini R.C.; Montgomery M.H.; Winget D.E. White dwarf line shape theory including ion dynamics and asymmetries. **2014**, in preparation.
12. Lorenzen, S. Comparative Study on Ion-Dynamics for Broadening of Lyman Lines in Dense hydrogen Plasmas. *Contrib. Plasma Phys.* **2013**, *53*, 368–374.
13. Stambulchik, E.; Maron, Y. Quasicontiguous frequency-fluctuation model for calculation of hydrogen and hydrogen-like Stark-broadened line shapes in plasmas. *Phys. Rev. E Stat. Nonlin. Soft Matter Phys.* **2013**, *87*, 053108, doi:10.1103/PhysRevE.87.053108.
14. Iglesias, C.A.; Vijay, S. Robust algorithm for computing quasi-static Stark broadening of spectral lines. *High Energy Density Phys.* **2010**, *6*, 399–405.
15. Woltz, L.A.; Hooper, C.F., Jr. Calculation of spectral line profiles of multielectron emitters in plasmas. *Phys. Rev. A* **1988**, *38*, 4766–4771.
16. Mancini, R.C.; Kilcrease, D.P.; Woltz, L.A.; Hooper, C.F. Calculational Aspects of the Stark Line Broadening of Multielectron Ions in Plasmas. *Comput. Phys. Commun.* **1991**, *63*, 314–322.

17. Calisti, A.; Khelfaoui, F.; Stamm, R.; Talin, B.; Lee, R.W. Model for the line shapes of complex ions in hot and dense plasmas. *Phys. Rev. A* **1990**, *42*, 5433–5440.
18. Alexiou, S.; Poquérusse, A. Standard line broadening impact theory for hydrogen including penetrating collisions. *Phys. Rev. E Stat. Nonlin. Soft Matter Phys.* **2005**, *72*, 046404, doi:10.1103/PhysRevE.72.046404.
19. Rosato, J.; Capes, H.; Stamm, R. Influence of correlated collisions on Stark-broadened lines in plasmas. *Phys. Rev. E Stat. Nonlin. Soft Matter Phys.* **2012**, *86*, 046407, doi:10.1103/PhysRevE.86.046407.
20. Boercker, D.B.; Iglesias, C.A.; Dufty, J.W. Radiative and transport properties of ions in strongly coupled plasmas. *Phys. Rev. A* **1987**, *36*, 2254–2264.
21. Talin, B.; Calisti, A.; Godbert, L.; Stamm, R.; Lee, R.W.; Klein, L. Frequency-fluctuation model for line shape calculations in plasma spectroscopy. *Phys. Rev. A* **1995**, *51*, 1918–1928.
22. Holtsmark, J. Über die Verbreiterung von Spektrallinien. *Ann. Phys.* **1919**, *58*, 577–630.
23. Iglesias, C.A.; Boercker, D.B.; Iglesias, C.A. Electric field distributions in strongly coupled plasmas. *Phys. Rev. A* **1985**, *31*, 1681–1686.
24. Gigosos, M.A.; Gonzalez, M.A.; Cardeñoso, V. Computer simulated Balmer-alpha, -beta and -gamma Stark line profiles for non-equilibrium plasmas diagnostics. *Spectrochim. Acta Part B* **2003**, *58*, 1489–1504.
25. Gigosos, M.A.; Cardeñoso, V. New plasma diagnostics table of hydrogen Stark broadening including ion dynamics. *J. Phys. B-At. Mol. Opt. Phys.* **1996**, *29*, 4795–4838.
26. Hegerfeldt, G.; Kesting, V. Collision-time simulation technique for pressure-broadened spectral lines with applications to Ly-α. *Phys. Rev. A* **1988**, *37*, 1488–1496.
27. Filon, L.N.G. On a quadrature formula for trigonometric integrals. *Proc. R. Soc. Edinb.* **1928**, *49*, 38–47.
28. Pfennig, H. On the Time-Evolution Operator in the Semiclassical Theory of Stark-Broadening of hydrogen Lines. *J. Quant. Spectrosc. Radiat. Transf.* **1972**, *12*, 821–837.
29. Lisitsa, V.S.; Sholin, G.V. Exact Solution of the Problem of the Broadening of the hydrogen Spectral Lines in the One-Electron Theory. *Sov. J. Exp. Theor. Phys.* **1972**, *34*, 484–489.
30. Gigosos, M.A.; González, M.A. Calculations of the polarization spectrum by two-photon absorption in the hydrogen Lyman-α line. *Phys. Rev. E Stat. Nonlin. Soft Matter Phys.* **1998**, *58*, 4950–4959, doi:10.1103/PhysRevE.58.4950.
31. Djurović, S.; Ćirišan, M.; Demura, A.V.; Demchenko, G.V.; Nikolić, D.; Gigosos, M.A.; Gonzalez, M.Á. Measurements of H_β Stark central asymmetry and its analysis through standard theory and computer simulations. *Phys. Rev. E Stat. Nonlin. Soft Matter Phys.* **2009**, *79*, 046402, doi:10.1103/PhysRevE.79.046402.
32. Frisch, U.; Brissaud, A. Theory of Stark broadening—I soluble scalar model as a test. *J. Quant. Spectrosc. Radiat. Transf.* **1971**, *11*, 1753–1766.
33. Frisch, U.; Brissaud, A. Theory of Stark broadening—II exact line profile with model microfield. *J. Quant. Spectrosc. Radiat. Transf.* **1971**, *11*, 1767–1783.
34. Günter, S.; Hitzschke, L.; Röpke, G. Hydrogen spectral lines with the inclusion of dense-plasma effects. *Phys. Rev. A* **1991**, *44*, 6834–6844.

35. Lorenzen, S.; Omar, B.; Zammit, M.C.; Fursa, D.V.; Bray, I. Plasma pressure broadening for few-electron emitters including strong electron collisions within a quantum-statistical theory. *Phys. Rev. E Stat. Nonlin. Soft Matter Phys.* **2014**, *89*, 023106, doi:10.1103/PhysRevE.89.023106.
36. Dufty, J.W. *Spectral Lines Shapes*; Wende, B., Ed.; De Gruyter: New York, NY, USA, 1981.
37. Stambulchik, E.; Maron, Y. Stark effect of high-n hydrogen-like transitions: Quasi-contiguous approximation. *J. Phys. B-At. Mol. Opt. Phys.* **2008**, *41*, 095703, doi:10.1088/0953-4075/41/9/095703.
38. Mossé, C.; Calisti, A.; Stamm, R.; Talin, B.; Lee, R.W.; Klein, L. Redistribution of resonance radiation in hot and dense plasmas *Phys. Rev. A* **1999**, *60*, 1005–1014.
39. Iglesias, C. Efficient algorithms for stochastic Stark-profile calculations. *High Energy Density Phys.* **2013**, *9*, 209–221.
40. Rosato, J.; Reiter, D.; Kotov, V.; Marandet, Y.; Capes, H.; Godbert-Mouret, L.; Koubiti, M.; Stamm, R. Progress on radiative transfer modelling in optically thick divertor plasmas. *Contrib. Plasma Phys.* **2010**, *50*, 398–403.
41. Rosato, J.; Capes, H.; Stamm, R. Divergence of the Stark collision operator at large impact parameters in plasma spectroscopy models. *Phys. Rev. E Stat. Nonlin. Soft Matter Phys.* **2013**, *88*, 035101:1–035101:3.
42. Rosato, J.; Capes, H.; Stamm, R. Ideal Coulomb plasma approximation in line shape models: Problematic issues. *Atoms* **2014**, *2(2)*, 277–298.
43. Lisitsa, V. Private communication.
44. Calisti, A.; Demura, A.V.; Gigosos, M.A.; GonzÃąlez-Herrero, D.; Iglesias, C.A.; Lisitsa, V.S.; Stambulchik, E. Influence of Microfield Directionality on Line Shapes. *Atoms* **2014**, *2*, 259–276.
45. Chung, H.-K.; Lee, R.W. Application of NLTE population kinetics. *High Energy Density Phys.* **2009**, *5*, 1–14.
46. Woolsey, N.C.; Hammel, B.A.; Keane, C.J.; Asfaw, A.; Back, C.A.; Moreno, J.C.; Nash, J.K.; Calisti, A.; Mossé, C.; Stamm, R.; *et al*. Evolution of electron temperature and electron density in indirectly driven spherical implosions. *Phys. Rev. E Stat. Nonlin. Soft Matter Phys.* **1996**, *56*, 2314, doi:10.1103/PhysRevE.56.2314.
47. Haynes, D.A.; Garber, D.T.; Hooper, C.F.; Mancini, R.C.; Lee, Y.T.; Bradley, D.K.; Delettrez, J.; Epstein, R.; Jaanimagi, P.A. Effects of ion dynamics and opacity on Stark-broadened argon line profiles. *Phys. Rev. E Stat. Nonlin. Soft Matter Phys.* **1996**, *53*, 1042–1050.
48. Mancini, R.C.; Iglesias, C.A.; Ferri, A.; Calisti, S.; Florido, R. The effects of improved satellite line shapes on the argon Heβ spectral feature. *High Energy Density Phys.* **2013**, *9*, 731–736.

Annexe H

Line shape modeling on warm and dense hydrogen plasma

Available online at www.sciencedirect.com
ScienceDirect
High Energy Density Physics 3 (2007) 81–85
High Energy Density Physics
www.elsevier.com/locate/hedp

Line shape modeling in warm and dense hydrogen plasmas

S. Ferri [a,*], A. Calisti [a], C. Mossé [a], B. Talin [a], M.A. Gigosos [b], M.A. González [b]

[a] PIIM, UMR6633, Case 232, St Jérôme, Université de Provence, 13397 Marseille Cedex 20, France
[b] Departamento de Óptica y Física Aplicada, Facultad de Ciencias, Universidad de Valladolid, 47071 Valladolid, Spain

Available online 27 February 2007

Abstract

A study of hydrogen lines emitted in warm ($T_e \sim 1$ eV) and dense ($N_e \geq 10^{18}$ cm^{-3}) plasmas is presented. Under such plasma conditions, the electronic and the ionic contributions to the line width are comparable, and the general question related to a transition from impact to quasi-static broadening arises not only for the far wings but also for the core of spectral lines. The transition from impact to quasi-static broadening for electrons is analyzed by means of Frequency Fluctuation Model (FFM). In parallel, direct integration of the semi-classical evolution equation is performed using electron electric fields calculated by Molecular Dynamics (MD) simulations that permit one to correctly describe the emitter environment. New cross comparisons between benchmark MD simulations and FFM are carried out for electron broadening of the Balmer series lines, and, especially, for the H_α line, for which a few experiments in the warm and dense plasma regimes are available.

PACS: 52.25Ya; 32.30.Jc; 52.65.Yy; 32.60.+I

Keywords: Spectral line broadening; Molecular Dynamics; Hydrogen plasmas

1. Introduction

The problem of hydrogen spectral line shape in plasma has been the subject for numerous investigations [1], as the determination of electron densities from hydrogen line widths is a well established and important diagnostic tool. Recent theoretical development of hydrogen line broadening is connected to experimental investigations in warm ($T_e \sim 1$ eV) and dense ($N_e \geq 10^{18}$ cm^{-3}) plasmas [2]. Under such plasma conditions the ionic and electronic contributions to line broadening are of the same order and the general concerns related to the transition from impact to quasi-static electron broadening arise not only in the far wings, but also for the line core. Since the work of Vidal and coauthors [3], where the quasi-static behavior of electrons was included in a model based on a binary collision theory, several models improving electron broadening have been developed [4–7].

The objective of this work is not to examine in detail experiments nor different theoretical models but to investigate the possibility of describing electron broadening from impact to quasi-static regime with the help of the Frequency Fluctuation Model (FFM) [8]. The FFM was initially developed to account for ion dynamics. Electron effects on line shapes were introduced via a homogeneous broadening operator obtained within the impact approximation [9]. Nevertheless, when the electrons can be described classically, their effects would be similar to those of the ions, with the major distinction being time scale. Therefore, any solution to the ion dynamics problem should also be applicable to the electrons.

In order to validate the use of the FFM to calculate electron broadening, the computed line widths are compared with new simulation results. It is well established that a robust procedure for line shape calculations is to simulate the evolution of the emitter system by generating time-dependent microfields [10,11]. Here, electric microfields are generated by Molecular Dynamics (MD) simulations [12], and a direct integration of the semi-classical evolution equation is performed using a fast integration process based on Euler–Rodrigues technique [13]. MD simulations allow one to obtain static and dynamics

* Corresponding author.
E-mail address: sandrine.ferri@univ-provence.fr (S. Ferri).

1574-1818/$ - see front matter © 2007 Elsevier B.V. All rights reserved.
doi:10.1016/j.hedp.2007.02.034

properties of electric fields accounting for all correlations between charged particles so that the direct resolution of the evolution operator equation does not require either the impact or static approximation. Such simulated line shapes provide essential reference data to benchmark more efficient phenomenological line shape models developed for plasma diagnostics.

The results presented here concern an electron density $N_e = 2.5 \times 10^{18}\,\mathrm{cm}^{-3}$ and a temperature ranging from 1 to 10 eV. In this range, the transition from impact to quasi-static behavior for electrons arises for low principal quantum number [14]. After presenting the FFM behavior versus density, temperature and principal quantum number, cross comparisons between MD simulations and FFM are carried out for Balmer lines. The behavior of the electron line width with temperature is discussed for the Balmer series. Then, the temperature dependence of total line width is presented for the H_α line for which a few experiments in warm and dense plasma regions are available.

2. Models

2.1. MD simulation of the emitter environment

Classical MD simulation is carried out with a few hundred particles moving in a cubic box with periodic boundary conditions. Particle motion is achieved using a Verlet's algorithm and attention is paid to minimize the total energy fluctuations during the evolution of the system. Each charge contribution to the field at neutral emitters results from a screened Coulomb field such as:

$$\mathbf{E}(r) = \frac{Ze}{r^2}\left(1+\frac{r}{\lambda}\right)\mathrm{e}^{-r/\lambda}\frac{\mathbf{r}}{r}. \tag{1}$$

The ion–ion and the electron–electron interactions are taken to be screened Coulomb

$$V_{12} = \frac{Z_1 Z_2 e^2}{r}\mathrm{e}^{-r/\lambda}, \tag{2}$$

where Z_1Z_2 is positive. These Coulomb interactions have been screened at a distance λ of the order of the cubic cell size: since the interactions among charges introduce a physical screening at Debye length $\lambda_D = (k_B T_e/4\pi N_e e^2)^{1/2}$, the use of a screening at $\lambda \gg \lambda_D$ does not affect the properties considered in this work [15].

The Coulomb interaction has to be modified for the attractive ion–electron interactions. A simple classical description accounting for quantum diffraction effects at short distance is used [16]:

$$V_{ie} = -\frac{Ze^2}{r}\left(1-\mathrm{e}^{-r/\delta}\right)\mathrm{e}^{-r/\lambda}, \tag{3}$$

where $\delta = (2\pi\hbar^2/m_e k_B T_e)^{1/2}$ is the thermal de Broglie wavelength.

Two types of simulations with neutral hydrogen atoms used as probes to measure electric fields have been performed.

(1) A One-Component Plasma (OCP) with only electrons as perturbers.
(2) A Two-Component Plasma (TCP) of protons and electrons. All interactions are accounted for to describe properly the whole forces in the vicinity of the emitter.

Here two observations need to be made. First concerns the use of a screened potential in the electron OCP simulation. When comparing the behavior of the electron–electron pair correlation function for (1) a TCP of interacting protons and electrons and (2) an OCP driven by electric forces screened at the Debye length λ_D, good agreement is found. In Fig. 1, pair correlation functions for the lowest temperature $T_e = 8500$ K of interest are reported. The comparison involves an MD simulation for a TCP with Coulomb interactions and a hyper-netted chain (HNC) [17], calculation for an electron OCP. As the plasma is neutral and the ion charge is $Z = 1$, the expected static properties for protons and electrons should be the same: the ion–ion and the electron–electron pair correlation functions obtained by MD TCP simulations are the same. In addition, Fig. 1 shows the good agreement between MD TCP simulations and HNC calculations for an electron OCP, giving indirect evidence of the efficiency of the electron–electron dynamics screening by the ions. The OCP without screening is also shown for comparison.

Second, as field distribution functions are a necessary ingredient to describe Stark broadening, comparisons have been made to investigate charge–charge correlation effects. The field distribution functions are calculated from a sample of independent configurations. For decreasing electron temperature, i.e. increasing plasma correlation, the electron field distribution function at the emitter undergoes some changes. In the following example, two different OCP MD simulations have been performed: (1) the electrons are considered as free particles and (2) the electrons interact with each other through a Debye

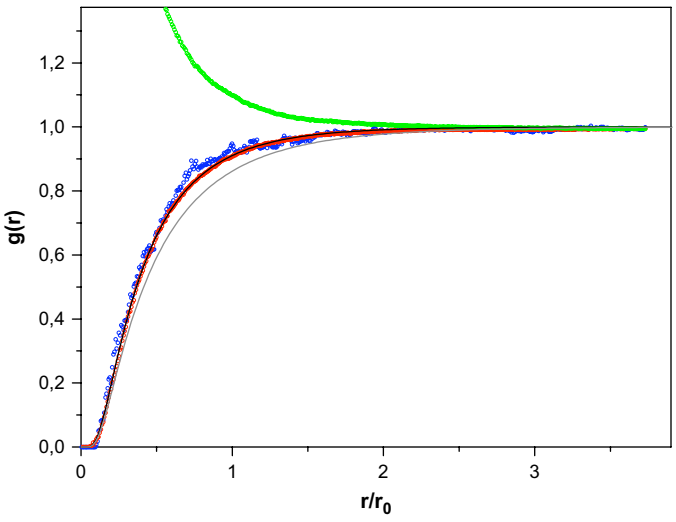

Fig. 1. Pair correlation functions for $T_e = 8500$ K and $N_e = 2.5 \times 10^{18}\,\mathrm{cm}^{-3}$: (circles) MD calculations for a TCP: (blue) ion–ion $g(r)$, (red) electron–electron $g(r)$ and (green) ion–electron $g(r)$. (solid) HNC calculations for an OCP: (black) with Debye screened forces (grey) without screening. (For interpretation of the references to colours in figure legends, the reader is referred to the web version of this article).

screened potential. Fig. 2 shows the different field distribution functions for the most strongly coupled case. It has been checked [18] that independent of the temperature, the MD simulation reproduces the Holtsmark distribution [19] when the electrons are not interacting with each other. The correlation effects lead to a shift of the order of 25% of the peak of the distribution. It is in good agreement with the Hooper field distribution [20].

2.2. Line shape calculations

The spectral line shape is expressed in terms of the autocorrelation function $C(t)$ of the emitter dipole moment $\mathbf{d}(t)$ via Fourier transform:

$$I(\omega) = \mathrm{Re}\frac{1}{\pi}\int_0^\infty \mathrm{d}t C(t)\mathrm{e}^{i\omega t}, \tag{4}$$

where $C(t)$ can be written in Liouville representation $C(t) = \mathrm{Tr}(\mathbf{d}\times\mathbf{U}(t)\rho\mathbf{d})$, where $\mathbf{U}(t) = \{U_q(t)\}_{\mathrm{av}}$ is the solution of the following stochastic equation:

$$\frac{\mathrm{d}U_q(t)}{\mathrm{d}t} = \big(L_0 + \mathbf{D}\times\mathbf{E}_q(t)\big)U_q(t),\ U_q(0) = 1. \tag{5}$$

In Eq. (5), the Liouville operator is related to the Hamiltonian H_0 for unperturbed states of the emitter by $L_0 \equiv 1/i\hbar[H_0,\cdot]$, and $\mathbf{D}\times\mathbf{E}_q(t)$ describes the perturbation due to the electric field $\mathbf{E}_q(t)$ that belongs to a sample set of independent field histories where $\mathbf{D}$ is the Liouville representation of $\mathbf{d}$. In general, no exact analytical solution exists to this equation. It is solved either by numerical simulation or by approximate methods. In the present study, the hydrogen Balmer series lines have been calculated in two different ways: (1) using a numerical integration that involves electric fields generated by MD simulations and (2) using the FFM.

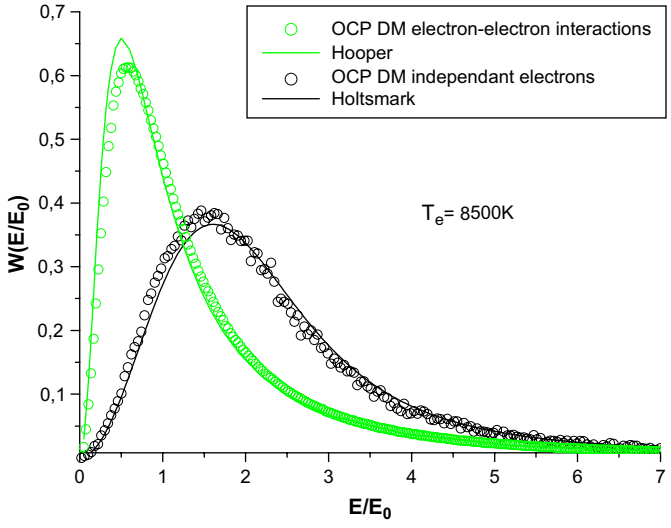

Fig. 2. Electron field distribution functions for $T_e = 8500$ K and $N_e = 2.5\times10^{18}$ cm^{-3}: (black) Hooper's model (black circles) MD calculations for an OCP with interacting electrons (green) Holtsmark's model (green circles) MD calculations for an OCP with independent electrons. (For interpretation of the references to colours in figure legends, the reader is referred to the web version of this article).

In the numerical integration method a sample set of microfield sequences, $\mathbf{E}_q(t)$, obtained by MD simulations is used in the dipole evolution equation, Eq. (5). The latter is solved for each field history and an algebraic average is performed to get the line profile. The calculations require a fast integration process based on the Euler–Rodrigues technique specific to hydrogen atoms (or hydrogen-like ions). Using the SO(4) symmetry, it leads to a large reduction in the computational time compared to a conventional simulation but does not include interactions between levels with different principal quantum numbers.

The FFM method does not treat the effect of the field fluctuations on the line shape directly, but assumes that they induce random fluctuations of the emitted radiation frequencies. In a first step, the line shape is calculated in the static approximation, where the electric field distribution obtained by MD simulations or by analytical models is used. The static profile is interpreted as a sum of radiative channels that correspond to its inhomogeneities. Then, the field fluctuation is accounted for using a Markovian process built on a fluctuation rate $\nu = v_{\mathrm{th}}/r_0$ that mixes the radiative channels. Here $v_{\mathrm{th}} \propto T_e^{1/2}$ is the perturbers thermal velocity and $r_0 \propto N_e^{-1/3}$. This results in the exchange of intensities between different spectral domains of the static line shape.

A study of hydrogen lines [14] has shown that the FFM possesses the correct dependencies on temperature, density and principal quantum number (n). That is in the impact limit, the line width is proportional to n^4, N_e and $T_e^{-1/2}$, whereas in the static limit, it is proportional to n^2, $N_e^{2/3}$ and does not vary with the temperature. Further, the smooth transition of the FFM from impact to quasi-static regime has been verified.

3. Results and discussion

The transition from impact to quasi-static regime is analyzed for the first four Balmer lines by means of MD simulations and FFM calculations. Calculations have been done for a fixed density ($N_e = 2.5\times10^{18}$ cm^{-3}) and temperatures varying from 8500 K to 200 000 K. This temperature–density domain includes recent experimental measurements [2].

In order to show the transition from impact to quasi-static provided by the FFM, the widths of the first four Balmer lines versus n are plotted in Figs. 3 and 4. At high temperature the impact model, the FFM and MD simulation are close to the n^4 impact behavior and when the temperature decreases, the FFM and MD simulations dependencies tend to the n^2 static behavior unlike the impact model. For the two presented temperatures, the H_α line width does not respect the trend because of the important role of the interference terms.

The line widths as a function of temperature are shown in Fig. 5. In the high temperature regime where the impact approximation becomes valid, all the three techniques converge toward the $T_e^{-1/2}$ trend. Further, the convergence is shifted to higher temperature as the value of the n increases. Within the entire range of temperatures the FFM and MD show the same trend.

As TCP MD simulations provide the total electric field sequences, the Balmer series lines can be calculated accounting

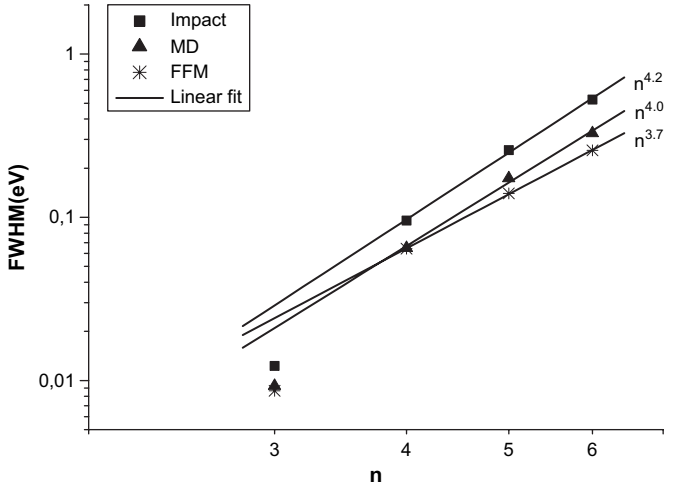

Fig. 3. Dependence of electron widths of Balmer series lines on principal quantum number n at $T_e = 200\,000$ K for the (triangles) MD simulations (stars) FFM and (squares) impact models.

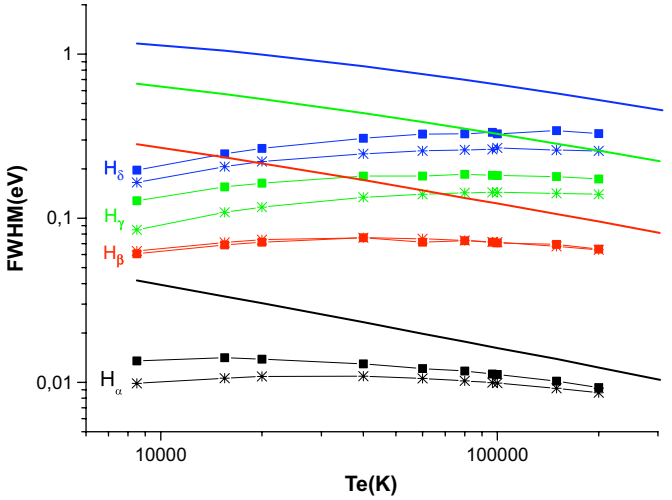

Fig. 5. Full Width at Half Maximum of the Balmer series line versus electron temperature. Comparisons between (squares) MD simulations (stars), FFM and (full lines) impact models.

for both ion and electron broadenings. Such calculation can also be performed with the FFM by calculating separately the electron-broadened profile and the ion-broadened profile. The electron and the ion fluctuation frequencies ν_e and ν_i are accounted for following the stochastic process implemented in the FFM. Finally, a convolution of the electron and ion profiles gives the total line shape. A TCP MD calculation neglecting ion–electron correlations but accounting for electron–electron and ion–ion correlations shows that the total width of the H_α does not differ from a full interacting particle's calculation. Thus, for the studied temperature range, the ion–electron correlations are negligible, justifying a separate ion–electron broadening calculation.

In Fig. 6, the total width of the H_α line is shown as a function of the electron temperature. The FFM results show the same trend as the TCP MD simulation, while a standard approach, i.e. impact electrons and static ions, overestimates the FWHM at low temperature. Both FFM and MD results give smaller widths than the experiments. Calculations (not presented here) accounting for couplings with higher principal quantum numbers show an increase of the width of the order of 20%. These results are confirmed by other groups [21].

In conclusion, the above results show that there is overall a good agreement between MD and FFM, confirming the capability of the FFM to provide relevant results from impact to quasi-static regime. Although the same trend is seen for both the MD simulations and FFM, some discrepancies do remain. More cross comparisons with MD simulations and with new experimental results in warm and dense plasmas would be helpful to improve the FFM.

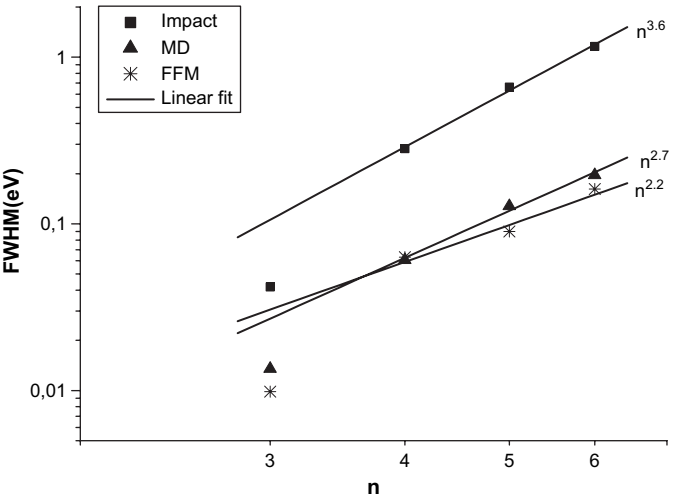

Fig. 4. Same as Fig. 3 but at $T_e = 8500$ K.

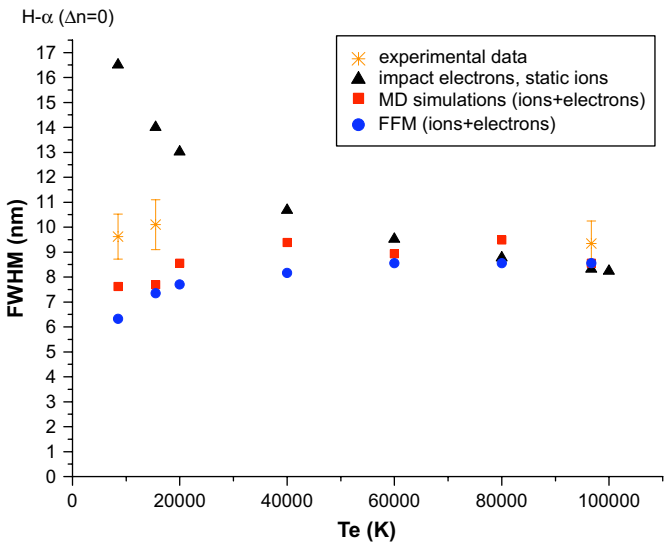

Fig. 6. Full Width at Half Maximum of the H_α line versus electron temperature. Comparisons between experiments [2], MD simulations, FFM and impact models.

Acknowledgments

The authors would like to thank L.A. Bureyeva and V.S. Lisitsa for their invaluable suggestion and discussions. This work has been partially supported by project INTAS 03-546348.

References

[1] H.R. Griem, Contrib. Plasma Phys. 40 (2000) 46.
[2] (a) A. Escarguel, B. Ferhat, A. Lesage, J. Richou, J. Quant. Spectrosc. Radiat. Transfer 64 (2000) 353;
(b) S. Büscher, Th. Wrubel, S. Ferri, H.-J. Kunze, J. Phys. B 35 (2002) 2889;
[c] S. Flih, E. Oks, Y. Vitel, J. Phys. B 36 (2003) 283.
[3] C.R. Vidal, J. Cooper, E.W. Smith, ApJS 25 (1973) 37.
[4] C. Stehlé, Astron. Astrophys. Suppl. 292 (1994) 699.
[5] E. Oks, J. Phys. B 35 (2002) 2251.
[6] S. Alexiou, Phys. Rev. E 71 (2005) 066403.
[7] H.R. Griem, J. Halenka, W. Olchawa, J. Phys. B 38 (2005) 975.
[8] B. Talin, A. Calisti, L. Godbert, R. Stamm, R.W. Lee, L. Klein, Phys. Rev. A 51 (1995) 1918.
[9] H.R. Griem, Spectral Lines Shapes in Plasmas, Mc Grow Hill, N.Y., 1982.
[10] R. Stamm, Y. Botzanowski, V.P. Kaftandjian, B. Talin, E.W. Smith, Phys. Rev. Lett. 52 (1984) 2217.
[11] R. Stamm, B. Talin, E.L. Pollock, A. Iglesias, Phys. Rev. A 34 (1986) 4144.
[12] B. Talin, A. Calisti, J. Dufty, Phys. Rev. E 65 (2002) 056406.
[13] M.A. Gigosos, J. Fraile, F. Torres, Phys. Rev. A 31 (1985) 3509.
[14] A. Calisti, L.A. Bureyeva, V.S. Lisitsa, D. Shuvaev, B. Talin, Eur. Phys. J. D., accepted for publicaton.
[15] B. Talin, E. Dufour, A. Calisti, M.A. Gigosos, M.A. González, T. del Rio Gaztelurrutia, J.W. Dufty, J. Phys. A: Math. Gen. 36 (2003) 6049.
[16] H. Minoo, M.M. Gombert, C. Deutsch, Phys. Rev. A 23 (1981) 924.
[17] F. Rogers, Chem. Phys. 73 (1980) 6272.
[18] S. Ferri, A. Calisti, C. Mossé, B. Talin, in: E. Dalimier (Ed.), Proceeding of the 17th ICSLS, Frontier Group, 448, 2004.
[19] J. Holtsmark, Ann. Physik. 58 (1919) 577.
[20] C.F. Hooper, Phys. Rev. 165 (1968) 215.
[21] E. Stambulchik, D. Fischer, Y. Maron, H.R. Griem, S. Alexiou, High Energy Density Phys. 3 (2007) 272.

Annexe I

The FFM applied to Stark-Zeeman spectral line shape in plasmas

Frequency-fluctuation model applied to Stark-Zeeman spectral line shapes in plasmas

S. Ferri,* A. Calisti, C. Mossé, L. Mouret, and B. Talin
Laboratoire PIIM, UMR 6633, Université de Provence-CNRS, Centre de Saint Jérôme, Case 232, F-13397 Marseille Cedex 20, France

M. A. Gigosos and M. A. González
Departamento de Óptica y Física Aplicada, Facultad de Ciencias, Universidad de Valladolid, E-47071 Valladolid, Spain

V. Lisitsa
Russian Research Center, Kurchatov Institute, Moscow RU-123182, Russia

(Received 15 January 2010; revised manuscript received 4 February 2011; published 18 August 2011)

A very fast method for calculating line shapes in the presence of an external magnetic field accounting for charge particle dynamics is proposed. It is based on a reformulation of the frequency fluctuation model, which provides an expression of the dynamic line shape as a functional of the static distribution function of frequencies. In the presence of an external magnetic field, the distribution of intensity and polarization of the emission depends on the angle between the observation line and the magnetic field's direction. Comparisons with numerical simulations and experimental results for various plasma conditions show very good agreement. Results on hydrogen lines in the context of magnetic fusion and the Lyman-α line, accounting for fine structure, emitted by argon in the context of inertial fusion, are also presented.

DOI: 10.1103/PhysRevE.84.026407 PACS number(s): 52.20.−j, 32.70.Jz, 32.60.+i, 52.25.−b

I. INTRODUCTION

The presence of a static magnetic field is common for many types of plasmas and revives the interest for modeling the line shapes affected simultaneously by Stark and Zeeman effects. Such a combined influence on profiles of spectral lines has been studied for several decades both theoretically and experimentally since the initial work [1]. Different methods have been developed or have been extended to magnetic plasmas, such as numerical simulations [2–4] and theoretical models [5–12]. The aim of the latter is to give a rapid and accurate description of the line shapes or to be implemented in transport codes dedicated to plasma spectroscopy.

Modeling the broadening due to both the Stark and the Zeeman effects is a complex problem that requires the knowledge of accurate atomic physics data, statistical mechanics, and plasma physics. A magnetic field has three essential effects on Stark-broadened spectral lines: (1) partial polarization of the emitted light, (2) additional splitting caused by the magnetic field according to value of the magnetic quantum number m, and (3) bending of the electron trajectories into a helical path around the magnetic lines of forces. The third point will not be considered in this paper. The magnetic field leads to an additional structure in the line profile due to the energy level splitting. A measure of the relative importance of the Stark and Zeeman effects is given by the ratio τ between the two respective average energy shifts [1]. For hydrogen, with the normal field strength $F_0 = 2.603eN_e^{2/3}$, τ is as follows:

$$\tau = 5.15 \times 10^{-11} n N_e^{2/3}/B, \tag{1}$$

where n is the principal quantum number, N_e is the electron density, expressed in cm^{-3}, and B is the magnetic field strength, expressed in teslas. The line profile coincides with the pure Stark profile if $\tau \gg 1$ and deviates progressively as τ decreases. When $\tau \approx 1$, profiles broadened by the combined Stark-Zeeman effect are an intricate function of N_e and B. Such cases are found in magnetically confined plasmas for low-n hydrogen lines emitted in the divertor region at $N_e > 10^{14}$ cm^{-3}, $kT_e \sim 1$ eV, and $B \simeq$ few teslas. In plasmas produced by laser impact or implosion (temperatures from 100 to 1000 eV and electron densities from 10^{21} to 10^{24} cm^{-3}), high magnetic fields ($B > 100$ T) are generated that can strongly affect the emission of highly ionized atoms. These conditions are favorable for the combined Stark-Zeeman effect on line profiles, not to mention astrophysical plasmas where the signature of uniform magnetic fields is observed on hydrogen lines in regions where $N_e \sim 10^{14}$ cm^{-3} and $kT_e \sim 1$ eV (see Ref. [6] and references therein).

The most difficult part of the line broadening problem is to properly identify the environment of the emitter. In particular, accounting for the fluctuations of electric fields produced at emitters, by moving electrons and ions, is a nontrivial problem that has been of constant interest for both experimental and theoretical points of view since the 1960s (see Ref. [7] and references therein). Moreover, the presence of a static magnetic field, by giving a preferential axis, imposes the orientation of the electric dipole and can alter the dynamical properties of the plasma. Few models accounting for both the magnetic and the fluctuating electric fields have been developed [6,8,12,13]. Here, a method based on a reformulation of the frequency fluctuation model (FFM) [14], extended to magnetized plasmas, is presented.

II. METHOD

The line shape function in the radiative dipole approximation is related to the imaginary part of the Fourier-transformed dipole autocorrelation function. This can be written as a

*sandrine.ferri@univ-provence.fr

normalized Liouville space-matrix element of the response function,

$$I(\omega) = \mathrm{Im}\langle\langle \mathbf{d}^\dagger | G(\omega) | \mathbf{d}\rho_0 \rangle\rangle, \tag{2}$$

with ρ_0 as the equilibrium density matrix operator and $\mathbf{d}$ as the dipole operator for the emitting system. The response function $G(\omega - i\varepsilon)$ is given by the one-sided Fourier transform of the bath averaged evolution operator of the emitter $U(t)$,

$$G(\omega) = \lim_{\varepsilon \to 0} i \int_0^{+\infty} U(t) e^{-i(\omega - i\varepsilon)t} dt. \tag{3}$$

$U(t) = \langle U_l(t) \rangle_{l \in \{F\}}$ with $U_l(t)$ as the solution of the following equation:

$$\frac{dU_l(t)}{dt} = -iL_l(t)U_l(t) \quad \text{and} \quad U_l(0) = \mathbf{1}. \tag{4}$$

Here, $\mathbf{1}$ is the unit operator and $L_l(t)$ is the sum of three terms: $L_l(t) = L_0 + l(t) + L_Z$, where L_0 describes the behavior of the unperturbed atom and where $l(t)$ and L_Z are the Liouvillians corresponding to the Stark and Zeeman effects, respectively. The latter are treated as perturbations to L_0. Here:

(i) $l(t) = -\frac{1}{\hbar}\mathbf{d} \cdot \mathbf{F}_l(t)$ is the time dependent Liouville perturbation operator that connects the quantum emitter via the dipole operator $\mathbf{d}$ to the external electric field $\mathbf{F}_l(t)$. The latter is assumed to belong to a measurable functional space $\{F\}$ that provides a statistical method for the calculation of average quantities,

(ii) and L_Z is written as $L_Z = \frac{1}{\hbar}\mu_B \mathbf{B} \cdot [\mathbf{J} + (g_S - 1)\mathbf{S}]$, with the spin $\mathbf{S}$ and the angular momentum $\mathbf{J}$; $g_S \cong 2.002\,32$ is the anomalous gyromagnetic ratio for the electron spin. Here, the diamagnetic term, proportional to B^2, is assumed negligible compared to the paramagnetic term, proportional to B, and is not taken into account.

Due to the stochastic behavior of the electric field, $U(t)$ can be obtained by numerical simulation integrating Eq. (4) on a simulated sampling of $\{F\}$. Alternatively, efficient analytical models (e.g., the quasistatic approximation, the impact approximation, the model microfield method, the FFM, and the Boerker-Iglesias-Dufty model [7]) have been developed.

One feature of the Stark-Zeeman line shape modeling is a quantization axis imposed by the magnetic field. Averaging over $\mathbf{F}_l$ implies considering the three directions of space separately. Considering the magnetic field in the direction z, i.e., $\mathbf{B} = B\mathbf{e_z}$, one can define $\mathbf{F}_\parallel$ and $\mathbf{F}_\perp$ as the microfield parallel and perpendicular, respectively, to the direction of the magnetic field.

The selection rules for electric dipole radiation are as follows:

$$\Delta J = 0, \pm 1 (0 \nrightarrow 0), \quad \Delta M = \begin{cases} \pm 1, & \sigma \text{ components}, \\ 0, & \pi \text{ component}, \end{cases} \tag{5}$$

with M as the magnetic quantum number. By observing perpendicular to the magnetic field, the σ and π components show a linear polarization, respectively, parallel and perpendicular to $\mathbf{B}$. Along the $\mathbf{B}$ direction, the σ components show a circular polarization, and the π components do not appear. The profile observed in a direction with an angle α to the magnetic field is given by

$$I(\omega,\alpha) = I_\parallel \cos^2\alpha + I_\perp \sin^2\alpha, \tag{6}$$

where the parallel $I_\parallel$ and the transverse $I_\perp$ profiles are expressed in terms of polarized emission as

$$I_\parallel = I_+(\omega) + I_-(\omega), \tag{7}$$

$$I_\perp = \tfrac{1}{2}[I_+(\omega) + I_-(\omega)] + I_0(\omega). \tag{8}$$

Decomposing the dipole operator along the polarization vector basis $\{\mathbf{e}_q; q = 0, \pm 1\}$, the line intensity $I_q(\omega)$ associated with each polarization state is given by

$$I_q(\omega) = \mathrm{Im}\langle\langle \mathbf{d}_\mathbf{q}^\dagger | G(\omega) | \mathbf{d}_\mathbf{q}\rho_0 \rangle\rangle. \tag{9}$$

In the FFM, the line shape calculation is initially performed by treating the electron collisions as impacts and the ion perturbation as quasistatic [15]. The time dependence is introduced at a later stage of the calculation. Considering a static ionic electric field and electrons as impact results in a quantum-emitter system evolution operator $l = -\frac{1}{\hbar}\mathbf{d} \cdot \mathbf{F}_l + i\Phi_e$ containing a non-Hermitian homogeneous electron-impact broadening contribution Φ_e and the ion microfield interaction $-\frac{1}{\hbar}\mathbf{d} \cdot \mathbf{F}_l$, which has to be numerically averaged with a static-field probability distribution $Q(\mathbf{F}_l)$ [16]. The evaluation of the Liouville operator matrix elements requires the calculation of the electric dipole matrix elements $\langle \gamma J M | \mathbf{d_q} | \gamma' \mathbf{J}' \mathbf{M}' \rangle$ and the matrix elements $\langle \gamma J M | \mathbf{J_0} + \mathbf{S_0} | \gamma' \mathbf{J}' \mathbf{M}' \rangle$ related to the paramagnetic matrix elements of L_z with $\mathbf{B} = B\mathbf{e_z}$ and $g_S = 2$. The calculation can be simplified by using the Wigner-Eckart theorem [17]:

(i) the electric dipole matrix elements become

$$\langle \gamma J M | \mathbf{d_q} | \gamma' \mathbf{J}' \mathbf{M}' \rangle = (-1)^{J-M} \begin{pmatrix} J & 1 & J' \\ -M & q & M' \end{pmatrix} \times \langle \gamma J || \mathbf{d} || \gamma' \mathbf{J}' \rangle, \tag{10}$$

where $\langle \gamma J || \mathbf{d} || \gamma' \mathbf{J}' \rangle$ is the reduced matrix element,

(ii) and in the LS representation, the paramagnetic matrix elements become

$$\begin{aligned} &\langle \gamma J M | \mathbf{J_0} + \mathbf{S_0} | \gamma' \mathbf{J}' \mathbf{M}' \rangle \\ &\quad = M \delta_{\gamma J M, \gamma' J' M'} - \delta_{\gamma L S M \gamma' L' S' M'} (-1)^{L+S+M} \\ &\qquad \times [J, J']^{1/2} \sqrt{S(S+1)(2S+1)} \\ &\qquad \times \begin{pmatrix} J & 1 & J' \\ -M & 0 & M \end{pmatrix} \begin{Bmatrix} L & S & J \\ 1 & J' & S \end{Bmatrix}. \end{aligned} \tag{11}$$

Here, the diagonal and off-diagonal ($J' = J - 1$) matrix elements are given by the analytical evaluation of the $3 - j$ and $6 - j$ symbols.

This implies the knowledge of J and S values of each state and the reduced matrix elements between states. Such information can be extracted from atomic structure codes (based on either LS or JJ coupling) [17–20].

In the absence of a magnetic field, models that rely on quasistatic approximation assume the plasma, surrounding the emitting atom, isotrope. The ion microfield distribution function is then a function of the ionic field strength, i.e., $W(F) = 4\pi F^2 Q(\mathbf{F})$. With the introduction of an external magnetic field, the symmetry is broken, and the integration over the electric field has to take it into account. If θ is the angle between the magnetic and the electric fields, then the parallel

and perpendicular components are defined by $F_\parallel = F_l\mu$ and $F_\perp = F_l\sqrt{1-\mu^2}$, where $\mu = \cos\theta$ and Eq. (9) is written as

$$I_q(\omega) = \int_0^\infty W(F_l)\int_{-1}^{1} J_q(F_l,\mu,\omega)\,d\mu\,dF_l, \qquad (12)$$

$J_q(F_l,\mu,\omega) = \mathrm{Im}\langle\langle \mathbf{d}_\mathbf{q}^\dagger \,|\, (\omega\mathbf{1} - L_0 - l - L_Z)^{-1} \,|\, \mathbf{d}_\mathbf{q}\rho_0\rangle\rangle$ represents the q-polarized intensity emitted by an ion in an external magnetic field and in a static ion field F_l having a direction μ compared to the magnetic field direction. In order to numerically treat Eq. (12), the integrations over F_l and μ are replaced by two weighted sums: Two-point integration weights $W_f^{(2)}$ are used for the summation over discrete ionic field intensities f, and Gauss-Legendre quadrature weights $W_\mu^{(G)}$, with the respective abscissa μ, are used for the angle summation [21,22]. Note that this discretization is possible because of the homogeneous electron broadening. Thus, the Fourier transform in Eq. (3) can be calculated in the $\{f,\mu\}$-dependent basis that makes the Liouville operator diagonal,

$$I_q(\omega)W = W\sum_f W_f^{(2)}\sum_\mu W_\mu^{(G)}\mathrm{Im}\big\langle\big\langle \mathbf{d}_\mathbf{q}^\dagger | M_{f,\mu} \times[\omega\mathbf{1} - L^d(f,\mu)]^{-1} M_{f,\mu}^{-1}|\mathbf{d}_\mathbf{q}\rho_0\big\rangle\big\rangle. \qquad (13)$$

Here, $M_{f,\mu}$ is the matrix that diagonalizes the Liouville operator L, $M_{f,\mu}^{-1}L(f,\mu)M_{f,\mu} = L^d(f,\mu)$. This procedure leads to the concept of the Stark spectral components emitted by a set of dressed two-level radiators [Stark-dressed transitions (SDTs)], which are defined by two complex numbers, the generalized intensity $a_{q,k} + ic_{q,k}$ and the generalized frequency $f_{q,k} + i\gamma_{q,k}$ (for more details, see Ref. [23]). Now, working in the Liouville space of the dressed two-level radiators, the static line shape is written [24]

$$I_q(\omega) = \mathrm{Re}\frac{1}{\pi}\sum_{kj} i\langle D_{q,k}|(\omega\mathbf{1} - L^d)^{-1}|D_{q,j}\rangle p_{q,j}, \qquad (14)$$

where L^d is the Liouville operator involving the transition frequencies of the SDT, $D_{q,j} = r_q\sqrt{1+ic_j/a_j}$ are the matrix elements of the dipole moment for the SDT in the q polarization state ($r_q^2 = \sum_k a_{q,k}$), and $p_{q,j} = a_{q,j}/r_q^2$ is the instantaneous probability of state j in the q polarization state.

The next step is to account for the fluctuations of the ionic electric field. The FFM is based on the assumption that an atomic system perturbed by a fluctuating microfield behaves like a set of SDTs that are subject to a stationary Markov mixing process induced by the field fluctuation. This results in an effective exchange between two-level transitions following a Poisson process with a fluctuation rate of $\nu = v_{th}/r_i$ where v_{th} is the ion thermal velocity and r_i is the mean distance between ions. According to Ref. [14], Γ is defined as the diagonal matrix of inverse state lifetimes with $\Gamma_{kj} = \nu\delta_{kj}$ and W as the matrix transition rates between different states, such as $W_{kj} = \nu p_{q,k}$. The expression of the Stark-Zeeman line shape accounting for ion dynamics and polarization is written as

$$I_q(\omega) = \mathrm{Re}\frac{1}{\pi}\sum_{kj} i\langle D_{q,k}|(\omega\mathbf{1} - L^d - i\Gamma + iW)^{-1}|D_{q,j}\rangle p_{q,j}, \qquad (15)$$

which leads to the line shape function for a given transition,

$$I_q(\omega) = \frac{r_q^2}{\pi}\mathrm{Re}\frac{\sum_k \frac{(a_{q,k}+ic_{q,k})/r_q^2}{i(\omega-\omega_{q,k})+\gamma_{q,k}+\nu}}{1-\nu\sum_k \frac{a_{q,k}/r_q^2}{i(\omega-\omega_{q,k})+\gamma_{q,k}+\nu}}. \qquad (16)$$

Thus, the observed Stark-Zeeman profile is the sum given by Eqs. (6)–(8).

If c_k is negligible and if the homogeneous broadening $\gamma_{q,k}$ does not depend on k, Eq. (16) can be written as a functional of the normalized static profile $W_q(\omega)$. The line shape is then expressed as the convolution of a Lorentzian function that represents the homogeneous broadening and the ion dynamic profile,

$$I_q(\omega) = \int d\omega'' \frac{\gamma_q/\pi}{\gamma_q^2 + (\omega-\omega'')^2}\mathrm{Re}\left[\frac{r_q^2}{\pi}\frac{\int \frac{W_q(\omega')d\omega'}{\nu+i(\omega''-\omega')}}{1-\nu\int \frac{W_q(\omega')d\omega'}{\nu+i(\omega''-\omega')}}\right]. \qquad (17)$$

III. RESULTS AND DISCUSSION

In this section, we present calculations of spectral line shapes of hydrogen for conditions relevant to magnetic fusion and argon lines emitted in dense magnetized plasmas.

For the present spectral line shape study, the high-density ($N_e \geqslant 10^{14}$ cm^{-3}) low-temperature ($kT_e \leqslant 10$ eV) tokamak edge plasmas are of particular interest: The optically thin Balmer lines of hydrogen and its isotopes present line profile features that depend directly on plasma properties. For example, odd principal quantum number transitions, such as the H_α line, are useful for determining the magnetic field strength from the measure of the Zeeman components separation. Even principal quantum number transitions, such as the H_β line are useful for determining the electron density from the wings of the Stark line shape [25].

In Fig. 1, we show the Balmer-α (H_α) Stark-Zeeman profiles without Doppler broadening for the plasma conditions $N_e = 10^{15}$ cm^{-3}, $kT_e = kT_i = 10$ eV, and $B = 4$ T. The profiles plotted above and under the abscissa correspond to an observation perpendicular and parallel to the magnetic field, respectively. Two different results are shown: the static profiles (dashed line) and the dynamic profiles (full line). The three Zeeman components (σ_+, π, and σ_-) are clearly distinguishable for an observation perpendicular to **B**, whereas, only the σ components appear for an observation parallel to **B**. The corresponding static line shape presents a plateau in the center of the line, which is explained by the asymmetry of each σ component: As the electric microfield has an arbitrary direction, all M sublevels that fulfill the condition $\Delta M = 0, \pm 1$ are coupled. Emission then appears on the three directions of polarization. In order to understand the ion dynamics effects on the Zeeman components, recall that the general behavior of a set of SDTs undergoing a Markovian mixing process is a collapse of the elements around the gravity center of the set when the fluctuation rate increases. Along this evolution, lines originally inhomogeneous become homogeneous, and their shape can get broader or thinner depending on ν and on the initial SDT distribution. At large ν, the perturbation becomes inefficient, and the line evolves toward the unperturbed shape, here, the pure electron

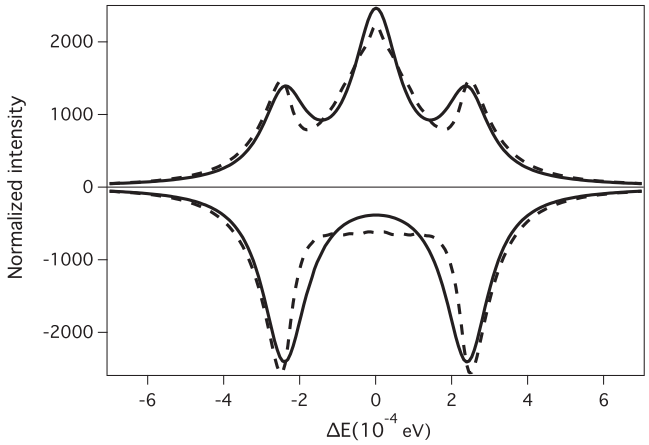

FIG. 1. H_α line shape with an external magnetic field ($B = 4$ T) for $N_e = 10^{15}$ cm^{-3} and $kT_e = kT_i = 10$ eV. Comparison between static profile (dashed line) and dynamic profile (full line). Observation perpendicular to **B** plotted above the abscissa. Observation parallel to **B** plotted under the abscissa.

broadened Zeeman profile. This quite unpredictable response is illustrated in Fig. 1: The π component is symmetric and gets narrower while the σ components, mainly nonsymmetric due to the presence of forbidden components, get shifted and broader for the fluctuation rate relevant to this case.

Figure 2 shows a comparison of the pure electron broadened Zeeman profile (gray curve) of the H_α line, presenting the three σ_+, π, and σ_- components, with dynamic profiles for different values of the fluctuation rate. In order to make a narrowing effect more pronounced, the values of ν were increased up to the value of $100 \times \nu$. The intensity of the line center is set to 1 in order to clearly show the convergence of the dynamic profiles to the pure Zeeman profile as ν increases.

The method presented here is validated by numerical simulation [2] involving hydrogenlike emitters in magnetized plasmas. Numerical simulations play a role as ideal experiments [26], considered as benchmarks. The simulation technique used here relies on (1) the generation of $F_l(t)$ by considering a set of ions and electrons moving along straight trajectories inside a spherical volume (a model of quasiparticles is used [27]) and (2) a fast numerical resolution of Eq. (4) [2,28]. Figure 3 shows the profiles of the H_α line obtained from simulation (circles) and from FFM (full line) for two different values of magnetic field ($B = 2$ T and $B = 4$ T) and for $N_e = 10^{15}$ cm^{-3} and $kT_e = kT_i = 8.5$ eV. Very good

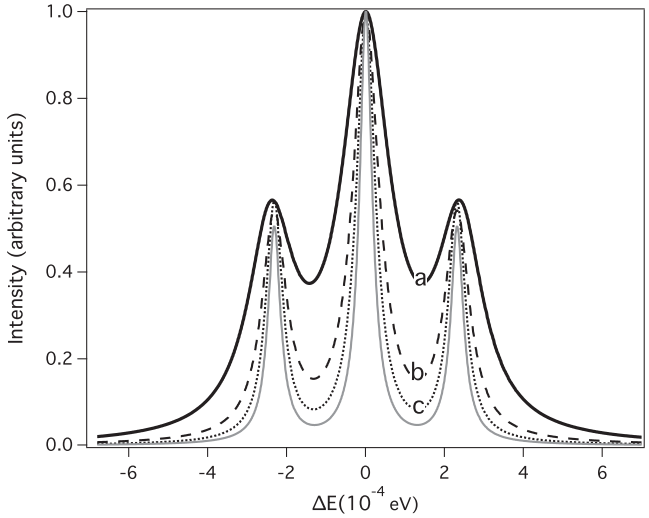

FIG. 2. Comparison of the pure electron broadened Zeeman profile (gray curve) of the H_α line calculated in same conditions as in Fig. 1 with dynamic profiles for different values of the fluctuation rate: ν, 10ν, and 100ν (a)–(c). The observation is perpendicular to **B**.

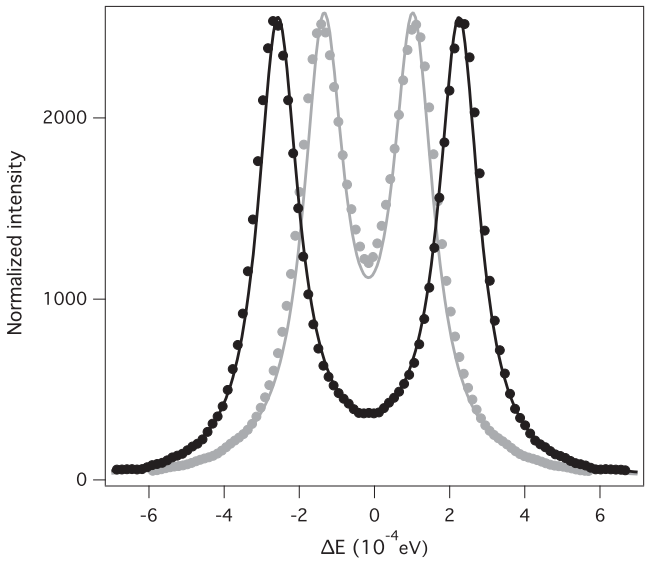

FIG. 3. H_α line shapes with external magnetic fields, $B = 2$ T (gray) and $B = 4$ T (black), for $N_e = 10^{15}$ cm^{-3} and $kT_e = kT_i = 8.5$ eV: FFM (full lines) and numerical simulations (circles). Observation parallel to **B**.

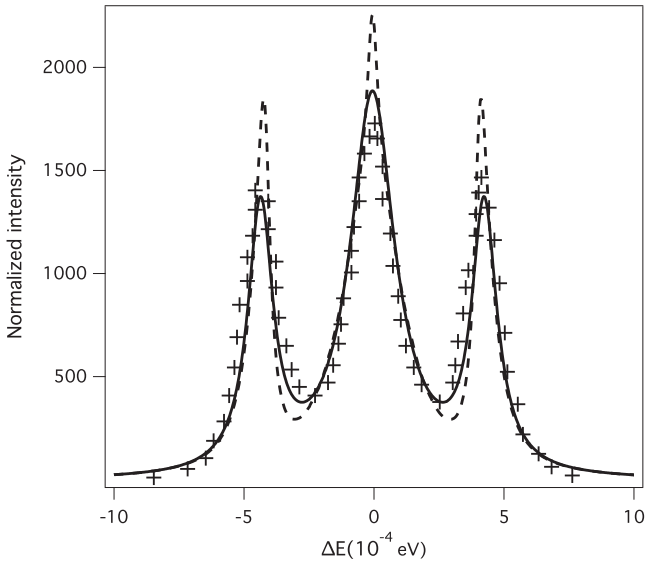

FIG. 4. Comparison between Alcator C-mod multifaceted asymmetric radiation from the edge (MARFE) D_α experimental line (crosses) with the Stark-Zeeman dynamic profile (full line) and the static profile (dashed line) for $N_e = 10^{15}$ cm^{-3}, $kT_e = kT_i = 1$ eV, and $B = 7$ T.

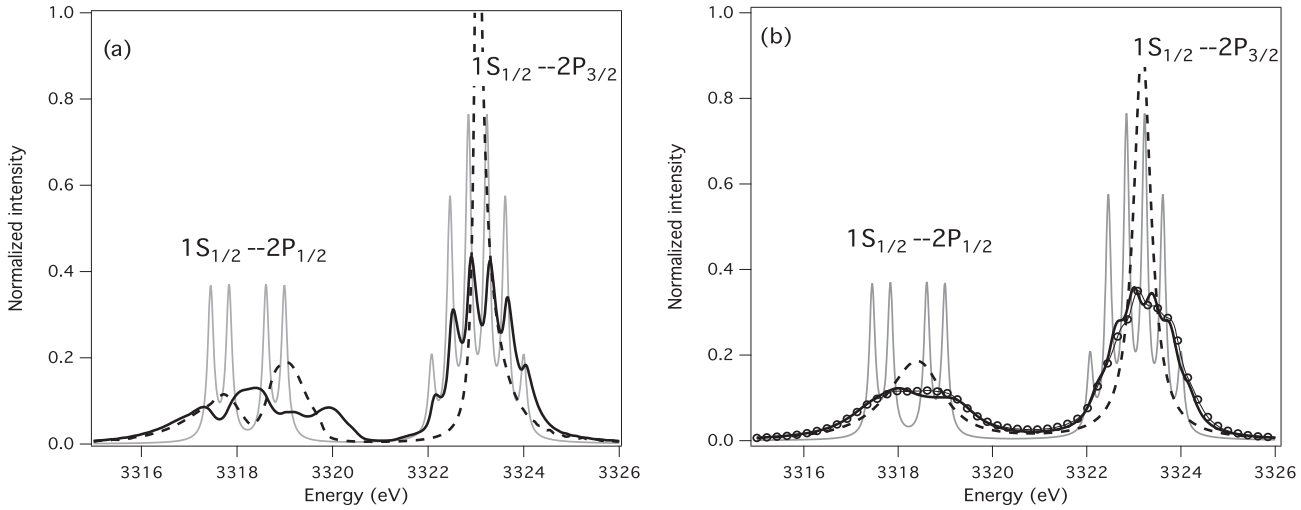

FIG. 5. Ar XVIII Lyman-α line profiles calculated within (a) the quasistatic approximation and (b) accounting for ion dynamics for an external magnetic field $B = 100$ MG and for $N_e = 1.5 \times 10^{23}$ cm^{-3} and $T_e = T_i = 10^7$ K: (gray line) electron broadened Zeeman profile with fine structure, (dashed line) Stark broadened profile, (full line) Stark-Zeeman profile, and (circles) numerical simulations. The direction of observation is perpendicular to **B**.

agreement is found between the simulation and the model. Note that none of these calculations are Doppler broadened and, of course, for such high ionic temperature, the Doppler effect brings an additional broadening.

In the present density range, the Stark-Zeeman profiles are intricate functions of N_e, T_e, and B. To use spectral line profiles as a diagnostic tool, one has to compare the whole measured profile to the whole theoretical one. As, for example, Fig. 4 shows a comparison between the FFM calculated static (dashed line) and dynamic (full line) Stark-Zeeman-Doppler profiles and the D_α (deuterium) line profile (crosses) observed in Alcator C-mod MARFE experiments [25]. The plasma parameters (N_e and T_e) were diagnosed independently and, as in the original paper, the theoretical profiles have not been instrumentally broadened. The dynamic profiles are rather sensitive to electron density variations, and the dynamic profile shows very good agreement with the experimental one for the diagnosed plasma conditions.

The second application concerns Stark-Zeeman line shapes of the Ar XVIII Lyman-α line, accounting for a fine structure calculated for plasma conditions relevant to plasmas produced by laser impact or implosion. In such plasmas, high magnetic fields on the order of 10 to 100 MG have been predicted or have been observed directly [29]. Various physical processes, such as perturbations due to ion microfield, self-generated magnetic field, motional electric field, and Doppler effect, can contribute to the broadening of such highly ionized emitter lines. We have considered a typical laser-driven implosion of a deuterium gas filled microsphere with impurities of argon with a temperature of $T_e = 10^7$ K, an electron density of $N_e = 1.5 \times 10^{23}$ cm^{-3}, and a magnetic field strength of $B = 100$ MG [30]. Even for such high values of magnetic field, the spin-orbit interaction dominates over the effect of the external magnetic field. This case is very advantageous because: First, the profile involves two patterns resulting from both linear and quadratic Stark splitting, respectively, associated with the two fine structure components $1S_{1/2}$-$2P_{1/2}$ and $1S_{1/2}$-$2P_{3/2}$ [14]; second, it presents a strong ion dynamics effect on the Zeeman components. Figures 5(a) and 5(b) show comparisons of the Lyman-α profiles for hydrogenlike argon obtained with pure Zeeman calculations (gray line), pure Stark calculations (dashed line), and Stark-Zeeman calculations (full line) within the quasistatic approximation for the ionic electric field and accounting for the ion dynamics, respectively. Considering the quasistatic case, the four Zeeman components of the $1S_{1/2}$-$2P_{1/2}$ disappear due to the linear Stark effect, whereas, the six Zeeman components of the $1S_{1/2}$-$2P_{3/2}$ are still distinguishable. The characteristic wing at high energies due to the quadratic Stark effect is visible. The ion dynamics effect results in an overall broadening of the line shape. Numerical simulations have been performed using the technique previously described but with electric fields generated by the molecular dynamics technique to account for ion correlations. Here again, comparisons with numerical simulations (circles) give very good agreement.

IV. CONCLUSION

In this paper, we have described a method to account for charged particle dynamics effects in calculations of Stark-Zeeman spectral line shapes. The method, not restricted to simple lines, relies on a reformulation of the FFM, which provides an expression of the dynamic line profile as a functional of the static distribution function of frequencies. Comparisons with numerical simulations and experiments, when they exist, validate the method.

In a first step, the Stark-Zeeman broadened profile is calculated in the quasistatic approximation. Next, the line profile accounting for ion dynamics is calculated via an expression, which depends only on two quantities: the static distribution function and a unique parameter, the fluctuation rate. Here, the method is not limited to a specific atomic physics as the Stark and Zeeman effects are added as perturbations. This highly efficient formalism provides Stark-Zeeman line

shapes for a wide range of density, temperature, and magnetic field values, which is of importance in plasma physics and astrophysics. In addition, this method is numerically fast enough to be implemented in codes that require spectral line shape calculations including all main effects as, for example, in the investigation of radiation effects on plasma transport in plasmas. As shown, spectral line profiles can easily be generated to be used as a diagnostic tool to infer electron density or magnetic field in magnetic fusion devices. Another domain of application is the study of x-ray lines emitted by plasmas produced by laser impact and inertial confinement where high magnetic fields (over 100 MG) can significantly modify the line profile of highly charged ions.

ACKNOWLEDGMENTS

Authors thank the anonymous referees for their very helpful comments and suggestions.

[1] N. Hoe, H. W. Drawin, and L. Herman, J. Quantum Spectrosc. Radiat. Transfer **7**, 429 (1967).
[2] M. Gigosos and M. González, J. Quantum Spectrosc. Radiat. Transfer **105**, 533 (2007).
[3] E. Stambulchik, K. Tsigutkin, and Y. Maron, Phys. Rev. Lett. **98**, 225001 (2007).
[4] J. Rosato, Y. Marandet, H. Capes, S. Ferri, C. Mossé, L. Godbert-Mouret, M. Koubiti, and R. Stamm, Phys. Rev. E **79**, 046408 (2009).
[5] A. Derevianko and E. Oks, Phys. Rev. Lett. **73**, 2059 (1994).
[6] S. Brillant, G. Mathys, and C. Stehlé, Astron. Astrophys. **339**, 286 (1998).
[7] H. R. Griem, *Principles of Plasma Spectroscopy* (Cambridge University Press, Cambridge, UK, 1997).
[8] S. Günter and A. Könies, J. Quantum Spectrosc. Radiat. Transfer **62**, 425 (1999).
[9] L. Godbert-Mouret, M. Koubiti, R. Stamm, K. Touati, B. Felts, H. Capes, Y. Corre, R. Guirlet, and C. De Michelis, J. Quantum Spectrosc. Radiat. Transfer **71**, 365 (2001).
[10] M. L. Adams, R. W. Lee, H. A. Scott, H. K. Chung, and L. Klein, Phys. Rev. E **66**, 066413 (2002).
[11] X. D. Li, S. S. Han, C. Wang, and Z. Z. Xu, J. Quantum Spectrosc. Radiat. Transfer **76**, 31 (2003).
[12] G. Mathys, Astron. Astrophys. **141**, 248 (1984).
[13] L. Godbert-Mouret, J. Rosato, H. Capes, Y. Marandet, S. Ferri, M. Koubiti, R. Stamm, M. González, and M. Gigosos, High Energy Density Phys. **5**, 162 (2009).
[14] A. Calisti, C. Mossé, S. Ferri, B. Talin, F. Rosmej, L. A. Bureyeva, and V. Lisitsa, Phys. Rev. E **81**, 016406 (2010).
[15] A. Calisti, F. Khelfaoui, R. Stamm, B. Talin, and R. W. Lee, Phys. Rev. A **42**, 5433 (1990).
[16] C. A. Iglesias, H. E. DeWitt, J. L. Lebowitz, D. Mac Gowan, and W. B. Hubbard, Phys. Rev. A **31**, 1698 (1985).
[17] R. D. Cowan, *The Theory of Atomic Structure and Spectra* (University of California Press, Berkeley, CA, 1981).
[18] I. P. Grant, B. J. McKenzie, P. H. Norrington, D. F. Mayers, and N. C. Pyper, Comput. Phys. Commun. **21**, 207 (1980).
[19] A. Bar-Shalom, M. Klapisch, and J. Oreg, Phys. Rev. A **38**, 1773 (1988).
[20] M. F. Gu, Can. J. Phys. **86**, 675 (2008).
[21] M. Abramowitz and I. A. Stegun, *Handbook of Mathematical Functions* (Dover, Mineola, NY, 1972).
[22] P. Sauvan and E. Dalimier, Phys. Rev. E **79**, 036405 (2009).
[23] A. Calisti, L. Godbert, R. Stamm, and B. Talin, J. Quantum Spectrosc. Radiat. Transfer **51**, 59 (1994).
[24] C. Mossé, A. Calisti, R. Stamm, B. Talin, R. W. Lee, and L. Klein, Phys. Rev. A **60**, 1005 (1999).
[25] M. L. Adams, H. A. Scott, R. W. Lee, J. L. Terry, E. S. Marmar, B. Lipschultz, A. Y. Pigarov, and J. P. Freidberg, J. Quantum Spectrosc. Radiat. Transfer **71**, 117 (2001).
[26] E. Stambulchik and Y. Maron, High Energy Density Phys. **6**, 9 (2009).
[27] J. Seidel and R. Stamm, J. Quantum Spectrosc. Radiat. Transfer **27**, 499 (1982).
[28] M. Gigosos, M. González, and V. Cardeñoso, Spectrochim. Acta, Part A **58**, 1489 (2003).
[29] J. A. Stamper, Laser Part. Beams **9**, 841 (1991).
[30] M. S. Murillo, M. E. Cox, and S. M. Carr, J. Quantum Spectrosc. Radiat. Transfer **58**, 811 (1997).

Annexe J

Line-shape code comparison through modeling and fitting of experimental spectra of CII 723-nm line emitted by the ablation cloud of carbon pellet

Atoms **2014**, *2*, 319-333; doi: 10.3390/atoms2030319

OPEN ACCESS

atoms

ISSN 2218-2004

www.mdpi.com/journal/atoms

Article

Line-Shape Code Comparison through Modeling and Fitting of Experimental Spectra of the C II 723-nm Line Emitted by the Ablation Cloud of a Carbon Pellet

Mohammed Koubiti [1,*], Motoshi Goto [2], Sandrine Ferri [1], Stephanie B. Hansen [3] and Evgeny Stambulchik [4]

[1] Aix-Marseille Université—CNRS, PIIM UMR7345, 13397 Marseille, France;
E-Mail: sandrine.ferri@univ-amu.fr

[2] National Institute for Fusion Science, Toki, 509-5292, Japan;
E-Mail: goto@nifs.ac.jp

[3] Sandia National Laboratories, Albuquerque, NM 87185, USA;
E-Mail: sbhanse@sandia.gov

[4] Faculty of Physics, Weizmann Institute of Science, Rehovot 7610001, Israel;
E-Mail: evgeny.stambulchik@weizmann.ac.il

* Author to whom correspondence should be addressed; E-Mail: mohammed.koubiti@univ-amu.fr; Tel.: +33-491-282-721.

Received: 9 May 2014; in revised form: 28 May 2014 / Accepted: 25 June 2014 / Published: 14 July 2014

Abstract: Various codes of line-shape modeling are compared to each other through the profile of the C II 723-nm line for typical plasma conditions encountered in the ablation clouds of carbon pellets, injected in magnetic fusion devices. Calculations were performed for a single electron density of 10^{17} cm^{-3} and two plasma temperatures (T = 2 and 4 eV). Ion and electron temperatures were assumed to be equal ($T_e = T_i = T$). The magnetic field, B, was set equal to either to zero or 4 T. Comparisons between the line-shape modeling codes and two experimental spectra of the C II 723-nm line, measured perpendicularly to the B-field in the Large Helical Device (LHD) using linear polarizers, are also discussed.

Keywords: carbon pellet ablation; plasma spectroscopy; LHD; Stark/Zeeman broadening; line-shape codes; atomic physics

Classification PACS: 52.25.Os; 32.60.+i; 32.70.Jz; 52.70.-m; 52.55.Hc

1. Introduction

Comparing synthetic line profiles in plasmas carried out with different codes and simulation methods is certainly an interesting issue, which can help to validate the underlying models. In order to use them for plasma diagnostics, such models have to be reliable. However, checking the reliability of a model requires its comparison with experimental data. This does not exclude model-model comparisons. Therefore, code comparisons become more challenging if they include confrontation with experimental measurements. Such comparisons, between theory and experiment, were not scheduled in the first workshop on Spectral Line Shapes in Plasmas: code comparison [1]. To fill this gap, data from two experiments were introduced in the second workshop (5–9 August, 2013, Vienna). These experimental cases were aimed to allow detailed discussion on the approaches adopted by different research groups to analyze experimental spectra. To have a better understanding of why different approaches might end up with different best-fit plasma parameters, it was recommended to contributors willing to analyze the proposed experimental data cases to calculate the relevant line profiles for a small prescribed grid of parameters. The first experimental case concerned the C II 723-nm $1s^2 2s^2 3p\ ^2P^\circ$-$1s^2 2s^2 3d\ ^2D$ line emitted by the ablation cloud of a carbon pellet injected in the Large Helical Device (LHD) [2]. The data for this case consisted of two spectra, both measured along a line-of-sight that is nearly perpendicular to the magnetic field line but with a polarizer rotated, either nearly parallel "horizontal", or nearly perpendicular "vertical", to the magnetic field (see Figure 1). The second experimental case concerned the Li 460.3-nm $1s^2 2p$-$1s^2 4d$ line and its forbidden components. The experimental setup, data processing, and plasma diagnostic techniques are described in [3]. The present paper deals only with the first experimental case, *i.e.*, the C II 723-nm line.

Figure 1. Geometry of observations for the experimental spectra of the C II 723-nm line measured from the ablation cloud of a carbon pellet injected in the stellarator LHD.

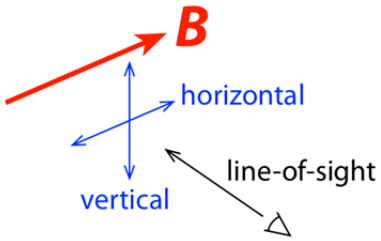

2. Description of the Atomic System and the Line-Shape Modeling Codes

In this section, we introduce all the line-shape codes used for the modeling and/or for the fitting of the previously mentioned experimental spectra of the C II 723-nm line and we briefly describe the atomic physics data necessary for the line profile calculations.

2.1. Description of the Line-Shape Modeling Codes

We present here the five numerical simulation codes and models used by the contributors to model the line-shapes of the C II 723-nm line for four cases sharing the same electron density of $n_e = 10^{17}$ cm^{-3} but for two distinct values of the electron temperature T_e = 2 eV and T_e = 4 eV, without and with a

magnetic field (B = 4 T). Note that the electron and ion temperatures were assumed equal. Even though there are differences in the treatment of the Stark effect by the various codes, they can be separated into two groups, according to the adopted approach to treat the Zeeman effect. Indeed, the line-shape codes used here can be divided into two groups. Those of the first group treat the Zeeman effect within the weak-field approximation [4,5] in which the magnetic field is a perturbation of the emitter fine-structure energy levels, shown in Figure 2a. This approximation is valid when the fine structure splitting exceeds the Zeeman splitting ($\Delta E_{FS} >> \Delta E_Z$). Three methods belong to this group: SCRAM (Sandia National Laboratory), PPP-B and WEAKZEE (CNRS/ Aix-Marseille Université). The PPP-B code [6] is an extension of the PPP standard Stark line-shape code [7,8], which accounts for ion dynamics. In PPP-B, the Zeeman effect is described in either the weak-field approximation or the opposite one, *i.e.*, the strong-field approximation [4,5]. The latter is valid when the Zeeman splitting is higher than the fine structure one ($\Delta E_Z >> \Delta E_{FS}$). Note that, when input MCDF atomic data are used, an asterisk is added to the code name PPP-B which becomes PPP-B *. WEAKZEE is a very simple version of PPP-B where only the electron Stark broadening is accounted for, the ion Stark broadening being neglected. In WEAKZEE, the Zeeman components are dressed by a Lorentzian shape with a given width. The later can be obtained from the Stark-B database [9,10]. In [9], one can find Stark broadening parameters (FWHM: Full Width at Half Maximum) by electrons and ions for few values of the electron density and the electron temperature. For all other temperatures, the Stark widths w (in Å units) can be obtained using the following fit formula [11]:

$$Log(w) = a_0 + a_1 Log(T_e) + a_2 \left[Log(T_e)\right]^2, \quad (1)$$

where a_0, a_1, and a_2 are fitting parameters depending on the line, perturbers (ions or electrons) and the electron density. In this relation, the electron temperature is expressed in Kelvin. For the present calculations, the Lorentzian width w used by WEAKZEE was calculated using Equation (1). SCRAM [12,13], which is primarily used for non-LTE diagnostics of emission spectra that cover a wide range of energies and access many charge states, satellites, *etc.*, uses the electron impact approximation for collisional broadening (based on allowed distorted wave transitions among fine structure states), the quasi-static approximation for the ionic Stark broadening, and can interpolate between the weak and strong field limits. Including forbidden collisional transitions increases the widths by about 10%. The second group of codes contains two models: SIMU [14,15] and INTDPH [16] (Weizmann Institute of Science). In these codes, the Zeeman effect is treated non-perturbatively, via a numerical solution of the static (INTDPH) or time-dependent (SIMU) Schrödinger equation. The initial atomic system is that shown on Figure 2a (see also Table 1). More precisely, SIMU is a combination of two codes: a molecular dynamics (MD) simulation of variable complexity and a solver for evolution of an atomic system with the MD field history used as a time-dependent perturbation. INTDPH is another Stark–Zeeman line-shape code using the quasi-static approximation for the ions. In order to account for the electron broadening, the output is convolved with a shifted Lorentzian at the post-processing step. The width and shift of the Lorentzian should be obtained separately from another code or a database. This is a very fast and accurate procedure (when electrons are strictly impact, e.g., for isolated lines). An application of INTDPH to diagnostics of magnetized plasmas can be found in [17]. For the calculations presented here, the impact broadening parameters were inferred from the SIMU line shapes obtained assuming B = 0.

Figure 2. Schematic energy diagrams of the radiator considered for the present study without (**a**) and with (**b**) the fine structure effect. Energy splitting between the $1s^22s^23p\ ^2P°$ and $1s^22s^23d\ ^2D$ doublets is exaggerated (magnified by a factor of 500) for both of levels. Arrows represent radiative dipolar transitions with solid ones representing those transitions considered for the present study.

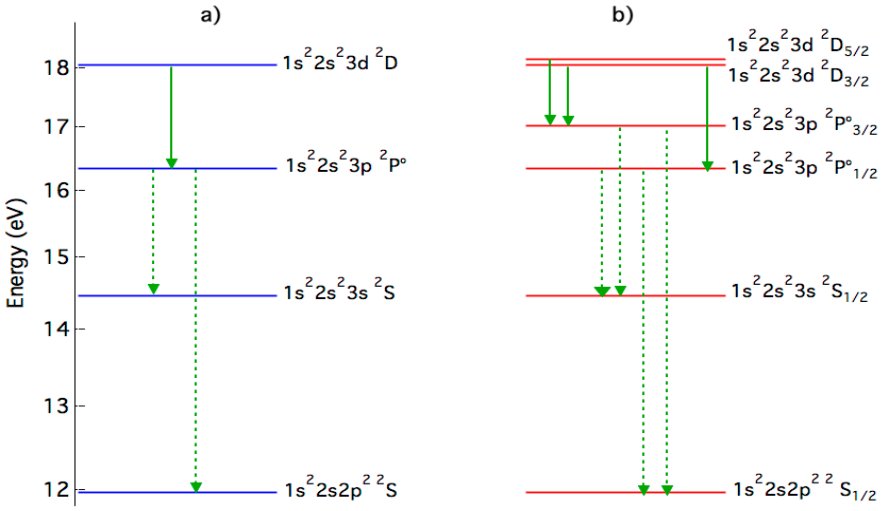

Table 1. Summary of the atomic data of the $1s^22s^23s\ ^2S$-$1s^22s^23p\ ^2P°$ and $1s^22s^23p\ ^2P°$-$1s^22s^23d\ ^2D$ transitions used by the different line-shape codes described in Subsection 2.2. For each transition i→k, the wavenumber σ_{ik} (cm^{-1}) is given in the 3rd column while either the line strength S_{ik} or the line oscillator f_{ki}, both in atomic units, are given in columns 4 and 5. The last column shows the corresponding line-shape codes. The sources of the atomic data are indicated in the table: National Institute for Standard and Technology NIST [18], Multiconfiguration Dirac-Fock MCDF [19], and Flexible Atomic Code FAC [20]. Note that PPP-B and PPP-B* codes differ only by the atomic physics: NIST for PPP-B and MCDF for PPP-B *.

Terms	Energies E_i–E_k (cm^{-1})	σ_{ik} (cm^{-1})	S_{ij}(a.u)	f_{ki}(a.u.)	Line-Shape Code(s)
$3s\ ^2S$-$3p\ ^2P°$	116,537.65–131 731.80	15,194.15		0.715[18]	INTDPH SIMU
$3p\ ^2P°$-$3d\ ^2D$	131,731.80–145 550.13	13,818.33		0.547[18]	INTDPH SIMU
$3p\ ^2P°_{1/2}$-$3d\ ^2D_{3/2}$	131,724.37–145,549.27	13,824.92	26.00[18]	-	PPP-B
			//	-	WEAKZEE
			11.66[19]	-	PPP-B *
			13.84[20]	-	SCRAM
$3p\ ^2P°_{3/2}$-$3d\ ^2D_{5/2}$	131,735.52–145 550.70	13,815.18	46.90[18]	-	PPP-B
			//	-	WEAKZEE
			21.00[19]	-	PPP-B *
			33.31[20]	-	SCRAM
$3p\ ^2P°_{3/2}$-$3d\ ^2D_{3/2}$	131,735.52–145 549.27	13,813.75	5.21[18]	-	PPP-B
			//	-	WEAKZEE
			2.33[19]	-	PPP-B *
			5.56[20]	-	SCRAM

2.2. Brief Description of the Atomic System Representing the Emitter

The calculation of the profile of the C II 723-nm line does not require a complicated atomic data system. However, even though only four energy levels and three dipolar radiative transitions are sufficient, calculations of such atomic physics data is complicated for this weakly charged non-hydrogen-like ion. For our case, different atomic codes give different values of the dipole reduced matrix elements. In the absence of magnetic field, one can use the atomic system shown on Figure 2, where the fine structure effect is shown only for the right part of the figure. In this figure, the fine structure splitting between the $1s^2 2s^2 3p\ ^2P°$ and $1s^2 2s^2 3d\ ^2D$ doublets have been magnified by a factor of 500. Energies are expressed with respect to the ground level of the C^+ ion, *i.e.*, $1s^2 2s^2 2p\ ^2P°_{1/2}$.

All line shape codes require some atomic information of the radiator including the energies, labels and quantum numbers of all the radiator energy levels involved in the considered radiative transitions, as well as the reduced matrix elements of the electric dipole or their squares, known as line strengths. Equivalently to line strengths, one can use line oscillators. Different atomic data have been used for the present code comparison. The atomic data including the electric dipolar matrix transitions were taken from NIST ASD [18]. One of the authors has used atomic data calculated by an MCDF code [19], differing only by reduced matrix elements of the dipole transitions about 1.5 times lower than those extracted from NIST ASD; another has used strength data from FAC [20]. The line strengths and/or line oscillators of the radiative transitions considered here are summarized on Table 1.

3. Cross-Comparison of the Line Profiles Computed with the Different Codes

3.1. Magnetic Field-Free Case

Let us start with the modeling of the C II 723-nm line profiles for the magnetic field-free cases with the following plasma parameters: $n_e = 10^{17}$ cm^{-3}, $T_e = T_i = 2$ eV and $T_e = T_i = 4$ eV. Whatever are the positively charged perturbers (D^+ or C^+ ions), calculations show that the above line is dominated by electron broadening, the ion contribution being close to zero. This is demonstrated in Figure 3, where the electron broadened profile of the C II 723 nm line is compared to the full pure Stark profile of the same line. The profiles shown on this figure, calculated with the PPP-B code using atomic data from NIST, demonstrate the dominance of the electron broadening over the ionic one for these typical conditions. Note that, in this paper, all the computed profiles are plotted against the wavenumber shift (in cm^{-1}) with respect to the line center wavenumber σ_0.

Before comparing the results of the different codes, it is interesting to discuss briefly the electron broadening which is treated in the frame of the impact theory in all the used codes. Different models and formulae exist for the electron collision operator [21,22]. The PPP-B and PPP-B * (as well as PPP) line shape codes use a modified electron broadening operator. This modified electron collision operator, which is based on the semi-classical GBK model due to Griem, Blaha, and Kepple [23], can be written as follows:

$$\Phi(\Delta\omega = 0) = \left(\frac{4\pi}{3}\right)\left(\frac{2m_e}{\pi k\, T_e}\right)^{1/2} n_e \left(\frac{\hbar}{m_e}\right)^2 \mathbf{R}.\mathbf{R}\left[C_n + \frac{1}{2}\int_y^\infty \frac{e^{-x}}{x}\,dx\right], \quad (2)$$

where:

$$y(\Delta\omega = 0) \approx \left(\frac{\hbar n^2}{2(z_e + 1)} \right)^2 \frac{\omega_p^2 + \Delta\omega_{\alpha\alpha''}^2}{E_H \quad kT_e} \tag{3}$$

Equation (3) arises from conditions on the limits of the integral over impact parameters ρ_{min} and ρ_{max} appearing in Equation (12) of [23]. More precisely, a strong collision term is added and different cutoffs are included in this Equation.

Figure 3. Comparison of Stark profiles of the C II 723-nm line emitted by a pure carbon plasma (electrons and C^+ ions) computed with the following parameters: $n_e = 10^{17}$ cm^{-3}, $T_e = T_i = 2$ eV and B = 0. Dashed line represents the electron broadening only while the solid one accounts for both ions and electrons, all other broadening mechanisms were ignored. Note the use of a semi-logarithmic scale. Both profiles were calculated using PPP-B with atomic data from NIST and by setting B = 0 T.

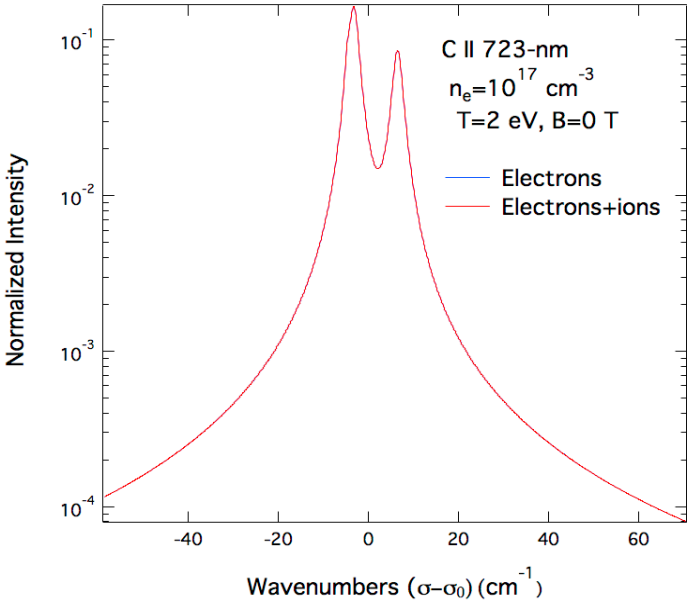

Here, m_e is the electron mass and **R** is the position operator of the radiator. C_n is a strong collision term whose value depends on the principal quantum number n as: $C_2 = 1.5$, $C_3 = 1.0$, $C_4 = 0.75$, $C_5 = 0.5$ and $C_n = 0.4$ for $n > 5$. In Equation (4), E_H and z_e represent respectively the hydrogen ionization potential and the net charge of the emitter while ω_p and $\Delta\omega_{\alpha\alpha''}$ designate the electron plasma frequency and the frequency separation between the state α involved in a given transition and its perturbing states α'' [24]. Moreover, the impact limit has been taken, *i.e.*, $\Delta\omega = 0$. Equation (2) indicates that the electron interactions with the emitter result in a homogeneous broadening represented by a Lorentzian function whose full width at half maximum (FWHM) is proportional to the plasma electron density n_e and inversely proportional to the square root of the electron temperature T_e. It should be noted that the dipole reduced matrix elements are involved through the operator **R.R** present in relation Equation (2). As the line considered here is of the same type as the Li-like (Li I, B III, N V) 2s-2p, *i.e.*, $\Delta n = 0$ transitions, we will not discuss the validity of impact electronic collision operators such the above one. Readers interested by that issue may refer to the discussion found in [25].

In Figure 8 of [2], various experimental and theoretical data representing Stark broadening widths (FWHM) of the C II 723-nm line were fitted with a linear function of the plasma electron density. An electron density $n_e = 10^{17}$ cm^{-3} corresponds to a Stark FWHM of about 0.1 nm or 1.9 cm^{-1} in terms of wavenumbers. A very close value can be obtained from the Stark-B database [9]. The C II 723-nm line profiles calculated by the various codes for $n_e = 10^{17}$ cm^{-3}, $T_e = T_{iv} = 2$ eV and B = 0 are shown on Figure 4. As the profile calculated with WEAKZEE was obtained using Lorentzian functions with FWHM taken from the Stark-B database, it can be considered as a "reference" profile with a Stark width $\Delta\sigma_0$. Several points can be noted from Figure 4. First, the calculations with SIMU and INTDPH as well as PPP-B* (PPP-B code but with MCDF atomic data) give lower Stark widths, *i.e.*, $\Delta\sigma < \Delta\sigma_0$. Note the agreement between SIMU/INTDPH and PPP-B * despite the differences between the used atomic physics: NIST atomic data for the former and MCDF data for the latter. Second, in term of Stark widths, the profiles obtained with PPP-B slightly higher than ($\Delta\sigma \geq \Delta\sigma_0$) while those obtained with SCRAM are very close to ($\Delta\sigma \approx \Delta\sigma_0$) the "reference" one. This means that the electronic collision operator given by Stark-B and GBK lead to the close results. This is confirmed in Table 2, which presents the ratios of the Stark FWHM $\Delta\sigma$ to the "reference" value $\Delta\sigma_0$ for the different codes. In terms of line-shapes, it can be seen from Figure 4 that PPP-B agrees with WEAKZEE for the line wings. While SCRAM appears to overestimate the line wings, which is due to its inclusion of continuum emission where the other codes included only the line features. The same remarks and conclusions about both Stark widths and shapes of the C II 723-nm line can be drawn for the case with $n_e = 10^{17}$ cm^{-3} and $T_e = T_i = 4$ eV in the absence of the magnetic field (B = 0).

Table 2. Comparison of the Stark Full Width at Half Maximum (FWHM) $\Delta\sigma$ of the C II 723 nm line extracted from the profiles synthetized by the different codes with respect to a reference FWHM $\Delta\sigma_0$ for $n_e = 10^{17}$ cm^{-3}, $T_e = T_i = 2$ eV and B = 0.

Code	PPP-B	PPP-B *	SIMU/INTDPH	SCRAM	WEAKZEE
$\Delta\sigma/\Delta\sigma_0$	1.2	0.6	0.5	0.9	1.0

3.2. Magnetic Field Case

Let us now compare the synthetic profiles in the presence of a magnetic field B = 4 T. The presence of the magnetic field imposes a constraint on the radiation polarization. Photons whose polarizations are parallel or perpendicular to the B-field form respectively the π and σ components of the spectral line profile. These components as calculated by the previously mentioned codes are shown in Figures 5 and 6. On the other hand, assuming a perpendicular observation with respect to **B**, the total spectral line profile is calculated from the σ- and π-polarized ones I_σ and I_π using the following formula:

$$I_{tot}(\sigma) = I_\pi(\sigma) + 2I_\sigma(\sigma) \quad (4)$$

Total profiles are compared on Figure 7.

While the overall agreement between codes in Figures 5–7 is quite good within a factor two in terms of Stark FWHM, there are some significant differences: The profiles provided by SIMU/INTDPH show more structures around the line center than the other results. This can be attributed to the fact the Zeeman effect is fully treated by these two codes but at the same time the Stark broadening is smaller

than that of the other codes, as illustrated in the B-field free case. Note that for C II 723-nm line, the fine structure splitting of its lower and upper energy levels are $\Delta E_{3p} = E(3p\ ^2P°_{3/2}) - E(3p\ ^2P°_{1/2}) \approx 11.2\ cm^{-1}$ and $\Delta E_{3d} = E(3d\ ^2D_{5/2}) - E(3d\ ^2D_{3/2}) \approx 1.4\ cm^{-1}$ respectively. The energy splitting of the same levels due to Zeeman effect is about $\Delta E_B \approx 0.8\ cm^{-1}$ for B = 2 T and $1.6\ cm^{-1}$ for B = 4 T. It is clear that for these values of the magnetic field, the Zeeman splitting is comparable to the fine-structure one for the upper energy levels and therefore the use of the weak-field approximation becomes questionable. As for the field-free case, PPP-B * reproduces well the wings computed by both SIMU and INTDPH codes. The profiles computed by WEAKZEE, PPP-B and SCRAM show less features because of the weak-field approximation used to treat the Zeeman effect but the line widths are more correct as compared to those obtained with SIMU/INTDPH. In terms of Stark widths these remarks corroborate those concerning the field-free case. Calculations of profiles of the C II 723-nm line for the same plasma parameters as above with T = 4 eV instead of 2 eV lead to the same conclusions.

Figure 4. Comparison of synthetic Stark profiles of the C II 723-nm line emitted by a plasma with $n_e = 10^{17}\ cm^{-3}$, $T_e = T_i = 2$ eV and B = 0 in a semi-logarithmic scale. The dashed line represents the profile obtained with the simulation code SIMU. Note that the profile calculated with INTDPH code is not shown here as it is almost identical to the one obtained with SIMU. The solid thick red line represents the profile calculated with the PPP-B code using the most accurate atomic data provided by NIST while the solid thin red line is the one obtained with the same code PPP-B (PPP-B *) but with atomic data calculated with an MCDF code. Solid blue and green lines represent the profiles obtained respectively with SCRAM (which includes continuum as well as line emission) and WEAKZEE.

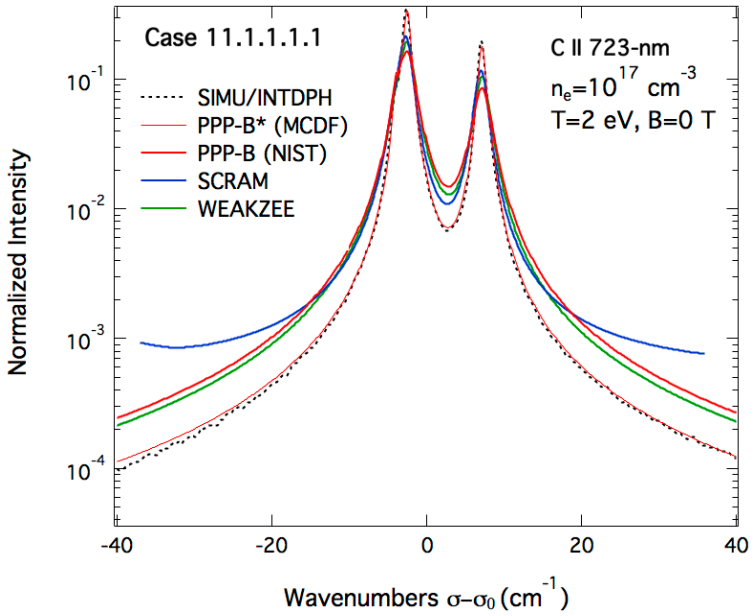

Figure 5. Comparison of the Stark–Zeeman σ-component of the C II 723-nm line as computed by the different line-shape codes for a carbon plasma with the following parameters: $n_e = 10^{17}$ cm^{-3}, $T_e = T_i = 2$ eV and B = 4 T.

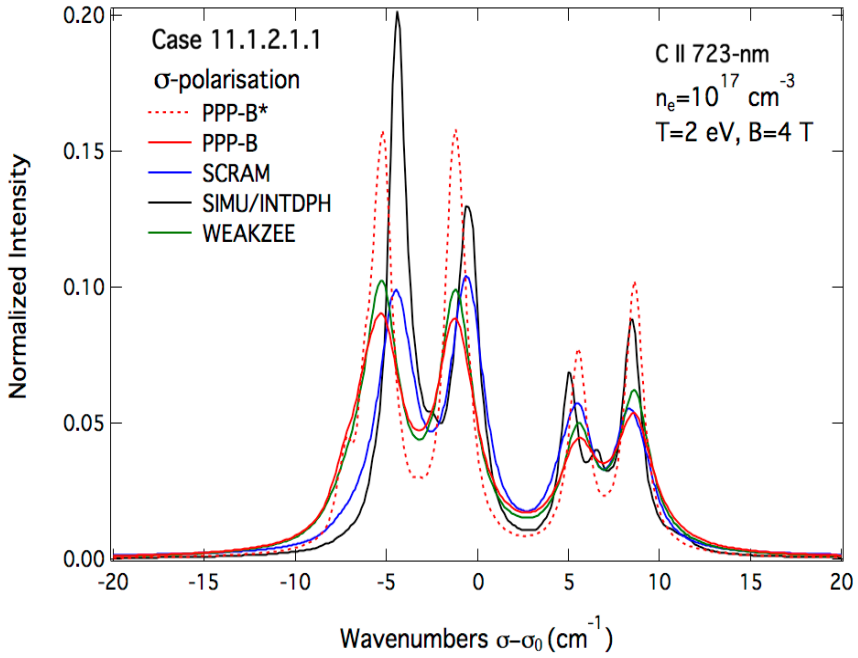

Figure 6. Comparison of the Stark–Zeeman π-component of the C II 723-nm line as computed by the different line-shape codes for the same conditions as in Figure 5.

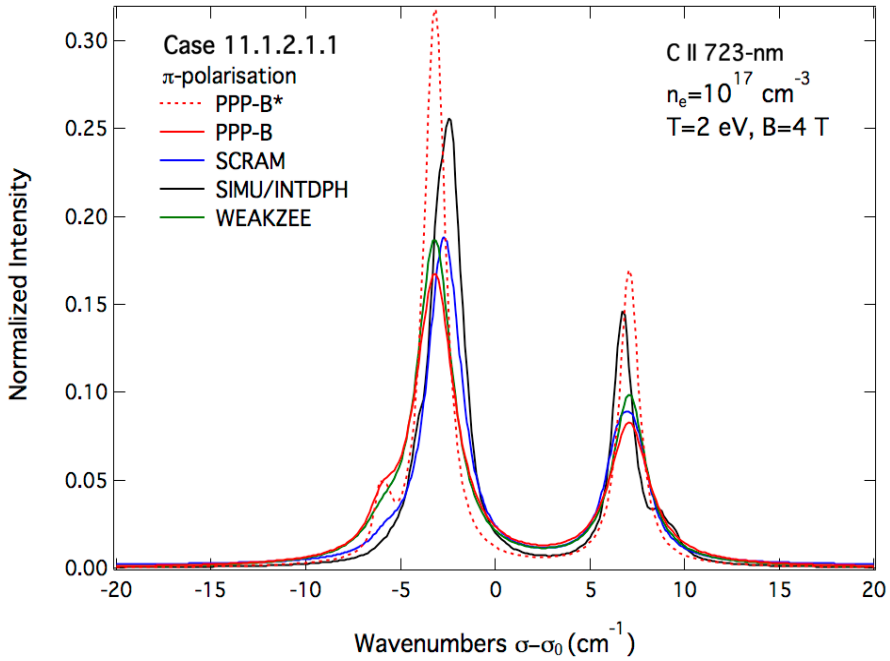

Figure 7. Comparison of the total Stark–Zeeman profiles of the C II 723-nm line as computed by the different line-shape modeling codes for the same conditions as in Figures 5 and 6 with an angle of observation of 90° with respect to the magnetic field direction.

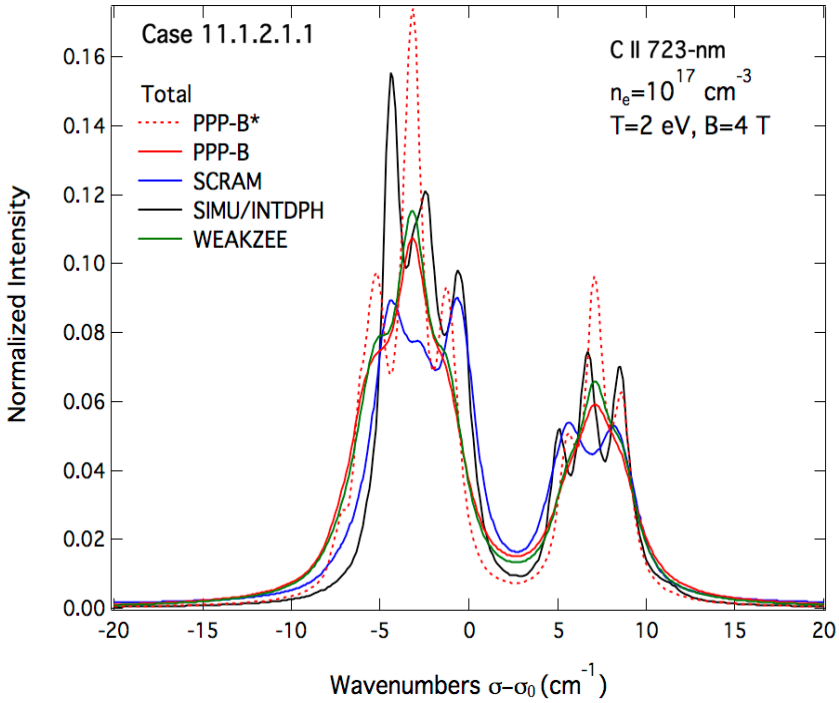

4. Comparison to the Experimental Spectra

As mentioned previously, the experimental data were obtained during the injection of a carbon pellet in the stellarator LHD. As all details concerning the experimental setup, the measurement system and pellet injection in LHD can be found in [2], we give here only the information necessary for the data analysis. The spectra were measured with a very high-resolution visible spectrometer. The instrumental function can be represented by a gaussian function with a FWHM $\Delta\lambda_{1/2}$ = 0.016 nm as compared to that of the high-resolution spectrometer used for the data of reference [2] ($\Delta\lambda_{1/2}$ = 0.075 nm). The spectra were measured almost perpendicularly to the magnetic field. In addition, thanks to linear polarizers two spectra were obtained: horizontal spectrum (π-polarization) and vertical spectrum (σ-polarization). These spectra are shown in Figure 8. These two spectra were proposed as a challenging case at the 2nd workshop on spectral line shapes in plasmas. Contributors were asked to do their best to fit these spectra in order to find the most reliable set of parameters (magnetic field, angle of observation, electron density and temperature).

Attempts to fit these experimental spectra are shown in Figures 9–11 corresponding, respectively, to the σ- and π-polarized spectra and the built un-polarized total spectrum.

Figure 8. Experimental spectra of the C II 723-nm line as measured in LHD almost perpendicularly to the magnetic field (see Figure 1) using a very high-resolution visible spectrometer and linear polarizers.

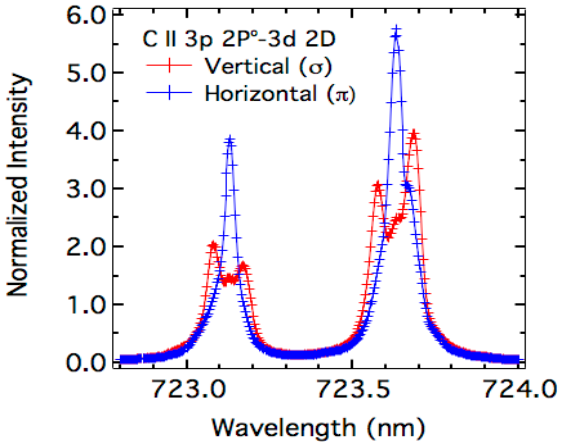

It can be seen from Figures 9–11 that none of the line-shape codes were able to fit perfectly the proposed experimental spectra. However, these attempts were fruitful and can be considered reasonably good. Using the code INTDPH, the best fit of the three spectra was obtained with the following parameters: a carbon plasma with an electron density $n_e = 9 \times 10^{16}$ cm^{-3}, an equal ion and electron temperatures of 1 eV and a magnetic field B = 2.15 T. In the calculations by the INTDPH code, the static profiles were convolved with a shifted Lorentzian whose shift δσ and FWHM Δσ were determined using the simulation method SIMU. For the above conditions, the following values were obtained: $\Delta\sigma = 0.9$ cm^{-1} and $\delta\sigma = 0.26$ cm^{-1}. Moreover, a contrast ratio of 4:1 was assumed for the polarizers. This is equivalent to assume that the line-of-sight is not strictly perpendicular to the magnetic field or alternatively to the existence of fluctuations of the field direction in the spectroscopic observation volume observed. It should be noted that a pure LS coupling was assumed and the 3p fine splitting was changed from the NIST value 11.15 to 11.24 cm^{-1} to better fit the data. The second fitting attempt was due to the SCRAM code. Using SCRAM without the ionic Stark broadening, the best-fit calculations were obtained for a magnetic field B = 2 T with the following carbon plasma parameters: an electron density $n_e = 6 \times 10^{16}$ cm^{-3} and an ion/electron temperature T = 2 eV. The angle of observation 0 was set to 90°. The third and last fitting attempt was due to the WEAKZEE method considering only the Stark broadening by electrons. The best fit was obtained for an angle of observation 0 = 70° and the following plasma parameters: electron density $n_e = 4 \times 10^{16}$ cm^{-3}, electron/ion temperature T = 2 eV. The B-field value was set to 2 T. In addition, in an attempt to fit at least partially the π-component, a profile calculated with PPP-B (NIST data) was added to the other results shown on Figure 10. Without the use of any fitting procedure but varying only the electron density, the parameters leading to a good agreement with the right peak of the experimental spectrum (in terms of line-shapes and Stark widths) were the following: $n_e = 4 \times 10^{16}$ cm^{-3}, T = 2 eV, B = 2 T and 0 = 90°. It should be noted that all calculations were done assuming an optical thin plasma emission zone. The spread of the obtained results concerning the plasma electron density was expected since all the parameters, including the angle of observation, were free for the fitting. Introducing constraints on the angle of observation would result in more consistent results providing the same

atomic physics is used. Each of the three methods used to fit the experimental spectra has its own advantages and drawbacks. As previously demonstrated, the electron broadening is correctly accounted for by the WEAKZEE and SCRAM codes while underestimated by the couple of codes SIMU/INTDPH. On the other side, Zeeman effect is correctly treated by SIMU/INTDPH while the weak-field approximation was used by both SCRAM and WEAKZEE methods. Therefore, it is clear that a correct plasma electron diagnostics based of the considered line spectra requires a full treatment of the Zeeman effect as well as the use of the appropriate electron line broadening and this should be integrated by these different line-shape codes.

Figure 9. Fitting attempts of the σ-polarized experimental spectrum of the C II 723-nm line as measured in LHD. All spectra are normalized to unity.

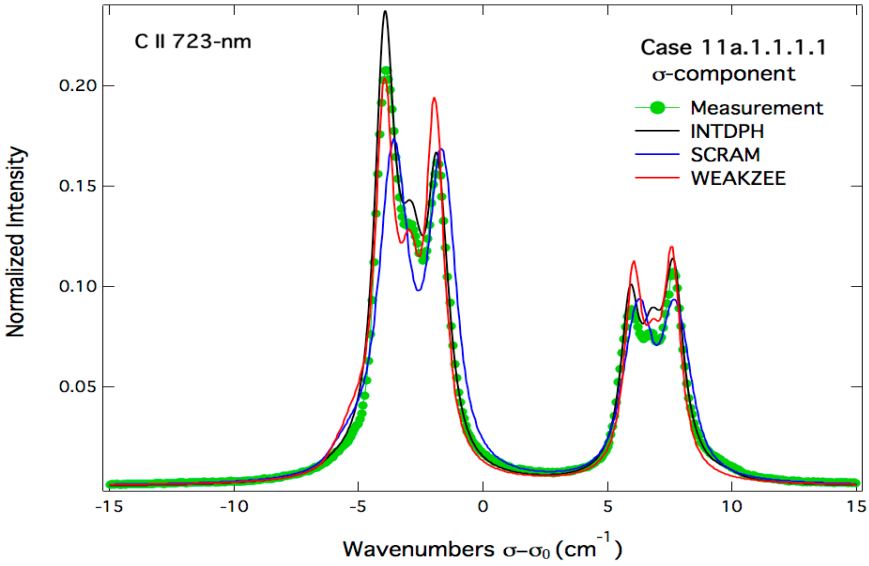

Figure 10. Fitting attempts of the π-polarized experimental spectrum of the C II 723-nm line as measured in LHD. All spectra are normalized to unity.

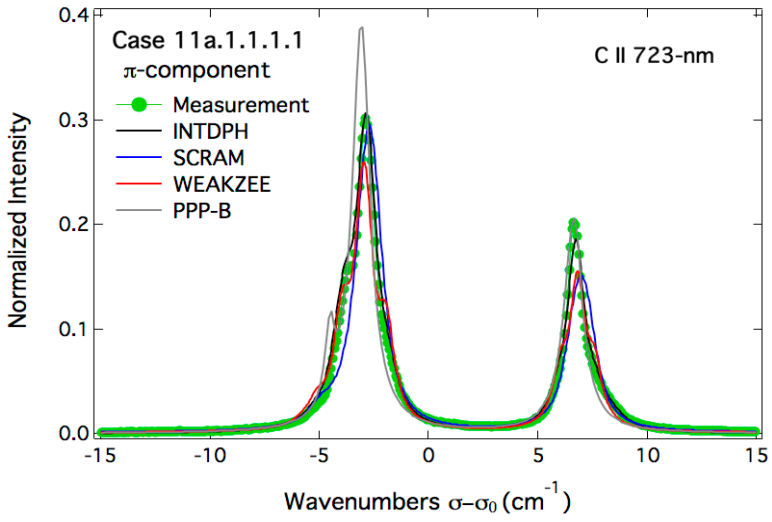

Figure 11. Fitting attempts of the un-polarized "experimental" spectrum of the C II 723-nm line as constructed from σ- and π-polarized spectra of Figures 9 and 10. Superscript [(a)] indicates that the area of the profile calculated with INTDPH is equal to 0.9 while all other spectra are normalized to unity.

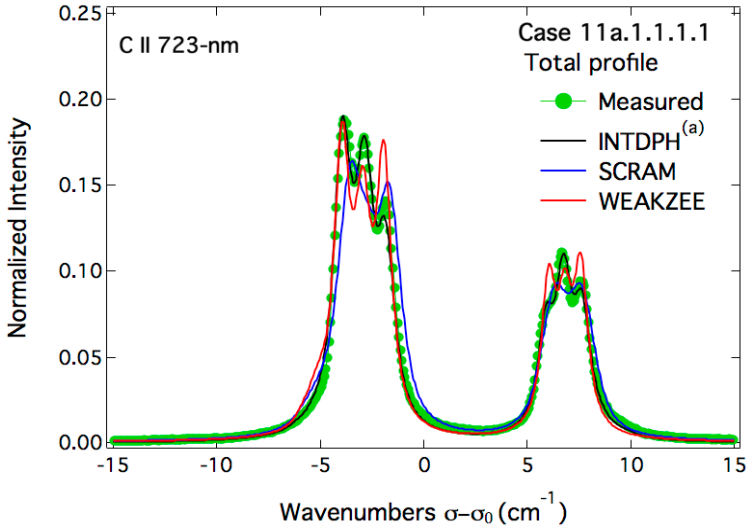

5. Conclusions

Several line-shapes codes were compared through the modeling of the C II 723-nm line profile for four situations corresponding to a fixed electron density of 10^{17} cm^{-3}, two temperatures (T = 2 and 4 eV) with and without the presence of a magnetic field B = 4 T. For these conditions, calculations have shown that the Stark broadening of the above line is mainly due to the plasma electrons. C II 723-nm line profiles calculated by five line-shape codes have been compared. For the magnetic-field free case (B = 0 T), a relatively good overall agreement has been obtained, despite the significant differences in the code results in terms of Stark width (FWHM) of the C II 723-nm line. Indeed, the overall agreement between the five line-shape codes is within a factor of 2. Two factors may contribute to this dispersion of the results: differences in the used atomic physics and/or in the electron collision operator. However, the former factor has been dismissed by partial comparisons between line-shape codes using the same more accurate atomic physics data, *i.e.*, from the NIST ASD database. Therefore, the dispersion in Stark widths is attributed to differences in the electron collision operators used by the various line-shape codes. For the case with B = 4 T, the differences in the treatment of the Zeeman effect by the different codes make more difficult the interpretation of the results. However, it is clear that the weak-field approximation adopted by some of the codes is not valid for the upper level of the C II 723-nm line, *i.e.*, (3d ^{2}D°). Therefore, codes able to deal with intermediate magnetic fields (comparable Zeeman and fine structure splittings of energy levels) are more suitable. In addition to code-code comparisons, σ- and π-polarized experimental spectra of the C II 723-nm line, measured from the ablation cloud of a carbon pellet injected in LHD, were fitted using several line-shape codes. By letting free all the parameters (magnetic field B, electron density n_e, electron/ion temperature T, angle of observation 0), attempts to fit the experimental spectra have shown a large dispersion in the inferred parameters in particular the electron density for which there is a factor of more than 2. However, even though not perfect, these fitting attempts are encouraging and suggest to use the best of

each code for the purpose of diagnostics of magnetized plasmas. It is recommended for this case to use a full-treatment of the Zeeman effect and elucidate and reduce the dispersion in the Stark widths due to the electron broadening. This requires more investigations and detailed comparisons with a prescribed atomic system.

Author Contributions

This work is based on the following author contributions: spectral measurements, data—M. Goto; code calculations, comparison with experimental data—all other authors; writing of the manuscript—M. Koubiti with contribution of the other authors.

Conflicts of Interest

The authors declare no conflict of interest.

References

1. Stambulchik, E. Review of the 1st Spectral line shapes in plasmas: Code comparison. *High Energy Density Phys*. **2013**, *9*, 528–534.
2. Goto, M.; Morita, S.; Koubiti, M. Spectroscopic study of a carbon pellet ablation cloud. *J. Phys. B-At. Mol. Opt. Phys.* **2010**, *43*, 144023.
3. Cvejić, M.; Gavrilović, M.R.; Jovićević, S.; Konjević, N. Stark broadening of Mg I and Mg II spectral lines and Debye shielding effect in laser induced plasma. *Spectrochim. Acta Part B*: *Atomic Spectrosc*. **2013**, *85*, 20–33.
4. Condon, E.U.; Shortley, G.H. One-Electron Spectra. In *The Theory of Atomic Spectra*; Cambridge University Press: London, UK, 1964; pp. 149–157.
5. Weissbluth, M. *Static Fields in Atoms and Molecules*; Student edition, Academic Press: New York, NY, USA, 1978; pp. 346–355.
6. Ferri, S.; Calisti, A.; Mossé, C.; Mouret, L.; Talin, B.; Gigosos, M.A.; Gonzalès, M.A.; Lisitsa, V. Frequency-fluctuation model applied to Stark–Zeeman spectral line shapes in plasmas. *Phys. Rev. E* **2011**, *84*, 026407.
7. Talin, B.; Calisti, A.; Godbert, L.; Stamm, R.; Lee, R.W.; Klein, L. Frequency-fluctuation model for line-shape calculations in plasma spectroscopy. *Phys. Rev. A* **1995**, *51*, 1918.
8. Calisti, A.; Mossé, C.; Ferri, S.; Talin, B.; Rosmej, F.; Bureyeva, L.A.; Lisitsa, V.A. Dynamic Stark broadening as the Dicke narrowing effect. *Phys. Rev. E* **2010**, *81*, 016406.
9. Sahal-Brechot, S.; Dimitrijević, M.S.; Moreau, N. Observatory of Paris, LERMA and Astronomical Observatory of Belgrade Stark-B Database. Available online: http://stark-b.obspm.fr (accessed on 16 April 2014).
10. Mahmoudi, W.F.; ben Nessib, N.; Sahal-Bréchot, S. Semi-classical calculations of Stark broadening impact theory of singly-ionized carbon, nitrogen and oxygen spectral lines. *Phys. Scr*. **2004**, *70*, 142.
11. Sahal-Bréchot, S.; Dimitrijević, M.S.; ben Nessib, N. Comparisons and comments on electron and ion impact profiles of spectral lines. *Balt. Astron*. **2011**, *20*, 523–530.

12. Hansen, S.B. Configuration interaction in statistically complete hybrid-structure atomic models. *Can. J. Phys*. **2011**, *89*, 633–638.
13. Hansen, S.B.; Bauche, J.; Bauche-Arnoult, C.; Gu, M.F. Hybrid atomic models for spectroscopic plasma diagnostics. *High Energy Density Phys*. **2007**, *3*, 109–114.
14. Stambulchik, E.; Maron, Y. A study of ion-dynamics and correlation effects for spectral line broadening in plasma: K-shell lines. *J. Quant. Spectr. Rad. Transf*. **2006**, *99*, 730–749.
15. Stambulchik, E.; Alexiou, S.; Griem, H.R.; Kepple, P.C. Stark broadening of high principal quantum number hydrogen Balmer lines in low-density laboratory plasmas. *Phys. Rev. E* **2007**, *75*, 016401.
16. Stambulchik, E.; Maron, Y. Effect of high-n and continuum eigenstates on the Stark effect of resonance lines of atoms and ions. *Phys. Rev. A* **1997**, *56*, 2713–2719.
17. Tessarin, S.; Mikitchuk, D.; Doron, R.; Stambulchik, E.; Kroupp, E.; Maron, Y.; Hammer, D.A.; Jacobs, V.L.; Seely, J.F.; Oliver, B.V.; *et al*. Beyond Zeeman spectroscopy: Magnetic-field diagnostics with Stark-dominated line shapes. *Phys. Plasmas* **2011**, *18*, 093301.
18. Kramida, A.; Ralchenko, Y.; Reader, J.; NIST ASD Team (**2013**). NIST Atomic Spectra Database (ver. 5.1). Available online: http://physics.nist.gov/asd (accessed on 9 May 2014).
19. Grant, I.P.; McKenzie, B.J.; Norrington, P.H.; Mayers, D.F.; Pyper, N.C. An atomic multiconfigurational Dirac-Fock package. *Comput. Phys. Commun*. **1980**, *21*, 207–231.
20. Gu, M.F. The Flexible Atomic Code. *Can. J. Phys*. **2008**, *86*, 675–689.
21. Calisti, A.; Ferri, S.; Stamm, R.; Talin, B.; Lee, R.W.; Klein, L. Discussion of the validity of binary collision models for electron broadening in plasmas. *J. Quant. Spectrosc. Radiat. Transf*. **2000**, *65*, 109–116.
22. Alexiou, S. Collision operator for isolated ion lines in the standard Stark-broadening theory with applications to the Z scaling of the Li isoelectronic series 3P-3S transition. *Phys. Rev. A* **1994**, *49*, 106–119.
23. Griem, H.R.; Blaha, M.; Kepple, P.C. Stark-profile calculations for Lyman-series lines of one-electron ions in dense plasmas. *Phys. Rev. A* **1979**, *19*, 2421–2432.
24. Calisti, A.; Khelfaoui, F.; Stamm, R.; Talin, B.; Lee, R.W. Model for the line shapes of complex ions in hot and dense plasmas. *Phys. Rev. A* **1990**, *42*, 5433–5440.
25. Alexiou, S.; Dimitrijević, M.S.; Sahal-Brechot, S.; Stambulchik, E.; Duan, B.; Gonzalez-Herrero, D.; Gigosos, M.A. The Second Workshop on Lineshape Code Comparison: Isolated Lines. *Atoms* **2014**, *2*, 157–177.

Annexe K

Line profiles of Ni-like collisional XUV laser amplifiers

High Energy Density Physics 9 (2013) 516–522

Contents lists available at SciVerse ScienceDirect

High Energy Density Physics

journal homepage: www.elsevier.com/locate/hedp

Line profiles of Ni-like collisional XUV laser amplifiers: Particle correlation effects

A. Calisti [a,*], S. Ferri [a], C. Mossé [a], B. Talin [a], A. Klisnick [b], L. Meng [b], D. Benredjem [c], O. Guilbaud [d]

[a] PIIM, UMR7345, Aix-Marseille Université – CNRS, Campus Saint Jérôme, 13397 Marseille Cedex 20, France
[b] ISMO, UMR8214, Université Paris-Sud 11 – CNRS, Bat. 350, 91405 Orsay Cedex, France
[c] LAC, UPR3321, CNRS, Université Paris-sud 11, 91405 Orsay, France
[d] LPGP, UMR8578, CNRS – Université Paris-Sud 11, Bat. 210, 91405 Orsay Cedex, France

ARTICLE INFO

Article history:
Received 6 May 2013
Accepted 6 May 2013
Available online 15 May 2013

Keywords:
Line broadening
Homogeneous and inhomogeneous profiles
Ni-like Ag XUV laser line
Particle correlation effects

ABSTRACT

We present a detailed analysis of the different processes that contribute to the spectral broadening of the Ni-like Ag XUV laser line, including the effects of particle correlations on the broadening due to the radiator motion (Doppler broadening). We consider two different regimes of collisional excitation pumping: the transient pumping for which the ionic temperature is relatively low and the plasma coupling parameter is large, and the quasi steady-state pumping for which the ionic temperature is higher and the plasma coupling parameter is of the order of 1. In both cases, by using classical molecular dynamics simulation techniques, we show that ionic correlations actually modify the radiator-motion broadened profiles and cannot be neglected in evaluating the Doppler effect. The subsequent narrowing of the Doppler component is small compared to the overall linewidth, which includes the effect of homogeneous collisional broadening. However, ionic correlations will also affect the amplification of the lasing line, especially when the laser enters the saturation regime, because it will lead to a homogenization of the spectral profile.

1. Introduction

There is increasing interest in better understanding the spectral behavior of plasma-based collisional XUV lasers in the recent years [1–5]. The main reason is that the shortest pulse duration that has been reached is limited to ~1 ps [6] by the extremely narrow bandwidth of these sources. For numerous applications, like the production of plasma in the Warm Dense Matter regime (WDM) [7], one needs XUV lasers with a shorter pulse duration, namely in the subpicosecond or even in the femtosecond range. This could be obtained if the XUV laser is operated in an injection-seeded mode, using femtosecond high-order harmonic radiation as a seed [5,6], but only on condition that the bandwidth be enlarged by a factor ~3 or larger. The ultimate duration τ_{FL} of the output pulse of such an injection-seeded XUV laser is controlled by the spectral bandwidth of the plasma amplifier, through $\tau_{FL} \sim \lambda^2/\Delta\lambda$. The bandwidth that should be considered here involves not only the intrinsic (optically thin) broadening of the lasing line, but also the effects of gain narrowing and potential saturation rebroadening occurring in the process of amplification, which depend on the degree of inhomogeneity of the intrinsic profile [8]. In order to define strategies to progress toward this goal, one needs to better characterize the various contribution of the different broadening mechanisms that occur in XUV laser plasmas.

The intrinsic spectral profile of emission lines in a plasma is determined predominantly by spontaneous emission rates, electron collisional rates, Stark broadening and Doppler broadening [9] with possible complications due to ion turbulence [10] and additional ion–ion interactions [10–13]. In a medium with population inversions and gain, the observed profile is modified by radiative transport effects in being narrowed approximately as the square root of the gain–length product in the small signal regime [8]. As the laser saturates, if the intrinsic profile is dominated by inhomogeneous rather than homogeneous broadening mechanisms, the line can be re-broadened to its intrinsic width. This indicates clearly the importance of having a good representation of the intrinsic profile together with a good understanding of the different mechanisms responsible for broadening. It is usual to consider that the inhomogeneous broadening mechanisms are caused by the local

* Corresponding author.
E-mail address: annette.calisti@univ-amu.fr (A. Calisti).

1574-1818/$ – see front matter © 2013 Elsevier B.V. All rights reserved.
http://dx.doi.org/10.1016/j.hedp.2013.05.004

inhomogeneities of the medium such as Doppler shifts, quasi-static electric microfields or turbulence and that homogeneous broadenings are mainly due to electron-radiator collisions and/or spontaneous emission. Nevertheless, similarly to the quasi-static electric field approximation which can become inappropriate in the Stark broadening theory due to perturber ion dynamics [14], the free particle formalism involved in the standard Doppler effect calculation could fail if ion velocities change over time scales of the same order of or shorter than the effective radiative lifetime of the oscillator, i.e., the inverse of homogeneous spectral linewidth. In other words, if the velocities change before the light emission happens, it is no longer possible to consider ions with straight trajectories and particle interactions have to be included in the calculation of the spectral profile. In some circumstances, the breakdown of the free particle approximation can have significant consequences by resulting in the narrowing of the intrinsic Doppler profile when the mean time of velocity-changing, t_c is shorter than the effective Doppler correlation time, an effect known as Dicke narrowing [15]. On the other hand, when t_c is less than the effective radiative lifetime it can result in the effective homogenization of the ordinarily inhomogeneous Doppler profile by velocity redistribution, and affect the spectral content and amplification behavior at saturation. In this paper we use a multi-electron radiator line broadening code, the PPP line shape code [16], to carry out a detailed analysis of the above broadening effects for the case of the XUV laser line emitted at $\lambda = 13.9$ nm, corresponding to the $4d$–$4p$ ($J = 0$–1) transition in Ni-like Ag. Lasing at this wavelength can be achieved over a broad range of plasma densities and temperatures, depending on the characteristics of the driving laser pulse, which is used to induce population inversions between the laser levels. Two pumping regimes were successfully implemented for XUV lasers and are considered in the present study. In the transient pumping regime [17], the free electrons are rapidly heated but the ionic temperature remains relatively low (around 20 eV) over the lasing timescale of few picoseconds. In the quasi-steady state (QSS) pumping regime [18], the longer lasing timescale ($\sim$100 ps) allows a more efficient thermalization of the ions with the heated electrons and the ionic temperature is higher (a few hundred eV). In both cases lasing is obtained over a relatively large range of electron densities, around 10^{20} cm^{-3}. It is thus expected that the relative contribution of Doppler broadening and collisional broadening will substantially vary over the considered plasma parameter range. This range also corresponds to a strong coupling plasma regime where correlations between particles can no longer be ignored. We thus investigate the accuracy of the usual free-particle Doppler approximation, by using classical molecular dynamics (MD) simulations. We show that for both pumping regimes, ionic correlations actually modify the radiator-motion broadened profiles and cannot be neglected in evaluating the Doppler effect. Similar MD techniques were previously used in the context of XUV laser by Pollock et al., in 1993 [11] to study the existence of ionic correlation effects in Ne-like Se and Ni-like Ta pumped in the QSS regime. The authors concluded that collisional ("Dicke") narrowing was not a factor in modeling the studied XUV laser line shapes. Our present results, performed for a different element and over a broader plasma parameter range, are not in contradiction with these results. Although collisional narrowing induced by ionic correlations can be significant, especially at high electron density, the net effect remains relatively small, due to the important contribution of collisional broadening to the overall (intrinsic) linewidth. However we show that ionic correlations will lead to a significant homogenization of the spectral line that should be taken into account in the description of amplification and saturation of the lasing line. We propose a simple model that reproduces the results of the MD simulations with good accuracy for the two considered regimes of pumping.

2. Spectral line shape modeling

If one accounts for the emitter motion, the general expression of the line profile reads [14]:

$$I(\omega) = \Re e \frac{1}{\pi} \int_0^\infty dt e^{i\omega t} < e^{i(\mathbf{k}\cdot\mathbf{r}(t) - \mathbf{k}\cdot\mathbf{r}(0))} \mathbf{d}(t)\cdot\mathbf{d}(0) > \quad (1)$$

where $<>$ denotes an ensemble average over the emitter plus plasma system, $\mathbf{d}$ is the radiator dipole operator and $k = 2\pi/\lambda$ with λ the wavelength of the considered line. The factors $e^{\pm i\,\mathbf{k}\cdot\mathbf{r}}$ accounts for the radiator's center-of-mass motion. Broadenings due to the interaction of the emitting ion with surrounding particles and to emitter motion are statistically dependent in the general case. Broadening due to interactions results from a modification of the internal state of the atomic oscillator. Both this internal state and the velocity of translational motion of the emitter can be altered in the same collision.

In this study, interactions with the electronic component of the plasma dominate, giving rise to a phase shift of the atomic oscillator. This phase shift is due to electronic collisions that substantially change the phase without altering the velocity of the emitter owing to the great difference of masses. So, it is quite accurate to ignore correlations between the ion translation $\mathbf{r}(t)$ and the dipole moment $\mathbf{d}(t)$:

$$I(\omega) = \Re e \frac{1}{\pi} \int_0^\infty dt e^{i\omega t} < e^{i(\mathbf{k}\cdot\mathbf{r}(t) - \mathbf{k}\cdot\mathbf{r}(0))} >< \mathbf{d}(t)\cdot\mathbf{d}(0) > . \quad (2)$$

The line shape appears as the Fourier-transformed of a product of two correlation functions, the radiator dipole operator correlation function, $C(t) =< \mathbf{d}(t)\cdot\mathbf{d}(0) >$, and the self-structure factor, $S_s(k,t) =< e^{i(\mathbf{k}\cdot\mathbf{r}(t) - \mathbf{k}\cdot\mathbf{r}(0))} >$ which can be calculated independently. The line shape is also the convolution of the respective profiles due to interactions with the bath, $I_{\mathrm{int}}(\omega)$ and to emitter motion $I_{\mathrm{D}}(\omega)$.

The correlation function, $C(t)$, of the radiator dipole operator, $\mathbf{d}$ can be written in Liouville space as [19,20]:

$$C(t) =<< \mathbf{d}^\dagger | \{U_l(t)\}_{\mathrm{bath}} | \mathbf{d}\rho_0 >> \quad (3)$$

where the double bra and ket vectors are defined as usual in Liouville space. Here ρ_0 is the equilibrium density matrix and $\{U_l(t)\}_{\mathrm{bath}}$ is the bath-averaged evolution operator of the emitter. $U_l(t)$ is the solution of the following stochastic Liouville equation (SLE):

$$\frac{\mathrm{d}U_l(t)}{\mathrm{d}t} = -iL_l \cdot U_l(t) \quad (4)$$

with the condition $U(0) = I$. L_l designates the Liouvillian of the radiator in the bath. We have $L_l = L_0 + l(t)$, where L_0 is the Liouvillian of the free radiator and $l(t)$ a random perturbation of the thermal bath (the plasma).

In the standard theory [9,14], due to their great difference of mass, ions and electrons are treated in different ways, leading to:

$$L_l(t) = L_0 - \mathbf{d}\cdot\mathbf{E_l}(t) - i\Phi \quad (5)$$

where $\mathbf{E_l}(t)$ is the electric field produced by surrounding ions in a given configuration l and Φ is the electronic collisional operator. The ionic electric field is usually considered as quasi-static and is represented by its static distribution $W(E_l)$ [21]. We then have

$$I_{\rm int}(\omega) \;=\; \Re e\frac{1}{\pi}\int_0^\infty dt e^{i\omega t}\int_0^\infty dE_l W(E_l) << \mathbf{d}^\dagger\left|e^{-iL_l t}\right|\mathbf{d} >> . \qquad (6)$$

In this work, the PPP line shape code [16] is used to calculate $I_{\rm int}(\omega)$. This code has been designed for calculating the profile of spectral lines emitted by multi-electron ionic emitters in hot and dense plasmas. The Stark broadening is taken into account in the framework of the standard theory by using the static ion approximation and an impact approximation for the electrons, or including the effects of ionic perturber dynamics by using the Fluctuation Frequency Model [22,23] when the static approximation fails. The atomic data required for the calculation are extracted from an external atomic structure code [24]. The effect of the electronic microfield component on the radiator is calculated in the framework of a binary collision relaxation theory, introducing a homogeneous damping and shift term, i.e., a collisional operator, to the emitter Hamiltonian. This operator depends on the density and temperature of the plasma and can be calculated either using a quantum mechanical relaxation theory or a classical path assumption for the perturbing electrons. Here, in the PPP code, the option of a modified semiclassical model, in which a strong (close) collision term is added to the semiclassical term, has been chosen [25].

The self-structure factor is well known in the free-particle limit resulting from the hypothesis that each radiating ion moves at constant velocity with a Maxwellian distribution of velocities, and is given by:

$$S_s(k,t) \;=\; e^{-k^2t^2/2\beta m}, \qquad (7)$$

with $\beta = 1/k_BT$ and m the ion mass. A Fourier transform then yields the usual area-normalized Gaussian Doppler line profile:

$$I_{\rm D}(\omega) \;=\; \frac{c}{\omega_0}\left[\frac{m}{2\pi k_BT}\right]^{1/2}\exp\left[\frac{-mc^2(\omega-\omega_0)^2}{2k_BT\omega_0^2}\right] \qquad (8)$$

with $\omega_0 = kc$, whose linewidth is given by:

$$\Delta\omega_{\rm D} \;=\; 2\sqrt{\frac{2k_BT}{m}\ln 2}\;\frac{\omega_0}{c}. \qquad (9)$$

A straightforward way to take into account interactions between ions in the calculation of the line shape, is to use a classical molecular dynamics simulation techniques (MD) to compute $S_s(k,t)$. A Fourier transform of $S_s(k,t)$ will yield the corresponding profile accounting for ionic interactions. In standard classical MD simulation, the plasma model consists of classical point ions interacting together through a Coulombic potential screened by electrons and localized in a cubic box of side L with periodic boundary conditions. The ionic interaction potential is chosen to account for the polarization of the electron gas by the ionic charge distribution, with the screening length equals to the electron Debye length, $\lambda_{\rm D} = \sqrt{k_BT_e/4\pi N_e e^2}$ in accordance with the plasma electronic densities, N_e, and temperatures, T_e. Newton's equations of particle motion are integrated by using a velocity-Verlet algorithm using a time-step consistent with energy conservation. Due to periodic boundary conditions, $k = 2\pi/\lambda$ must satisfy:

$$k_{x,y,z} \;=\; n_{x,y,z}2\pi/L, \qquad (10)$$

$n_{x,y,z}$ being an integer number. The number of particles, N (thus L), is chosen to find k as close as possible to that of the considered laser line. Integrating Newton's equation gives access to the positions and velocities of the ions as a function of time and thus to the associated static and dynamic statistical properties such as structure factors, velocity correlation functions, diffusion coefficients, ion–ion collision rates, etc.

3. Calculated linewidths

In this section, we investigate the broadening of the Ni-like Ag laser $4d$–$4p$ ($J = 0$–1) line at 13.9 nm over a broad range of densities and temperatures, over which collisional excitation pumping of this transition can be achieved. Electronic densities are in the range 5×10^{19}–8×10^{20} cm^{-3}, the electron temperature can vary between 200 and 700 eV [26]. For the ionic temperature two different regimes of pumping were considered. For the transient pumping regime, the ionic temperature remains relatively low, typically 20–50 eV. For the quasi-steady state pumping regime, the ionic temperature is higher, typically 200 eV. The different causes of broadening (radiative decay, interaction with surrounding particles and Doppler effect) have been investigated over this extended plasma parameter range. In the following, we will discuss two series of results corresponding respectively to the transient pumping case ($T_i = 20$ eV, $T_e = 200$ eV) and to the QSS pumping case ($T_i = T_e = 200$ eV) pumping, for different electronic densities.

The PPP code was used to provide the optically thin spectral profile of the lines of interest for given values of density and temperature of the emitters and of the surrounding free electrons. It has been checked that the Stark effect associated with the ionic microfield has a negligible contribution to the line profile whatever the densities and temperatures of interest. The homogeneous broadening consists in natural broadening and electronic collisional broadening. Accounting for both effects does not yield difficulties as they are statistically independent, giving rise to a linewidth equal to the sum of the respective linewidths. In the following, this broadening will be referred to as lifetime broadening. The broadening due to the translational motion of the emitter (Doppler effect) has been obtained by using the self-structure factors computed by MD simulations, which account for velocity changing effects. The simulated linewidths were compared to the usual free-particle limit approximation given in Eq. (9). Some typical numbers for the physical quantities of the simulated plasmas over the considered density range, and some technical details of the MD simulations are given in Table 1. The second and third columns show the values taken by the plasma coupling parameter $\Gamma = Z^2e^2/(r_0kT_i)$, r_0 being the ion sphere radius, $r_0 = (3/(4\pi N_i))^{1/3}$, for the transient pumping case (trans) and for the QSS case respectively. One can see that in the transient case Γ has large values, ranging between $\sim$5 and $\sim$14, while in the QSS case Γ is smaller, ranging between $\sim$0.6 and $\sim$1.4. As shown in

Table 1
Characteristic quantities used in MD simulations.

N_e (cm^{-3})	$\Gamma_{\rm trans}$	$\Gamma_{\rm QSS}$	N	$kr_0^{\rm laser}$	$kr_0^{\rm MD}$	$\omega_{\rm pi}$ (eV)	$\Delta\omega_{\rm D}^{\rm trans}$ (eV)	$\Delta\omega_{\rm D}^{\rm QSS}$ (eV)
5×10^{19}	5.79	0.58	300	2.03	2.016	2.57×10^{-3}	2.95×10^{-3}	9.34×10^{-3}
1×10^{20}	7.29	0.73	300	1.61	1.647	3.64×10^{-3}	–	–
2×10^{20}	9.19	0.92	300	1.28	1.302	5.14×10^{-3}	–	–
4×10^{20}	11.57	1.16	300	1.01	1.008	7.27×10^{-3}	–	–
7×10^{20}	13.95	1.39	300	0.82	0.843	9.62×10^{-3}	–	–

Table 1 the number of particles, N, in the simulation box has been chosen equal to 300 for all conditions. This choice leads to a simulation box size L large compared to the correlation lengths ensuring the results are independent of N while allowing one to find values of k that satisfy Eq. (10) and kr_0^{MD} values that match the laser wave number kr_0^{laser}. The remaining columns of Table 1 show the plasma frequency, $\omega_{\mathrm{pi}} = \sqrt{4\pi N_i (Z_i e)^2/m}$, and the Doppler frequency widths $\Delta\omega_{\mathrm{D}}$ obtained in the free particle limit for the two considered pumping regimes.

Fig. 1 shows the spectral linewidths (FWHM) obtained for the different broadening mechanisms of the $4d-4p$ laser line calculated as a function of the electron density for the transient pumping case. Here, the ionic temperature is relatively low ($T_i = 20$ eV) and the electronic densities are in the range 5×10^{19}–7×10^{20} cm^{-3}. The electron temperature is taken as $T_e = 200$ eV.

One can see that the lifetime broadening (dashed line and stars) increases almost linearly with the electron density, through the effect of electronic collisions. It becomes larger than the radiator motion broadening at the relatively low density of $N_e \geq 1 \times 10^{20}$ cm^{-3}. The radiator motion broadening calculated in the free-particle limit (dotted line) is compared to the results of MD simulations (solid line and stars), accounting for interactions between particles. In these cases, the plasmas are strongly coupled (Γ from $\sim$6 to $\sim$14) compromising the concept of binary collisions between ions because the ions are always in interaction with each other. Collective effects involving multiple collisions inducing velocity changing are expected to affect the profiles. Despite the fact that a significant narrowing of the line is clearly seen over the entire considered range of electron density (compare dotted line to solid line and stars), the overall linewidth is not really altered (compare gray squares to black circles), as the lifetime broadening dominates the profile. However, the effect of correlations, not significant on overall linewidth, will affect the nature of the line profile, in contributing to its homogenization, as will be discussed below.

For the QSS pumping case, the ionic temperature was taken equal to the electron temperature, $T_i = T_e = 200$ eV and four different electron densities were considered: $N_e = 1 \times 10^{20}$, 2×10^{20}, 4×10^{20} and 7×10^{20} cm^{-3}. Because the ionic temperature is higher, the plasma coupling parameter in this regime is smaller than in the transient pumping case, ranging between 0.7 and 1.4 (see Table 1). The results of the PPP and MD simulations in terms of linewidth are shown in Fig. 2.

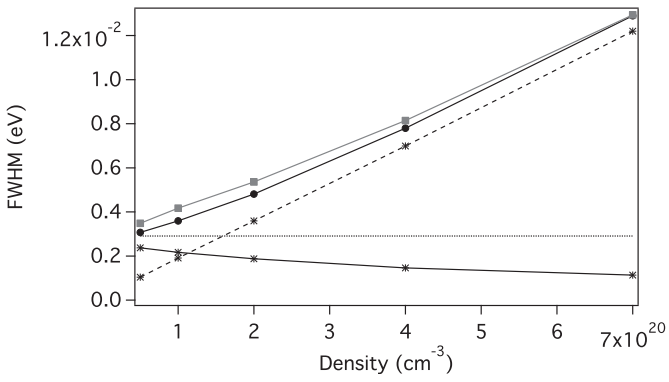

Fig. 1. Full-width at half-maximum spectral width versus density of the $4d-4p$ laser line in the transient pumping case. Dashed line and stars: Lifetime (radiative + collisional) broadening. Dotted line: Doppler (free-particle limit) broadening. Solid line and stars: radiator motion broadening accounting for particle interactions. Upper curves: overall linewidth including all broadening contributions, in the free-particle limit (gray solid line and squares), and accounting for interactions (black solid lines and circles).

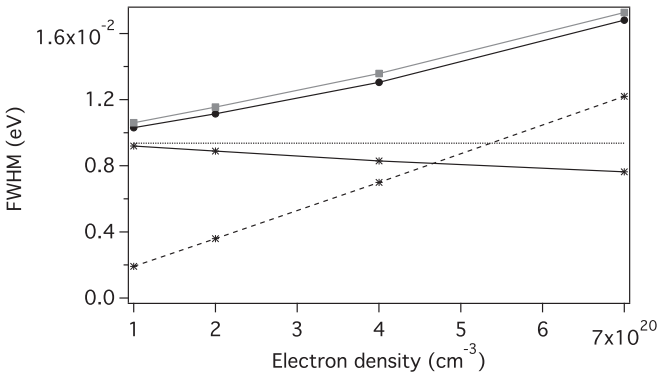

Fig. 2. Same as Fig. 1 but for the QSS pumping regime.

As in the transient pumping case (Fig. 1), the lifetime broadening contribution increases linearly with N_e. However here it becomes dominant over the radiator motion broadening at large density only, typically above 5–6 $\times$ 10^{20} cm^{-3}. This illustrates again the strong dependence of the contribution of lifetime broadening of the XUV laser intrinsic profile with respect to the local plasma parameters in the gain region. The narrowing of the radiator-motion linewidth induced by the correlations between particles is still clearly observed in Fig. 2 (compare dotted line to solid line and stars). Finally, even though the collisional narrowing is still apparent in the overall linewidth, here again the main effect of particle correlations will be the homogenization of the profile.

Similar results have been obtained for other electron temperatures (not shown in Figs. 1 and 2). The contribution of the lifetime broadening to the intrinsic line profile has been calculated for different densities and for several electron temperatures up to 700 eV. The results were fit with analytical functions and a simple expression was derived for the FWHM:

$$\Delta\lambda_{\mathrm{h}}(N_e, T_e) = \alpha_1 (kT_e)^{-\beta_1}\left(1 - \frac{N_e}{8\times 10^{20}}\right) + \alpha_2 (kT_e)^{-\beta_2}\left(\frac{N_e}{8\times 10^{19}} - 1\right) \quad (11)$$

where $\Delta\lambda_{\mathrm{h}}$ is in mÅ and N_e in cm^{-3}. The numerical values of the coefficients α_1, α_2, β_1 and β_2 derived from the fits are as follows: $\alpha_1 = 8.111 \times 10^{-3}$; $\alpha_2 = 8.533 \times 10^{-3}$; $\beta_1 = 0.2053$; $\beta_2 = 0.2373$. This formula reproduces the results of the detailed PPP calculations with an accuracy of better than $\pm$2% within the range of interest. This relation can be easily included in radiative transfer simulation codes, which require accurate values for the optically thin linewidth to calculate the spectral profile of the amplified XUV beam.

In the free-particle limit approximation, the Doppler line profile is inhomogeneous and can be described by a Gaussian function given in Eq. (8) and the Doppler linewidth depends on only T_i as shown in Eq. (9). The lifetime broadening yields a homogeneous profile, which can be described by a Lorentzian function. As is well known, the resulting spectral profile will be the convolution of the homogeneous and inhomogeneous profiles, leading to the Voigt profile. The overall linewidth, $\Delta\lambda_{\mathrm{tot}}$, is a complex combination of both homogeneous, $\Delta\lambda_{\mathrm{h}}$, and inhomogeneous, $\Delta\lambda_{\mathrm{D}}$, linewidths. It has been checked that the formula derived in Ref. [27]:

$$\Delta\lambda_{\mathrm{tot}} = \frac{1}{2}\Delta\lambda_{\mathrm{h}} + \left(\frac{1}{4}\Delta\lambda_{\mathrm{h}}^2 + \Delta\lambda_{\mathrm{D}}^2\right)^{1/2} \quad (12)$$

fits our results to better than 1%.

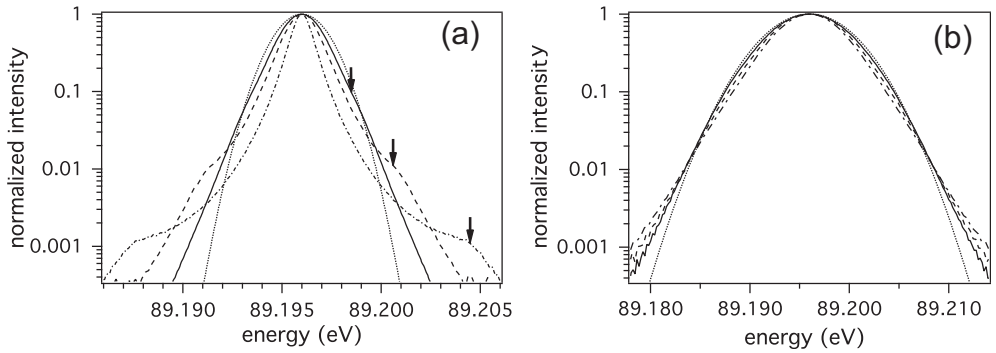

Fig. 3. Spectral profile of the $4d$–$4p$ laser line including the radiation-motion broadening in the presence of ionic correlations for three different electron densities. (a) Transient pumping case, $T_i = 20$ eV; (b) QSS pumping case, $T_i = 200$ eV. The different densities curves are: solid line: $N_e = 5 \times 10^{19}$ cm^{-3} in (a) and $N_e = 1 \times 10^{20}$ cm^{-3} in (b). Dashed line: $N_e = 2 \times 10^{20}$ cm^{-3} in (a) and (b). Dash-dot line: $N_e = 7 \times 10^{20}$ cm^{-3} in (a) and (b). Dotted line: Doppler profile in the free-particle limit. In (a) the black arrows show the positions of the shoulder structures, which are given by the oscillation frequency of the velocity autocorrelation function.

It can be easily checked that the formula given by Eq. (12) does not fit our results if ionic interactions are taken into account. The ionic correlations do not only affect the linewidths but also induce an homogenization of the spectral profile. The radiator-motion profile is no longer Gaussian, and the overall profile is no longer a Voigt profile [13]. Not only Eq. (12) no longer applies, but also the relative weight of homogeneous versus inhomogeneous components in the overall intrinsic profile, which controls the behavior at saturation, is significantly modified. It is thus necessary to investigate in more detail the modification induced to the spectral profile by the effect of velocity-changing collisions, which is the purpose of the next section.

4. Calculated spectral profiles

In this section, we will focus our discussion on the radiator-motion broadening component, ignoring the contribution of the lifetime broadening to the spectral profile.

The narrowing of the radiator-motion profile, observed for both the transient and QSS pumping regime in Figs. 1 and 2, can be understood in terms of the correlation function $S_s(k,t)$ for a moving emitter. In the free particle limit, $S_s(k,t) = e^{-k^2t^2/2\beta m} \equiv e^{-k^2t^2\bar{v}^2/4}$, the characteristic Doppler correlation time, $\tau_D \approx \lambda/\bar{v}$, can then be understood as the time taken by a radiator having the mean thermal velocity $\bar{v}$ to move a distance equal to the laser wavelength λ. Any factor restricting or hindering the movement of the emitter will broaden $S_s(k,t)$ and hence narrow the line shape. Due to the strong coupling plasma parameters involved here (in particular in the transient pumping case), ions are in constant interaction and they are more and more hindered from moving freely as the plasma density – or the coupling factor Γ – increases.

For a better understanding of the effect of these long range interactions, line profiles calculated for different densities are plotted in the same graph in logarithmic units, for two ionic temperatures corresponding to the transient (Fig. 3(a), $T_i = 20$ eV) and QSS (Fig. 3(b), $T_i = 200$ eV) pumping regimes respectively. In both graphs the unaffected Doppler profile is also plotted for comparison. It can be seen that the effect of ionic correlations yields distinct features in the profile in each pumping regime. In the transient pumping case, Fig. 3(a), the profile is not only narrowed but also a shoulder structure appears in the wings, at a distance form the line center that increases with N_e. In the QSS pumping case (Fig. 3(b)), the line shape is modified and the width is slightly reduced, but no structures are apparent in the wings. The frequency shifts, $\Delta\omega_{osc}$, delimiting the position of the shoulders are shown by black arrows in Fig. 3(a). We have checked that the values of those frequency shifts are actually close to the ionic plasma frequency for the given N_e. More precisely they correspond to the oscillation frequency of the velocity autocorrelation function, $C_v(t) = <\mathbf{v}(t)\cdot\mathbf{v}(0)>$. This function reveals the properties of single-particle motion in the plasma. $C_v(t)$ is calculated from our MD simulations and the oscillation frequency, $\Delta\omega_{osc}$ is deduced from $C_v(t)$ by a Fourier transform. Examples of calculated velocity autocorrelation functions and of their Fourier transforms are given in Fig. 4(a), (b), for several values of Γ. For the largest values of Γ the decay of $C_v(t)$ is characterized by the appearance at large times of oscillations at a frequency close

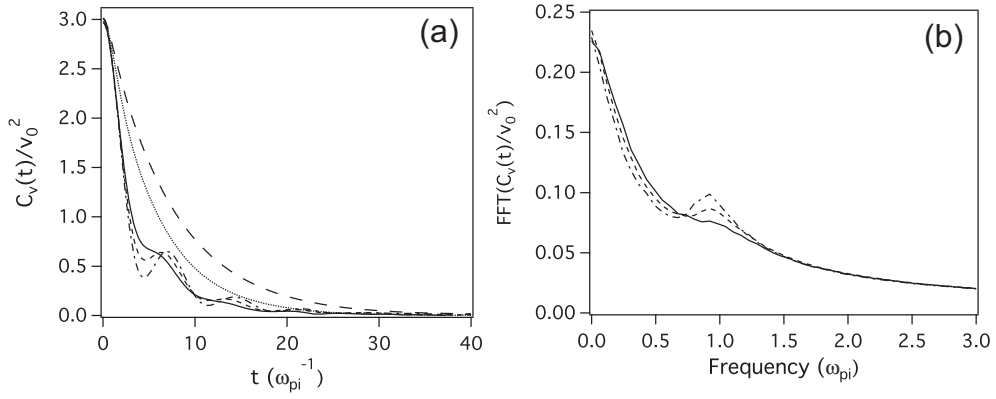

Fig. 4. (a) Velocity autocorrelation function $C_v(t)$ for increasing values of the coupling factor Γ. Dashed line: $\Gamma = 0.73$. Dotted line: $\Gamma = 1.39$. Solid line: $\Gamma = 5.79$. Short-dashed line: $\Gamma = 9.19$. Dash-dotted line: $\Gamma = 13.95$. (b) Fourier transform of $C_v(t)$ for $\Gamma = 5.79$, 9.19 and 13.95 (same plotting code). The velocities are in units of kT_i/m and the time in units of ω_{pi}^{-1}.

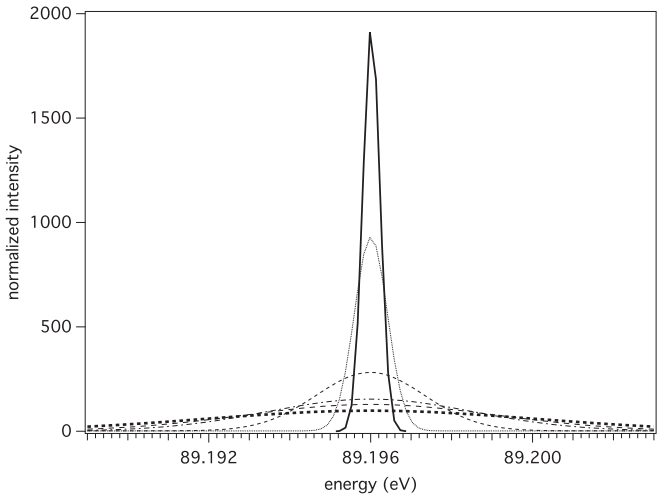

Fig. 5. Evolution with time of the frequency distribution function of a set of particles with an initial velocity such as $\mathbf{k}\cdot\mathbf{v}(0) = 0 \pm \Delta\omega$ for plasma conditions relevant to the QSS pumping case at $N_e = 1 \times 10^{20}$ cm^{-3}. Times $t = 0$ (solid line), $0.24\ \omega_{pi}^{-1}$ (dotted line), $1.0\ \omega_{pi}^{-1}$ (short-dashed line), $2.5\ \omega_{pi}^{-1}$ (dash-dotted line) and $3.83\ \omega_{pi}^{-1}$ (dashed line). The frequency distribution gets broader with time, on a timescale that is comparable with the radiative lifetime. The bold dash line corresponds to the Doppler free-particle limit that would be reached at infinite time.

to ω_{pi}. The oscillations are already seen at $\Gamma = 5.786$ ($N_e = 5 \times 10^{19}$ cm^{-3}) and become more pronounced as Γ increases. They are due to the coupling between the collective density fluctuations and the single particle motion [28].

In order to have a more detailed insight into the dynamics of a particle in those XUV laser plasmas, we have calculated the evolution in time of the frequency distribution associated to a set of particles chosen to have an initial velocity $\mathbf{v}(0)$ such as $\mathbf{k}\cdot\mathbf{v}(0) = \omega \pm \Delta\omega$ for $\omega = 0$ and $\Delta\omega$ chosen sufficiently large to have a representative number of tagged particles. The plasma conditions are those relevant to the QSS pumping case at $N_e = 1 \times 10^{20}$ cm^{-3}, i.e., conditions where the plasma coupling parameter is not large ($\Gamma = 0.73$), and collisional narrowing is small (see Fig. 2). The results of the calculation are shown in Fig. 5. The sharper distribution corresponds to the initial time when the set of particles such as $\mathbf{k}\cdot\mathbf{v}(0) = 0$ emit at a frequency equals to $\omega_0 \pm \Delta\omega$. As time increases the frequency distribution gets broader, as a result of velocity-changing collisions, and tends to the infinite time limit corresponding to a frequency distribution given by the equilibrium velocity distribution. This limit is the usual Doppler distribution in the free-particle limit, also shown in Fig. 5 (black dashed curve). Four different times of evolution ($0.24\ \omega_{pi}^{-1}$, $1.0\ \omega_{pi}^{-1}$, $2.5\ \omega_{pi}^{-1}$ and $3.83\ \omega_{pi}^{-1}$) have been chosen, the latter corresponding to the radiative lifetime of the laser transition. It can be seen that during their effective lifetime, the radiating and absorbing ions sample many velocities, not just one as it is supposed in the Doppler free particle limit. The effect of this rapid velocity redistribution will be to effectively homogenize the radiator-motion broadening component of the intrinsic line profile. A similar effect is also obtained for conditions relevant to the transient pumping case. This means that collisional redistribution cannot be ignored when evaluating the spectral behavior of the laser line following amplification and saturation.

An interesting feature that can be noticed in Fig. 5 is that interactions between particles give rise to small changes in the velocity at short time-scale: the frequency redistribution at $t = 0.24\ \omega_{pi}^{-1}$ is limited to frequencies around the initial frequency suggesting that the interactions give rise to small-angle scattering. Moreover, it is necessary to wait long enough to fill the entire distribution. This behavior suggests that the dynamics of the ions in the present plasmas could be modeled by a Brownian-motion model [13,29]. In this model, the following expression was derived for the self-structure factor:

$$S_s(k,t) = e^{-\frac{k^2}{2}<x_k^2>}, \quad <x_k^2> = \frac{\bar{v}^2}{\nu_d^2}\left(\nu_d t - 1 - e^{-\nu_d t}\right) \tag{13}$$

where $<x_k^2>$ is the mean square displacement in the direction of k over the time t and $\bar{v} = \sqrt{2k_BT_i/m}$. It is shown in Ref. [29] that ν_d is related to $C_v(t)$ by:

$$C_v(t) \equiv <\mathbf{v}(t)\cdot\mathbf{v}(0)> = \frac{3}{2}\bar{v}e^{-\nu_d t}. \tag{14}$$

The values of ν_d have been obtained by fitting the velocity autocorrelation functions obtained from our MD simulations, see, e.g., Fig. 4, with an exponential decreasing function. The ν_d values have been used in Eq. (13) to calculate $S_s(k,t)$, from which the line profile was derived through a Fourier transform. The results are presented in Fig. 6 and compared with our detailed MD calculations.

It can be seen in Fig. 6 that the Brownian-motion model gives a very good approximation to the spectral profiles calculated from detailed MD simulations, for both transient and QSS pumping cases and over a broad range of electron densities, even though the wings and the shoulder structures are not reproduced correctly. This is mainly because the velocity autocorrelation function, $C_v(t)$, can be very far from an exponential decreasing function, as can be seen in Fig. 4. Fitting $C_v(t)$ by an exponential form eliminates the oscillations expected at a frequency near ω_{pi}. Moreover the Markovian

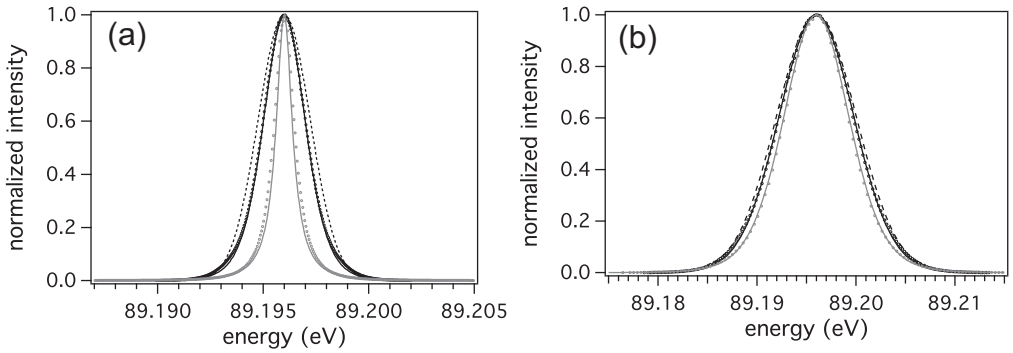

Fig. 6. Spectral profile (radiator motion broadening component) of the $4d$–$4p$ laser line calculated using the Brownian-motion model to account for ionic correlation effects. (a) Transient pumping: $N_e = 5 \times 10^{19}$ (solid black); $N_e = 7 \times 10^{20}$ (solid gray). (b) QSS pumping: $N_e = 1 \times 10^{20}$ (solid black); $N_e = 7 \times 10^{20}$ (solid gray). The Brownian-motion model reproduces the detailed MD simulation results (circles). The dotted line corresponds to the usual Doppler profile in the free-particle limit.

approximation used in the Brownian-motion model, e.g., any memory associated with the motion of the particle is ignored, is not valid in the plasmas of interest here, where the diffusing particles are similar to their neighbors [29]. Nevertheless, the Brownian-motion model without memory proposed here provides a simple and rapid way to account for the homogenization of the laser line profile due to ionic correlations, in good agreement with more sophisticated MD simulations. Such a model could be easily implemented in a radiative transfer calculation to investigate the saturation behavior of the laser line in the transient and QSS pumping regime.

5. Conclusion

In this paper we have presented a detailed analysis of the different broadening processes that affect the intrinsic profile of a XUV laser line, over an extended range of plasma parameters. Such a study is important to clarify the prospects of broadening the laser profile of existing collisional XUV lasers to achieve shorter femtosecond durations. Two different regimes of collisional excitation pumping have been considered: transient pumping for which ionic temperature is relatively low, so the plasma coupling parameter is large, and quasi steady state pumping for which the ionic temperature is higher and the plasma coupling parameter is of the order of 1. We show that the relative contribution of the lifetime broadening to the overall line profile strongly depends on the local plasma parameters in the lasing plasma. Using molecular dynamics simulations we have investigated the effect of ionic correlations on the radiator-motion broadening component. We find that for the entire plasma parameter range explored, this effect cannot be ignored. We show that ionic correlations lead to a significant narrowing of the radiator-motion broadened component compared to the usual Doppler (free-particle) limit, especially in the low ionic temperature transient pumping case. However this effect is largely masked when accounting for the lifetime broadening in the overall linewidth. We show that ionic correlations will also affect the inhomogeneous nature and, to a lesser extent, the shape of the profile, which are both important in evaluating the behavior of the laser line during amplification and saturation. By investigating the velocity autocorrelation function we show that the spectral features observed in the radiator-motion broadened profile are related to the plasma ionic oscillations. Finally we propose to use the Brownian-motion model to calculate the self-structure factor and the radiator-motion broadened line profile. This study will be the scope of our future work.

References

[1] O. Guilbaud, A. Klisnick, D. Joyeux, D. Benredjem, K. Cassou, S. Kazamias, D. Ros, D. Phalippou, G. Jamelot, C. Möller, Eur. Phys. J. D 40 (2006) 125.
[2] D. Benredjem, C. Möller, J. Dubau, T. Ball, Phys. Rev. A 73 (2006) 063820.
[3] O. Guilbaud, F. Tissandier, J.-P. Goddet, M. Ribière, S. Sebban, J. Gautier, D. Joyeux, D. Ros, K. Cassou, S. Kazamias, A. Klisnick, J. Habib, Ph. Zeitoun, D. Benredjem, T. Mocek, J. Nedjl, D. de Rossi, G. Maynard, B. Cros, A. Boudaa, A. Calisti, Opt. Lett. 35 (2010) 1326.
[4] F. Tissandier, S. Sebban, M. Ribière, J. Gautier, Ph. Zeitoun, G. Lambert, A. Barszczak Sardinha, J.-P. Goddet, F. Burgy, T. Lefrou, C. Valentin, A. Rousse, O. Guilbaud, A. Klisnick, J. Nejdl, T. Mocek, G. Maynard, Phys. Rev. A 81 (2010) 063833.
[5] D.S. Whittaker, M. Fajardo, Ph. Zeitoun, J. Gautier, E. Oliva, S. Sebban, P. Velarde, Phys. Rev. A 81 (2010) 043836.
[6] Y. Wang, M. Berrill, F. Pedaci, M.M. Shakya, S. Gilbertson, Z. Chang, E. Granados, B.M. Luther, M.A. Larotonda, J.J. Rocca, Phys. Rev. A 79 (2009) 023810.
[7] U. Zastrau, C. Fortmann, R.R. Faustlin, L.F. Cao, T. Doppner, S. Dusterer, S.H. Glenzer, G. Gregori, T. Laarmann, H.J. Lee, A. Przystawik, P. Radcliffe, H. Reinholz, G. Ropke, R. Thiele, J. Tiggesbaumker, N.X. Truong, S. Toleikis, I. Uschmann, A. Wierling, T. Tschentscher, E. Forster, R. Redmer, Phys. Rev. E 78 (2008) 066406.
[8] G.J. Pert, J. Opt. Soc. Am. B 11 (1994) 1425.
[9] H.R. Griem, Spectral Line Broadening by Plasmas, Academic, New York, 1974.
[10] H.R. Griem, Phys. Rev. A 33 (1986) 3580.
[11] E.L. Pollock, R.A. London, Phys. Fluids B 5 (1993) 4495.
[12] J.A. Koch, et al., Phys. Rev. A 50 (1994) 1877.
[13] S.G. Rautian, I.I. Sobel'man, Usp. Fiz. Nauk 90 (1966) 209.
[14] H.R. Griem, Principles of Plasma Spectroscopy, Cambridge University Press, 1997.
[15] R.H. Dicke, Phys. Rev. 89 (1953) 472.
[16] A. Calisti, F. Khelfaoui, R. Stamm, B. Talin, R.W. Lee, Phys. Rev. A 42 (1990) 5433.
[17] A. Klisnick, P. Zeitoun, D. Ros, A. Carillon, P. Fourcade, S. Hubert, G. Jamelot, C.L.S. Lewis, A.G. Mac Phee, R.M.N. O'Rourcke, R. Keenan, P.V. Nickles, K. Janulewicz, M. Kalashnikov, J. Warwick, J.-C. Chanteloup, A. Migus, E. Salmon, C. Sauteret, J.P. Zou, J. Opt. Soc. Am. B 17 (2000) 1093.
[18] J. Zhang, A.G. MacPhee, J. Nilsen, J. Lin, T.W. Barbee Jr., C. Danson, M.H. Key, C.L.S. Lewis, D. Neely, R.M.N. O'Rourke, G.J. Pert, R. Smith, G.J. Tallents, J.S. Wark, E. Wolfrum, Phys. Rev. Lett. 78 (1997) 3856.
[19] M. Baranger, in: D.R. Bates (Ed.), Atomic and Molecular Processes, Academic, New York, 1964.
[20] U. Fano, Phys. Rev. 131 (1963) 259.
[21] C.A. Iglesias, H.E. DeWitt, J.L. Lebowitz, D. MacGowan, W.B. Hubbard, Phys. Rev. A 31 (1985) 1698. C.A. Iglesias, et al., J. Quant. Spectrosc. Radiat. Transf. 65 (2000), 303.
[22] B. Talin, A. Calisti, L. Godbert, R. Stamm, R.W. Lee, L. Klein, Phys. Rev. A 51 (1995) 1918.
[23] A. Calisti, et al., Phys. Rev. E 81 (2010) 016406.
[24] I.P. Grant, et al., Comput. Phys. Commun. 21 (1980) 207.
[25] H.R. Griem, M. Blaha, P.C. Kepple, Phys. Rev. A 19 (1979) 2421.
[26] G.J. Pert, Phys. Rev. A 73 (2006) 033809.
[27] T.J. Manning, J.D. Winefordner, B.A. Palmer, D.E. Hof, Spectrochim. Acta B Atom. Spectros. 45 (1990) 1031.
[28] J.P. Hansen, I.R. McDonald, E.L. Pollock, Phys. Rev. A 11 (1975) 1025.
[29] J.P. Hansen, I.R. McDonald, Theory of Simple Liquids, Academic Press, London, 1976.